

A FRAMEWORK FOR MODELING EVOLUTION OF THE CORE MASS FUNCTION

By

THEO RICHARDSON

A DISSERTATION PRESENTED TO THE GRADUATE SCHOOL
OF THE UNIVERSITY OF FLORIDA IN PARTIAL FULFILLMENT
OF THE REQUIREMENTS FOR THE DEGREE OF
DOCTOR OF PHILOSOPHY

UNIVERSITY OF FLORIDA

2025

© 2025 Theo Richardson

To Mom and Dad

ACKNOWLEDGEMENTS

I'd like to effusively thank my advisor, Adam Ginsburg, for his guidance on this work and through graduate school in general. He has consistently been a very capable, reliable, and adaptable mentor who managed to generally keep me on track while also sending me to some pretty interesting places, both intellectually and in real life. In that same vein, I want to extend my thanks to the people that have collaborated with me: Erik Rosolowsky, Josh Peltonen, Rémy Indebetouw, and Tom Robitaille. Each of you provided extremely helpful insight and critique of the work described in this thesis, and it's much stronger now than it would have been without you. Further, I thank the members of my committee—Desika Narayanan, Jaehan Bae, and Mickey MacKie—for their assistance in getting my thesis over the finish line. However, I do NOT thank them for competing with me for computing time. (A corollary thank-you goes to anyone who has refereed one of my papers. Since the process is anonymized, I have no idea who those people might be, but if you ever read this, you also helped.)

In addition to the people directly involved with the crafting of this work, I'd like to extend my thanks to the members of my research group for being an excellent sounding board, grounding influence, and general good source of information. I would also like to acknowledge University of Florida Research Computing, as well as the software packages Astropy ([Astropy Collaboration et al., 2013, 2018, 2022](#)), Dask ([Dask Development Team, 2016](#)), Matplotlib ([Hunter, 2007](#)), NumPy ([Harris et al., 2020](#)), Scikit-learn ([Pedregosa et al., 2011](#)), and SciPy ([Virtanen et al., 2020](#)). Without these, my research would have been significantly more difficult if not outright impossible, and then where would be we?

This also seems like a good time to appreciate those who helped me exist outside of my thesis. In particular, I'd like to thank my parents, who supported me through the journey of graduate school in so many ways that to recount them all risks ballooning the already high page count of this thing. I'd also like to thank my fellow graduate students for being my friends and consistently creating a welcoming environment at and beyond work. Finally, I recognize my

roommate Mallory, whose attempted edits to my work were not requested but are duly acknowledged¹.

¹ now please stop walking across the keyboard?

TABLE OF CONTENTS

	<u>page</u>
ACKNOWLEDGEMENTS	4
LIST OF TABLES.....	8
LIST OF FIGURES.....	10
LIST OF ABBREVIATIONS	11
ABSTRACT.....	13
CHAPTER	
1 INTRODUCTION AND OPENING REMARKS	15
2 AN UPDATED MODULAR SET OF SYNTHETIC SPECTRAL ENERGY DISTRIBUTIONS FOR YOUNG STELLAR OBJECTS	18
2.1 Motivation	18
2.2 The Robitaille (2017) Models.....	20
2.2.1 Geometries	20
2.2.2 Dust	23
2.2.3 SEDs	23
2.3 Additions.....	24
2.3.1 Mass Calculation.....	25
2.3.2 Temperatures.....	27
2.3.3 Disk Properties.....	28
2.3.4 Extinction.....	29
2.3.5 Convenience Additions	30
2.3.6 Completed YSO Models	32
2.3.7 Content Updates.....	33
2.4 Results	35
2.4.1 Mass Measurements	35
2.4.2 YSO Classification	42
2.5 Closing Remarks	52
3 A FRAMEWORK FOR MODELING THE EVOLUTION OF YOUNG STELLAR OBJECTS	54
3.1 Motivation	54
3.2 Framework	55
3.2.1 The R24 Models	55
3.2.2 YSO Composition.....	57
3.2.3 Proximity	62
3.3 Results	64
3.3.1 Flux Predictions.....	64
3.3.2 Performance	69

3.3.3	Caveats	75
3.4	Further Uses.....	76
3.4.1	Comparison to a Contemporary Grid	77
3.4.2	YSO Classification	85
3.5	Closing Remarks.....	101
4	A REVIEW OF YSO CLASS AND STAGE DEFINITIONS	104
4.1	Motivation	104
4.2	Class.....	105
4.3	Stage.....	108
4.4	Congruence	111
4.4.1	Class	112
4.4.2	Colors	116
4.4.3	Other	118
4.5	Closing Remarks.....	120
5	A FRAMEWORK FOR MODELING THE EVOLUTION OF PROTOSTELLAR POP- ULATIONS	122
5.1	Motivation	122
5.2	Cluster Construction	124
5.2.1	Procedure.....	124
5.2.2	Components	126
5.3	Model Populations.....	138
5.3.1	Accretion History	138
5.3.2	Star Formation History	145
5.4	Closing Remarks.....	148
6	SUMMARY AND CONCLUSIONS	150
APPENDIX		
A	MODEL BOLOMETRIC LUMINOSITIES	153
B	ADDITIONAL COLOR-COLOR DIAGRAMS	158
C	THE IMPACT OF ACCRETION LUMINOSITY.....	164
D	MORE ON YSO COMPOSITION.....	167
E	ADDITIONAL PLOTS	172
F	ZHANG & TAN (2018) CLASS-CLASS PLOTS.....	174
LIST OF REFERENCES.....		178
BIOGRAPHICAL SKETCH		188

LIST OF TABLES

<u>Tables</u>	<u>page</u>
3-1 Comparing to literature modeling approaches	70
5-1 Population modeling framework overview.....	127

LIST OF FIGURES

<u>Figures</u>	<u>page</u>
2-1 Sample model density profile.....	21
2-2 R17 dust opacity.....	24
2-3 Sample model temperature profile	27
2-4 Sample model disk Q profile	29
2-5 Main sequence comparison.....	32
2-6 Newly completed models.....	34
2-7 Comparing “observed” masses to true masses	38
2-8 Performance of a representative dust temperature	39
2-9 Dust temperatures vs. observed flux	41
2-10 Class color-color diagrams	44
2-11 Stage color-color diagrams	47
2-12 Set-wide class-stage confusion matrix	51
3-1 Comparison of a sample of accretion models	59
3-2 Illustrating model selection.....	63
3-3 Predicting flux evolution	66
3-4 Uncertainty in predicted SEDs.....	72
3-5 Accuracy in predicted SEDs.....	73
3-6 Zhang & Tan (2018) SED recovery	79
3-7 Comparing Zhang & Tan (2018) vs. Robitaille (2017) dust opacities	81
3-8 RT with Zhang & Tan (2018) vs. Robitaille (2017) dust models	82
3-9 The impact of Wood et al. (2002) dust on flux recovery	84
3-10 Physically motivated confusion matrices	89
3-11 Confusion matrix with a narrowed scope.....	94
3-12 Examining Class definitions	97
3-13 Contextualizing Stage definitions with flux predictions.....	99
5-1 Comparison of all accretion models.....	130
5-2 The impact of multiplicity on modeled YSOs.....	134

5-3	The impact of multiplicity on the stellar IMF.....	136
5-4	Output from a simulated protocluster	139
5-5	Evolution of protostellar properties per accretion history	141
5-6	Evolution of predicted fluxes per accretion history.....	143
5-7	Evolution of protostellar properties per formation history	146
5-8	Evolution of predicted fluxes per formation history	147
A-1	Bolometric vs. source luminosities	155
A-2	...for θ -dependent models	156
A-3	...for models with envelopes	157
B-1	Alternate view of Class color-color diagrams.....	159
B-2	Alternate view of Stage color-color diagrams.....	160
B-3	Bare star color-color diagrams.....	161
B-4	Bare star + medium SED comparison	162
B-5	IRAC color-color diagrams.....	163
C-1	Intrinsic vs. total luminosity illustrated	164
C-2	Intrinsic vs. total luminosity in predictions.....	166
D-1	Comparing distance definitions	170
E-1	Illustrating model selection for a lower-mass star	172
E-2	Illustrating model selection for a higher-mass star	173
F-1	Class 0/I comparison for Zhang & Tan (2018).....	175
F-2	...colored by various model properties	177

LIST OF ABBREVIATIONS

2CCA	Two-component competitive accretion
2CTC	Two-component turbulent core accretion
ALMA	Atacama Large Millimeter Array
au	Astronomical unit
CA	Competitive accretion
CMF	Core Mass Function
core	A gravitationally bound condensation of gas and dust observed in low-temperature, high-density regions. Thought to be related to the formation of stars, likely serving as a source of mass.
ET	Exponentially tapered accretion
IMF	(Stellar) Initial Mass Function
(N/M/F)IR	(Near-/Mid-/Far-) Infrared
IRAC	IR Array Camera
IS	Isothermal-sphere accretion
JWST	James Webb Space Telescope
Jy	Jansky
K	Kelvin
MIST	Mesa Isochrones and Stellar Tracks
MIRI	Mid-IR Instrument
(P/ZA)MS	(Pre/Zero-age) main sequence
NIRCam	Near-IR Camera
pc	Parsec

PEM	Protostellar evolutionary model
protocluster	A cluster of forming stars.
protostar	An object that will become a star (i.e. will burn deuterium and hydrogen over the course of its lifetime). Also: The central source of luminosity in a young stellar object.
RT	Radiative transfer
RTM	Radiative transfer model
SED	Spectral energy distribution
S/N	Signal-to-noise ratio
SVO	Spanish Virtual Observatory
TC	Turbulent-core accretion
TCA	Tapered competitive accretion
TIS	Tapered isothermal-sphere accretion
TTC	Tapered turbulent-core accretion
young stellar object	A broad term for the precursor to a star. Conceptualized here as the combined system of a protostar and any surrounding bound material.
YSO	Abbreviation for “young stellar object”.

Abstract of Dissertation Presented to the Graduate School
of the University of Florida in Partial Fulfillment of the
Requirements for the Degree of Doctor of Philosophy

A FRAMEWORK FOR MODELING EVOLUTION OF THE CORE MASS FUNCTION

By

Theo Richardson

May 2025

Chair: Adam Ginsburg

Major: Astronomy

Our current picture of the observable Universe is supported by knowledge of the behavior and evolution of stars. However, the earliest stages of the lives of stars are a subject of considerable uncertainty, with central questions such as where the observed distribution of stellar masses originates or how stars gain their mass remaining unanswered. It is difficult to comprehensively evaluate or compare the many theories developed to explain the star formation process, given the limited amount of observational data and current modeling capacity. In this work, I present a collection of models and modeling tools developed to make a direct connection between theory and observation, opening the way to a comprehensive assessment of our picture of star formation.

I make significant updates to a set of young stellar object (YSO) models with spectral energy distributions (SEDs) calculated through radiative transfer. Such sets are commonly used to measure properties of YSOs; my additions expand the amount of measurable information. Moreover, I use this set to probe the validity of assumptions commonly made in observations of stellar precursors, including the temperature of circumstellar dust and the relationship between a YSO's appearance and its actual evolutionary state.

I develop an innovative method for modeling the evolution of YSOs which associates the radiative transfer models of my set with protostellar evolutionary tracks. This method connects the theoretical parameters of star formation directly to observables and allows the many existing theories for protostellar accretion to be considered on even footing. I show that YSOs following multiple accretion models exhibit distinct behavior that may be identified through far-IR and

millimeter photometric observations. Further, I assess the impact of model construction on radiative transfer simulations and extend analysis of observational YSO evolutionary indicators done with the base models.

Finally, I use this YSO modeling procedure as the heart of a framework for modeling populations of forming stars. I compare the distributions of several physical and observational properties for the members of populations with varying prescriptions for stellar mass assembly and formation history, finding that different theories have distinct and measurable effects on population-level observables.

CHAPTER 1

INTRODUCTION AND OPENING REMARKS

Stars play a key role across many areas in astrophysics, and understanding their evolution is necessary to model and interpret the behavior and spectra of galaxies, star clusters, and planetary systems. Much work has therefore been devoted to building appropriate models of stellar evolution and spectra, and a good deal of information has been amassed regarding what happens to a star once it arrives on the main sequence. Less agreed on, however, is its journey to that point from an initial cloud of dust and gas. Put another way, current theoretical understanding of the process of star formation contains areas of considerable uncertainty. These areas include (but are not limited to) how stars assemble their mass, where in the prestellar environment the material to form stars originates, and the relative importance of different physical processes and environmental factors in shaping the population of stars created in a formation event; each of these are nontrivial questions with large ramifications for how stars form.

These uncertainties are closely bound up with a central unknown in star formation theory: the origin of the stellar initial mass function (IMF). First introduced as a concept in [Salpeter \(1955\)](#), the IMF is the mass distribution of newly formed stars. Since the mass of a star is the single quantity that most defines its subsequent evolution, and the evolution of stars is a central component in shaping the visible Universe, the IMF is a quantity of great importance both within star formation theory and beyond. However, while a large amount of work has been dedicated to determining how the IMF originates (reviewed by [Bonnell et al., 2007](#); [Kroupa et al., 2013](#); [Offner et al., 2014](#); [Krumholz, 2014](#); [Lee et al., 2020](#); [Hennebelle & Grudić, 2024](#)), and progress has been made through improvements in theoretical modeling, the question remains open. This is due in no small part to the difficulty in measuring the IMF, which cannot be done directly due to the differing lifetimes of high- and low-mass stars. The observational determination of the IMF is a subject which has merited many reviews of its own (e.g. [Bastian et al., 2010](#); [Luhman, 2012](#); [Hopkins, 2018](#); [Smith, 2020](#)), and the numerous methods that have been developed often arrive at conflicting conclusions in addition to having unique deficiencies.

The Core Mass Function (CMF) is the mass distribution of prestellar “cores”, here conceived of as gravitationally bound condensations of gas and dust generally thought to be the predecessors to stars. As formulated, the CMF is similar in concept to the IMF; moreover, some measurements have indicated that the two distributions have a broadly similar shape (e.g. Motte et al., 1998; Alves et al., 2007; André et al., 2010; Könyves et al., 2015) (although some deviation has also been measured, e.g. Pouteau et al., 2022), prompting speculation that the origin of the IMF is related to that of the CMF. Establishing such a link would significantly advance the study of star formation for multiple reasons: for one, it would imply a theoretical throughline between the origin of the CMF and IMF, marking a major step forward in star formation theory, while also representing a relatively simple pathway to IMF observations requiring minimal inference (though not without its own complications, e.g. Louvet et al., 2021).

However, as it currently stands, the nature of any link that exists between the CMF and IMF is difficult to determine. This difficulty is a result of two broad issues. Firstly, the “theory space” of star formation is broad, spanning a wide range of potentially relevant physics and environmental properties which can have a pronounced impact on the relationship between the CMF and IMF (Offner et al., 2014). For example, proposed theories for stellar mass assembly alone include spherically symmetric collapse (Shu, 1977) modified by including turbulence (McKee & Tan, 2002, 2003), competitive accretion (Bonnell et al., 1997, 2001), stellar collision (Bally & Zinnecker, 2005), mass inflow from a turbulent medium (Padoan et al., 2020; Pelkonen et al., 2021), and variants that fall between these (e.g. McKee & Offner, 2010; Offner & McKee, 2011; Myers, 2014), which prescribe a wide range of behavior for forming stars. As a result, the current infrastructure for creating theoretical models of forming stars and stellar populations is somewhat scattershot. Of the existing models that make testable predictions, many are limited to the context of particular theories or narrow ranges of parameters, limiting their use as probes within this wide theory space. Furthermore, the quantities predicted by models do not always align with the observable qualities of forming stars. Secondly, the amount of data on forming stars is somewhat scarce when compared to the vast reserves of observations of main-sequence stars,

and interpreting the existing observations of young stellar objects (YSOs)—a general term for stellar precursors—is complicated by the high extinction present in the dense environments where stars are born. Taken together, probing a hypothetical relationship between the CMF and IMF requires models that are better able to make use of existing data to constrain the available theory space of star formation.

In this work, I present a set of theoretical models and modeling tools that aims to meet these demands. The tools I have developed combine theoretical prescriptions for the evolution and properties of forming stars with radiative transfer, connecting the theory of star formation directly to observables on an individual and population level. The resulting models therefore capture the intermediate stages of a hypothetical evolution between the CMF and IMF. My approach to modeling is flexible enough to accommodate the wide theory space of star formation and produce observational predictions which are directly comparable to data. Consequently, my tools open the door to a comprehensive evaluation of the congruence between theory and observation in star formation, paving the way for a fuller understanding of how stars are born across the Universe.

In Chapter 2, I describe the model set that serves as a base for the tools developed in this thesis. In Chapter 3, I outline my newly developed approach to modeling the evolution of individual YSOs. Spurred by the results of Chapter 3, I review the current state of efforts to measure the evolutionary status of forming stars in Chapter 4. In Chapter 5, I present a framework for simulating populations of forming stars, built on the tools developed for Chapter 3, and predict how different aspects of star formation theory can be expected to manifest in observation. I make concluding remarks in Chapter 6.

CHAPTER 2

AN UPDATED MODULAR SET OF SYNTHETIC SPECTRAL ENERGY DISTRIBUTIONS FOR YOUNG STELLAR OBJECTS

2.1 Motivation

Measuring the properties of young stellar objects (YSOs) is an important aspect of star formation research. Currently forming stars provide direct insight into the mechanics of star formation, which remains a subject with numerous unknowns. Common tools for making these measurements, particularly in cases where the YSOs are unresolved, are grids of SED models that have been pre-computed using radiative transfer simulations. Properties of an observed YSO can then be measured via fitting the measured SED to these template models.

Given the number of theories that exist to explain the process of star formation, many such model grids have been made for the purpose of measuring YSO properties (e.g. [Robitaille et al., 2006, 2007](#); [Furlan et al., 2016](#); [Haworth et al., 2018](#); [Zhang & Tan, 2018](#)). However, these grids often face common limitations. By construction, many grids assume a particular theory of star formation (i.e. a particular accretion history and expected envelope/disk/surrounding mass density distribution) that influences the parameters included in the models and the area of parameter space sampled. Models in these grids also often span small regions of this parameter space or are purposefully sampled to prioritize particular combinations of values which are deemed “realistic” by an underlying theory. At times, as in the case of [Robitaille et al. \(2006, R06\)](#), the models in a grid may all be very similar (e.g. having the same basic components of a central source, a disk, a rotationally flattened envelope, and outflow cavities), varying only in physical parameters that have minimal effect on observables. These practices limit the extent to which a grid of SED models may be used to accurately determine the properties of an observed YSO. Moreover, building a model grid with the assumption of a particular theory removes the ability to use the grid as a tool to test the theory, as it will be implicit in all results obtained through use of the grid.

Published in the Astrophysical Journal as [Richardson et al. \(2024\)](#); reprinted with permission. Minor edits have been made for inclusion.

The SED models presented in [Robitaille \(2017, R17\)](#) remove these limitations by providing a large set of models spanning a number of different geometries (defined by the presence or absence of features like disks or outflow cavities) each of which are shaped by a common set of randomly sampled parameters. These choices make this set widely applicable as a tool for measuring YSO properties that is, by design, agnostic to accretion history and stellar evolution model. However, the physical parameters of each YSO in R17 are limited to those that are required for the calculation of an SED via radiative transfer. There are additional properties that can be derived for each model that can facilitate the interpretation of observations. As an example, R17 does not include the mass present in the circumstellar envelope of each model YSO (i.e. the core mass). In many theories, a core mass uniquely maps to a final stellar mass with a fixed efficiency (e.g. [McKee & Tan, 2002, 2003](#); [Federrath & Klessen, 2012](#)). The core mass is therefore a sought-after observable quantity to test such theories and is often a crucial component in drawing larger conclusions about the mechanics of star formation (e.g. [Motte et al., 2022](#); [Ginsburg et al., 2022](#); [Pouteau et al., 2022](#)). The randomly sampled properties can also give rise to YSO models that are not consistent with any theory of star formation or are otherwise unphysical; for example, some central sources exist below the stellar main sequence or have disks with inner radii larger than their outer radii. These “unrealistic” models can be difficult to identify based only on the information included in R17. Finally, while the SEDs in R17 have been convolved with filters from several IR instruments, the advent of JWST brings a wealth of new data that the models could be used to interpret. The existing convolutions also do not make use of the full wavelength range of the R17 SEDs, when these models may also be useful as a point of comparison for non-IR observers.

In this chapter, I present a substantial update to the R17 SED models that addresses these limitations. Chapter [2.2](#) contains an overview of the models circa 2017. In Chapter [2.3](#) I outline my additions to the models, and in Chapter [2.4](#) I demonstrate how my additions may be used to improve measurements of YSO properties. I make concluding remarks in Chapter [2.5](#).

2.2 The Robitaille (2017) Models

In this section, I provide an overview of the state of the YSO SED models as released alongside R17. A comprehensive presentation of the models is available in the companion paper; my focus is instead on details either directly relevant to this work or useful in understanding the structure of the model set.

2.2.1 Geometries

Models in R17 are grouped by geometry, defined by the presence or absence of dust density structures. A full list of the free parameters that shape the models, corresponding value ranges, and effect on the resulting geometry can be found in Tables 1 and 2 of R17. Broadly, the geometries are defined as a source plus zero or more features, which may include envelopes, disks, bipolar cavities, and an ambient medium. In the following subsections, I provide a short discussion of how these features are implemented, and point to the appropriate sections of R17 for those interested in greater detail. A visualization of a model with all of these features present is plotted in Figure 2-1.

2.2.1.1 Envelopes

Dust in every R17 envelope follows one of two density profiles. The majority of models have a rotationally flattened envelope as prescribed by [Ulrich \(1976, U76\)](#), hereinafter U76. This profile is given by the following equation:

$$\rho(r, \theta) = \rho_0^{\text{env}} \left(\frac{r}{R_c} \right)^{-3/2} \left(1 + \frac{\mu}{\mu_0} \right)^{-1/2} \left(\frac{\mu}{\mu_0} + \frac{2\mu_0^2 R_c}{r} \right)^{-1} \quad (2-1)$$

In (2-1), ρ_0^{env} is a density scale defined as:

$$\rho_0^{\text{env}} = \frac{\dot{M}_{\text{env}}}{4\pi (GM_{\star}R_c^3)^{1/2}} \quad (2-2)$$

where R_c is the “centrifugal radius” where infalling material piles up due to angular momentum, $\mu \equiv \cos \theta$, and μ_0 is the cosine of the initial polar angle of the streamline intersecting the point

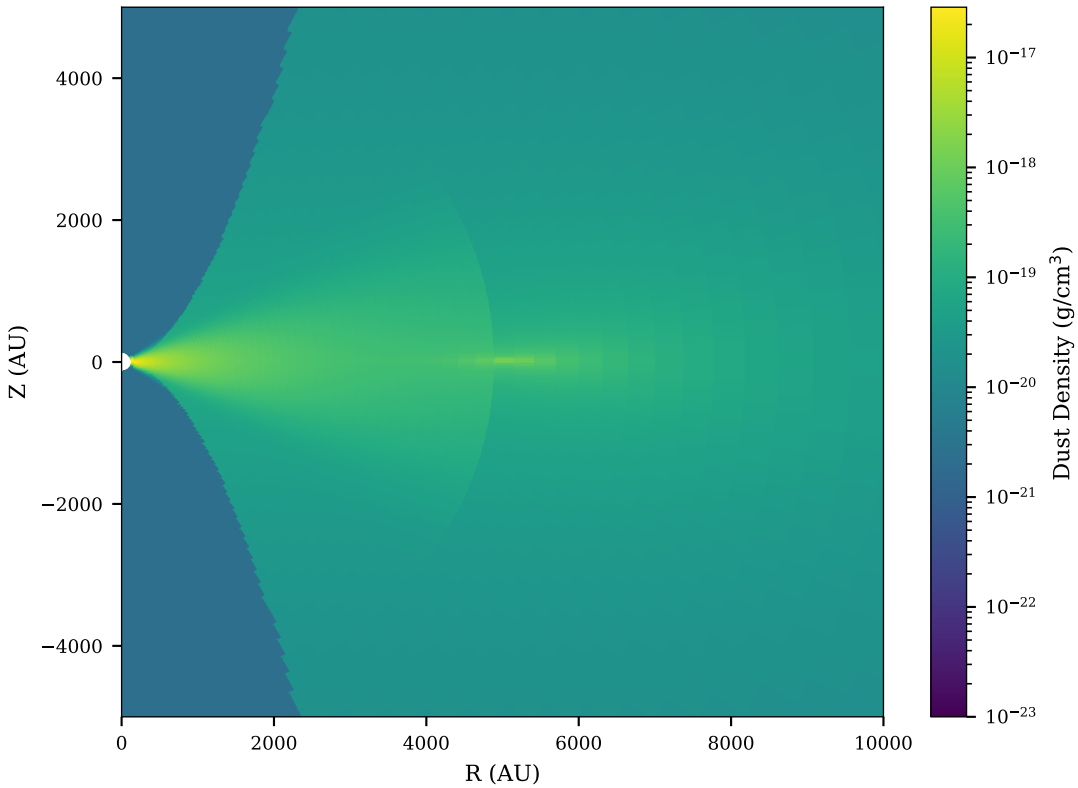


Figure 2-1. The dust density profile of an R17 model following U76, an axisymmetric profile resulting from rotational flattening of an envelope and infalling material (2-1). The model is chosen from the most populated ‘spubhmi’ geometry as a representative of the most common shape of modeled YSO. This provides a sample visualization of bipolar cavities, a passive disk, and the overdensity resulting from mass inflow at the outer edge of an accretion disk (or alternatively, the centrifugal radius) as put forth in U76.

(r, θ) . The remainder of envelopes have simple power-law density profiles:

$$\rho(r) = \rho_0^{\text{env}} \left(\frac{r}{r_0} \right)^\gamma \quad (2-3)$$

where ρ_0^{env} is the density defined at $r_0 = 1000$ AU and γ the constant power-law exponent. In the model names, the U76 and power-law envelope density profiles are respectively denoted ‘u’ and ‘p’ as the third character in the geometry identifier. For more details, see Section 3.2.3 of R17.

2.2.1.2 Disks

Envelopes with a U76 density profile may also have an accompanying flared disk (denoted ‘p’ as the second character in the geometry identifier.) The density profile of the disk is as follows:

$$\rho(R, z, \phi) = \rho_0^{\text{disk}} \left(\frac{R_0}{R} \right)^{\beta-p} \exp \left[-\frac{1}{2} \left(\frac{z}{h(R)} \right)^2 \right] \quad (2-4)$$

where the disk scale height h_0 defines the corresponding polar radius R_0 and $h(R)$:

$$h(R) = h_0 \left(\frac{R}{R_0} \right)^\beta \quad (2-5)$$

The disk mass that determines ρ_0^{disk} , surface density profile p , flaring power β , spatial extent $R_{\min}^{\text{disk}}/R_{\max}^{\text{disk}}$, and scale height h_0 are free parameters that are assigned randomly when constructing a model.

I note that by construction, disks are intended to be passive (i.e. non-accreting and heated solely by the central source.) The impact of ignoring accretion onto a YSO’s central source is minimal, or degenerate with an increase in luminosity of said source. Ignoring accretion within the disk itself does have a larger impact on the shorter-wavelength parts of the model SEDs down to the MIR and particularly in the UV regime. For more details, see Section 3.2.2 of R17.

2.2.1.3 Cavities

Many envelopes in R17 include bipolar cavities (denoted ‘b’ as the fourth character in the geometry identifier) that replace parts of the envelope with a constant, lower density ρ_0^{cav} . The cavity walls are defined by the relationship between distance from the $\mu = 0$ plane z and distance from the z-axis R :

$$z(R) = R_0 \cos \theta_0 \left(\frac{R}{R_0 \sin \theta_0} \right)^c \quad (2-6)$$

where R_0 is set to 10,000 AU, c is the cavity power, and θ_0 is the angle to the cavity wall from the z-axis at R_0 . The lower-density cavity persists out to the radius where the surrounding envelope reaches ρ_0^{cav} . For more details, see Section 3.2.4 of R17.

2.2.1.4 Ambient medium

An ambient medium is included in the models to simulate the presence of an interstellar medium. It acts as a lower limit to the dust density in geometries that include it (denoted ‘m’ as the sixth character in the geometry identifier.) Every model with an envelope also has an ambient medium, while for models that are only a star or a star and disk, the medium may or may not be present. Dust in the medium is always set to a density of 10^{-23} g/cm³ and a temperature of 10 K. For more details, see Section 3.2.5 of R17.

2.2.2 Dust

All models in R17 utilize a dust model from [Draine \(2003a,b, D03\)](#) with the [Weingartner & Draine \(2001\)](#) Milky Way grain size distribution A for $R_V = 5.5$ and carbon abundance C/H renormalized to 42.6 ppm. Mie scattering properties were calculated using a modified `bhmie` routine from [Bohren & Huffman \(1983\)](#).

A large component of the work I present in this chapter is concerned with the dust mass present in a YSO and the ability to measure it accurately (Chapters 2.3.1, 2.4.1), for which the opacity to absorption κ_ν of this dust is required. In the file containing the dust model released alongside R17, the opacity to extinction χ_ν and albedo of the dust a are included. κ_ν can be obtained by subtracting the scattering component from χ_ν , as follows:

$$\kappa_\nu = \chi_\nu \times (1 - a) \quad (2-7)$$

The resulting opacities are plotted in Figure 2-2. A set of commonly used dust opacities from [Ossenkopf & Henning \(1994, OH94\)](#) is also shown for comparison. The OH94 opacities are for dust grains with thin ice mantles, coagulated at 10^6 cm⁻³ after 10^5 years. Dust from OH94 is generally more opaque; the values are greater by a factor of ≈ 4 than the dust from D03 at wavelengths longer than 100 μm .

2.2.3 SEDs

All models in R17 are associated with a suite of SEDs. Flux values for each SED are derived from the simulated radiation of the YSO as viewed within 20 log-spaced apertures

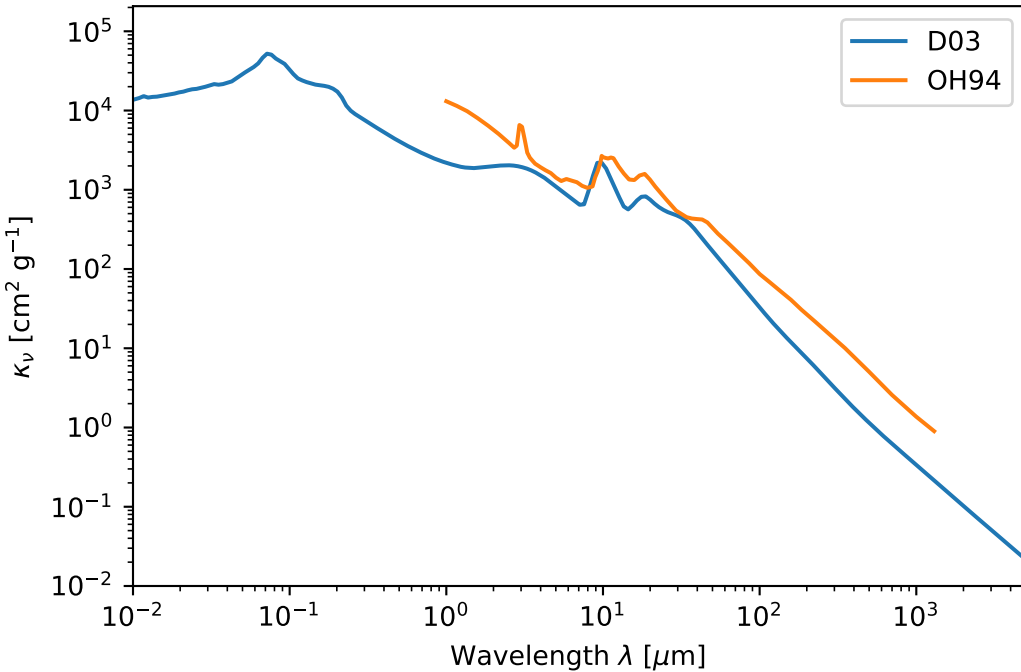


Figure 2-2. The opacity to absorption of dust from D03, κ_ν , used in the R17 models. Opacities from OH94 for dust grains with thin ice mantles are plotted for comparison, assuming a density of 10^6 cm^{-3} after 10^5 years of coagulation.

between 10^2 - 10^6 AU. All SEDs span a wavelength range of $0.01 \mu\text{m}$ to 5 mm evaluated at 200 log-spaced wavelengths. Models with density profiles dependent on the θ coordinate (i.e. models with cavities/disks) have multiple associated SEDs calculated at different inclinations. These viewing angles have been randomly sampled within 10° increments from 0° – 90° to preserve even coverage. All flux values are normalized to a distance of 1 kpc.

SEDs were calculated by running Hyperion¹, an open-source Monte Carlo radiative transfer code² (Robitaille, 2011).

2.3 Additions

In this chapter, I provide an outline of the additions made to the R17 models.

1 <https://github.com/hyperion-rt/hyperion>

2 In the data released alongside R17, some models did not have associated SEDs; a fraction of the Hyperion runs were not completed with the resources allotted to them. I discuss this further in Chapter 2.3.6.

2.3.1 Mass Calculation

In R17, the spatial extent and density distribution of each protostellar envelope is specified, but the emergent parameter of mass in the envelope is not included. However, this is an important property that is often sought out and would therefore be useful information for those looking to constrain YSO properties using these models. Knowing the mass also opens up more utility for the models in other areas; for example, quantifying the relationship between the flux measured from a core and its mass, as done in Chapter 2.4.1. The mass contained in the envelope of each model is, consequently, a very useful quantity to calculate.

All R17 models are defined on a 400×300 spherical grid of cells in radius r and polar angle θ . All models are constructed to be axisymmetric, so no ϕ variation is required. Cells are log-spaced in radius over the interval $(R_{\text{env,min}}, \sqrt{2}R_{\text{env,max}})$ and roughly linearly spaced in angle over $(-\pi, \pi)$. $R_{\text{env,min}}$ is the inner radius of an envelope (or disk) and $R_{\text{env,max}}$ is the outer extent of the model. $R_{\text{env,min}}$ is set either at the dust sublimation radius around the source, R_{sub} , or a randomly sampled value; this is determined through the model geometry. R_{sub} is model-dependent; it is defined as the radius where optically thin dust in the envelope would reach a temperature of 1600 K when heated by the central source in each model. $R_{\text{env,max}}$ is not explicitly defined in R17, but is functionally either the radius where dust in the non-ambient density structures no longer exceeds ρ_{ISM} (defined as 10^{-23} g/cm³ across all models) or where the optically thin dust temperature reaches the ambient temperature of 10 K, whichever is larger.

I calculate the mass present in each model by integrating the dust density profile. Integration is performed using the cells as differential elements, multiplying the volume of each cell with the density defined at its center in log space to calculate the mass within each. Cell centers and sizes for each model are imported from the output of the associated Hyperion run. The SEDs are defined in a series of radial apertures; the mass contained within spheres of those radii, $M_{\text{core,dust}}(< R)$, is calculated by identifying the cells within each radius and summing their masses. To ensure that material outside the envelope does not contribute to the mass, I only consider cells within the radius where any non-ambient dust density structure exceeds the ambient

density. This treatment of numerical integration allows the calculation of masses in a way that is consistent with the setup for `Hyperion` without overweighting an ambient medium. It is also flexible enough to account for the multiple geometries present in R17, as the grid of cells is able to resolve the features of each model by construction.

This method of integration successfully calculates the dust mass present within the density structures of each YSO. To extend that to the total mass, I assume a constant gas-to-dust ratio (GDR) of 100; this is a common approximation to the metallicity- and distance-dependent values found in [Draine et al. \(2007\)](#) (e.g. [Elia et al., 2013](#); [König et al., 2017](#)). The mass values used and reported hereinafter are therefore total mass values where a GDR has been assumed, as opposed to dust masses directly calculated from the R17 models. $M_{\text{core},\text{total}}(< R)$ has been calculated for each model within every aperture in which the SEDs are defined.

In addition to the mass contained in spherical apertures around the central source of each YSO, I have calculated an alternate set of masses that sum cells along the line of sight (i.e. within a cylindrical viewing aperture centered on the source as opposed to within a spherical radius from the source.) For these masses, I maintain the same set of radii. These results are intended to serve as “observable” masses, as this treatment corresponds more closely with observations of YSOs, which occur along external sightlines within some viewing aperture. This approach is also more consistent with how fluxes are calculated in `Hyperion`, where the photons received within a given circular aperture along a sightline are summed. Per Section 4.2 of R17, each model SED in the set has been background-subtracted within each viewing aperture, where the background consists of a slab of dust with density 10^{-23} g/cm³, thickness of $2 \times R_{\text{max}}$ for the model, and emitting modified blackbody radiation at 10 K. To ensure only material contributing to the model SEDs is tracked, I do not include cells at the ambient density in this set of mass calculations either, effectively “background-subtracting” the calculated masses.

For the masses within spherical radii, the mass within apertures that exceed the extent of the model is set to NaN as an indication of which apertures are out of bounds.

2.3.2 Temperatures

`Hyperion`, as part of a run, calculates the specific energy absorbed by the dust in each cell for each model. This was used in R17 to create temperature profiles for each model. An example of such a temperature profile can be seen in Figure 2-3. In the course of this work, I have used these profiles to calculate mass-weighted average temperatures within each viewing aperture. Each cell in the grid on which a model is defined has an associated temperature. To calculate the mass-weighted average, I sum the products of the temperatures and masses of all cells within an aperture and divide by the total mass in the aperture. As in Chapter 2.3.1, temperatures are calculated both in spheres around the source and in cylinders along the line of sight. Material at the background density is not included in the calculations.

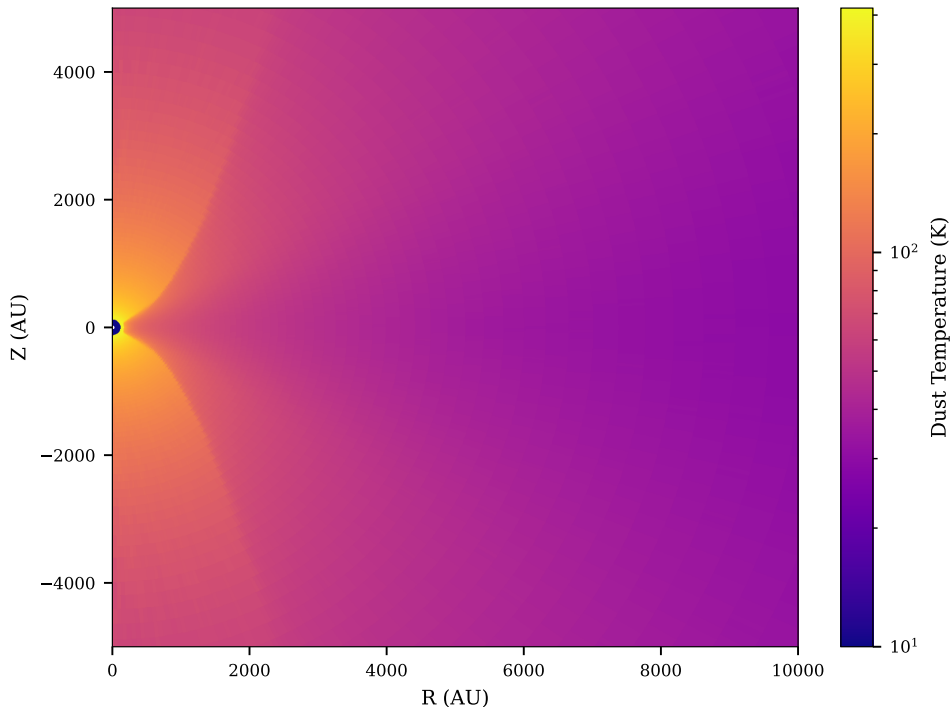


Figure 2-3. The same as Figure 2-1, but colored using the dust temperature in each cell.

Combining this with the mass contained in each cell allows calculation of the mass-weighted average dust temperature within a series of radial apertures. The model geometry, `spubhmi`, features rotationally flattened envelopes with bipolar cavities and passive disks.

2.3.3 Disk Properties

Many models in R17 include a passive disk (with properties given in Section 2.2.1.2). Here as elsewhere in the models, the randomly sampled parameters may result in unrealistic disks in the sense that they may be too unstable to be observed. As a check on the “realism” of each model, I determine whether or not the disks present in these models are stable. The basis for disk stability is the Toomre Q parameter, defined as:

$$Q = \frac{c_s \kappa}{\pi G \Sigma} \quad (2-8)$$

for a disk with sound speed c_s , epicyclic frequency κ , and surface density Σ . I adopt the smallest value of Q in the midplane of each model as a lower bound on stability.

To calculate Q as a function of radius R for each disk, I find the variables in (2-8) as functions of R individually. Assuming gas in the disk is roughly ideal allows the calculation of the sound speed using the following:

$$c_s = \sqrt{\frac{P}{\rho}} = \sqrt{\frac{k_B T(R)}{\mu m_p}} \quad (2-9)$$

where the mass-weighted average temperature $T(R)$ is directly calculable from the models, as described in Chapter 2.3.1. I adopt a μ of 2.4 in accordance with the calculated mean molecular weight per free particle from Kauffmann et al. (2008). To calculate $\Sigma(R)$, I begin at $M_{\text{disk}}(R)$, which emerges directly from the dust density profile of each disk, and average that mass over a circle with radius R . For the epicyclic frequency, I assume all disks are Keplerian. κ is therefore equivalent to the angular frequency of the disk $\Omega(R) = \sqrt{GM(R)/R^3}$. However, R17 does not directly assign masses to the central sources in its YSOs, which are included alongside $M_{\text{disk}}(R)$ in the total mass profile $M(R)$. I set a floor of $0.1 M_\odot$ for each source to calculate a minimal κ for each model. Based on Eqn. (2-8), a lower bound on κ will give the minimum Q possible for an associated disk, Q_{\min} . Since there are no assigned stellar masses for the central sources, a lower bound on Q provides a measure of the lowest possible level of stability for a disk (i.e. if a disk is stable by this metric, it is virtually certain to actually be stable.) The actual Q for any model may

then be revised upwards based on actual masses assigned to the central sources. This minimum source mass is chosen to exist roughly at the substellar boundary, given that a brown dwarf source will not reach the minimum temperature of 2000 K covered by R17. A visualization of how $Q(R)$ (and therefore Q_{\min}) is calculated can be seen in Figure 2-4.

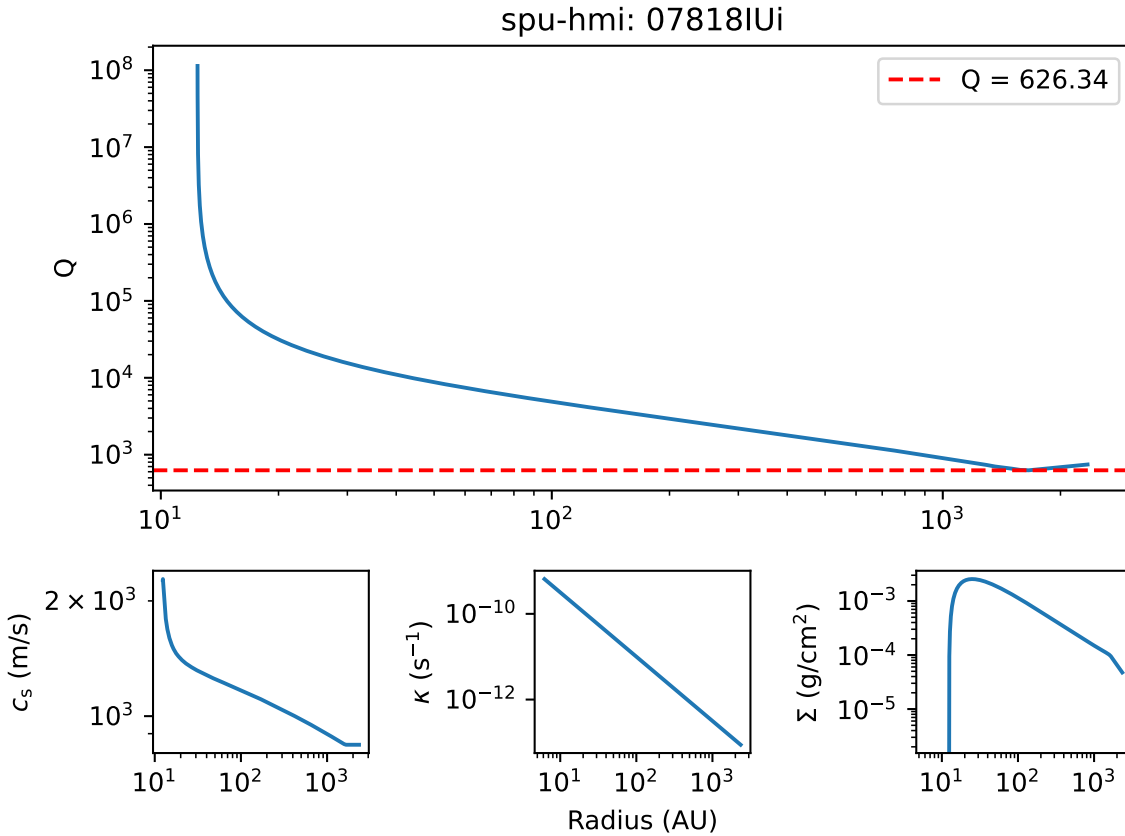


Figure 2-4. $Q(R)$ for a disk in one of the R17 models. The floor for Q is plotted in red; this value is used to determine the minimum stability of a disk against collapse. **Lower row:** The calculated sound speed c_s (left), epicyclic frequency κ (middle), and surface density Σ (right) in the disk as a function of R .

2.3.4 Extinction

I have calculated the circumstellar A_V for each model along the sightlines where the SEDs are defined. This is a property that was included in the R06 model grid, but was not present in R17. Since this is a quantity that provides additional information about the physical state of a YSO, useful when using these models as templates for SED fitting, I include it in the release.

A_V along a line of sight is equivalent to $1.086 \times$ the sightline's optical depth τ . I calculate the extinction as a function of frequency A_ν , using:

$$A_\nu = 1.086\tau = 1.086 \int \kappa_{\nu, \text{dust}} \rho_{\text{dust}} ds \quad (2-10)$$

where the dust density present in every cell (§2.3.1) and the opacity of the dust as a function of frequency, κ_ν (§2.2.2), are both known. I calculate A_V by evaluating A_ν at the standard V-band wavelength of 551 nm. As in previous subsections, I only consider dust above the ambient density.

2.3.5 Convenience Additions

Here, I outline additions I have made to the models that do not require a significant investment in time or resources to replicate, but still provide new information or functionality to the models as presented in R17.

The largest such addition is the introduction of several new sets of convolutions of the model SEDs. At release, the SEDs in R17 were convolved with filters from instruments across the visible and IR. Since the release of R17, however, new IR instruments have been introduced. The SEDs also span a wavelength range that makes them useful for work outside the near-IR. I have convolved the SEDs with filters from JWST, Paranal, additional filters from Herschel, and ALMA bands 3 and 6. Most of these filters were obtained from the SVO's Filter Profile Service ([Rodrigo et al., 2012](#); [Rodrigo & Solano, 2020](#)). Beyond that, I have created a script to easily integrate convolutions either from the SVO or user-defined filters into the existing infrastructure, included with the dataset released alongside the original paper.

I have also calculated the infrared spectral index α for all SEDs within each aperture, defined by the following equation:

$$\alpha = \frac{d \log (\lambda F_\lambda)}{d \log \lambda} \quad (2-11)$$

This quantity can be used to place observed YSOs into particular observational classes, which is a common tactic used to gain physical insight into the evolutionary state of a YSO (I discuss this practice more in Chapter 2.4.2). I take α to be the slope of the log-space line joining the flux at 2

and 25 microns, the endpoints of the standard wavelength range (Kennicutt & Evans, 2012). Only the endpoints are considered when calculating the spectral index, i.e. I do not fit to all points within the wavelength range to determine the slope.

In addition, I have made explicit the luminosity of the central source of each model. As an example of its utility, I evaluate the extent to which random sampling of stellar radius and temperature for each model results in sub-main-sequence sources. For the main sequence, I use the ZAMS (EEP # = 2) temperatures and luminosities from a set of MIST evolutionary tracks (Dotter, 2016; Choi et al., 2016; Paxton et al., 2011, 2013, 2015). I adopt the values from the tracks with $v/v_{\text{crit}} = 0.4$ and $[\text{Fe}/\text{H}] = -2.00$; this metal abundance is chosen to correspond with the simulated stellar photospheres of Brott & Hauschildt (2005) and Castelli & Kurucz (2003) used in the models (see R17 section 3.2.1 for more detail). In Figure 2-5, I plot this main sequence over the region of T-L space covered by the models.

I use these main-sequence T and L values to interpolate the main-sequence luminosity L_{MS} of the models based on their temperatures. Based on the results, 23% of all models have $L < L_{\text{MS}}$ and therefore occur below the main sequence. Another 24% of all models have temperatures that are too low to be interpolated. As a check on the placement of these sources relative to the main sequence, I use the temperature range and average radius of L dwarf objects from Kirkpatrick (2005) to map out a rough continuation of the main sequence below MIST values. Based on this extrapolation, most—if not all—of these cooler sources would likely occur above the main sequence. I include the MIST $T_{\text{MS}}/L_{\text{MS}}$ values in the release for those interested in repeating this analysis. In Appendix A, I also use this luminosity information to check the energy conservation of the radiative transfer performed by Hyperion.

Finally, I have included the radii where non-ambient density structures begin and end for each YSO model in units of physical distance. Previously, the outer radii for envelopes were not included, and the inner radii for every model were either in terms of the variable quantity R_{sub} or not included.

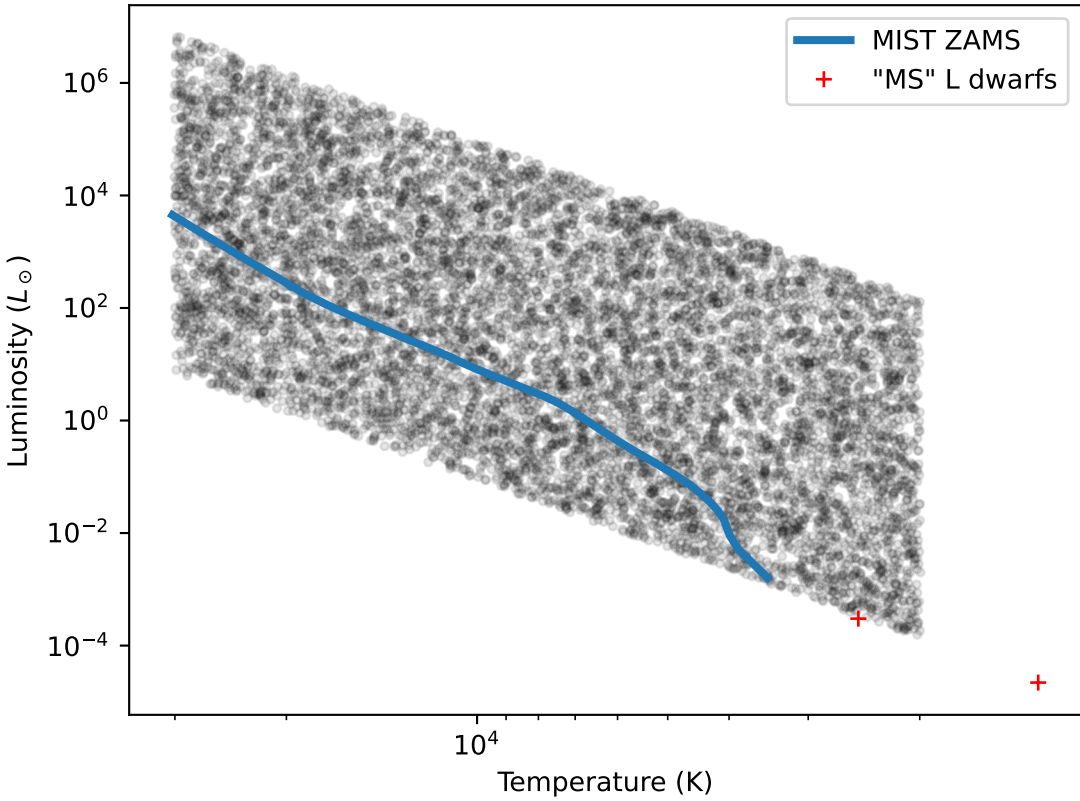


Figure 2-5. Main sequence taken from MIST evolutionary tracks, plotted over the central sources of `s---s-i`, a geometry that only includes bare stars. The evolutionary tracks used to construct the main sequence assume $v/v_{\text{crit}} = 0.4$ and $[\text{Fe}/\text{H}] = -2.00$. The individual data points are rough estimates of the position of “main sequence” L dwarf objects across their temperature range using values from [Kirkpatrick \(2005\)](#), plotted to give an indication of how the main sequence continues below temperatures accessible by the chosen MIST tracks.

2.3.6 Completed YSO Models

Some models included in the initial release of R17 had assigned parameter values but did not have associated SEDs. These models were not run successfully run to completion in Hyperion. While multiple geometries had incomplete models, those with U76 density profiles exhibited a lower rate of completion on average. (The exact completion rate varies with geometry features, and tends to be lower for the U76 models without cavities.) The incomplete models exhibit a bias towards denser envelopes, as seen in Figure 2-6; the failure to complete is therefore likely due to the high optical depth resulting from the shallow fall-off of U76 density profiles with radius. The models are otherwise distributed akin to the broader set.

I have run incomplete models in `Hyperion`, version 0.9.10, to further fill in the parameter space. The models run for the initial release were performed on a cluster of 120 cores; I use at minimum a cluster of 256 cores. This is sufficient to complete the majority of outstanding models, though some particularly intractable models require ≥ 1500 cores to complete within the allowable time. These holdouts are so optically thick that there may not be a sufficient number of photons to construct an SED, particularly at long wavelengths. As a result, the impact of their exclusion from the model SEDs is less pronounced than it might be otherwise; however, these models will be completed and included in a future update.

In the initial release, model runs produced a raw output file that would then be post-processed according to Section 4.2.4 of R17. I have followed the same procedure for the newly completed models and will continue to do so for future additions, both of the as-yet-uncompleted models from the initial release and any newly created models.

2.3.7 Content Updates

In the course of this work, I have primarily built on top of the existing R17 models without making changes. In using my additions to attain further results, though, I have come across a property of the model SEDs that is worth altering in this release.

In the data products published alongside R17, each model's associated SED is defined in a common set of apertures, as described in Chapter 2.2.3. However, each SED is calculated within its own set of apertures based on the physical size of its associated model. This calculated SED is then interpolated to the final set of apertures. For models with large inner radii, the smallest calculation aperture may be larger than apertures in the final set. In these cases, `Hyperion` does not have sufficient resolution to capture the SED inside these smaller apertures. In the initial release, such cases were handled by assigning any out-of-bounds apertures the same flux as in the closest in-bounds aperture. This resulted in inner apertures in the final set appearing brighter than they should, given the amount of material they contain. In this release, I have elected to instead assign NaN values to model SEDs in any aperture below the resolution of the model, so that these results cannot introduce noise.

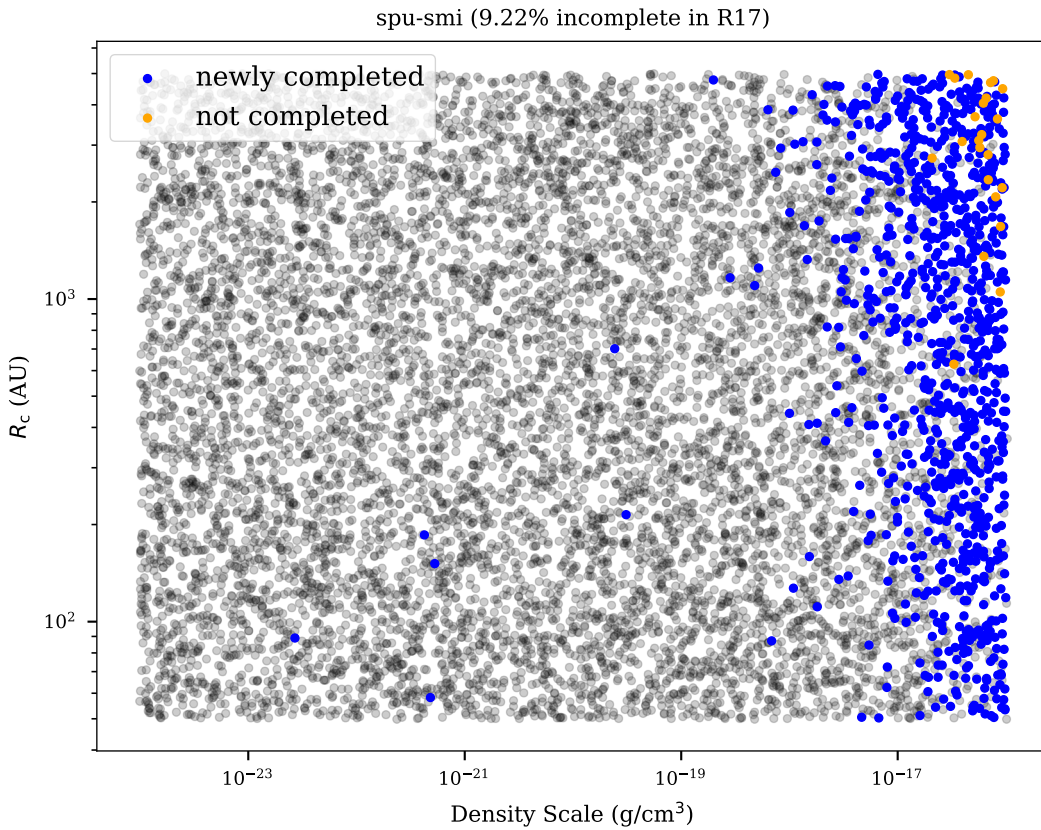


Figure 2-6. A 2D projection of the R17 model parameter space for a geometry with a U76 density profile (2-1). The free parameters are the centrifugal radius R_c and density scale ρ_0 . Highlighted models were not run to completion in Hyperion in the initial release; those in blue have since been completed. There is a bias towards higher-density envelopes resulting from high optical depth. The apparent “wedge” is caused by the radial behavior of U76 density profiles. All instances of radial dependence are scaled as R_c/r , causing the density to fall more slowly as R_c increases, particularly when $r < R_c$. As a result, the optical depth of envelopes is correlated with increasing R_c . The net effect is to depopulate the high-density models.

It is also possible for the final set of apertures to extend outside of those native to a model (into an ambient medium, should the model have one.) However, since flux from material at the background density and temperature is subtracted in post-processing, any such additional material does not produce any additional flux. Assigning these apertures the closest in-bounds value is therefore self-consistent and allows these models to retain their use as templates for SED fitting, so I do not alter this component of post-processing.

In the updated set of models, every SED has been appropriately interpolated into the final set of apertures. However, this set of apertures places its own limit on the resolution of the SEDs. Care should therefore be taken when applying these models to high-resolution data. As an example, JWST’s maximum resolution of 0.1” has a physical size < 100 AU for distances within 1 kpc, so the models would fail to predict JWST fluxes for nearby targets and cannot be used to fit data at that resolution.

2.4 Results

In this chapter, I present use cases for the updated version of the R17 models that are made possible through my additions.

2.4.1 Mass Measurements

A common assumption made when inferring the mass of a pre- or protostellar core from an observed flux is that the dust in the core is optically thin. Low optical depth permits the calculation of mass through the following equation:

$$M_{\text{core}} = \frac{S_{\nu,\text{dust}} d^2}{\kappa_{\nu,\text{dust\&gas}} B_{\nu}(T_{\text{dust}})} \quad (2-12)$$

for an observed flux $S_{\nu,\text{dust}}$ at a distance d with total material opacity $\kappa_{\nu,\text{dust\&gas}}$ and dust temperature T_{dust} . In addition, a constant dust temperature (often ≈ 20 K) is generally adopted. The accuracy of mass measurements made using Eqn. (2-12)—and any further uses of those measurements—hinges on those assumptions. With the newly calculated masses, I test the accuracy of the optically thin, isothermal assumption.

I compare the amount of mass inferred using Eqn. (2-12) and the flux from a model to the mass I calculate is present in that same model. I adopt the same dust properties used in R17, as described in Chapter 2.2.1. The dust opacity from D03, plotted in Figure 2-2, is scaled to include gas mass at the assumed GDR. The method for mass calculation is described in Chapter 2.3.1. Since I am interested in evaluating the impact of the assumed dust temperature, I consider both a constant 20 K and a mass-weighted average temperature within each aperture, which I calculate as described in Chapter 2.3.2. I consider the mass-weighted average temperature on the expectation that a modified blackbody at this temperature will reasonably approximate the total emission of dust in an optically thin system. I use the calculated “line-of-sight” masses and temperatures, which are by construction observational analogues.

To begin, I examine a specific mock-observational case: a flux of 10 mJy at 1.1 mm at a distance of 1 kpc within an aperture of ≈ 1000 AU. I consider models over all geometries with envelopes that exhibit a flux of 10 ± 1 mJy in that aperture. I make additional cuts to the set of models that also have disks, keeping those with an average optical depth $\bar{\tau}_{\text{disk}} < 10^{-3}$ and $Q_{\text{disk}} > 0.1$. $\bar{\tau}_{\text{disk}}$ is calculated by multiplying the dust opacity at 1.1 mm by the average disk surface density. The resulting models are those that best follow the assumption of low optical depth. They are therefore best positioned to illustrate the relationship between the mass I calculated to be present (the “true” mass) and the mass inferred through Eqn. (2-12).

Results from the comparison are plotted in Figure 2-7. When assuming a constant dust temperature of 20 K (the top plot in Figure 2-7) there is no apparent correlation between the inferred masses and true masses. This indicates that even when observing YSOs that satisfy the $\tau \ll 1$ criterion, assuming isothermal dust at 20 K will not reliably provide accurate mass measurements. Under these assumptions, the majority of models have their mass overestimated by a factor of 2 or more.

Conversely, assuming the dust in each model is at its weighted-average dust temperature causes consolidation into a linear relationship between inferred mass and true mass, as should be the case if Eqn. (2-12) holds. I consider two weighting schemes; one by the mass present in each

cell, as calculated in Chapter 2.3.2, and one by the product of the mass and dust temperature in each cell as an approximation of the photon-weighted dust temperature at long wavelengths.

These are the bottom left and bottom right plots in Figure 2-7, respectively. In both cases, there is good agreement between the inferred and true masses for the sample of optically thin YSOs. In the mass-weighted case, there is a strong correlation between the inferred and true masses, although the inferred masses are systematically greater than the true masses by approximately 10%. In the photon-weighted case, the inferred mass effectively serves as a lower limit to the true mass, and 46% of models are within 10% of a one-to-one correlation. (87% of models are within 20%).

It is clear that an assumption of 20 K dust is not representative of the models in this specific case. However, if all dust is instead assumed to be at the median mass-weighted average dust temperature of this set of optically thin models with $S_{1.1 \text{ mm}, 1000 \text{ AU}} = 10 \pm 1 \text{ mJy}$, the picture improves. In this test case, the median temperature is approximately 40 K. Returning to Figure 2-7, I have also plotted a line showing where models with an average dust temperature of 40 K fall. Per Figure 2-8, more than half of the models in this sample would have inferred masses within $\approx 50\%$ of their true mass if 40 K dust is assumed. These results suggest that the assumption of a constant dust temperature to measure a core mass may be appropriate as long as the dust is at a sufficiently low optical depth and the temperature is representative of the dust in the core. However, if the dust is optically thick but assumed to be optically thin, the mass will be severely systematically underestimated.

To provide a way to systematically choose a more correct dust temperature than the canonical 20 K, I repeat the procedure of identifying models that exhibit a particular flux within a given aperture across a wider range of fluxes and aperture sizes. For each resulting population, I find its median mass-weighted average dust temperature. I compare the masses inferred using these temperatures to the true masses. As in the test case, the majority of inferred masses are within 50% of the true masses across all apertures as long as an appropriate temperature is assumed. In Figure 2-9, I plot the median of the mass-weighted average dust temperatures of the models that exhibit a particular flux. Within a single aperture, the average dust temperature of the

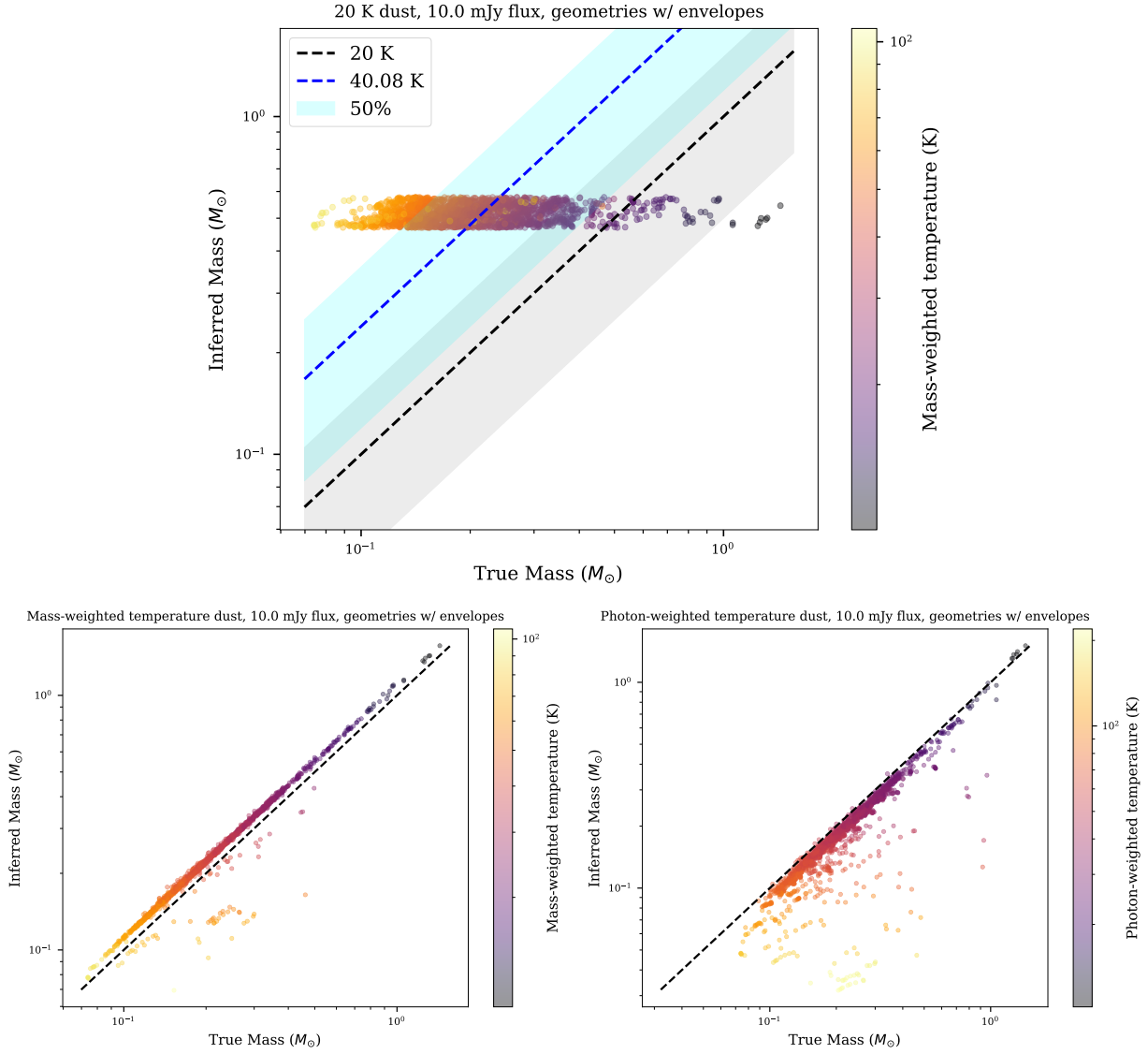


Figure 2-7. Top: Mass inferred for a set of models assuming a constant 20 K dust temperature plotted against the “true” masses for each model, calculated along the line of sight. **Bottom:** Mass inferred using the mass-weighted (*left*) and mass \times temperature-weighted/“photon-weighted” (*right*) average dust temperature of each model plotted against its calculated mass. Each model exhibits a 10 ± 1 mJy flux at 1 millimeter in an aperture of ≈ 1000 AU at a distance of 1 kpc. All model geometries with envelopes are included in this plot. Models included in this plot are optically thin, based on the criteria in §2.4.1. The expected scenario for optically thin dust, $y = x$, has been plotted for comparison (*black dashed line*). In the constant-temperature case, another line is plotted where models at the median mass-weighted dust temperature, ≈ 40 K, occur. The shaded regions in the top plot indicate where models have an inferred mass within 50% of the mass corresponding to their respective dust temperatures. Models are colored by their average dust temperature.

40 K dust, 10.0 mJy flux, geometries w/ envelopes

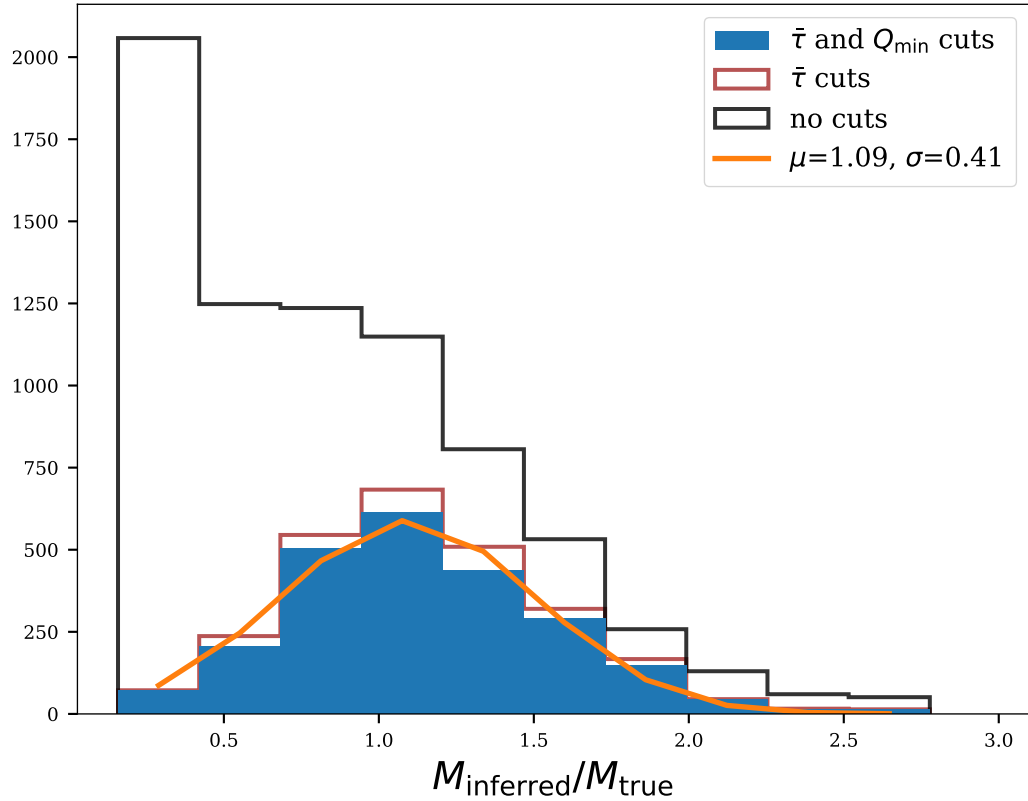


Figure 2-8. Histograms of the ratio of the inferred mass to the true mass of models in the observational case in Figure 2-7, assuming dust at the median mass-weighted average dust temperature of 40 K. **Filled:** With cuts made based on the average optical depth and stability of disks (§2.4.1). A Gaussian is fit to the histogram as a model for the peak and width of this distribution. The majority of the models fall within a range of .4 around the mean of 1.1, which translates to the majority of models having an inferred mass of $\approx 70\text{-}150\%$ of the calculated value. **Unfilled, brown:** With cuts made based only on the average disk optical depth. While this histogram includes models that are unlikely to be observed based on their stability (i.e. small Q_{\min}), the disk stability cut has a minimal effect on the results. **Unfilled, black:** No cuts made at all. The shape is no longer Gaussian, as this includes models that are not optically thin and therefore have more mass than is visible from the observed flux. Including models that exhibit a flux without making cuts based on optical depth decreases the median dust temperature, as additional cold material in disks is hidden from view by higher optical depth.

models tends to increase with the observed flux. This result provides the most appropriate dust temperature to use for mass measurements based on the measured flux and aperture size.

The temperature floor and physical parameter sampling limit the range of masses to which these temperature assumptions apply. By construction, the models in R17 have a floor dust temperature of 10 K. Consequently, his analysis cannot be extended to temperatures below 10 K. This imposes an unphysical lower limit on dust temperature as a function of flux in Figure 2-9. This limitation is expected to be more pronounced as the flux measured in an aperture decreases.

This analysis is also limited by a dearth of models at higher fluxes within each aperture. As an example, the number of models that exhibit a flux of $S_{1000 \text{ AU}} > 100 \text{ mJy}$ is insufficient to repeat Figure 2-8. The expected dust temperatures in this area of flux space are therefore more uncertain. However, while the brighter end of flux space in each aperture is poorly sampled, models in this space are expected to be less likely to occur in nature or are otherwise not relevant for my purposes here. Producing a higher flux from dust while remaining within the same aperture requires some combination of a higher temperature and more dust mass. Higher temperatures require increased energy input, which in turn requires more luminous central sources. These are less common than dimmer sources in the models, which is also generally true for observed stars. The extent to which this flux space is depopulated in the models by the dearth of extremely bright sources is therefore likely mirrored in nature. Meanwhile, introducing more dust to the same physical space will increase its optical depth. Past a certain amount of additional mass, then, a model will likely fail to meet the criterion of low optical depth for inclusion in the sample.

As an addition to the previous caveat, predicted temperatures within apertures smaller than 1000 AU for large fluxes are more likely to have decreased accuracy. To illustrate, the median dust temperature in the smallest aperture in Figure 2-9 does not uniformly increase alongside the measured flux above $\approx 5 \text{ mJy}$, which runs counter to expectations. There is a known decrease in sample size at higher in-aperture fluxes, and smaller apertures are also less likely to have a long-wavelength flux due to post-processing for noise (see Section 4.2.4 of R17.) Taken together, and with a lack of apparent correlation to any parameter of the models, these facts imply that this

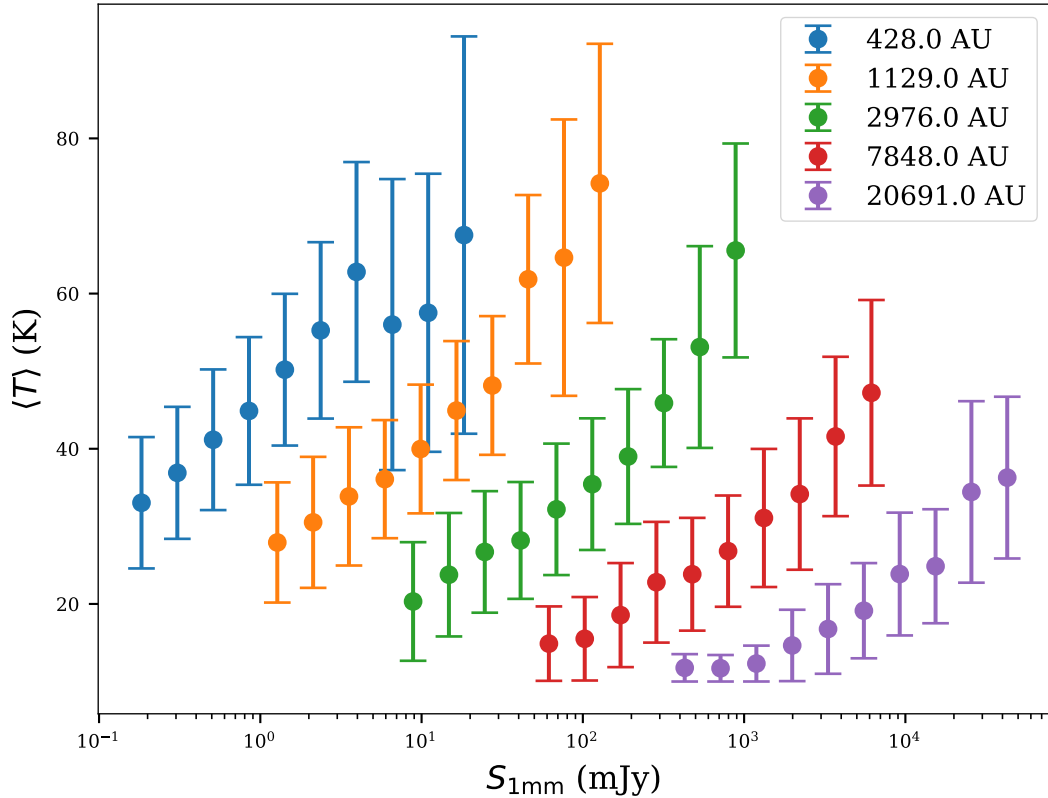


Figure 2-9. The median mass-weighted average dust temperature of models exhibiting a particular flux. All models used to derive these statistics are optically thin, based on the criteria in §2.4.1. As the flux observed from a YSO increases within the same aperture, the temperature of the models that represent it tends to increase as well. Error bars are the median absolute deviation of the dust temperatures. Temperatures in the 428 AU aperture exhibit non-monotonic behavior with increasing flux, unlike in larger apertures. This behavior is endemic to large fluxes within smaller apertures, so care should be taken when applying these results to bright objects observed with small beams.

non-monotonic behavior is related to a sample size issue. Predicted temperatures at high fluxes within small apertures should consequently be treated with care, as they may be artificially lowered. Mass estimates made using these temperatures, then, are effectively upper bounds on the true mass.

2.4.2 YSO Classification

A common tactic used to constrain the physical state of a YSO via observation is to determine its SED class, based on its near- to mid-infrared spectral index. These observational classes are thought to correspond to related evolutionary stages. For example, YSOs of Class I have positive spectral indices, which implies that the SED is dust-dominated. In turn, dust domination of the SED is thought to occur during the stage when most of the mass of a YSO is in its envelope ([Dunham et al., 2014](#), D14).

The position of a YSO in color space is often used to determine the class (e.g. [Gutermuth et al., 2009](#), G09). However, since class is a fundamentally observational method of characterization, there is no guarantee that it actually corresponds to the physical stage. YSOs may be mischaracterized due to observational effects such as inclination or reddening. R06 attempted to provide a more directly physically motivated tool for identifying and characterizing YSOs by placing its YSO models in color space grouped by physical stage as opposed to class. My additions to R17 allow the extension of this analysis by comparing the positions of YSOs grouped by class and by stage in color space. I use these groups to determine the extent to which different classes and stages can be distinguished observationally, and more broadly, the extent to which the concepts of “class” and “stage” are related.

In each diagram, I include an arrow that indicates the effect of ten magnitudes of V-band extinction ($A_V = 10$). Extinction is assumed to take place according to the [Fitzpatrick \(1999\)](#) extinction law as modified by [Indebetouw et al. \(2005\)](#). Throughout this chapter, diagrams are colored according to the density of models in color space, which is done individually for each class and stage. In Appendix B I present an alternate view of these diagrams that instead show where in color space each class and stage is most dominant.

2.4.2.1 Class

Classification of an SED is based on its spectral index, which I have calculated (§[2.3.5](#)). I adopt the spectral classification scheme from [Greene et al. \(1994\)](#) as described in D14, which is as follows:

- Class I: $\alpha \geq 0.3$
- Flat: $-0.3 \leq \alpha < 0.3$
- Class II: $-1.6 \leq \alpha < -0.3$
- Class III: $\alpha < -1.6$

D14 also includes a “Class 0” from [Andre et al. \(1993\)](#) for protostars that are undetectable in NIR wavelengths but are identified via millimeter continuum detection of dust. Observationally, a source is Class 0 if it has $L_{\text{smm}}/L_{\text{bol}} > 0.5\%$, where L_{smm} covers $\lambda \geq 350 \mu\text{m}$. I assign Class 0 to all models that meet this criterion and do not already have a defined spectral class. The remaining SEDs (approximately 5% of the total number of SEDs) are not assigned a spectral class; these cover both SEDs which fail to meet the criteria for all other classes as well as those that are as yet incomplete (see Chapter [2.3.6](#) for details). In Figure [2-10](#), I separate the models by class and visualize them in JWST color space. (I do not include Class 0 models, as by definition they will generally not be detectable by JWST.)

In NIRCam color space (Figure [2-10](#), top) there is a general trend towards the blue from Class I to Class III. Class I models span the largest range in both colors and are capable of having $[\text{F115W}]-[\text{F150W}] > 5$ and $[\text{F150W}]-[\text{F200W}] > 4$, redder than other classes can achieve. Flat and Class II YSOs generally occupy the same region of color space; most have $[\text{F115W}]-[\text{F150W}] < 3$ and $[\text{F150W}]-[\text{F200W}] < 2$, with a small fraction of redder models. Class III YSOs mostly have both colors < 2 . Class I YSOs occupy a unique area of color space, so it is theoretically possible to distinguish them from the other classes. However, this area of space is located along the direction of extinction, so significant degeneracy between interstellar and circumstellar extinction is expected for more deeply-embedded and/or more distant sources. Proper classification therefore hinges on being able to deredden appropriately.

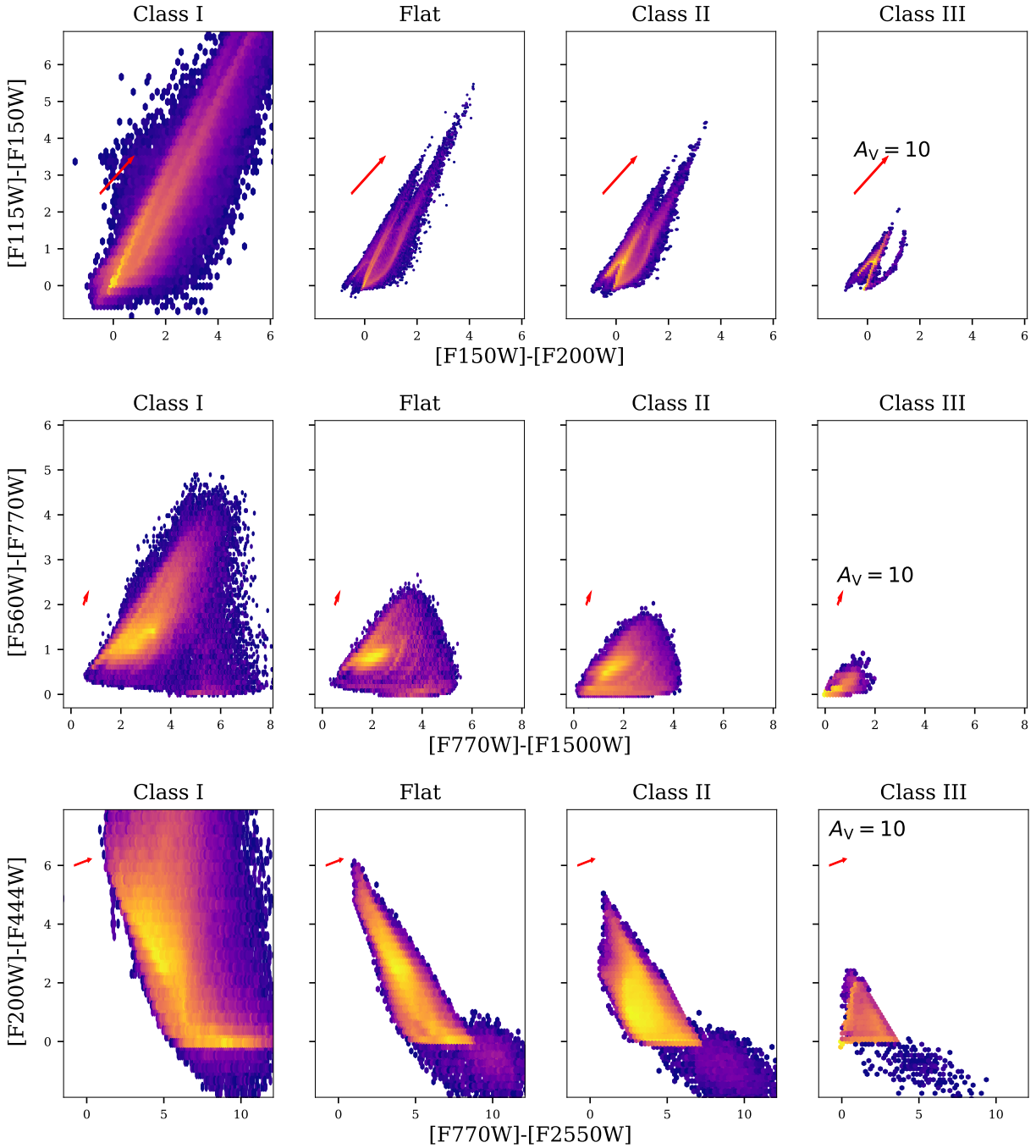


Figure 2-10. Color-color diagrams of models with different classes, based on the classification scheme from D14. I provide one in NIRCam filters (*top*), one in MIRI filters (*middle*), and one spanning the full wavelength range accessible by each instrument (*bottom*). An arrow is plotted on each panel showing the effect of 10 magnitudes of visual extinction according to the [Fitzpatrick \(1999\)](#) extinction law as modified by [Indebetouw et al. \(2005\)](#). All colors are based on model SEDs calculated within a 1000 AU aperture at a distance of 1 kpc.

In MIRI (Figure 2-10, middle), as for NIRCam, there is a clear trend blueward with increasing class number. Class I models are bounded by $[F560W]-[F770W] < 5$ and $[F770W]-[F1500W] < 8$. Flat models can have colors out to 3 and 5, respectively, while Class II models remain within 2 and 4. Class III models are generally bounded by 1 and 2. Unlike NIRCam, there are distinctions in this color space that are separable from interstellar extinction, which affects $[F560W]-[F770W]$ more strongly than $[F770W]-[F1500W]$. Models with $[F770W]-[F1500W] > 5$, caused by warm disks with significant emission around 15 microns, are probably Class I. YSOs are also progressively more likely to have zero color along either axis, but particularly $[F560W]-[F770W]$, going from Class I to III.

In a combined NIRCam + MIRI color space (Figure 2-10, bottom), different classes are easily separable. Despite similar ranges in NIRCam colors (as above), the range in $[F770W]-[F2550W]$ shifts between Classes I, II, and III such that they occupy different “slices” of color space. In this color space, the effect of extinction is most pronounced in $[F770W]-[F2550W]$, meaning that accurate dereddening is important to be able to distinguish between sources with $[F200W]-[F444W]$ close to 0. On the whole, however, degeneracy with extinction can be avoided by combining near-IR and mid-IR photometry.

2.4.2.2 Stage

I adopt the following “stagification” scheme, which uses the definitions from [Crapsi et al. \(2008\)](#) and [Evans et al. \(2009a\)](#) as a base:

- Stage 0: $M_{\text{env}} > 0.1M_{\odot}$, $T_{\star} < 3000\text{K}$
- Stage I: $M_{\text{env}} > 0.1M_{\odot}$, $T_{\star} > 3000\text{K}$
- Stage II: $M_{\text{env}} < 0.1M_{\odot}$, disk present
- Stage III: Bare pre-main-sequence star (no envelope, no disk)

I extend the E09 definition by separating Stages 0 and I by stellar temperature on the grounds that Stage 0 sources should be too cool to be proper pre-main-sequence stars, unlike those in Stage I (i.e. Stage 0 sources will not have reached the Hayashi or Henyey tracks, which begin at

approximately 3000 K). I repeat the color-color diagrams from the previous subsection and plot them in Figure 2-11.

Stages are difficult to distinguish in NIRCam color space (Figure 2-11, top). In each stage, models are mostly concentrated close to zero color—as dictated by the stellar photosphere models—and the models reddened by dust are largely found along the direction of extinction. The majority of all models are bounded by $[F115W]-[F150W] < 6$ and $[F150W]-[F200W] < 5$. Since Stage III is entirely photospheres surrounded by an ambient medium, the position of Stage III models is particularly concentrated in color space. The shape of models in earlier stages is wider around the direction of extinction by comparison. This is particularly true in Stage I, which can achieve $[F115W]-[F150W] > 3$ at low $[F150W]-[F200W]$ and $[F150W]-[F200W] > 2$ at low $[F115W]-[F150W]$. It is therefore possible to distinguish non-Stage III YSOs from reddened stars, and Stage I YSOs in particular, using NIRCam colors. However, doing so relies on proper dereddening.

In MIRI space (Figure 2-11, middle) there is a clear evolution redward in $[F770W]-[F1500W]$ from Stage 0 to Stage II. Models of Stages I and II reach $[F770W]-[F1500W] > 4$, unlike the majority of Stage 0. Some of these models have $[F560W]-[F770W]$ commensurate with the effects of extinction; however, some are also redder in $[F770W]-[F1500W]$ compared to $[F560W]-[F770W]$ than could be achieved by extinction alone. Stages I and II encompass the transition from envelope domination to disk domination, so the appearance of preferential reddening in $[F770W]-[F1500W]$ for Stage I and II models shows that the mid-IR colors involving longer-wavelength emission are disk-dominated. Redder colors result from emission by heated disks, which can be seen through the small or nonexistent envelopes of late Stage I and Stage II. These longer-wavelength colors may therefore be useful in separating more envelope-dominated sources from more evolved ones that have cleared more of their surroundings. Stage III models mostly have colors largely close to zero, though as for NIRCam, some models are reddened by the ambient medium. These models tend to be redder in $[F770W]-[F1500W]$ than expected from

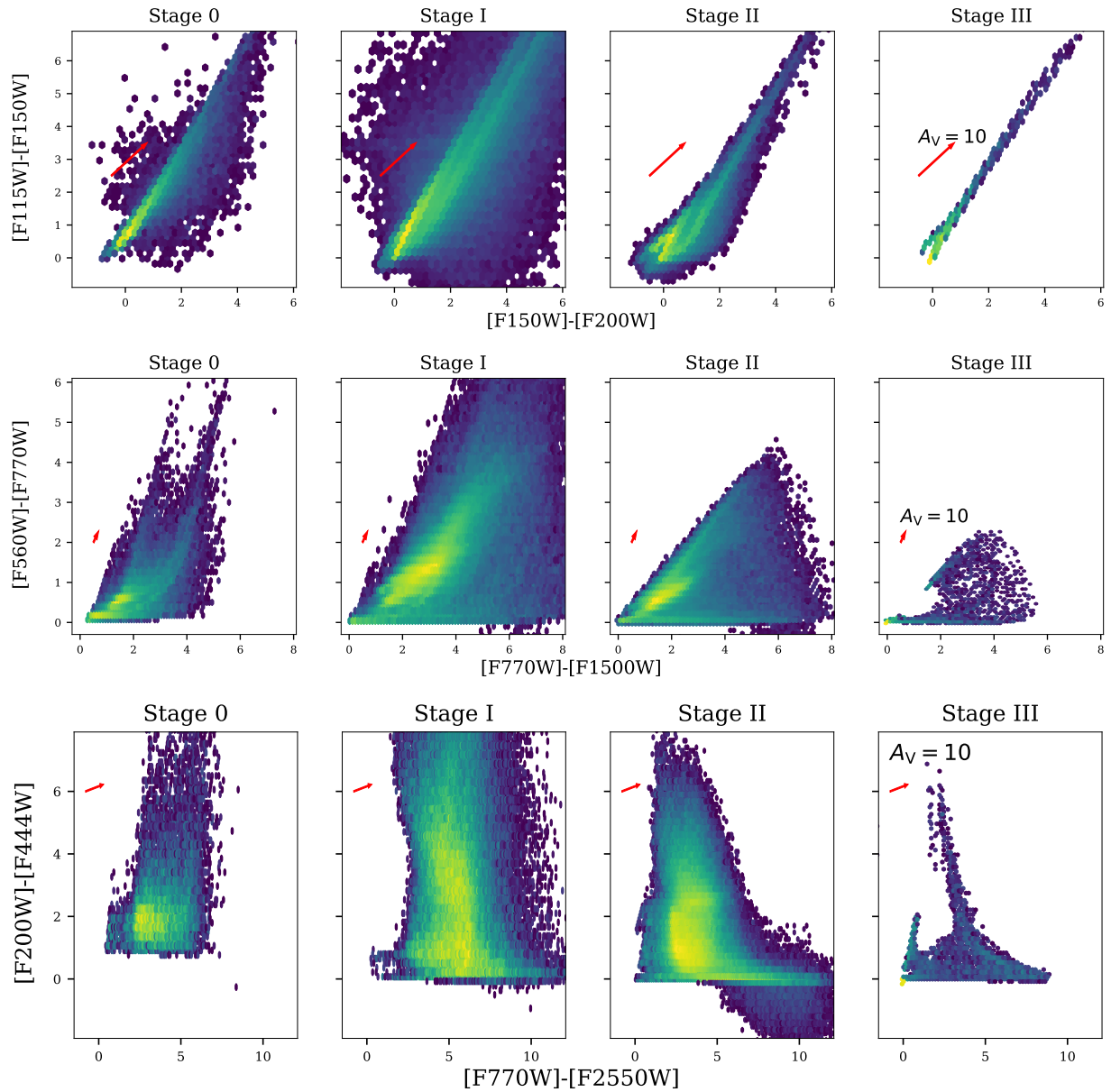


Figure 2-11. The same as Figure 2-10, but with models separated by physical stage instead (see §2.4.2.2 for details).

sightline extinction, driven by emission from a medium that is heated by higher-temperature sources.

Trends from the individual instruments are also visible in a combined NIRCam + MIRI space (Figure 2-11, bottom). Stage I models extend into NIRCam colors that are redder than Stages 0 and II ($[F200W]-[F444W] > 7$) and Stage I and II models are generally capable of being redder in MIRI than Stage 0 ($[F770W]-[F2550W] > 5$). This last point is especially true for Stage II, which has a higher concentration of models that are red in MIRI than the others. However, in this case, the direction of extinction is primarily redward in MIRI, and thus must be disentangled from the effects of evolution.

An examination of Figure 2-11 reveals a nontrivial fraction of models in Stages II and III that exhibit very red colors. In Stages 0 and I, redness resulting from the combination of extinction and excess emission from the circumstellar envelope is expected, but this envelope is essentially absent from later stages by definition. Red colors in Stage III are instead caused by additional emission from heated dust in the ambient medium present in some models (see Section 2.2.1.4 for properties), in turn due to high energy input from extremely luminous sources. Reddening for Stage II models is mostly caused by emission and extinction by the disk, but models with hot sources can also be reddened by a heated medium along sightlines that do not go through the disk. These make up the tail feature in the Stage II panel of Figure 2-11. Most of the red Stage III models come from the `s---smi` geometry, but not all; edge cases are discussed later in this section.

In the models, dust is destroyed by sublimation at 1600 K. However, this is the only modeled pathway for dust destruction; no other mechanisms are implemented by R17 or this work. The floor dust density of $10^{-23} \text{ g cm}^{-3}$ is likely denser than what might be expected in the vicinity of a bare high-temperature star. While some Stage III YSOs could theoretically exhibit some redness via this phenomenon of heated dust, observing such an object is unlikely. These models, which consist of the combined SEDs of a hot star and heated dust, could see an alternate use as model

contaminants; for example, main-sequence stars traveling through a dusty medium. Some additional discussion of reddening by medium emission is contained in Appendix B.

This scheme for determining stages has some quirks when interacting with the models. The definition of Stage III includes models with no non-ambient density structures, which is nominally only two of the eighteen available geometries (`s---s-i` and `s---smi`). However, geometries with an ambient medium—including all geometries with envelopes and half of the others (bare star and star + disk only)—can be Stage III under particular circumstances. The medium is intended as a lower limit to density in models that have it. Some Stage III models therefore ostensibly have envelopes and/or disks with assigned properties, but they are treated as nonexistent by the radiative transfer because they fail to rise above the floor density of the ambient medium at any point, so they are functionally bare PMS stars with a medium. Similarly, the randomly sampled nature of the models can cause models with disks (with or without a medium) to have disks with larger inner than outer radii. In such a case, the disk is not created, and the model is run as if there were no disk. Should the disk be the only non-ambient density structure, these models therefore become part of Stage III.

Stagification also produces models with no defined stage ($\approx 11\%$ of all models). Models with a class but no stage have envelopes with less than $0.1 M_{\odot}$ of mass, but no disk. These can be useful in portraying emission from cores at long wavelengths, but are not assigned a stage because they do not conform to the adopted definitions and are generally not accounted for in any theory of star formation. Models with neither a class nor a stage are incomplete (again, see Chapter 2.3.6).

E09 contains an alternate definition for YSO evolutionary stages, put forth in R06. In this definition, boundaries between stages are set by the ratio of envelope infall rate to stellar mass ($\dot{M}_{\text{env}}/M_{\star}$) and the ratio of disk mass to stellar mass ($M_{\text{disk}}/M_{\star}$). I do not make use of this definition; applying it requires knowledge about the mass and accretion rate of the central source of each YSO, which R17 purposefully does not include.

2.4.2.3 Comparison

Using the previous sections, I compare the distributions of models in color space by class and by stage. While there is overlap between the two, the evolution in class generally tends monotonically blueward to zero color while the evolution in stage tends to push redward before returning to zero. While models of a particular class often coexist in color space with their corresponding stage, these coexistent areas are also often occupied by other classes and stages. Semi-reliable distinction can be achieved by including longer-wavelength (e.g. F2550W) emission driven by the presence of warm disks. The degree to which YSOs of different classes and stages may be identified and distinguished using their position in IR color space is therefore qualitatively in line with R06 and G09.

In addition to comparing class and stage observationally, I evaluate the extent to which the concepts themselves are related. In Figure 2-12, I show a confusion matrix for class and stage. There are clear correlations between class and stage. Majorities of Class I and Class II models are also Stage I and Stage II, respectively, and there is a clear shift towards later stages as class increases in general. However, models of a given spectral class are capable of being many different stages, and vice versa. Approximately a third of Class I sources have a stage other than I, more than a quarter of Class II sources have a stage other than II, and the majority of Class III sources are not Stage III.

This confusion illustrates the magnitude of the effects of confounding factors. Stage II models, for example, have only disks by definition. However, they would be misidentified as having envelopes (i.e. classified as I/Flat) about as often as they would be classified “correctly” if these numbers are taken at face value. They could also be misidentified as bare stars a non-negligible amount of the time. The disjunction between class and stage is driven by the viewing angle, which causes edge-on models to appear to have earlier spectral classes and face-on disks/models to appear to have later ones, and by foreground extinction from the models’ ambient medium. Effects from the latter can also be seen in Stage III models, which have no envelope or

disk by definition, and yet are likely to have a class that is not III due to the presence of an ambient medium.

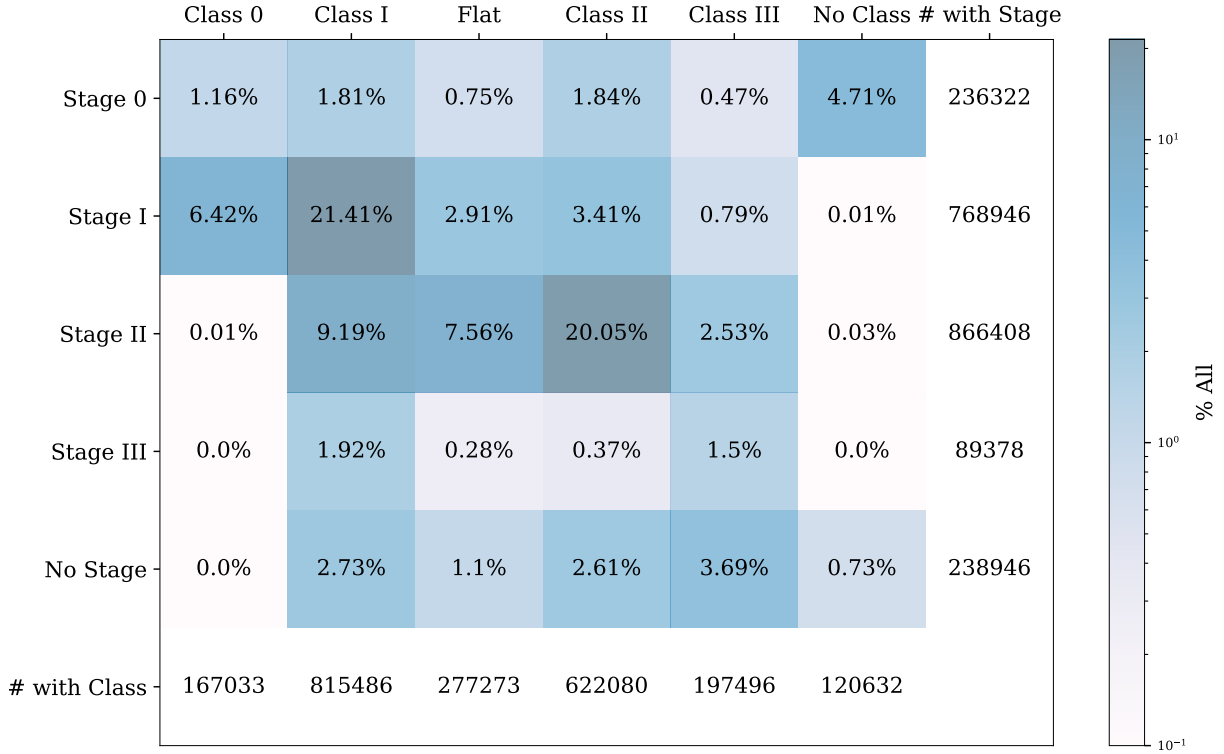


Figure 2-12. Confusion matrix for class and stage. Each cell displays the amount of models that have a given class and a given stage as a percentage of the total number of available models. Classes are assigned using the SED in the largest aperture available to the models, 10^6 AU. The total number of models that have a given stage (across all classes) and class (across all stages) are also displayed. “No class” models are a mixture of optically thick models and incomplete SEDs. “No stage” models exist outside of the definition (see §2.4.2.2) or are incomplete.

I have used the models to outline the distinction between observational class and evolutionary stage. However, I caution against over-interpretation of these results. The number of models in each geometry of R17 is determined by model complexity rather than its ability to accurately represent evolutionary stages or observational classes. The distribution of models within the classes and stages in Figure 2-12 (the numbers in “# with Class” and “# with Stage”) is consequently not representative of the relative fraction of these sources in real star-forming clouds. I also reiterate that all models have randomly sampled properties and intentionally do not

conform to any single model of protostellar evolution. The results from this section therefore include SEDs from models that may not occur in nature, and the degree to which the confusion matrix may be impacted by model feasibility is not quantified here. (I expect the conclusions drawn from color-color diagrams to be minimally affected by model feasibility given their qualitative agreement with the literature; see Appendix B for a direct comparison to R06.) I also acknowledge that the method for assigning evolutionary stages to the YSO models is distinct from schemes used by other works. This definition is based on commonly used distinctions between stages where possible and relies on accepted physics for any further additions. I therefore expect it to sort models appropriately, but assigned stages may differ depending on the scheme. These caveats will be revisited in Chapter 3.4.2, after the ability to evaluate the “physicality” of these models has been introduced and where the impacts of alternate definitions for class and stage can be examined in more detail.

2.5 Closing Remarks

In this chapter, I have presented a significant update to the Robitaille (2017) set of YSO models. I have calculated several quantities using the existing model parameters and infrastructure. Through these calculations, I have substantially expanded the utility of the existing models within contexts where they are currently in use. Models from the original set are commonly used as template SEDs to determine YSO properties. The additional content increases the number of quantities that may be constrained through this method, including:

- the “observed” mass of a core within an aperture (“Line-of-Sight Masses”)
- the “actual” mass present around the source (“Sphere Masses”)
- the average dust temperature (“Sphere Mass-Weighted Temperatures, Line-of-Sight Mass/Photon-Weighted Temperatures”)
- the extinction as a result of circumstellar dust (“Av”)

all of which provide a more complete characterization of an observed YSO. I have also provided further insight into the physical state of each model by calculating a baseline for the stability of the disk for models with disks as well as the average dust temperatures within the series of apertures in which the SEDs are defined.

Beyond this work’s application to existing use cases, I have utilized my new additions to derive new results previously inaccessible to users of these models. In particular, I use my updates to provide guidance for measuring the mass of an optically thin core based on the observed flux. I find that assuming a constant dust temperature may yield an inferred mass within a factor of two of the correct value. However, that level of precision requires assuming a representative dust temperature. The “correct” temperature is often not the canonical 20 K, and varies with the observed flux and aperture size. Moreover, the inferred mass may be underestimated by over a factor of two if the dust being observed is insufficiently optically thin.

The newly calculated properties also enable assigning each model an observational class and evolutionary stage. I use the convolved SEDs (now including every filter on the James Webb Space Telescope) to locate each model in IR color space and map out the regions that are home to each class and stage. I find that mid-IR colors are sensitive to the presence of disks, making them a useful tool to identify YSOs and distinguish between evolutionary stages. Further, the expanded scope and larger size of this set enables users to probe other color spaces and set expectations for newly obtained data. I also use these assigned classes and stages to evaluate the extent to which the concepts of “class” and “stage” are related in this set of models. I find a correlation between the two, as expected, but also find that the mapping from class to stage can be confused by viewing angle and foreground extinction in a nontrivial fraction of cases.

The models and associated scripts have been made publicly available at
<https://doi.org/10.5281/zenodo.8114592>.

CHAPTER 3

A FRAMEWORK FOR MODELING THE EVOLUTION OF YOUNG STELLAR OBJECTS

3.1 Motivation

Numerous theories have been developed to explain the process by which stars are born.

Because these theories typically focus on particular physics (e.g. gravitational collapse, turbulence, Bondi-Hoyle accretion, etc.), the resulting pictures of star formation they lay out are often in tension and sometimes completely incompatible. The case for each theory is built by comparing measurements of YSO properties—usually made using template SEDs like the kinds described in Chapter 2—to predictions for observable quantities made following a particular theoretical model. However, the current infrastructure supporting comparisons of this kind has pervasive deficiencies which limit the ability to perform a comprehensive evaluation of any of the proposed theories, leading to continued uncertainty in our picture of star formation.

Many previous approaches to modeling YSOs rely on the assumption of particular protostellar evolutionary tracks or accretion histories (e.g. [Robitaille et al., 2006, 2007](#); [Zhang & Tan, 2018](#)). These works produce grids of self-consistent YSO evolutionary tracks and SED models; however, their capacity to measure YSO properties when used as templates for SED fitting is limited by the narrow range of parameters allowed by their evolutionary tracks. That narrowness generally limits the extent of the theory space that the resulting SED models are able to cover. These model grids are therefore generally unable to distinguish between different models of star formation (e.g. isothermal vs. turbulent-core initial conditions). Other YSO model grids that do not assume any particular evolutionary theory exist, as in the cases of [Furlan et al. \(2016\)](#) or [Haworth et al. \(2018\)](#). However, these grids similarly cover a relatively narrow range of protostellar parameter space and often focus on modeling a single YSO morphology (i.e. star + disk systems, star + disk + envelope systems, etc.).

In this chapter, I create a method to model YSO evolution that can be used more broadly without sacrificing the quality of existing model grids. Instead of prefacing the creation of YSO

Submitted to the Astrophysical Journal as [Richardson et al. \(2025\)](#); reprinted with permission. Minor edits have been made for inclusion.

models with assumptions, I link YSO SED models with no foundational evolutionary history and spanning a wide range of parameters and morphologies with separately generated protostellar evolutionary tracks, enabling prediction over a wider theory space.

I base this work on the model set of Richardson et al. (2024, R24), which is the updated version of Robitaille (2017, R17) outlined in Chapter 2. This set is a collection of 3D YSO radiative transfer models that provides templates for SED fitting. The free parameters in R24 are sampled randomly from a parameter space made from properties of stars, cores, and disks. This approach results in roughly even coverage in every dimension. While this treatment produces a number of models that are unphysical in the sense that they are not compatible with any self-consistent accretion history, and it does not include information about the masses or ages of its stars, the grid does not privilege any theory of accretion or evolution over any other by construction. This approach to YSO modeling has precedent in Nandakumar et al. (2018), which also used R17 to constrain the stellar mass of a set of observed YSOs by determining the proximity of the illuminating sources in well-fitting models to protostellar evolutionary tracks from Bernasconi & Maeder (1996).

My method for modeling the evolution of YSOs allows generation of YSOs according to multiple proposed mechanisms of accretion with variation in quantities such as star formation efficiency over a wide range of stellar masses. This freedom in modeling enables probing theory space to a previously unattempted extent, which in turn allows greater insight into the physical mechanisms taking place in regions of star formation. I present this method in Section 3.2, present results from modeled YSOs in Section 3.3, show some further uses of my framework in Section 3.4, and conclude in Section 3.5.

3.2 Framework

3.2.1 The R24 Models

This chapter makes heavy use of the set of YSO SED models from R24. Here, I provide a brief overview of the relevant aspects of the model set. A full accounting of the properties and construction of the models can be found in Chapter 2 and R17. To avoid confusion with other

instances of “models” or “modeling” in this chapter, I will refer to constituent models from R24 as “radiative transfer models”—abbreviated to “RTMs”—or “R24 models” going forward. (The other main instance is in reference to models of protostellar evolutionary tracks, which will be introduced in Section 3.2.2.)

R24 models are divided into subsets based on the presence or absence of certain circumstellar density structures. I refer to these subsets as “geometries” through the remainder of this chapter. While all RTMs possess a central luminosity source, they may exhibit combinations of circumstellar envelopes, circumstellar disks, bipolar cavities, and an ambient medium. There are some constraints placed on these combinations: geometries with cavities must also have envelopes and geometries with envelopes must also have an ambient medium, which allows a cutoff point for an envelope to be defined. Each of these features has its own set of associated parameters that determine its shape and density profile. The number of RTMs in each geometry is influenced by its complexity (i.e. number of free parameters); the two most complex geometries make up a plurality of the total set of models. Every geometry is axisymmetric about the z axis (i.e. no ϕ dependence) and reflectionally symmetric across the $x - y$ plane, but many features introduce a θ dependence in the dust density profile. Geometries are identified by a series of seven characters, e.g. `spubhmi`, indicating which features are present or absent; see Table 2 of R17 for more detail.

Each set of parameters has an accompanying SED modeling the dust continuum emission, created through the use of the Monte Carlo radiative transfer code `Hyperion` (Robitaille, 2011). The SEDs are given as flux densities (i.e. S_ν) in units of mJy. They are calculated over the wavelength range of 0.01-5000 μm within a series of circular apertures that have radii evenly log-spaced between 10^2 - 10^6 au. RTMs with a θ dependence have SEDs with nine lines of sight randomly sampled from ten-degree bins from 0° (face-on) to 90° (edge-on). RTMs with no θ dependence have only one SED, since they are spherically symmetric and look the same along every sightline. All dust in R24 is a model from Draine (2003a,b, D03) with the Weingartner &

[Draine \(2001\)](#) Milky Way grain size distribution A for $R_V = 5.5$ and carbon abundance C/H renormalized to 42.6 ppm.

As of R24, each RTM is also associated with several properties that emerge from its shape parameters and temperature profile. The quantity most relevant to this work is the circumstellar mass, which is calculated around each source in spherical regions with the same radii as the SEDs. This “sphere mass” tracks the amount of dust and gas around the central source out to the radius at which the envelope (along with any disk or cavities present) blends into the ambient medium. Since the native density profiles only track dust density, these masses assume a gas-to-dust ratio of 100 to arrive at a total mass.

3.2.2 YSO Composition

In this section, I lay out the steps followed to create a model of an evolving YSO within my framework, as well as the assumptions made in the course of modeling. For the sake of clarity, I adopt the linguistic convention that a “YSO” refers to the combined system of a central luminosity source (star, PMS star) and surrounding density structures (envelope, disk, etc.) while a “protostar” refers only to the source. This is consistent with the usage of these terms in the work that I build upon, but may differ from the parlance and working definitions of other entries in the literature.

The process begins by generating evolutionary tracks for protostars using the [Klassen et al. \(2012\)](#), K12 code for modeling protostellar evolution. Each of the tracks created by the K12 code predicts mass, radius, luminosity, and other intrinsic properties of a protostar from the initiation of gravitational collapse to arrival on the main sequence, given its final (zero-age main-sequence) mass as input. As published, the code implements an isothermal-sphere (IS, [Shu, 1977](#)) accretion history following the [Offner et al. \(2009\)](#) implementation of the protostellar evolution model of [Nakano et al. \(1995\)](#), as extended by [Nakano et al. \(2000\)](#) and [Tan & McKee \(2004\)](#). I have modified this code to also generate both turbulent-core (TC, [McKee & Tan, 2002, 2003](#)) and competitive (CA, [Bonnell et al., 1997, 2001](#)) accretion histories according to prescriptions for

accretion rates laid out in [McKee & Offner \(2010, M10\)](#). I will refer to these evolutionary tracks as “protostellar evolutionary models”—abbreviated “PEMs”—throughout the rest of the work.

M10 accretion history models all follow the the form:

$$\dot{m} = \dot{m}_1 \left(\frac{m}{m_f} \right)^j m_f^{j_f} \quad (3-1)$$

where m_f is the final stellar mass and j and j_f are real-valued exponents that vary with accretion history. \dot{m}_1 is the final accretion rate for a star of unit mass and is set by a scaling parameter, which also varies with history. For IS accretion, this scaling parameter is the gas temperature T , for which I adopt a value of 10 K. For TC accretion, the scaling parameter is the gas clump surface density Σ_{cl} , which I take to be 0.1 g cm^{-2} . For CA, given the hierarchical nature of the theory, the scaling parameter is the average number density of hydrogen atoms across a cloud \bar{n}_{H} , which I take to be 10^4 cm^{-3} . (These are the fiducial values by which the respective accretion rates are scaled in M10.) Figure 3-1 shows a sample comparison of accretion rates prescribed by these histories. Varying these scaling parameters changes the accretion rate of a protostar, which will in turn affect protostellar properties sensitive to the accretion rate and the timescale of accretion. This means that the predictions made using these PEMs will also be affected by these scaling parameters; however, a full analysis of their impact is out of scope for this work.

I adopt different timesteps for the K12 code depending on the assumed accretion history and zero-age mass to ensure that evolution is tracked on appropriate timescales. IS accretion in M10 is a constant rate, meaning that it can be well captured with timesteps that scale with zero-age stellar mass. The timestep is set to be 0.1% of the total accretion time. The M10 prescriptions for TC and CA depend both on instantaneous and final stellar mass, resulting in accretion that increases with time. Per [Bonnell et al. \(2001\)](#), the characteristic time for star formation in CA is roughly the initial free-fall time of the parent cloud of a stellar population, $t_{\text{ff}} = 0.435 \bar{n}_{\text{H},4}^{-1/2} \text{ Myr}$, where $\bar{n}_{\text{H},4} \equiv \bar{n}_{\text{H}} / (10^4 \text{ cm}^{-3})$. Since CA in M10 is tuned to produce stars that accrete in roughly this characteristic time regardless of final mass, the timestep is set at 0.1% of this timescale, as with

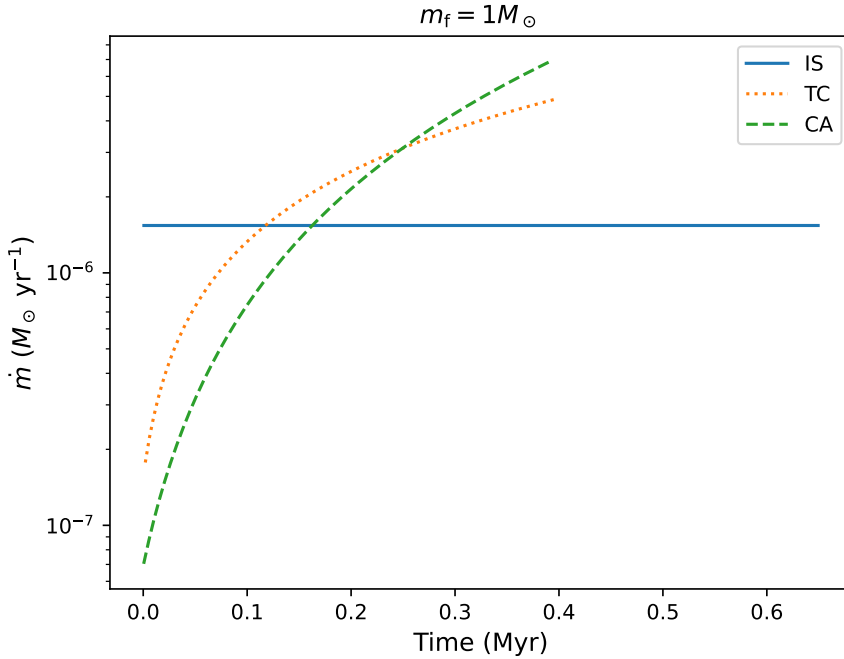


Figure 3-1. Accretion rates from PEMs generated from a modified K12 code, following prescriptions from M10. The lines show isothermal-sphere (IS), turbulent-core (TC), and competitive (CA) accretion rates as a function of time for a star with a final stellar mass of $1 M_{\odot}$, attained at the end of each line.

IS. For TC, which has no such characteristic time, evolution is modeled for 2 Myr with a fixed timestep of 2×10^3 yr. These choices provide a time span that is long enough for the most massive protostars to accrete and sampled well enough to capture the increase in accretion rate.

Once the PEMs have been generated, I use the time evolution of the mass for a given protostar to track the time evolution of the corresponding mass contained in its circumstellar material (i.e. the core mass). For the purpose of this chapter, each modeled protostar is assumed to accrete via monolithic collapse, a paradigm where one core forms one star. (This assumption is at odds with the theory behind CA, where an entire stellar population competes for the material in a single mass reservoir, i.e. hierarchical collapse. However, the nature of the theory makes it difficult to model CA accretion rates without making some choices for the sake of implementation. M10's parameterization of CA is intended to preserve the dependence of the accretion rate on tidal effects and a formation time roughly equivalent to the free-fall timescale, which are important aspects of the theory. Since these broad strokes of CA are factored into this

treatment, I use the protostellar mass to track the mass of material around a protostar in the same way as for IS and TC models.) I further assume a core-to-star mass accretion efficiency ϵ_{SF} such that $M_{\star, \text{final}} = \epsilon_{\text{SF}} \times M_{\text{core, initial}}$; as a result, the mass of the core evolves as

$M_{\text{core}}(t) = M_{\text{core, initial}} - M_{\star}(t)/\epsilon_{\text{SF}}$. For the sake of internal consistency, I adopt the commonly-used value of 1/3 for ϵ_{SF} (e.g. Motte et al., 1998; Alves et al., 2007; Nutter & Ward-Thompson, 2007). This value is used for the results in Chapter 3.3, but ϵ_{SF} is implemented as a variable parameter, and variation is allowed in Chapter 3.4.2.

I note that all of M10’s formulations prescribe steady, non-episodic accretion. Observations of YSOs indicate that accretion is generally variable over a wide range of timescales and is often episodic or stochastic (Fischer et al., 2023). If implemented, accretion variability would likely cause modeled protostellar behavior to differ from the steady state, particularly in the case of YSOs in outburst. Moreover, the current treatment of YSO construction, in concert with the assumed PEMs, paints a physical picture in which a single protostar forms from a finite mass reservoir with either a constant or accelerating accretion rate. Since mass from the natal material of a star is ejected during formation, decreasing the total available mass and lengthening the free-fall time, a non-decreasing infall rate cannot be supported without replenishment of the protostellar envelope (i.e. a protostar drawing from a finite reservoir should have a decreasing accretion rate). I acknowledge that the IS/TC/CA models utilized here are therefore not, as implemented, fully consistent with modern understanding of star formation. I elect to employ simplified models of accretion to broadly examine the observational consequences of distinct physical models for protostellar growth; evaluation of accretion histories which incorporate additional physics (e.g. tapered or episodic accretion) is deferred to a future work.

Once the star-to-core mapping is performed, the PEMs are translated into a parameter space that enables comparison to the RTMs. I construct this space using the source temperature T_{\star} , source luminosity L_{\star} , and circumstellar mass M_{core} of each R24 model. L_{\star} is the total luminosity of the protostar, meaning that it includes both the intrinsic luminosity of the source and luminosity from accretion. The choice between tracking intrinsic or total luminosity impacts flux predictions

for wavelengths sensitive to L_\star ; I use the total luminosity to ensure the radiation emitted from the central source is fully captured, regardless of origin. More discussion about the impact of source luminosity on downstream results is in Appendix A. Each RTM has a calculated mass within each aperture where the SEDs are defined; I adopt the mass contained within the eleventh aperture, which has radius $\sim 10,000$ au (notated as $M_{10\text{ k au}}$) as a proxy for M_{core} . This size encompasses the majority of the mass contained in the envelopes of most of the RTMs without including background dust.

Since I am primarily interested in modeling the phase of a protostar's evolution where it is actively accreting, I limit this parameter space to RTMs from the geometries that have circumstellar envelopes. This makes a set capable of modeling all the evolutionary stages of a YSO in which the central protostar has not yet depleted its mass reservoir (more discussion about these stages and how they intersect with the R24 models can be found in Chapter 3.4.2). These geometries represent about 75% of the total set of RTMs.

Finally, I model the SED of a YSO by associating the R24 models with the PEMs. To arrive at an evolving SED, a nearest-neighbor search is performed within the $T_\star - L_\star - M_{\text{core}}$ space to match the K12 output to R24 models at each timestep. In order to reduce noise in the predicted SED, I identify the ten nearest RTMs across all geometries in the set and average between them by taking the median of their SEDs. The majority of RTMs have SEDs defined at nine inclinations, which are randomly sampled from within nine evenly spaced inclination bins between $0 - 90^\circ$ (see §3.2.1). I preserve this inclination dependence in the predicted SEDs. Keeping the same bins, I ensure that each selected RTM contributes the appropriate SED to each inclination bin and average within each bin independently, producing nine SEDs per PEM timestep. RTMs from spherically symmetric geometries, which do not have inclination-dependent SEDs, contribute the same SED to each inclination bin for consistency with other geometries.

This step-by-step search allows me to tie any modeled protostellar evolutionary theory to a series of proximal YSO RTMs in the R24 set. I demonstrate nearest-neighbor selection in the constructed parameter space for IS, TC, and CA accretion histories in Figure 3-2. This figure

shows the single nearest neighbor to each point on the tracks and restricts itself to R24’s second-most-populous model geometry (see §3.2.1 for more detail) for the sake of visual clarity. In practice, I base the modeled SED on a larger set of RTMs and average over more neighbors to reduce noise.

3.2.3 Proximity

In the previous section, I laid out my procedure for creating models of evolving YSOs: tracking the nearest RTMs to protostellar evolutionary models. The question of how to define “nearest” in the parameter space I use, however, is a substantive one. Working with different definitions results in different RTMs being identified as “nearest”, which has repercussions for the predicted flux values and uncertainties obtained by averaging over multiple nearest neighbors.

The most common way to define distance in 3D space is by the Cartesian distance metric, $ds^2 = dx^2 + dy^2 + dz^2$. This is a definition that is easy to adopt, but is not necessarily optimal. The range of values in each of the employed parameters spans at least two orders of magnitude, meaning that the Cartesian metric will not capture distance evenly at different magnitudes. Beyond this numerical consideration, a Cartesian metric is built on the assumption that each included dimension has the same underlying physical significance. For these parameters, this is not the case. Each corresponds to a physical quantity that means something different for the YSO it describes, meaning that a metric that does not allow for independent handling of each dimension may not be desirable.

I adopt an alternate method for characterizing distance that addresses these concerns. Starting from the initial data set of the source temperatures/luminosities and core masses of every YSO with a circumstellar envelope, I use this data to construct a quantile transformer. This transformer maps each parameter to a uniform distribution between 0 and 1 independently by estimating the cumulative distribution function (CDF) of the parameter values. Once this transformer is constructed, I apply it to the evolutionary track and find the nearest neighbors by minimizing the Cartesian distance in this transformed space. Proximity to the evolutionary track

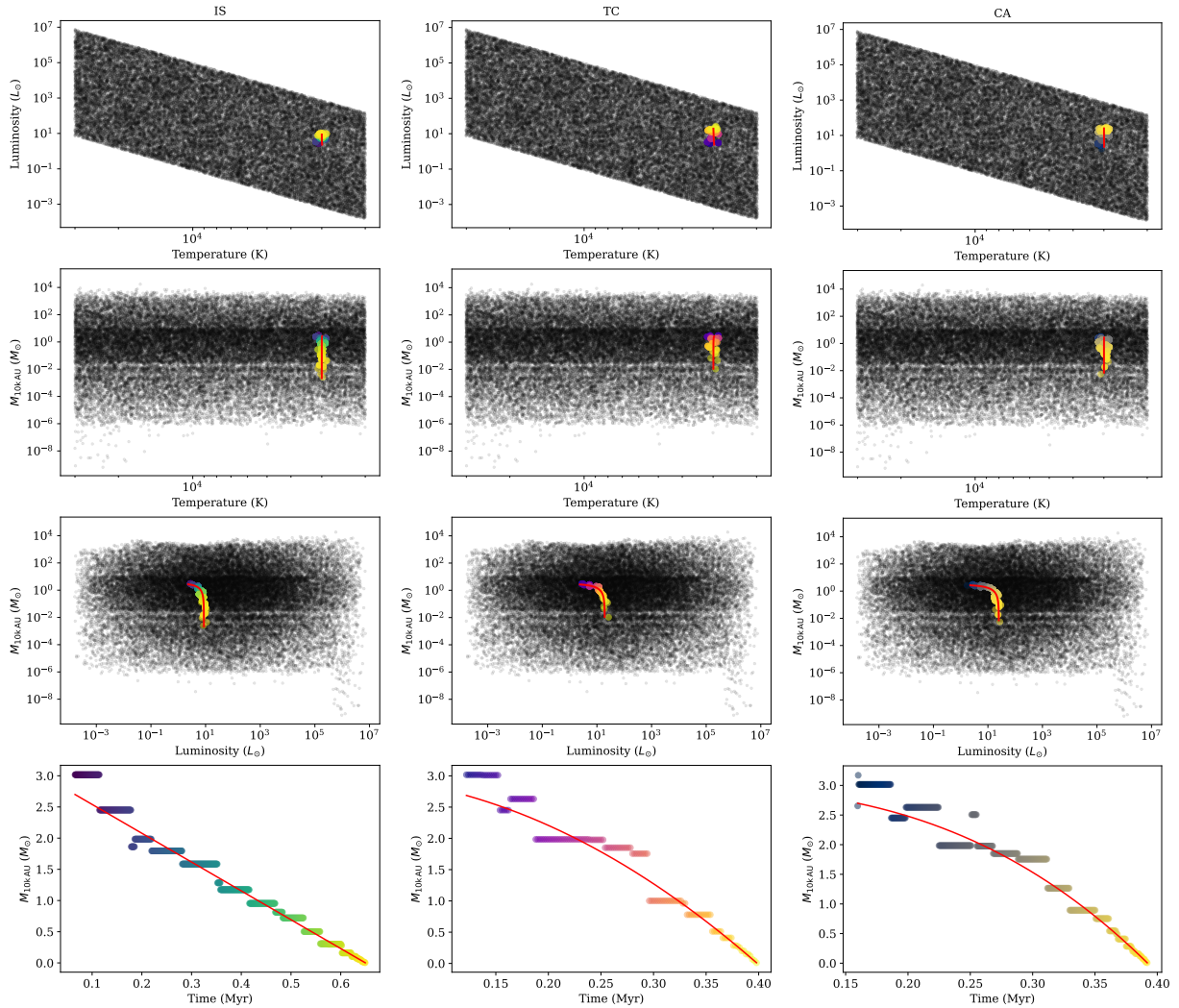


Figure 3-2. 2D projections of the 3D parameter space constructed from stellar temperature, stellar luminosity, and surrounding core mass of all models in one of the R24 geometries. Evolutionary tracks for $1M_{\odot}$ stars generated by the modified K12 code are traced in red. I show IS (left), TC (middle), and CA (right) histories. The nearest neighbor RTM (per §3.2.3) to the track at each timestep is highlighted. Coloration is determined by time.

is therefore characterized using the following equation:

$$D_{\text{quant}}^2 = (\text{QT}_T\{T_{\text{RTM}}\} - \text{QT}_T\{T_{\text{PEM}}\})^2 + \\ (\text{QT}_L\{L_{\text{RTM}}\} - \text{QT}_L\{L_{\text{PEM}}\})^2 + \\ (\text{QT}_M\{M_{\text{RTM}}\} - \text{QT}_M\{M_{\text{PEM}}\})^2 \quad (3-2)$$

for the quantile transform of quantity x QT_x . This scheme for determining distance adequately addresses the issues of straightforward Cartesian distance. Transforming independently based on the CDF of each parameter effectively allows distance in each parameter to be considered within its own physical context, while mapping to a uniform distribution aligns the value ranges of the disparate dimensions.

I find that this quantile-transform approach produces good results with low uncertainty (see §3.3.2) and can be easily applied to any set of parameters, making it a very attractive general-purpose definition for distance. The results I present throughout this chapter therefore use this definition. In the course of research, I have devised numerous alternate conceptions of “distance”; Appendix D discusses these alternates, but the quantile-transform approach generally matches or outperforms them.

3.3 Results

In this section, I provide an overview the kinds of results that can be obtained from YSO models generated with my framework.

3.3.1 Flux Predictions

The primary functionality of my framework is predicting the flux exhibited by YSOs across time for a given theory. An example is Figure 3-3, which shows the time evolution of YSO flux at multiple wavelengths for IS, TC, and CA histories. In this figure, I track the flux at $100\ \mu\text{m}$ and $3\ \text{mm}$. These wavelengths are often used to trace the luminosity and mass of dusty sources, respectively. It is generally assumed that the bolometric temperature of dust peaks around $30\ \text{K}$ such that the $100\text{-}\mu\text{m}$ flux is a good proxy for the total luminosity. Dust is also generally assumed

to be optically thin at longer wavelengths, therefore allowing its mass to be well traced by 3-mm emission.

These results can be used to set expectations for how a YSO will appear to an observer over the course of its lifetime. Starting as a clump of gas and dust at stellar densities, a protostar grows by consuming mass from the core and heats its surroundings. For low-mass sources, this growth manifests primarily in a decrease of both 3-mm and $100\text{-}\mu\text{m}$ intensity. Since low-mass protostars also have low temperatures, the heating from the source is negligible. Most of the dust, and by extension gas, is at the floor temperature of 10 K imposed by the RTM parameters. As such, evolution in flux space for low-mass YSOs is mostly witnessing gas being consumed by the star. High-mass protostars, on the other hand, are able to heat their surrounding material enough to outpace the loss of material. A decrease in flux at both wavelengths is seen only once the dust is almost entirely consumed. The resulting “knee” feature in the high-mass tracks is akin to the transition between the “accelerating envelope” and “clean-up” phases hypothesized in [Molinari et al. \(2008\)](#) and [Elia et al. \(2010\)](#), representing the point where the envelope begins to dissipate due to the high energy output of the central source. (Since these phases are conceived using the TC model of accretion, I do not claim exact congruence with this scenario, but note that the general picture of YSO evolution painted by these predictions is qualitatively similar.)

The three modeled accretion histories (see §[3.2.2](#) for details) lay out distinct visions of protostellar evolution. These results allow the impact these histories have on the expected flux from my modeled YSOs to be quantified. For a YSO with some final stellar mass, the assumed history does not significantly change the shape of the path it cuts through the flux space. The change instead occurs primarily in the timescale of accretion and evolution, which is highly dependent on assumed history.

Accretion rates for both CA and TC histories exhibit some dependence on both final and instantaneous stellar mass, and IS accretion depends on neither. This causes accretion following TC or CA histories to be slowed down relative to IS accretion—to varying degrees—for low-mass stars. As an example: in the implemented PEMs, a $0.2M_\odot$ star takes roughly 0.13 Myr to accrete

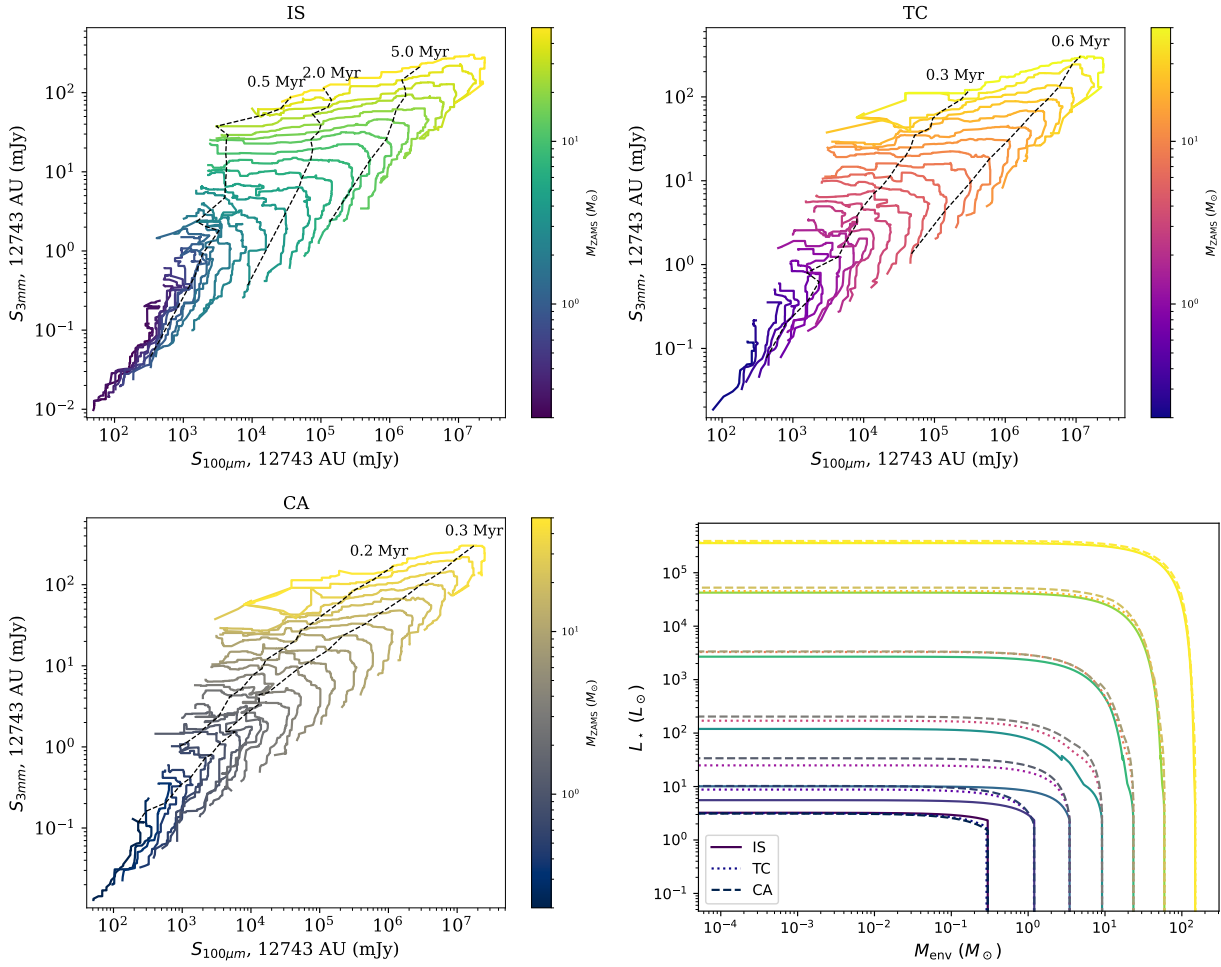


Figure 3-3. The 3-mm vs. 100- μm flux of evolving YSOs, constructed through my selection procedure (§3.2.2). I show IS (top left), TC (top right), and CA (bottom left) histories. Tracks correspond to zero-age stellar masses evenly log-spaced between $0.2 - 50 M_\odot$. Each line spans the ignition of a source to depletion of the surrounding mass reservoir, roughly from left to right. Coloration is determined by final stellar mass (M_{ZAMS}). The flux values plotted here have been smoothed by taking a rolling median of the predicted flux values at each timestep; the number of timesteps included in the median depends on the length of the track, with tracks corresponding to more massive stars including more timesteps. I plot isochrones (black, dashed) to track the passage of time. There is a clear distinction between the movement of models produced by each history within this flux space. In the bottom right, I plot the evolution of the envelope mass and total bolometric source luminosity corresponding to a subset of evolutionary tracks from all three histories; time travels in the direction of decreasing envelope mass. The plotted tracks correspond to the same set of final stellar masses for each accretion history; colorbars remain the same.

in an IS scenario, approximately 0.25 Myr for TC, and about 0.36 Myr for CA. Low-mass stars will therefore deplete their dust on different timescales, and will consequently be visible at long wavelengths for varying times (putting aside that sources near the substellar boundary are difficult to observe in general).

Conversely, the mass dependences of TC and CA histories accelerate the accretion of high-mass stars relative to an IS scenario to varying degrees. A $5M_{\odot}$ star takes about 0.4 Myr to accrete following a CA PEM, approximately 0.6 Myr for TC, and over 3 Myr for IS. Since these higher-mass protostars are the main driver of 100- μm flux, the far-IR luminosity of these YSOs will peak on drastically different timescales, and will linger around peak for different amounts of time as well.

Given the difference in time scales, it is theoretically possible to distinguish the mechanism of accretion at play through observation. CA YSOs should be expected to reach peak 100- μm and 3-mm flux around the same time, while low-mass YSOs should peak sooner than high-mass YSOs following TC or IS histories (and much more so for IS histories than TC). For a given 3-mm flux, then, populations following different accretion histories should exhibit markedly different 100- μm fluxes at the same time. It is possible that YSOs within different mass regimes may operate in different modes of accretion. High-mass stars have been hypothesized to behave more competitively than low-mass stars, which are generally thought to form from the collapse of isolated mass reservoirs ([Kennicutt & Evans, 2012](#)). Such a mixed-mode population would consequently exhibit different time behavior in this flux space than any of the modeled PEMs, and therefore likely appear distinct from other accretion histories.

Aside from the long-wavelength emission of a YSO, if the central protostar reaches a high enough mass to begin burning deuterium during the time it is actively accreting, its evolution in temperature and luminosity also varies significantly with the assumed accretion history. This turnover point in the PEMs occurs at about $2 M_{\odot}$ for IS, $4 M_{\odot}$ for TC, and $5 M_{\odot}$ for CA. (Less massive stars still enter a deuterium-burning phase, but only after they have accreted all of their mass according to the PEM.) Changing the accretion history therefore changes the properties of

protostellar sources in the selected RTMs. The cumulative effect from variation in source temperature and luminosity is unlikely to have a large influence on the long-wavelength flux of a YSO (see Appendix D) but may have a stronger effect at shorter wavelengths where the stellar SED is more influential. Differences between the evolutionary tracks can be seen in Appendix E.

My framework opens a new pathway to observationally determining the evolutionary history of a YSO. Many previous studies have attempted to compare observations of YSOs to predictions from various theoretical models for protostellar evolution and accretion. The majority of these, however, do not link evolution with radiative transfer as this work does. Instead, their focus is on “summary” properties emerging directly from the accretion models, typically the total protostellar luminosity L_{tot} or envelope mass M_{env} .

Table 3-1 provides a comparison between the foundations and predictive capacity of this work and those of previous entries in the literature. Broadly, these previous entries break down into two main categories: those that chiefly compare distributions of observationally derived summary properties to overall model behavior, and those that focus more on the evolution of individually simulated models. [Offner & McKee \(2011\)](#), [Duarte-Cabral et al. \(2013\)](#), [Fischer et al. \(2017\)](#), and [Sheehan et al. \(2022\)](#) exemplify the former category. [Offner & McKee \(2011\)](#) compares the observed distribution of protostellar luminosities to simulated distributions constructed using a wide array of modeled accretion histories; the remainder compare L_{tot} and M_{env} from a sample of YSOs against the coverage of protostellar evolutionary tracks in this total-luminosity/mass space. [Duarte-Cabral et al. \(2013\)](#) also performs a similar comparison for L_{tot} ¹ and CO momentum flux F_{CO} . (The measured luminosities and masses [Fischer et al. \(2017\)](#) and [Sheehan et al. \(2022\)](#) use for comparison are derived by comparison to radiative transfer models; however, the radiative transfer is not directly connected with an evolutionary history.)

[Dunham et al. \(2010\)](#) and [Dunham & Vorobyov \(2012\)](#) are good examples of works focusing on detailed modeling. These papers, following the lead of [Young & Evans \(2005\)](#), derive

1 The original paper notates this as L_{bol} , but defines L_{bol} as the sum of stellar and accretion luminosity, aligning it with the definition of L_{tot} used by the other works.

accretion histories for the components of modeled YSOs, tie these histories to prescriptions for envelope and disk evolution, and create radiative transfer models by using the resulting star/disk/envelope properties as input in a manner similar to model grids such as [Zhang & Tan \(2018\)](#). These simulations allow the prediction of bolometric temperature T_{bol} and luminosity L_{bol} in addition to total luminosity and envelope mass; however, these papers do not make predictions for fluxes at specific wavelengths, also accessible through radiative transfer. (L_{bol} is the luminosity derived from integrating over an observed SED; I distinguish this from L_{tot} because L_{bol} is subject to observational effects, though the two are sometimes equated.)

The ability to tie modeled accretion histories to fluxes through radiative transfer to produce direct observables across a wide mass range therefore expands the set of tools used to probe YSO evolution. The majority of papers in both categories also focus on modeling the evolution of YSOs over a mass range corresponding to low- to mid-mass stars, whereas this work is able to extend further across the stellar mass spectrum.

3.3.2 Performance

I have demonstrated an ability to predict the observed flux for a YSO across multiple wavelengths and according to multiple evolutionary theories using theory-agnostic YSO RTMs. However, the utility of these predictions is limited without an understanding of their accuracy and level of uncertainty. To characterize the performance of my framework, I attempt to recover the SEDs of existing R24 models following my nearest-neighbor averaging approach. Recovery is performed as in Chapter [3.2.2](#), with the difference that each model is excluded from the set of models used to recover its flux (i.e. I perform a kind of leave-one-out cross-validation of the method on the models used for prediction).

To quantify the uncertainty in my predictions, I adopt σ_{MAD} (the median absolute deviation of the ten SEDs, scaled to standard deviation) as a proxy. σ_{MAD} is defined as follows:

$$\sigma_{\text{MAD}} \equiv k_{\text{normal}} \times \text{median} \left(|S_{\nu, i} - S_{\nu, \text{true}}|_{i=1, \dots, n} \right) \quad (3-3)$$

Table 3-1. A comparison between the coverage of this work and that of other works which attempt to match observations of YSOs to predictions made assuming particular accretion models.

Work	$M_{\star, \text{final}} (M_{\odot})$	Accretion model	Predicted properties	RT linked?
This work	0.2-50	IS/TC/CA	S_{ν} , T_{bol} , L_{bol} , L_{tot} , M_{env}	Y
Offner & McKee (2011)	<3 ($M_{\text{protostar}}$)	IS, TC, CA, 2CTC, 2CCA ^{ab}	PLF ^c	N
Dunham & Vorobyov (2012) ^d	0.1-3 (M_{core})	MHD-driven	S_{ν} , T_{bol} , L_{bol} , L_{tot} , M_{env}	Y
Duarte-Cabral et al. (2013)	0.06-50	Const., Exp. taper, Taper w/ bursts	L_{tot} ^e , M_{env} , F_{CO} ^f	N
Fischer et al. (2017)	0.12-2.8	Exp. taper	L_{tot} , M_{env}	N
Sheehan et al. (2022)	0.01-5	Exp. taper	L_{tot} , M_{env}	N

a “2C” refers to two-component accretion models, which blend the base history with IS-like accretion.

b Tapered versions of each are also included.

c Protostellar luminosity function.

d Extends Dunham et al. (2010).

e This paper equates a YSO’s observed bolometric luminosity L_{bol} with its total protostellar luminosity L_{tot} .

f CO momentum flux.

where k_{normal} is 1.4826, the scale factor applied to the MAD in order to make it an estimator for the standard deviation of normally distributed data. Uncertainty quantification is based on the MAD to avoid overweighting larger values. To provide a sense of the uncertainty in the fluxes predicted in Chapter 3.3.1, I calculate σ_{MAD} for every RTM in the set at a wavelength of 1 millimeter, which I take to be generally representative of behavior at long wavelengths. Given that R24’s RTMs exhibit a wide range of flux values, I standardize between models by considering σ_{MAD} as a fraction of the recovered flux. I show the distribution of this fractional σ_{MAD} for every recovered SED in Figure 3-4, along with an example of full SED recovery.

To characterize the overall behavior of the distribution of fractional σ_{MAD} , I fit it with a log-normal distribution and extract the arithmetic mean and standard deviation of the fit log-normal through its shape parameters (μ and σ), using the following equations:

$$\text{mean} = e^{\mu+\sigma^2/2} \quad (3-4)$$

$$\text{std} = e^{\mu+\sigma^2/2} \times \sqrt{e^{\sigma^2} - 1}. \quad (3-5)$$

I choose a log-normal because σ_{MAD} is strictly positive and is capable of spanning multiple orders of magnitude, rendering a normal distribution unfit for this use case. The fit indicates that σ_{MAD} is, on average, about half of the recovered 1-millimeter flux value, with an arithmetic standard deviation of about 14%.

With the uncertainty of my predicted SEDs characterized, I turn to the accuracy. In Figure 3-5, I evaluate the ability to recover the flux of every YSO in the set across a set of wavelengths commonly used for observations of YSOs, with a particular focus on 1 millimeter in keeping with the uncertainty quantification. My primary diagnostic tool for evaluating accuracy is the ratio of the recovered flux values to the true fluxes. Since the distributions of these flux ratios are not well fit by a log-normal or other analytical function, I instead characterize them using percentile values, meaning that the 50th percentile serves as the “mean” and the 16th and 84th percentiles serve as the “ $1-\sigma$ ” bounds.

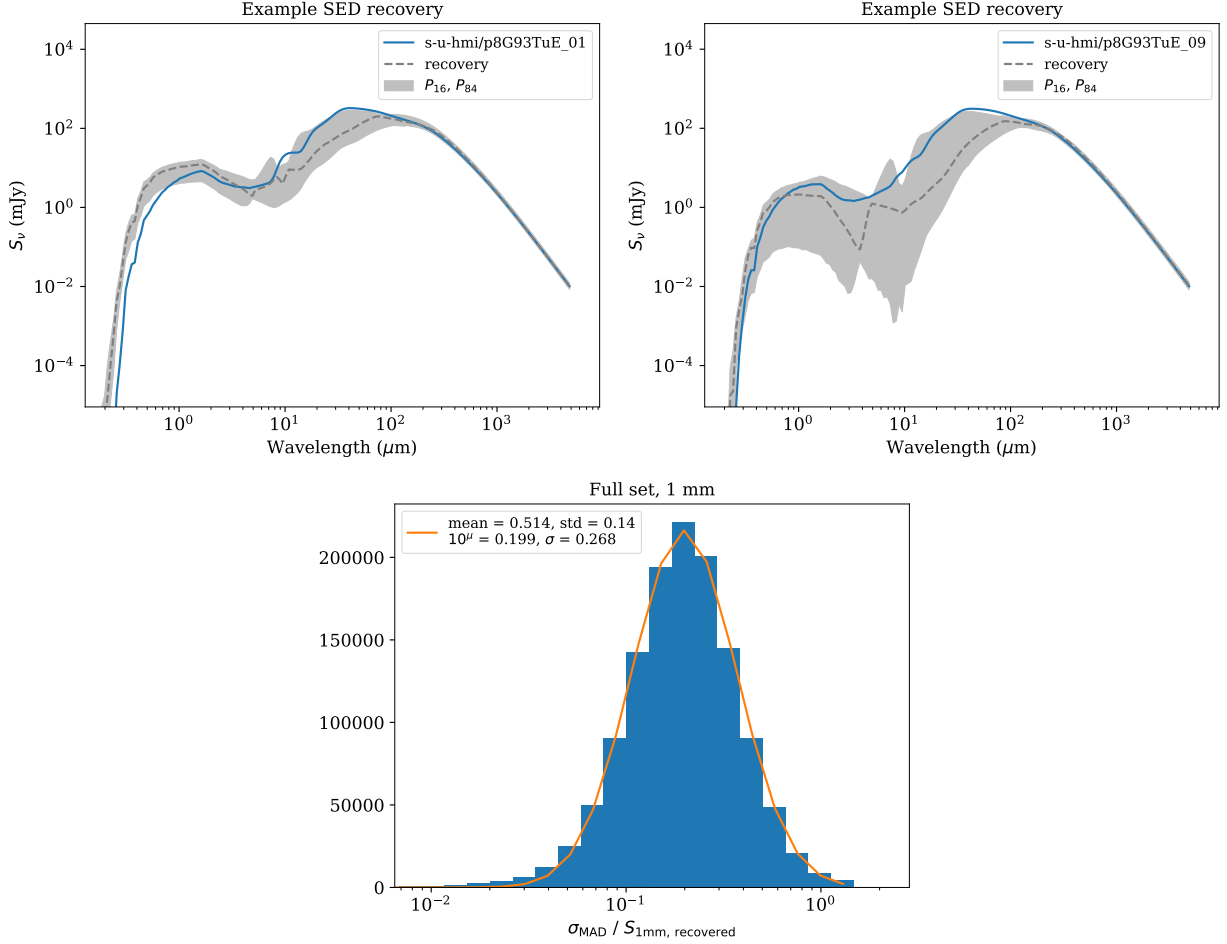


Figure 3-4. **Top row:** An SED from the `s-u-hmi` geometry in the R24 model set (*blue*) plotted against the recovered SED (*gray, dashed*). The shaded region indicates the region between the 16th and 84th percentile of the SEDs used in the reconstruction; percentiles are plotted here to avoid negative values in regions with σ_{MADS} greater than the associated flux. I show recovery for the same SED at both face-on (*left*) and edge-on (*right*) inclinations. The model identifier for the SED is shown in the legend, and the trailing digits indicate the inclination bin (see §3.2.1). **Bottom row:** σ_{MADS} (median absolute deviation, scaled to standard deviation) for every recovered SED at 1 millimeter (as a fraction of recovered 1-mm flux). A log-normal distribution is fit to the histogram. I show the arithmetic mean and standard deviation of the log-normal, along with its shape parameters μ and σ .

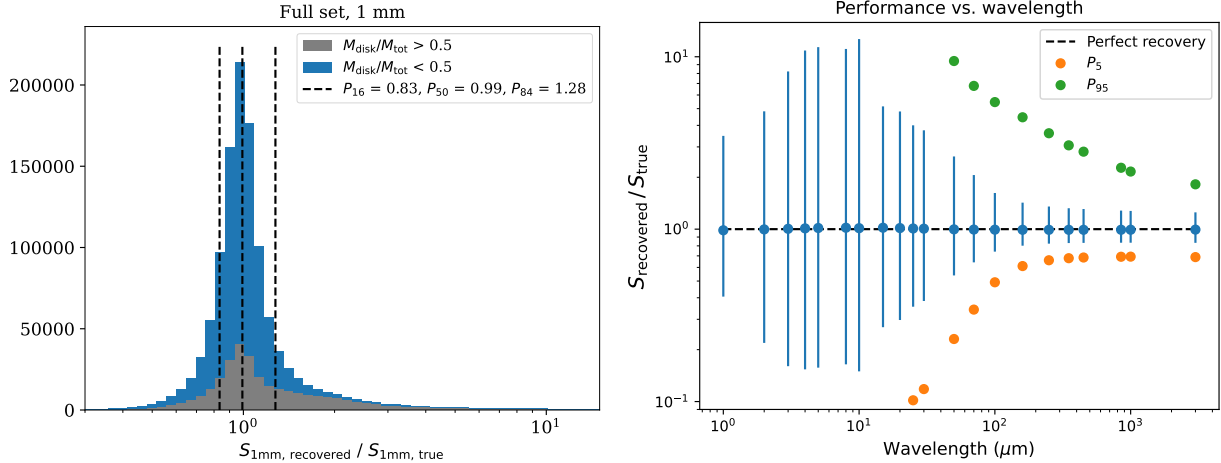


Figure 3-5. **Left:** Recovered 1-mm fluxes within an aperture of $\sim 10,000$ au as a fraction of true 1-mm flux. Dotted lines indicate the locations of the 16th, 50th, and 84th percentiles of the distribution to indicate its mean and spread. The histogram is broken down into models with over half their total mass contained in a disk (gray) and models with less than half their total mass contained in a disk (blue). Disk-dominated models exhibit a skew to higher recovered flux that non-disk-dominated models do not. **Right:** Accuracy of flux recovery at wavelengths commonly used for observation. The error bars show the 16th, 50th, and 84th percentile of the distributions, as in the left panel. The 5th- and 95th-percentile values are also plotted.

These recovery statistics are a comprehensive visualization of the performance of my modeling approach across the spectrum. On the whole, the “mean” of every distribution is very close to 1, meaning that on average I am able to recover the true flux of models at every considered wavelength. However, the spread in these distributions is uneven across wavelengths. At sub-millimeter and millimeter wavelengths (spanning the range covered by Figure 3-3) I am generally able to recover the true value of the RTM SEDs within about 20-30%, meaning that predictions at these wavelengths are likely to exhibit a similar performance. In the infrared, however, the 16th and 84th percentiles of the flux ratio distribution can be anywhere from a factor of two to an order of magnitude away from the 50th percentile. While the correct fluxes at these wavelengths are recovered on average, the spread is such that individual predictions are not likely to be accurate.

Figures 3-4 and 3-5 show the intrinsic uncertainty in flux predictions made on the basis of T_\star , L_\star , and M_{core} (which are the tracked quantities from PEMs; see §3.2.2). I am able to

reproduce the sub-millimeter and millimeter flux (starting at $\sim 100 \mu\text{m}$) of the base SED with reasonable accuracy and with an uncertainty (i.e. σ_{MAD}) that is consistently less than the predicted value. At shorter wavelengths, however, my predicted fluxes often diverge significantly from the true value and the σ_{MAD} of the predicted SEDs (relative to the predicted value) increases. This disparity in performance between long and short wavelengths is tied to the construction of my framework. Long wavelengths are dominated by dust emission, which is highly dependent on dust mass and source luminosity. In contrast, shorter-wavelength radiation depends much more on dust geometry such as disk inner and outer radii, disk flaring power, or cavity opening angle in the near- and mid-IR (e.g. [Whitney et al., 2004](#); [Robitaille et al., 2006](#); [Furlan et al., 2016](#)).

The reduced IR performance of this framework therefore originates in a limitation of star formation theory: T_\star , L_\star , and M_{core} only predict the IR flux to the observed level of accuracy. In this modeling procedure, I currently marginalize over disk and cavity properties by drawing from a set of RTMs that includes both asymmetric models, which have disks and/or cavities, and spherically symmetric models, which lack those features. It is possible that, were the disk and cavity to be included, the flux predictions at shorter wavelengths could improve. However, as it stands, there is little understanding of the degree to which these features are actually predictive of a YSO's IR flux. Likewise, there are currently no good models for how these features are expected to evolve with time, in these PEMs or otherwise. Higher uncertainty at shorter wavelengths is therefore expected and useful to preserve.

My goal with this work is to develop a way to predict properties of YSOs like mass and luminosity that are visible on a population level. These observables are generally tracked well by longer-wavelength radiation. Consequently, I prioritize good performance at long wavelengths in order to better recover these key properties, and focus on predictions in the sub-millimeter and millimeter regimes in the remainder of the work. Overall, this approach to modeling YSO SEDs accurately recovers the long-wavelength fluxes of R24 RTMs, and therefore makes good predictions for observable quantities that rely on dust continuum emission. It is also possible to utilize this framework to make predictions in the IR, with the knowledge that these predictions

will come with markedly greater uncertainties. Discussion on the robustness of these results is contained in Appendix D.

Overestimates in the flux recovery distribution are thick disks. There are a nontrivial fraction of cases where the recovered 1-mm fluxes are over a factor of two larger than the true value, and in general the distributions of flux ratios skew greater than 1 regardless of wavelength (see Figure 3-5). Flux overestimations occur in cases where the mass of the RTM is largely contained within an optically thick disk. Since the mass that is used to find nearest neighbors includes all circumstellar material (i.e. both envelopes and disks), these RTMs are matched with ones that have the same amount of material, but distributed in a way that renders the dust more optically thin. In turn, this leads to a recovered flux that is higher on average due to more dust being visible in the matched RTMs.

3.3.3 Caveats

In the previous sections, I presented and evaluated the quality of flux predictions made using my modeling framework. Overall, these predictions are reasonably accurate regardless of where they occur in parameter space, and therefore enable good modeling of a wide range of theoretical scenarios. However, there are some aspects of the framework worth keeping in mind when examining and interpreting the predicted SEDs.

Firstly, to reiterate a point from Chapter 3.3.2, the setup of the modeling framework causes better performance in the sub-millimeter and millimeter than in the near- or mid-IR. I essentially track properties of the central protostar and the overall dust content, while flux in that regime is also sensitive to the shapes of dust density structures (i.e. disk inner radius) that are not tracked by any available PEMs. The uncertainty for predictions in that regime is therefore markedly higher compared to longer wavelengths.

Beyond performance over specific wavelength ranges, my procedure for SED modeling causes the quality of results to be fundamentally dependent on the density of RTMs in parameter space. Since the parameters of R24 models are randomly sampled, flux values predicted using this framework may be vulnerable to reduced accuracy due to decreased model density in the relevant

area. While I acknowledge this possibility, I do not anticipate this to be a major source of error in general. Given the large size of the model set, even after down-selection to geometries with envelopes, the degree to which any combination of parameters within coverage will be underpopulated is limited. (It should also be noted that this density issue is not unique to my approach. While I place a greater emphasis on interpolation between models in the parameter space than most literature model grids, sampling every possible combination of relevant parameters is highly infeasible, hence why no currently used grids attempt completeness in this sense even when based within a single theoretical framework.)

I am also somewhat limited in my ability to model some high-mass stars as a consequence of the chosen set of RTMs. The maximum source temperature in R24 (as in R17) is 30000 K. This places some constraints on the ability to model the evolution of proto-O stars; based on output from the K12 code, temperatures at or over that level are expected for stars with mass $\gtrsim 16M_{\odot}$ once they have moved onto the main sequence, regardless of assumed history. Predictions for the short-wavelength radiation of high-mass YSOs are therefore likely to be underestimates for YSOs with high-mass MS sources due to artificially low stellar temperatures.

Finally, the PEMs underlying the predictions in Chapter 3.3.1 are dependent on scaling parameters which are held invariant in this chapter (see §3.2.2). Changes in the values of these parameters should be expected to impact, at minimum, the absolute timescales of the flux evolution laid out here (though applying a different scaling parameter across the mass range of PEMs is not expected to significantly alter the relative behavior of low- and high-mass YSOs). A change in scaling parameter will also likely impact the specific predicted 100- μm flux values, which are sensitive to accretion rate. The impact of scaling parameters on my predictions will be revisited.

3.4 Further Uses

I have outlined the functionality of my modeling framework and provided some examples of the base output. In this section, I leverage its infrastructure to pursue open questions in star formation theory.

3.4.1 Comparison to a Contemporary Grid

In Chapter 3.3.2, the focus is largely on being able to reproduce known results within my set of RTMs as a way to evaluate the performance of my modeling approach. However, with that performance evaluated, the wider purpose of my framework is to be able to make predictions with the same level of quality across multiple theories of protostellar growth. Ideally, then, I should be able to reproduce not only my own results, but also those of contemporary grids of YSO models purposefully built on those theories. I perform a detailed comparison of my results to the RTM grid of [Zhang & Tan \(2018, ZT18\)](#) as a case study of my ability to replicate the results of other model grids.

3.4.1.1 Zhang and Tan (2018) SED recovery

The ZT18 grid is a set of 432 YSO models based on the theory of TC accretion. Every model is assumed to have a central source, a circumstellar envelope, a disk, and bipolar cavities. ZT18 does not include an ambient medium. The grid has three fundamental physical parameters: core mass M_{core} , mass surface density of a star-forming clump containing the core Σ_{cl} , and protostellar mass m_{\star} . Model parameters are sampled from within this space along protostellar evolutionary tracks generated using [Hosokawa & Omukai \(2009\)](#) and [Hosokawa et al. \(2010\)](#). These tracks enable the calculation of other quantities, such as the source temperature and disk mass, at the sample points along the track.

The SED associated with each RTM is calculated using the radiative transfer code HOCHUNK3D ([Whitney et al., 2003a, 2013](#)). Every SED has 20 viewing inclinations, evenly sampled in $\mu \equiv \cos \theta$ over the interval of $(0.975, 0.025)$, for a total of 8640 SEDs in the entire grid. The SEDs are entirely produced by the modeled YSOs; no emission from a theoretical parent clump is included.

To test my ability to recreate the results of ZT18, I attempt to recover the 1-mm flux of each RTM in the same way as with my own models (see §3.3.2, Figure 3-5). Each ZT18 RTM has an instantaneous core mass M_{env} forward-modeled from the initial core mass, accretion rate, and assumed ϵ_{SF} as well as a disk mass M_{disk} tied to the mass of the central protostar. I use the

combined envelope and disk mass for RTM selection in order to remain consistent with my internal treatment. Since the envelopes of ZT18 models have defined outer radii (necessary due to the lack of an ambient medium), I use the masses and fluxes associated with the closest radius in the set of apertures for R24 (see §3.2.1) to ensure that the ZT18 models are captured appropriately. Since each ZT18 RTM has 20 associated SEDs corresponding to different viewing angles, I compare each ZT18 SED to the recovered SED within the appropriate 10° inclination bin (see §3.2.1) to match the lines of sight as closely as possible. I show results from this comparison in Figure 3-6.

Overall, as with my own flux values, I am able to recover the long-wavelength fluxes of ZT18's RTMs fairly well. The mean ratio of recovered flux to true flux is approximately 1.32, meaning that on average the true flux is overestimated by $\sim 30\%$; however, this offset is systematic and can consequently be compensated for. (I discuss the origin of this offset further in §3.4.1.2.) With that adjustment, I am generally able to recover the true flux of any ZT18 SED to within approximately 30-45%, based on the 16th and 84th percentile values; there is a slight bias towards the upside in these results, with the 84th percentile being further away from the median than the 16th. This performance is generally consistent with my results in Chapter 3.3.2 in the millimeter regime, though the difference between percentiles is slightly larger. The spread is likely exacerbated relative to my internal recovery by a smaller sample and by noise in the long-wavelength fluxes of ZT18, which is an artifact from radiative transfer. The bottom panels of Figure 3-6 reveal an inclination dependence in the ratio of recovered flux to true flux. The flux of highly inclined SEDs (i.e. closer to edge-on) is generally overestimated by slightly more than that of models closer to face-on, with the mean ratio increasing from 1.16 at an inclination of 12° to 1.52 at an inclination of 89° .

As in the internal recovery, shorter-wavelength fluxes of ZT18 are not recovered at the same level of fidelity as at long wavelengths; flux at shorter wavelengths has a strong dependence on geometric features I marginalize over due to a general lack of models for their evolution (see §3.3.2 for more discussion). ZT18 does contain prescriptions for some of these features (disk

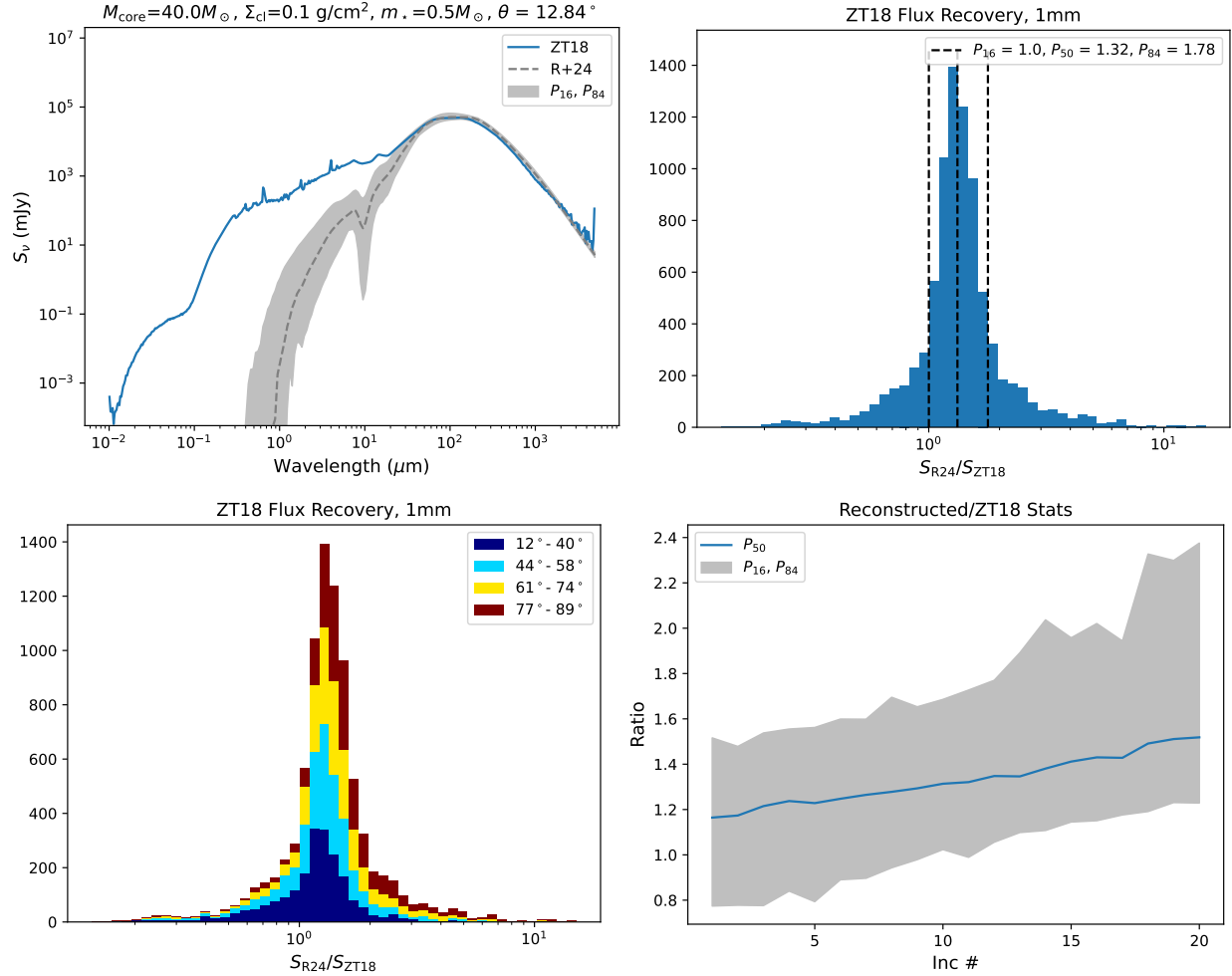


Figure 3-6. **Top left:** The SED of a model in ZT18 (blue), along with my reproduction (gray) and its uncertainty (shaded), as in Figure 3-4. **Top right:** The left panel of Figure 3-5, but comparing the predicted 1-millimeter fluxes to the models of ZT18 instead. As there, I indicate the locations of the 16th, 50th, and 84th percentiles as proxies for the mean and $1-\sigma$ of the distribution. **Bottom left:** The histogram in the top right panel broken down into four viewing angle bins. The bins contain five inclinations each from the set of inclinations defined in ZT18. **Bottom right:** The 50th percentile (blue) and 16th/84th percentiles (shaded) of the distribution of flux ratios at each inclination in ZT18.

outer radius, cavity opening angle); I continue to marginalize over these in order to better capture the uncertainty in the current approach.

3.4.1.2 The impact of model construction

In reconstituting SEDs from ZT18, I have attempted to follow their parameters and structure as closely as possible within the context of my framework. However, there remains a systematic offset between their long-wavelength fluxes and my attempted reproductions, the accuracy of which also exhibits an inclination dependence. Since I am able to reproduce the fluxes of my own models at long wavelengths, these disparities are likely due to the varying ways in which the sets of models are constructed. Where the differences originate is a substantive question, as it indicates ways in which the construction of a set of models may affect the predictions it makes. In turn, this may introduce additional uncertainty into measurements made using the model set. I evaluate the effect of two major differences between R24 and ZT18: the different dust opacities used by the model sets, and the differences in the treatment of disks.

As stated in Chapter 3.2.1, R24 employs a single dust type sourced from D03 for every density structure. By contrast, dust in ZT18 follows the configuration of Whitney et al. (2003a), which varies the model used by region within a YSO. Disks in ZT18 include two dust species, separated by a density threshold. Dense regions in the disk are modeled with the large-grain dust from Wood et al. (2002, W02); these regions have gaseous hydrogen number density $n_{\text{H}} > 2 \times 10^{10} \text{ cm}^{-3}$. Regions in the disk below this density use a model of intermediate grain size from Cotera et al. (2001). Envelopes contain the ice-covered grains from Whitney et al. (2003b). Dust in the cavity uses the small ISM grains of Kim et al. (1994). The opacities of these dust models are illustrated in Figure 3-7. The opacities of these dust models are all distinct from that of D03, particularly for the dust in dense regions of ZT18's disks. While the impact of changing the dust model is difficult to predict solely by comparing the opacities, it is reasonable to expect the use of these differing dust models to alter the resulting emission.

To quantify the impact of dust opacity model on the resulting SED, I rerun a subset of R24 models with ZT18's dust configuration to isolate the effect of the dust opacity. This subset is

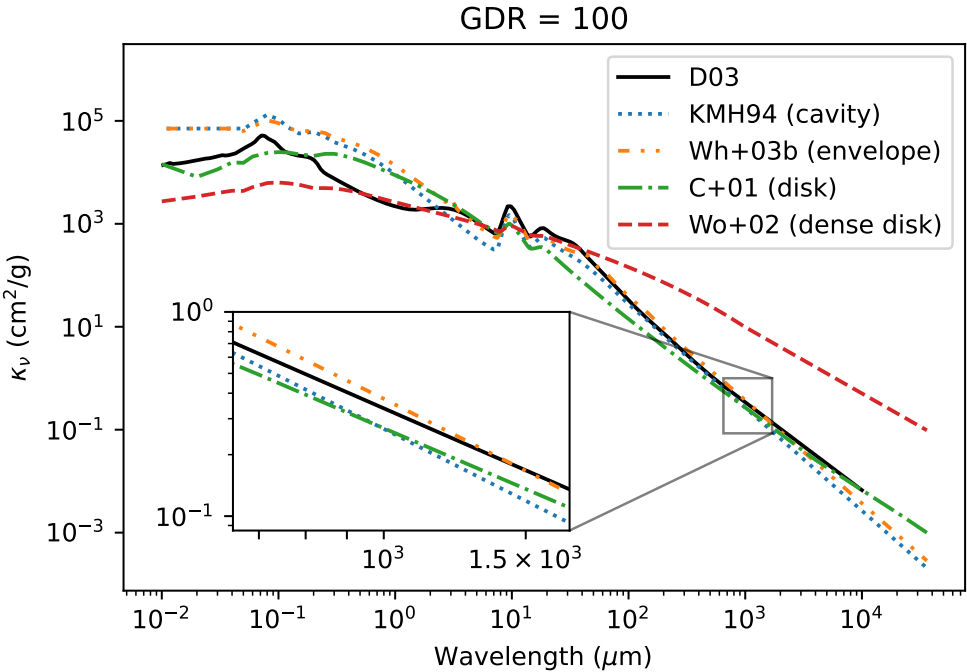


Figure 3-7. Dust opacities (in $\text{cm}^2 \text{ g}^{-1}$) for each dust type used in the RTMs of ZT18, compared to the D03 dust used in R24. I assume a GDR of 100 to place all values in terms of dust opacity, as opposed to total material opacity. The ZT18 opacity models originate from [Kim et al. \(1994\)](#), [Whitney et al. \(2003b\)](#), [Cotera et al. \(2001\)](#), and [Wood et al. \(2002\)](#).

composed of 500 randomly selected RTMs from the `spubhmi` and `spubsmi` geometries (250 each). I choose these geometries to ensure that every RTM being rerun has envelopes, disks, and bipolar cavities, which are the common features of ZT18's RTMs. Since Hyperion is capable of including multiple dust models and handling the properties of envelopes, disk, and cavities independently, I am able to reproduce the setup of dust in ZT18, though with the addition of an ambient medium, which is required when setting up an R24 RTM. As in R24, I set the temperature of the medium at 10 K and its dust density at $10^{-23} \text{ g cm}^{-3}$. I assign the dust model of [Kim et al. \(1994\)](#) used in the cavities to the ambient medium as well, due to the similarly low density. To determine which parts of the disk are above the density threshold for the larger-grain dust species, I divide the mass density of dust in each disk cell by the mass of hydrogen to arrive at a number density, which is scaled assuming a GDR of 100. For the reruns, I retain the same grid configurations as the original R24 RTMs and post-process the SEDs in the same way by

subtracting the background radiation from the ambient medium, making S/N cuts, and interpolating to a common set of apertures (see §4.2.4 of R17 for details).

As a caveat, my reruns are not an exact match to the full model setup of ZT18, which also includes gas opacities, adiabatic heating/cooling, and advection for the purpose of outflow modeling and providing corrections to calculated thermal energies (Zhang & Tan, 2011; Zhang et al., 2013). I do not implement these additions. While they do impact the temperature profiles of YSOs, that impact is primarily felt in very hot regions ($>10^4$ K) and at the edges of outflows, which contribute small fractions of the total flux at the wavelength considered herein. The effects on the radiative transfer from including additional physics are therefore expected to be secondary to those from the dust model at long wavelengths.

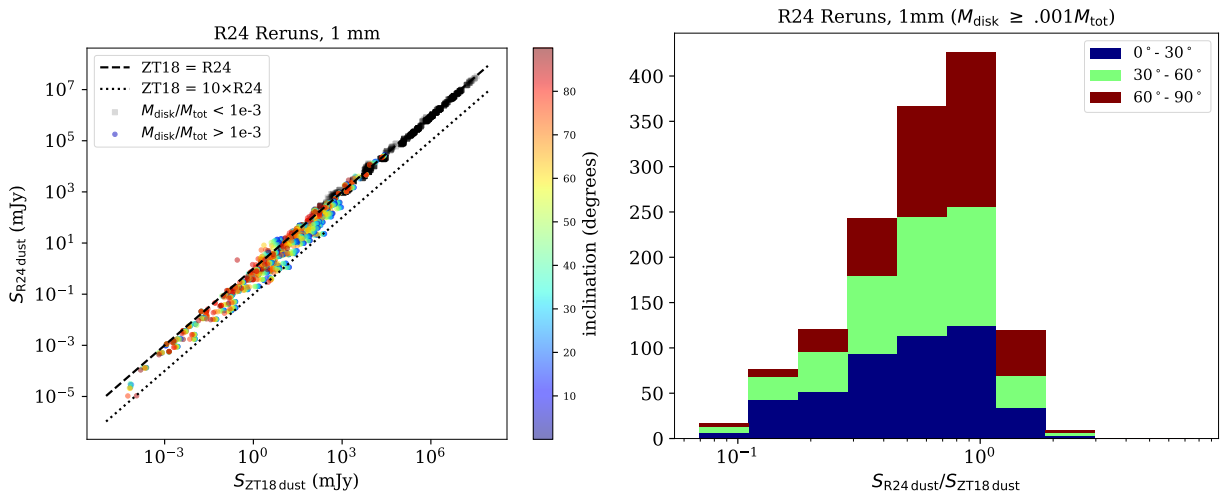


Figure 3-8. Left: The 1-millimeter fluxes of R24 models rerun with the ZT18 dust configuration, plotted against the original fluxes. I separate the models into two regimes based on the fraction of total model mass contained in the disk. Models with disks comprising less than 0.1% of the total mass are represented by black squares, while models with disks greater than 0.1% of total mass are colored by inclination. **Right:** The same as the bottom middle plot of Figure 3-6, but comparing the original R24 fluxes to the rerun models, and split into three inclination bins with three viewing angles each to better match the setup of R24. Only models that are in the “disky” regime in the left panel (i.e. models with $M_{\text{disk}} / M_{\text{tot}} > 10^{-3}$) are included in this histogram.

In Figure 3-8, I compare the 1-mm fluxes of my rerun RTMs to the originals. In general, fluxes from the rerun models are higher than their counterparts with R24’s dust opacity model.

Beyond that larger trend, the reruns generally fall into two categories separated by the ratio of disk mass to envelope mass. The first category is RTMs where the disk is less than $\sim 0.1\%$ of the total mass in the model. The correlation between the original flux and the flux in the rerun model is very linear; most rerun models in this group are approximately 15-20% brighter than the originals, with very little variation. The majority of these models also exhibit fluxes greater than 10^3 mJy. The second category is composed of RTMs where the disk is 0.1% or more of the total mass. Fluxes of models in this category exhibit more spread around a linear correlation and also an inclination dependence, with the discrepancy between the rerun and original flux growing the closer a viewing angle is to being face-on. The average increase in flux for this group of models is approximately 70-80% of the original, though with a higher variance.

With the information from these rerun RTMs, I return to the recovery of ZT18 RTM fluxes in Section 3.4.1.1. The difference in dust model provides a straightforward explanation for the inclination dependence in my recovery, as almost every RTM in ZT18 falls into the “disky” regime observed in the rerun R24 RTMs. However, since the net effect of changing the adopted dust opacities is to increase the fluxes relative to the originals, the difference in dust configuration is unlikely to be the sole cause of the systematic offset between ZT18’s fluxes and my recoveries for the simple fact that the fluxes of ZT18 are generally lower than the recoveries.

Since the difference in dust opacities is not enough to explain the systematic flux offset in and of itself, I turn to the other major disparity between the setup of ZT18 and R24; the properties of their circumstellar disks. Disks in ZT18 are generally more massive (mass between $.16 - 53.3 M_\odot$, median $2 M_\odot$) and more compact (outer radius between 5–1354 au, median 70 au) than disks in R24 (mass between $10^{-6} - 10 M_\odot$, median $\sim 3 \times 10^{-3} M_\odot$, outer radius between 50–5000 au, median ~ 500 au)², which creates disks that are higher density in ZT18 than in R24 on average. (It should be noted that many of the massive and dense disks in ZT18 would likely be considered Toomre unstable, and are therefore unlikely to contribute meaningfully to the observed radiation from populations of YSOs. As constructed, then, the ZT18 models have components which are

² These mass values refer to the total mass in the disk, assuming a GDR of 100 as both ZT18 and R24 do.

potentially physically unrealistic, or at least unlikely to have observable real-world analogues.) Disks in ZT18 also include W02 dust, which has a much higher opacity than D03. While dust opacity is insufficient to explain the nature of the offset alone, I examine the possibility that this very opaque dust model is interacting with the construction of ZT18 disks to affect flux recovery.

To determine the impact of disk structure in concert with the effect of W02 dust in the reruns, I examine the relationship for each model between its flux ratio, mass fraction in W02 dust, and the column density of its disk in Figure 3-9. Increasing the mass fraction of a model in

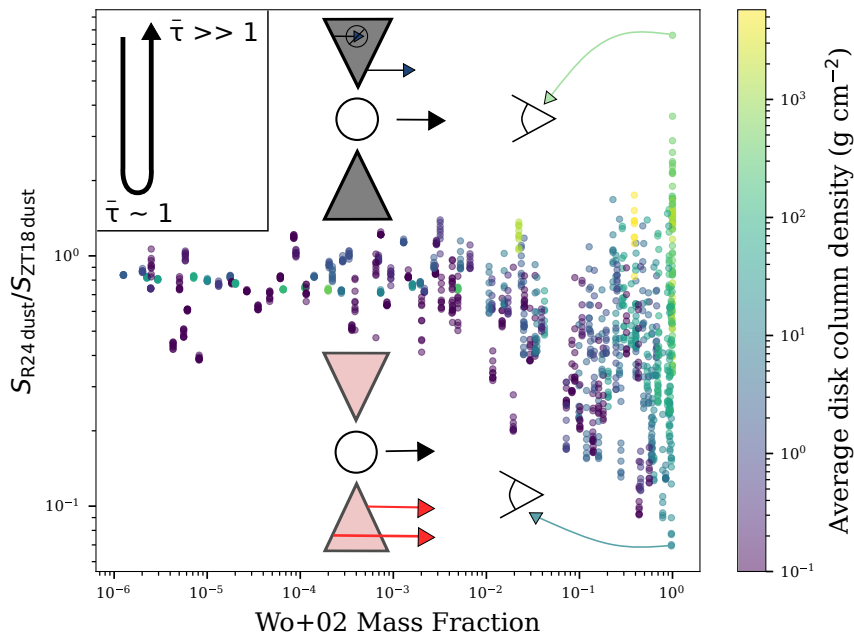


Figure 3-9. The ratio of 1-mm R24 flux to rerun flux for the set of rerun models, plotted against the fraction of mass in the model in W02 dust. Models are colored by the average disk column density. The x-axis is limited to mass fractions of over 10^{-6} ; some models have lower W02 mass fractions, but those models fall into the “non-disky” regime in Figure 3-8 and do not exhibit any trends in this space. (Models that have become brighter when rerun have an increased $S_{ZT18\text{ dust}}$, meaning that they are below 1 in this plot. I plot the ratio of $S_{R24\text{ dust}}$ to $S_{ZT18\text{ dust}}$ for consistency with Section 3.4.1.1, where ZT18 is the “true” flux and is therefore the denominator.) I illustrate the reason behind the spread in recovered fluxes using cartoon elements. The opaque W02 dust has higher emissivity, powering additional dust emission for disks with low optical depth. However, for denser disks, the high optical depth resulting from W02’s high opacity hides dust emission, decreasing the flux.

W02 dust has a clear impact on the agreement between the original and rerun models. In general,

the more a model is composed of W02 dust, the higher the rerun flux becomes. Since W02 dust has a higher opacity than D03 at long wavelengths, it also has a higher emissivity, meaning that for the same amount of visible W02 and D03 dust, the W02 dust will be brighter. (Models that are envelope-dominated also exhibit a slight increase in flux in the reruns, which in a similar fashion is due to the increased opacity of [Whitney et al. \(2003b\)](#) dust relative to D03.) However, there are also cases where a higher W02 mass fraction results in a lesser increase—or even a decrease—in flux. This is a result of the high column density of these models’ disks, which prevents the light emitted by W02 dust from escaping due to the resulting high opacity. The spread in flux ratios is therefore essentially visualizing the transition from low to high disk optical depth.

When considering these results within the context of recovering the fluxes of ZT18 models, the combination of disk structure and dust opacity provides a reasonable explanation for the general tendency to over-recover the fluxes of actual ZT18 models. Every disk in ZT18 has an average column density that is roughly 10^2 g cm $^{-2}$ or greater, placing them squarely within the “dense disk” regime in the reruns. The emission from higher-opacity dust which would otherwise power additional flux is therefore blocked due to high optical depth, leading to a recovered flux that is higher than the original. The results of my attempted recovery of ZT18 fluxes can consequently be fully explained through a combination of the assumed dust opacities and model construction. With sufficient knowledge about these aspects of a model grid, then, I am able to produce predictions with my modeling framework that are consistent with predictions made by current grids.

3.4.2 YSO Classification

Despite the plethora of available PEMs, there is consensus on a general qualitative picture of YSO evolution. This picture is broken down into several evolutionary Stages, with each successive Stage becoming less envelope-dominated and closer to a bare pre-main-sequence star ([Evans et al., 2009a](#); [Kennicutt & Evans, 2012](#)). Insight into the physical state of an observed

YSO generally comes from its IR spectral index³, α , defined as follows:

$$\alpha = \frac{d \log \lambda F_\lambda}{d \log \lambda} \quad (3-6)$$

This index allows the YSO to be assigned one of several Classes, which are empirically determined ranges of spectral index thought to exist at roughly the same Stage.

In practice, these concepts are often conflated, with the Class of a YSO taken to represent its evolutionary Stage. However, since YSO Class is a fundamentally observational quantity, its measurement may be impacted by observational effects. For example, a YSO observed at Stage II (i.e. when it is disk-dominated) may appear to be Class I when observed edge-on through the disk due to extinction. Without direct insight into the orientation and spatial structure of dust in a YSO, the extent to which its Stage and Class may be confused is difficult to ascertain through observation.

In Chapter 2, I characterized this potential for confusion by comparing the Classes and Stages of every RTM in the R24 set. In general, I found that while the Classes and Stages of many R24 models aligned as expected, there were significant fractions of RTMs with mismatched Classes and Stages. However, given R24's lack of a foundational evolutionary theory, I did not attempt to narrow the scope of this comparison based on "physicality", i.e. whether the models comport with a particular modeled accretion history. The results in that chapter therefore indicate the ways in which Class and Stage may be confused and provide a general sense of proportion, but do not attempt to represent YSOs as they occur in nature.

The major advancement presented in this chapter, then, is the ability to determine whether an RTM is "physical", i.e., whether it can occur assuming a given PEM. I therefore revisit the comparison between the Classes and Stages of the RTMs with this additional constraint, making the results more directly applicable to observed YSOs. In this chapter, I adopt the following definitions for Class and Stage:

3 I interpret the spectral index as the slope of the line connecting the SED at 2 and 25 μm , instead of fitting a power law to data points within that range.

- Class:
 - 0: $L_{350+\mu\text{m}}/L_{\text{bol}} > 0.005$, no calculated spectral index
 - I: $\alpha \geq 0.3$
 - Flat: $-0.3 \leq \alpha < 0.3$
 - II: $-1.6 \leq \alpha < -0.3$
 - III: $\alpha < -1.6$
- Stage:
 - 0: $M_{\text{env}} > 0.1M_{\odot}$, $M_{\star} < M_{\star, \text{final}}/2$
 - I: $M_{\text{env}} > 0.1M_{\odot}$, $M_{\star} > M_{\star, \text{final}}/2$
 - II: $M_{\text{env}} < 0.1M_{\odot}$, disk present
 - III: Bare pre-main-sequence star (no envelope, no disk)

These definitions are generally the same as in Chapter 2.4.2; however, the dividing line between Stages 0 and I has been changed. This definition incorporates the Stage 0/I boundary employed by Fischer et al. (2017, F17), occurring when half of the final stellar mass has been accreted⁴, which is generally preferable from an observational standpoint. Section 3.4.2.3 contains more discussion on Class and Stage definitions.

To determine which RTMs should be included in the comparison, I repeat my procedure for YSO composition from Chapter 3.2.2. For each modeled accretion history, I consider a set of fifty final stellar masses evenly log-spaced between $0.2\text{-}50 M_{\odot}$, similar to Figure 3-3. To translate the PEMs into RTM parameter space, I have so far assumed a mass accretion efficiency ϵ_{SF} of 1/3. I now allow ϵ_{SF} to vary across the set $\epsilon_{\text{SF}} \in (1/6, 1/4, 1/3, 1/2, 2/3)$ in order to include scenarios where this efficiency varies (ZT18, for example, allows this quantity to vary between approximately 0.2-0.6 as a function of core mass and clump density, which is now accommodated by this value range). Each RTM that is selected along a PEM track is included in the resulting matrix. In cases where the same model is selected multiple times along the same track, it is

⁴ I note that F17 implicitly define the Stage 0/I boundary in two ways. The first of these is when the envelope mass equals the star mass, originating from Andre et al. (1993), while the second is when the star reaches 50% of its final mass. These definitions agree in the specific case where accretion onto a protostar from an isolated mass reservoir is 100% efficient, in keeping with the SIS formation of Shu (1977); however, other scenarios would cause these definitions to diverge. I illustrate this point further in Chapter 3.4.2.3.

included in the comparison each time to ensure that the resulting percentages are representative of the full population of selected RTMs.

Results from this Class/Stage comparison can be seen in Figure 3-10. In this figure, I consider two cases for each PEM. The first is the “all-inclusive” case, which includes all RTMs associated with every final mass, age, and ϵ_{SF} . The second is the “detectable” case, which include the RTMs with fluxes detectable by ALMA at a distance of 5 kpc. “Detectability” is here defined as exhibiting a 1-millimeter flux of at least 1 mJy within an aperture of physical radius \sim 2000 au (aperture 7 in the R24 models); in keeping with the focus on long wavelengths, this definition is targeted at a typical ALMA Band 6 observation of YSOs within the Milky Way. These cases are intended to provide a general overview of Class/Stage confusion within the context of particular accretion histories as well as an indication of the extent to which they may be confused in observation. (I consider more cases in §3.4.2.2.)

Given that the RTMs underlying this confusion matrix are now more “physical”, the matrix may now be used more directly to interpret observations. YSOs observed in a particular Class can be mapped back to Stages by summing the percentages of objects with that Class (i.e. in a particular column)—disregarding any “no-stage” models⁵—and determining what fraction of those total percentages are contained in each Stage. (Since percentages are all in relation to the total number of models in the matrix, they can be summed.)

As an illustration, I consider some simple cases using the all-inclusive matrices. For an IS PEM, the mapping is as follows (I assume 100 of each Class for the sake of simplicity):

- Class 0 → 7 Stage 0 / 93 Stage I
- Class I → 8 Stage 0 / 87 Stage I / 5 Stage II
- Flat → 8 Stage 0 / 73 Stage I / 19 Stage II
- Class II → 6 Stage 0 / 51 Stage I / 43 Stage II

⁵ These are models that do not comport with my definition for “Stage”. Their envelopes are not massive enough for Stages 0 or I, they have no disks and therefore cannot be Stage II, and they are precluded from being Stage III due to having non-ambient circumstellar dust. §4.2 of R24 discusses these in greater detail.

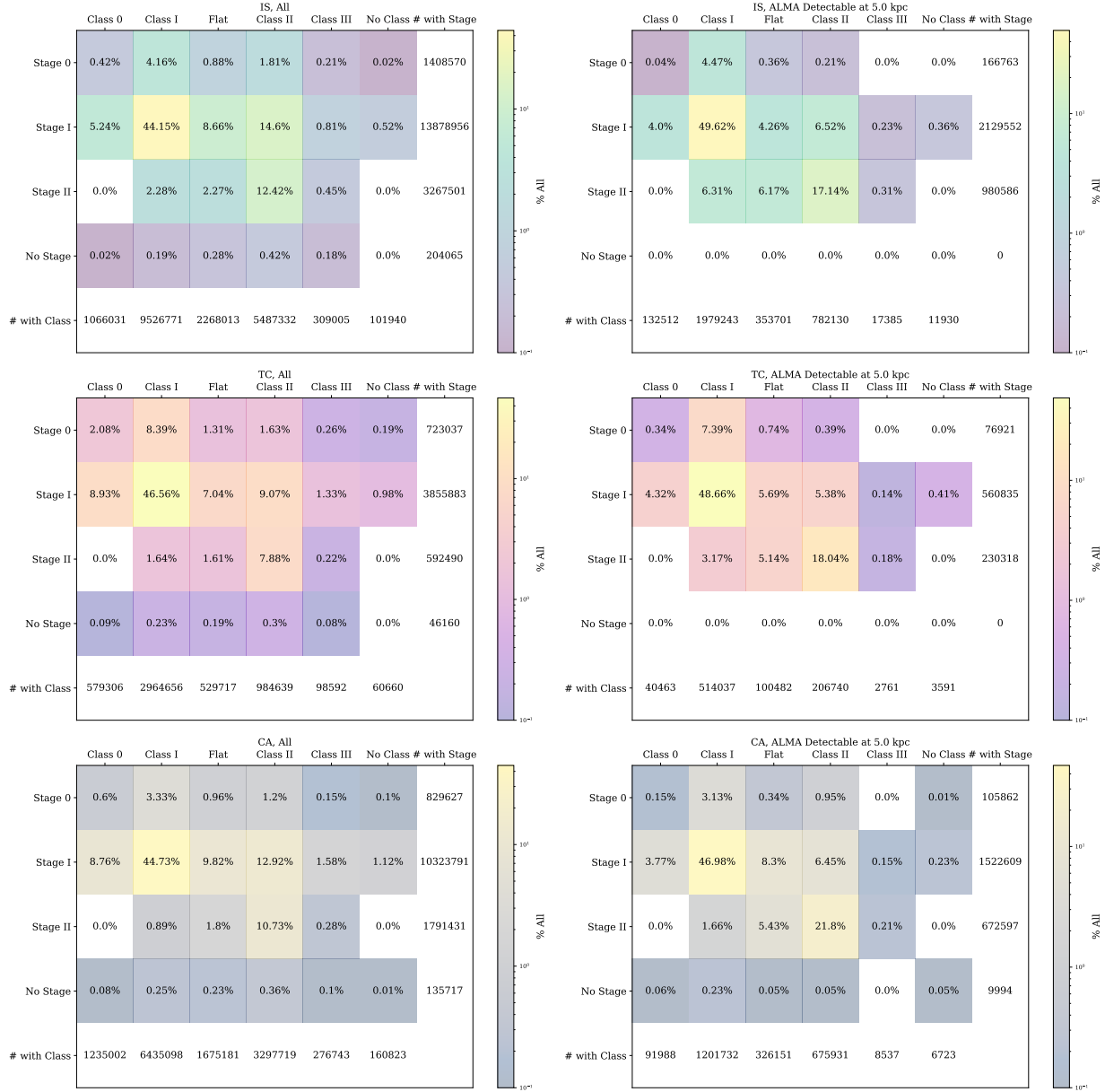


Figure 3-10. Class/Stage confusion matrices for RTMs consistent with IS (*top*), TC (*middle*), and CA (*bottom*) PEMs. I show matrices that include all selected models (*left*) as well as ones restricted to models that are plausibly ALMA-detectable at 5 kpc (*right*).

If instead a TC PEM is considered, the numbers are as follows:

- Class 0 → 19 Stage 0 / 81 Stage I
- Class I → 15 Stage 0 / 82 Stage I / 3 Stage II
- Flat → 13 Stage 0 / 71 Stage I / 16 Stage II
- Class II → 9 Stage 0 / 49 Stage I / 42 Stage II

and for CA:

- Class 0 → 6 Stage 0 / 94 Stage I
- Class I → 7 Stage 0 / 91 Stage I / 2 Stage II
- Flat → 8 Stage 0 / 78 Stage I / 14 Stage II
- Class II → 5 Stage 0 / 52 Stage I / 43 Stage II

These mappings provide another clear indication of how interpretation of observations is dependent on the assumed PEM. IS and CA exhibit similar Stage counts, while the inferred counts for TC are shifted to earlier Stages. The variable accretion rate of TC causes YSOs to spend more of the time they are accreting (proportionally) in Stages 0 and I, since the bulk of accretion occurs at later times. CA is similarly variable; however, the acceleration of CA accretion is mass-dependent, unlike TC, causing the point at which half of the protostellar mass is assembled (i.e. the transition from Stage 0 to I) to come later for many mid- to high-mass stars in TC than it does in CA. Consequently, TC stars spend longer in Stage 0 than CA when considering the entire population. Variation in behavior with PEM mainly manifests in Classes 0 and I (and Flat, to an extent). These matrices provide a better sense of the extent to which Class and Stage may be confused in scenarios with some physical motivation.

Class III YSOs. My modeling framework captures the time when a protostar has circumstellar material, i.e. it does not extend to Stage III, leaving it out of the matrices. I therefore do not extend this analysis to Class III YSOs. Given the low extinction necessary for a YSO to be Class III, failing to include Stage III models (the only models with no non-ambient circumstellar dust) would yield unrealistic results, unlike for classes implying greater extinction where such models are easier to discount.

3.4.2.1 Example application

As a further demonstration of how to apply the matrices to observed populations of YSOs, I consider the data of the c2d sample ([Evans et al., 2009b](#)), a comprehensive survey of YSOs in nearby molecular clouds. I use the Class counts from the fifth row of their Table 6 (24 Class 0, 125 Class I, 223 Class II) which are derived through de-reddened bolometric temperature. c2d is estimated to be complete in mass down to the stellar/substellar boundary and has few other constraints on the acceptable theory space from observation. I therefore use the all-inclusive matrices from Figure [3-10](#) to map Class to Stage. For the IS case:

- 24 Class 0 → 2 Stage 0 / 22 Stage I
- 125 Class I → 10 Stage 0 / 109 Stage I / 6 Stage II
- 223 Class II → 14 Stage 0 / 113 Stage I / 96 Stage II

For the TC case:

- 24 Class 0 → 5 Stage 0 / 19 Stage I
- 125 Class I → 19 Stage 0 / 103 Stage I / 3 Stage II
- 223 Class II → 20 Stage 0 / 109 Stage I / 94 Stage II

For the CA case:

- 24 Class 0 → 2 Stage 0 / 22 Stage I
- 125 Class I → 9 Stage 0 / 114 Stage I / 2 Stage II
- 223 Class II → 11 Stage 0 / 116 Stage I / 96 Stage II

Summing the Stage counts, the physical interpretation of c2d's Class counts following different PEMs would be as follows:

- IS: 26 Stage 0 / 244 Stage I / 102 Stage II
- TC: 44 Stage 0 / 231 Stage I / 97 Stage II
- CA: 22 Stage 0 / 252 Stage I / 98 Stage II

Regardless of the assumed PEM, the c2d sample maps to a population of YSOs much more weighted towards earlier Stages than would be assumed through the Class counts alone. Current estimates of the durations of various phases of star formation are based on these counts, with the Class 0/I lifetime estimates from [Evans et al. \(2009b\)](#) made in relation to the estimated Class II lifetime. Interpreting the c2d sample using these matrices would give reason to reexamine the canonical values, likely in the direction of increasing the Stage I lifetime relative to Stage II (as well as Stage 0 for a TC-like scenario). These matrices include models selected in the time when a protostar is actively accreting according to these PEMs; the estimated lifetime for Stage II, however, also depends on the longevity of protoplanetary disks after accretion has ended, which I do not model.

3.4.2.2 Binned confusion matrices

By tying RTMs to protostellar evolutionary tracks, the scope of the Class/Stage comparison is narrowed to physically motivated scenarios. However, these scenarios still encompass a wide range of final masses, ages, ϵ_{SFS} , and levels of detectability. In practice, there will likely be additional constraints placed on YSO measurements, whether theoretical (e.g. the mass-varying ϵ_{SF} of ZT18) or observational (e.g. observing YSOs at a particular age, only being able to resolve within a particular mass range, etc.).

In addition to the all-inclusive confusion matrices, I generate a set of matrices that captures various slices of the full set of “physical” RTMs for more direct applicability to observations performed under these additional constraints. As an example, if one were to observe an embedded cluster in which the maximum YSO mass is known and the age is well-constrained, the all-inclusive matrix will likely include models predicted to be more massive at that age than any detected YSOs. Instead of using the full matrix that contains these overly-massive stars, one should use a downselected set that includes only the range of possibly-detected YSOs, as well as restricting the time span covered by the matrix to times consistent with the measured age.

I establish bins in mass and age by constructing histograms of the values associated with the PEM tracks. The set of mass bins covers the range of $0.2\text{--}50 M_{\odot}$, as in Figure 3-3; it is invariant

with accretion history and is roughly even in log space to promote even mass coverage in each bin. Age values included in the bins cover the time that every protostar in a set of tracks (i.e. over the entire mass range) is actively accreting; the edges therefore vary with accretion history given the disparate time scales. TC and CA PEMs are given linearly-spaced time bins, since the difference between the earliest start and latest end of accretion within the set of tracks is about an order of magnitude at most (within \sim 0.1-1 Myr), so linear spacing is able to capture the distribution of ages. IS PEMs are given log-spaced bin edges because the timescale of accretion can span multiple orders of magnitude (\sim 0.1-10+ Myr).

Like the matrices in Figure 3-10, I allow the underlying PEMs for this set of cut-down matrices to vary by accretion history. I also allow ϵ_{SF} to vary and add three additional potential values to the set: (1, 2, 3). These are intended to capture scenarios where mass accreted onto a protostar may come from outside the core, similar to the behavior of the YSOs modeled by F17 in their effort to match an exponentially tapered accretion model to the distribution of YSO bolometric luminosities observed by [Furlan et al. \(2016\)](#). The precise mass accretion efficiency implied by their modeling varies with final stellar mass between approximately 150-400%; I consider a broadly similar range of values. Additionally, for each combination of bins and accretion histories, I compute matrices with cuts for detectability at the following distances: 0.1, 0.5, 1, 5, and 10 kpc. “Detectability” retains its former definition: exhibiting a flux > 1 mJy at 1 mm within an aperture of radius \sim 2000 au.

I generate matrices for a given scenario by including the Classes and Stages of RTMs that are selected along PEMs which follow a particular accretion history, occur within a particular mass and age range (specified by the outer edges of a set of mass/time bins), exhibit some set of ϵ_{SF} , and are detectable at a particular threshold. These scenarios cover every unique continuous combination of bins (e.g. IS accretion, mass bins 3-5, time bins 2-4, efficiencies 5-7, detectable at 10 kpc). I do not consider discontinuous combinations (e.g. mass bins 1-2 + 5-6). Figure 3-11 shows an example of a matrix with narrowed scope. This matrix includes RTMs that were selected along IS tracks with final stellar masses between 0.2 - $0.45 M_\odot$ and ages between

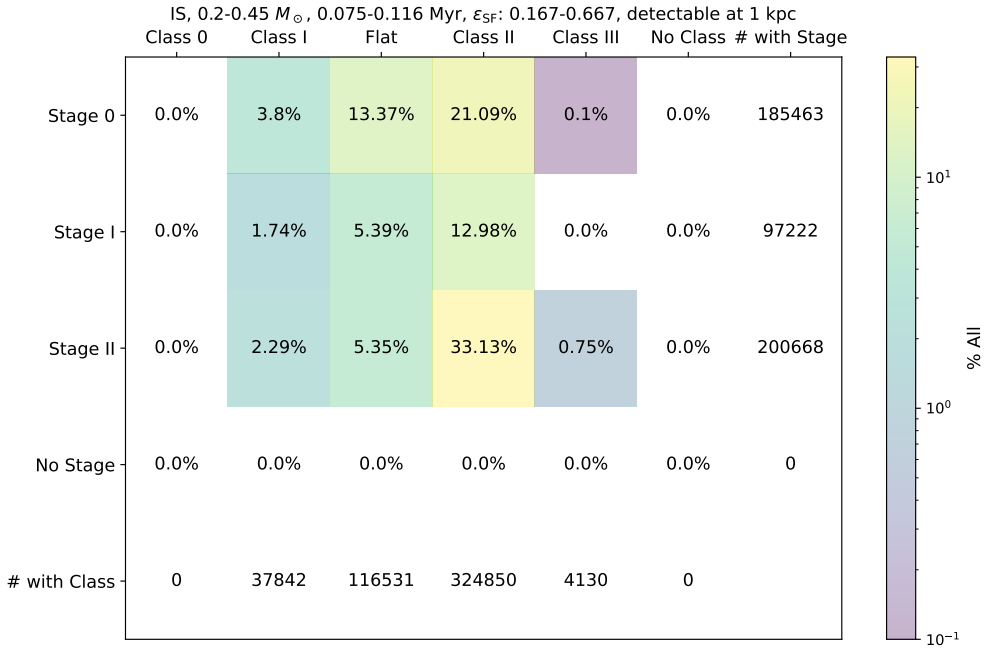


Figure 3-11. The same as Figure 3-10, but restricted to a smaller range of final stellar masses and ages.

.075-0.116 Myr that have ϵ_{SF} values within the range of 1/6-2/3 and are detectable at a distance of 1 kpc. (ϵ_{SF} is still limited to values in the set.)

Repeating the number mapping with the matrix shown in Figure 3-11 yields:

- Class I → 49 Stage 0 / 22 Stage I / 29 Stage II
- Flat → 56 Stage 0 / 22 Stage I / 22 Stage II
- Class II → 32 Stage 0 / 19 Stage I / 49 Stage II

which provides a clear demonstration of how constraints beyond just the PEM can change the physical scenario. For one, there are no Class 0 objects here; the RTMs making up this confusion matrix do not have enough dust to reach Class 0 by my definition, which requires a significant contribution from the dust to the bolometric luminosity. This matrix is also significantly shifted towards Stages 0/II and away from Stage I due to the low masses of the protostars and surrounding envelopes; the time window in which these YSOs have protostars with more than half of their final masses but still more than $0.1 M_{\odot}$ in their envelopes (my definition for Stage I) is small. The imposition of additional constraints therefore has large ramifications for the Stage counts inferred

through the use of a confusion matrix, meaning that care should be taken to use a matrix suitable for a given set of observations.

I have released a data table containing all of the matrices calculated for this chapter, which may be found in [this Zenodo repository](#).

3.4.2.3 Class and Stage definitions

Earlier in this section, I laid out my adopted definitions for YSO Class and Stage. Alternate definitions for these concepts have been proposed and used throughout the literature, raising the question of how these definitions differ in a practical sense, as well as which are the most appropriate or useful. Here, I use my modeling framework to compare the observational and theoretical consequences of various categorization schemes.

Class. My adopted Class definitions have remained the same from R24 and are consistent with the scheme laid out in [Andre et al. \(1993\)](#) and [Greene et al. \(1994\)](#), which forms the basis of many studies of YSO Classes. However, due to the difficulty in obtaining the submillimeter photometry necessary to identify a Class 0 YSO via this definition, many surveys (e.g. [Dunham et al., 2013](#); [Furlan et al., 2016](#); [Pokhrel et al., 2023](#)) instead employ the bolometric temperature T_{bol} of a YSO to discriminate between Classes 0 and I, with the usual dividing line occurring at 70 K (from [Chen et al., 1995](#)). Class 0 is intended to correspond to Stage 0, i.e. to identify deeply embedded YSOs where most of the total mass is contained in circumstellar material. As I have assigned Stages to a number of RTMs in R24, I compare the performance of these definitions at recovering Stage 0 models, calculating T_{bol} individually for each RTM SED with Equation (1) from [Myers & Ladd \(1993\)](#):

$$T_{\text{bol}} = 1.25 \times 10^{-11} \int_0^{\infty} \nu S_{\nu} d\nu \left/ \int_0^{\infty} S_{\nu} d\nu \right. \text{ K Hz}^{-1} \quad (3-7)$$

I construct samples for each accretion history, starting from the set of RTMs constituting the “all-inclusive” matrices from Figure 3-10. From this set, I apply a cut for detectability; however, as the submillimeter luminosity is now the chief concern, I consider “detectability” as exhibiting a 350- μm flux greater than 1 mJy at the R24 models’ native distance of 1 kpc. Further, as low-mass YSOs are the majority of constituents in most surveys of forming stars within the Galaxy, I limit

each of these samples to models whose central protostars have a bolometric luminosity of less than $100 L_{\odot}$ for better congruence with data. I calculate all values within the sixth aperture in R24, which has a physical radius of ~ 1000 au; this is sufficient to capture most circumstellar material at a resolution commensurate with these local YSO surveys. Figure 3-12 shows the results of this comparison for each history, as well as the location of every non-bare star model in $T_{\text{bol}} - L_{\text{smm}}/L_{\text{bol}}$ space.

Comparing T_{bol} and $L_{\text{smm}}/L_{\text{bol}}$ for all of R24's RTMs (except the uniformly Stage III models of bare-star geometries `s---s-i` and `s---smi`), it becomes apparent that the majority of models considered Class 0 by virtue of T_{bol} would also be considered Class 0 by their luminosity ratios. On the other hand, there are many RTMs that have $T_{\text{bol}} > 70$ K and high luminosity ratios. These results are largely consistent with the comparison between class definitions performed by [Dunham et al. \(2014\)](#) using YSOs from various surveys.

Regardless of definition, examining the constructed samples yields few apparent correlations between the Stages of the RTMs and either their bolometric temperatures or luminosity ratios. The majority of Stage 0 models identified along all three of the PEMs would not be considered Class 0 by either criterion. In addition, neither definition draws a strong distinction between Stages 0 and I; models in these two Stages are instead similarly distributed in this space. Stage I models have a stronger correspondence with both definitions of Class I in comparison with Class 0 (i.e. they mostly have $T_{\text{bol}} > 70$ K and $L_{\text{smm}}/L_{\text{bol}} < 0.005$). At the same time, many Stage 0 and I models also have $T_{\text{bol}} > 650$ K, meaning that they would be considered Class II according to the usual T_{bol} classification scheme. These results—regardless of definition—do not support a link between Class 0 and Stage 0, the evolutionary state of a YSO to which it is meant to correspond. In light of these findings, I retain the Class 0 definition of [Richardson et al. \(2024\)](#), though with the understanding that its physical import is somewhat limited.

Stage II is a notable exception to this lack of trend; the majority of Stage II sources have $T_{\text{bol}} > 650$ K, i.e. would be considered Class II, though it is worth pointing out that a divide closer to ~ 2000 K would yield a cleaner break from models in Stages 0/I. Some Stage II models have

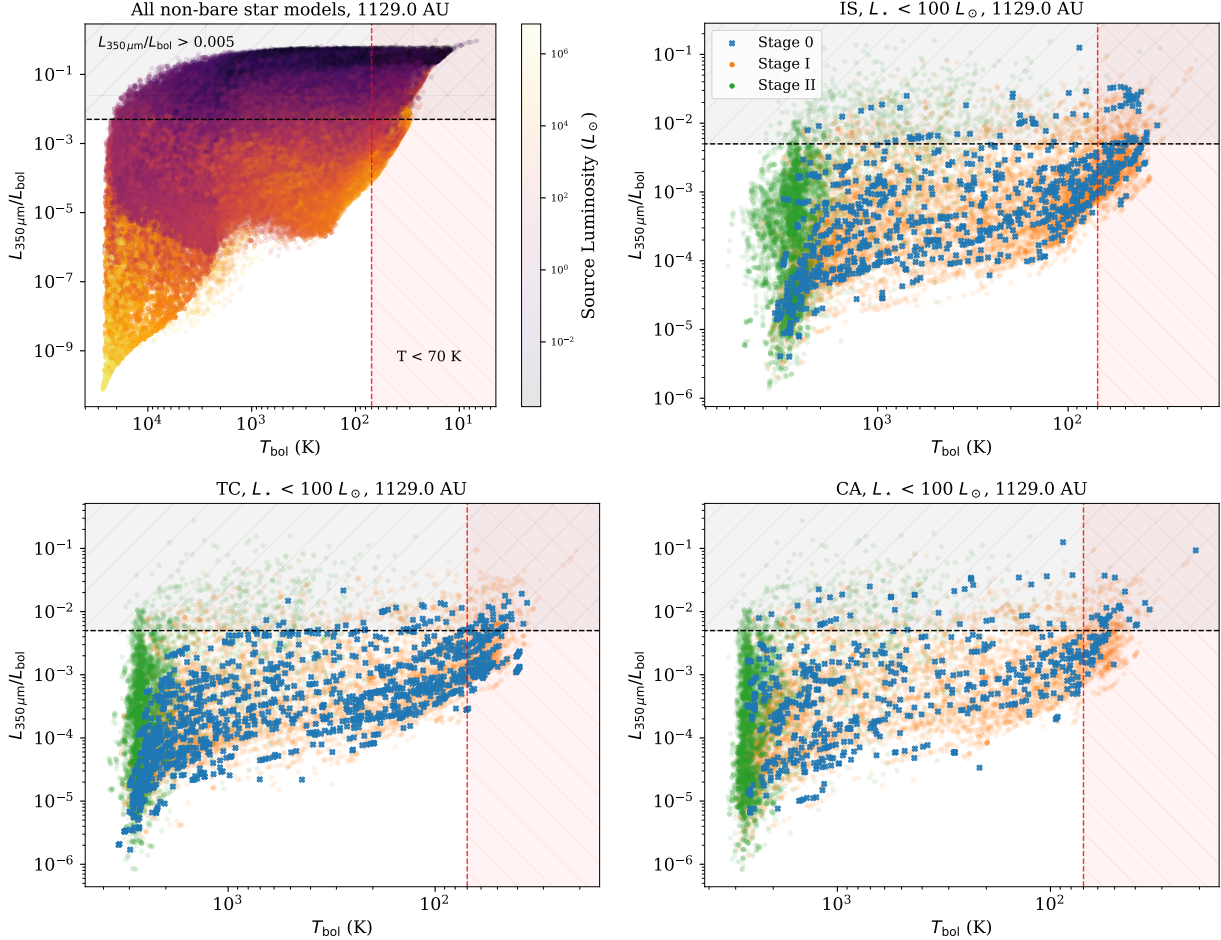


Figure 3-12. The line-of-sight mass-weighted temperatures and ratios of submillimeter to bolometric luminosity for R24 models. Regions corresponding to different definitions of Class 0 are shaded. The top left plot shows every model in R24 save the bare-star-only geometries (which are necessarily Stage III), colored by the bolometric luminosity of the central source. The remaining plots show the same thing, but restricted to a sample of models selected alongside IS (*top right*), TC (*bottom left*), and CA (*bottom right*) histories whose central protostars are less luminous than $100 L_\odot$, selected to enable fair comparison with local YSO samples. Models in these plots are colored by Stage, with Stage 0 models highlighted specifically to illustrate their relationship to the Class 0 definitions.

bolometric temperatures placing them in Classes 0 or I; these occurrences are due to a combination of low source luminosities and edge-on viewing. The connection between Class II and Stage II is therefore still subject to observational effects.

Stage. The main difference between the Stage definitions of this work and those of R24, which extends Crapsi et al. (2008), is the changed divide between Stages 0 and I. R24 distinguished these Stages using the temperature of the source; Stage 0 YSOs had sources with temperatures of < 3000 K, i.e. sources that had not yet entered the Hayashi or Henyey tracks. Part of the motivation for these Stage definitions was the absence of an evolutionary history underlying R24’s models. The half-mass definition for Stages 0 and I requires knowledge of the final stellar mass associated with a particular YSO, in turn requiring the assumption of a history. This requirement is now satisfied through the ability to associate R24 models with PEMs, allowing the implementation of alternate dividing lines. To evaluate the impact of this redefinition on the models, I compare the consequences of adopting the R24 and half-mass Stage criteria within the context of the flux predictions (as in Figure 3-3) in Figure 3-13. I also include the traditional definition of “Stage 0” from Andre et al. (1993, A93), that being where $M_\star < M_{\text{env}}$, taking the converse of that inequality to be their Stage I⁶. I consider ϵ_{SFS} of both 1/3 and 3 in order to locate Stage dividing lines for both isolated collapse with mass ejection and collapse with external infall.

R24’s Stage definitions generally bookend the predicted flux tracks, except for very low-mass ($\lesssim M_\odot$) stars, which spend a non-trivial fraction of their accretion time in Stage II (in other words, with an envelope mass $< 0.1 M_\odot$). The transition from R24’s Stage 0 to I consistently corresponds to the beginning of the tracks, regardless of mass. This close correspondence between the R24 dividing line and my ability to make predictions for the flux of a YSO indicates that the R24 definitions for Stages 0/I correspond to a meaningful physical divide in YSO evolution. However, the implication of the resulting lack of predictive capability for Stage 0 is that R24’s concept of a Stage 0 YSO is difficult to model and observe.

⁶ Another set of definitions that sees use is that of Robitaille et al. (2006), which distinguishes Stages based on a YSO’s instantaneous protostellar mass M_\star , envelope infall rate \dot{M}_{env} , and disk mass M_{disk} . Since only M_\star is explicitly included in the PEMs and M_{disk} is not tracked at all, I do not evaluate this definition here.

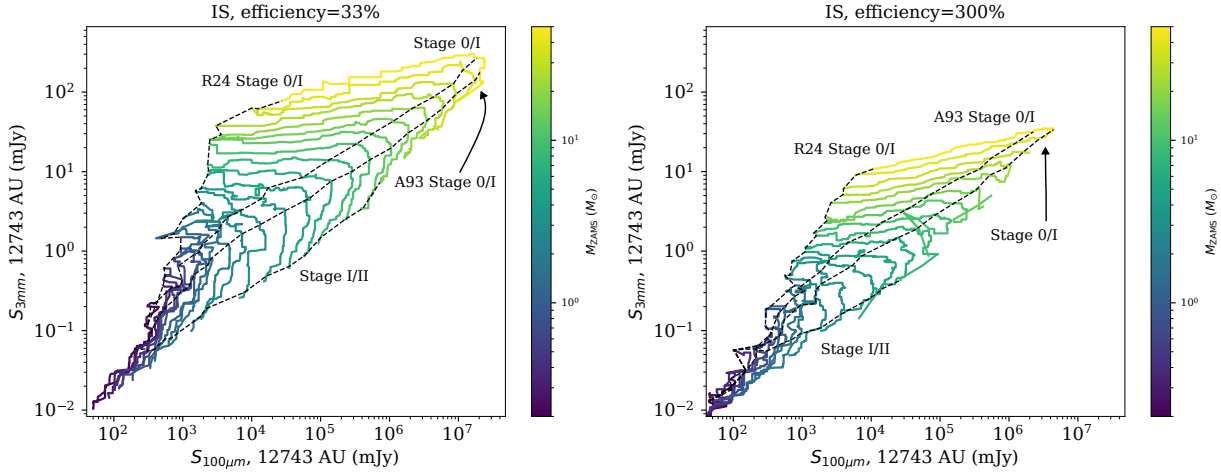


Figure 3-13. One of the plots from Figure 3-3, but the dotted lines now indicate the timestep corresponding to the dividing line between the Stage definitions of Andre et al. (1993), Richardson et al. (2024), and this work (§3.4.2). Predictions are shown for scenarios where $\epsilon_{SF} = 1/3$ (left) and $\epsilon_{SF} = 3$ (right); axis limits are the same for both plots.

The half-mass-assembly Stage 0/I dividing line, in contrast with R24, exhibits a general correspondence with the “knee” feature in the predicted flux tracks. These Stage definitions essentially create two distinct observational phases; an increase in far-IR flux at roughly constant millimeter flux and a decrease in millimeter flux at roughly constant far-IR flux. Consequently—with a sufficiently good measurement of its mass—it should be possible to determine which phase a YSO is in from its position in this flux space, and therefore to directly identify and distinguish Stage 0 and I YSOs through photometric observations at multiple wavelengths⁷. My adoption of the half-mass-assembly divide between Stages 0 and I over R24’s is in response to this generally higher level of observational significance, though the definitions are more closely aligned for lower-mass YSOs.

Comparing the half-mass-assembly criterion with the A93 mass-ratio divide, both behave similarly. However, the location of the A93 divide within the predicted tracks exhibits a

⁷ Figure 3-13 compares flux at 100 μm and 3 mm; however, sources for new sub-millimeter data are limited when compared to the near- and mid-IR or millimeter regimes. Identification of Stages 0 and I by comparison of flux across wavelength regimes is in principle not limited to these particular wavelengths, but use of shorter-wavelength data will likely be complicated by the reduced predictive capacity of the models in the IR, for reasons discussed in Chapter 3.3.2.

dependence on the efficiency of mass accretion, occurring after half mass assembly in sub-100% (isolated-collapse) scenarios and before half mass assembly in super-100% (external-infall) scenarios. This mirrors the expected order of events within the corresponding evolutionary tracks (see Figure 14 of F17 for an illustration of star+envelope evolution with external infall). As a result, the A93 definition also does not correspond as closely as the half-mass criterion to the transition between behavioral phases in either modeled scenario, although it occasionally exhibits greater agreement with the predicted peaks in 100- μm flux in the low-efficiency case. The same behavior occurs across all of the modeled accretion histories. Within the context of my approach to YSO modeling, then, the time at which half of a star's final mass is assembled appears to be a reasonable discriminator between predicted behavioral phases that is consistent across modeled accretion histories and more robust to variation in mass accretion efficiency than the traditional M_\star/M_{env} criterion.

In addition to examining Stage definitions within the context of the predicted fluxes, Figure 3-13 also allows the impact of variable efficiency on the predictions themselves to be evaluated. While the shape of the tracks generally remains the same, YSOs with lower mass accretion efficiency are consistently brighter than their high-efficiency counterparts, with a difference in flux of roughly an order of magnitude at both 100 μm and 3 mm for the highest-mass YSOs at the modeled efficiencies. This disparity implies that star formation via localized collapse should appear brighter in the FIR/mm regimes than formation fed via external infall. Overall, this behavior is consistent with expectations; the mass of the envelope component for a YSO corresponding to the same eventual stellar mass will be systematically less in a scenario where most of the stellar mass originates outside the YSO than one in which stellar growth is entirely fed by the birth mass reservoir, therefore leading to less emission from the dust in the envelope.

As a general caveat to these predictions, the Stage I fluxes calculated for the more massive super-efficient YSOs are subject to increased noise and lack of predictive capability in most apertures. These YSOs are composed of highly luminous sources with minimal non-ambient circumstellar dust, meaning that they are likely to fall below the long-wavelength S/N threshold

employed by R17 due to widespread emission from the heated medium (see Section 4.2.4 of that paper for more detail on SED post-processing). Consequently, many models selected by my procedure within the Stage I phase do not exhibit defined fluxes within most apertures. Predictive capacity is less diminished in larger apertures, which are more likely to have sufficient signal. Moreover, many of these high-mass YSOs correspond to proto-O and B stars which will also interact with a medium through ionization, the effects of which are currently not modeled within the framework.

3.5 Closing Remarks

I have developed a new approach to modeling the evolution of young stellar objects. By associating existing radiative transfer SEDs from a well-populated and formation-agnostic set of YSO models with independent models of protostellar evolution, I create a modeling framework that is capable of predicting the properties and flux of a YSO regardless of the assumed pathway of star formation.

I used this framework to predict the flux emitted by YSOs with initial stellar masses ranging from 0.2-50 M_{\odot} across the time they are actively accreting following isothermal-sphere, turbulent-core, and competitive accretion histories. By comparing the 100- μm and 3-mm flux of these modeled YSOs, I found that the different rates of protostellar growth projected by these histories translate into observable differences in the long-wavelength flux of YSOs. This is particularly true for more massive stars, where the timescale of accretion differs the most. This modeling approach links the evolutionary history of YSOs to direct observables, advancing the practice of comparing theory to observation, which is often done through the use of intermediate quantities which require additional inferences (e.g. bolometric temperature or luminosity).

I characterized the uncertainty in these predictions by attempting to reproduce the 1-mm flux of the SEDs of Richardson et al. (2024) used in my framework, finding that I am generally able to recover the expected flux to within approximately 20%, though with a slight bias to the upside. This good performance is not uniform across the spectrum; my approach does not recover shorter-wavelength radiation to the same degree, largely due to the dependence of this radiation on

quantities that are not well-modeled. In particular, I highlight the near- and mid-IR as areas suffering from this issue; given their frequent usage in studies of star formation, better modeling of the evolution of disks and outflow cavities is needed to maximize the impact of the current- and next-generation data in this regime.

As a test of the flexibility of my framework, I have applied it to the YSO models of [Zhang & Tan \(2018\)](#), a contemporary grid based on the turbulent-core theory of protostellar growth. As with my own models, I am able to recover long-wavelength fluxes that are reasonably consistent with ZT18's predictions. Furthermore, I investigated the extent to which the assumed dust opacity models are responsible for differences between my SEDs and their ZT18 counterparts by recalculating the SEDs of a subset of R24 models with the dust configuration of ZT18. I found that alterations of the dust model are capable of reproducing the kinds of discrepancies observed between ZT18's fluxes and my recoveries, illustrating the potential uncertainty introduced into radiative transfer modeling by the choice of dust. I developed an explanation for the over-recovery of ZT18's fluxes based on its higher disk dust opacities and densities.

Leveraging the ability to associate R24 models with evolutionary histories, I have revisited the concept of confusion between the observational Class and evolutionary Stage of YSOs. I created confusion matrices quantifying the relationship between Class and Stage for every available slice of a parameter space composed of accretion history model, final stellar mass, protostellar age, mass accretion efficiency, and level of detectability at long wavelengths. In doing so, I provide a tool to infer the physical reality of observed protostellar populations from observed class counts that is applicable across a wide range of theoretical scenarios. These confusion matrices are released to the public at [10.5281/zenodo.13922040](https://doi.org/10.5281/zenodo.13922040). Further, I have investigated the theoretical and observational significance of various commonly used definitions for Class and Stage using the RTMs identified as being consistent with the implemented PEMs. The results do not evidence a strong connection between Stage 0 and Class 0 YSOs by any definition, calling into question the utility of Class 0 as an indicator of protostellar evolution. However, I also find that a Stage 0/I dividing line set when a star accretes half of its final mass creates distinct behavioral

phases in the fluxes of modeled YSOs, potentially facilitating identification of YSOs in the earliest phases of their evolution through an observable other than Class.

CHAPTER 4

A REVIEW OF YSO CLASS AND STAGE DEFINITIONS

4.1 Motivation

Much of the modern picture of star formation, particularly for less massive stars, hinges on the theoretical and observational framework built up around the collapse of prestellar cores over the better part of the last century. Within that time, that theoretical picture has been divided into a set of qualitatively distinct “Stages” that a YSO passes through as a star forms within it, and observations have been divided into a set of empirically determined “Classes”; further, since the seminal work of [Adams et al. \(1987\)](#) it is widely accepted that observed Classes are broadly associated with a particular Stage.

The concepts of Class and Stage are frequently invoked throughout the literature, and considerable space has been devoted to them in numerous reviews ([Allen et al., 2007](#); [White et al., 2007](#); [Kennicutt & Evans, 2012](#); [Dunham et al., 2014](#); [Tobin & Sheehan, 2024](#)). As such, the *words* have long since been adopted into the vernacular of star formation. The devil, however, is in the details. In the modern era, these terms carry a great deal of baggage stemming from multiple proposed classification schemes and years of colloquial usage. As a consequence, the actual *meaning* carried by the terms can (and often does) vary across uses. An obvious example is in the tendency not simply to associate, but to *equate* a YSO’s Class with its Stage. While there is a general physical basis for a correlation between the two, it is also frequently acknowledged that the connection between the physical reality and appearance of a YSO may be obscured by observational effects (e.g. [Calvet et al., 1994](#); [Gutermuth et al., 2009](#); [Evans et al., 2009b](#); [Furlan et al., 2016](#); [Sheehan et al., 2022](#)), a possibility which spurred the creation of formal Stage definitions to begin with. If the proper context is not made explicit when using these terms, the message received may differ from the message conveyed to some extent, which introduces an unnecessary source of uncertainty into the study of star formation.

[Evans et al. \(2009a\)](#) compiled a number of quantitative and qualitative definitions for these concepts then used across the literature in an effort to promote clearer communication. In a similar vein, I review the history and current state of Classes and Stages while providing

additional context from work performed within the intervening time period, with the objective of evaluating the utility of each system given the current state of star formation research. (In keeping with the remainder of this work, I use the term “YSO” to refer to a combined system of luminosity source and circumstellar material, while a “protostar” refers to the source alone. Usage of these terms also varies across the literature and within the community; however, since this terminology is largely a matter of semantics, I do not review it here.)

4.2 Class

Multiple systems for classification are used within the literature. I provide a brief history of the development of each, give an overview of currently used quantitative definitions, and discuss the state of the field.

The Class system as initially developed is based on the infrared spectral index $\alpha \equiv d(\lambda F_\lambda)/d\lambda$ originating from [Lada \(1987\)](#). Across the literature, α has been calculated between various wavelengths, but these generally fall within the near- to mid-infrared regime with typical endpoints occurring at roughly 2 and 25 μm . (Occasionally, different endpoints are used; for example, [McClure et al. \(2010\)](#) instead calculate α between 5.3 and 12.9 μm in order to minimize the impact of interstellar extinction on classification.) This scheme separated observations from [Lada & Wilking \(1984\)](#) into three Classes numbered from I-III, with successive Classes having more negative indices (i.e. becoming less IR-dominated and more blackbody-like). This was later extended by [Greene et al. \(1994\)](#), which altered the Class boundaries and introduced a “Flat” class to encompass sources with $\alpha \sim 0$ which straddled the line between Classes I and II. Within the same time period, [Andre et al. \(1993\)](#) proposed the addition of a “Class 0” to identify sources with particularly strong sub-millimeter photometry, which provided a unique home for the “extreme Class I” sources of [Lada \(1991\)](#). Rather than being classified based on their infrared spectral index, Class 0 sources were identified by comparing their sub-millimeter luminosity to their bolometric luminosity.

This system provided a more quantitative basis on which to study forming stars. In particular, it allowed for relatively simple identification of YSO candidates whose sources were

thought to be deeply embedded within gas and dust, thus separating them from candidate T Tauri stars and PMS stars (i.e. more evolved sources). However, in many cases, obtaining the necessary photometric observations to calculate a spectral index was difficult with the existing technology, prompting the development of an alternate system less reliant on having access to particular wavelengths. [Myers & Ladd \(1993\)](#) proposed the “bolometric temperature” T_{bol} as a basis for a system, where T_{bol} is defined as:

$$T_{\text{bol}} = 1.25 \times 10^{-11} \int_0^{\infty} \nu S_{\nu} d\nu \left/ \int_0^{\infty} S_{\nu} d\nu \right. \text{ K Hz}^{-1}, \quad (4-1)$$

i.e. the temperature of a blackbody with the same mean frequency as the observed spectrum.

[Chen et al. \(1995\)](#) provided quantitative bounds between Classes by calculating T_{bol} for a set of YSOs already classified through spectral index and finding temperatures which generally separated them into distinct ranges in T_{bol} as well. With the benefit of a larger population of YSOs classified through their SEDs as “flat-spectrum” emerging from survey data, [Evans et al. \(2009b\)](#) proposed additional ranges for T_{bol} corresponding to these sources, both with and without extinction corrections on T_{bol} .

The commonly-used definitions for YSO Classes are, therefore, as follows:

Class 0:

- $L_{\text{smm}}/L_{\text{bol}} > 0.005$ ([Andre et al., 1993](#))
- $T_{\text{bol}} < 70 \text{ K}$ ([Chen et al., 1995](#))

Class I:

- $0 < \alpha < 3$ ([Lada, 1987](#))
- $\alpha > 0.3$ ([Greene et al., 1994](#))
- $70 \text{ K} < T_{\text{bol}} < 650 \text{ K}$ ([Chen et al., 1995](#))

Class “Flat”:

- $-0.3 < \alpha < 0.3$ ([Greene et al., 1994](#))

- $350 \text{ K} < T_{\text{bol}} < 950 \text{ K}$ (no correction), $500 \text{ K} < T_{\text{bol}} < 1450 \text{ K}$ (dereddened) ([Evans et al., 2009b](#))

Class II:

- $-2 < \alpha < 0$ ([Lada, 1987](#))
- $-1.6 < \alpha < -0.3$ ([Greene et al., 1994](#))
- $650 \text{ K} < T_{\text{bol}} < 2800 \text{ K}$ ([Chen et al., 1995](#))

Class III:

- $-3 < \alpha < -2$ ([Lada, 1987](#))
- $\alpha < -1.6$ ([Greene et al., 1994](#))
- $T_{\text{bol}} > 2800 \text{ K}$ ([Chen et al., 1995](#)).

Within this system, [Großschedl et al. \(2019\)](#) made a further subdivision within Class III meant to distinguish sources with thin disks ($\alpha > -2.5$) and without ($\alpha < -2.5$) based on the boundary between populations observed in [Lada et al. \(2006\)](#).

Various other methods for observationally characterizing YSOs have been proposed, but have not seen widespread adoption (e.g. [Adams, 1990](#); [Ladd et al., 1991, 1993](#)).

Synthesis. [Dunham et al. \(2014\)](#) reviewed the Class system within the context of data from the Spitzer and Herschel telescopes. Within their comparison of Classes 0 and I based on T_{bol} and $L_{\text{smm}}/L_{\text{bol}}$ for the c2d+GB and HOPS surveys ([Dunham et al., 2013](#); [Stutz et al., 2013](#)), they found about 80% agreement between the schemes as evaluated by those metrics (though classification through α is not factored in). They also found, however, that T_{bol} is particularly sensitive to inclination, often varying enough to cross a Class boundary depending on the viewing angle ([Jørgensen et al., 2009](#); [Fischer et al., 2013](#); [Launhardt et al., 2013](#)). [Evans et al. \(2009b\)](#) and [Furlan et al. \(2016\)](#) compared Classes as determined by spectral index and T_{bol} for their samples of YSOs, finding general agreement between the schemes, although [Evans et al. \(2009b\)](#) also observed that T_{bol} is a poor discriminator between Classes II and III as determined from α both with and without extinction correction. Given the results of these broad assessments of the

internal coherence of the Class system, most works elect to employ a scheme depending on the available photometric information.

4.3 Stage

The modern concept of distinct theoretical phases of YSO evolution appears to largely have been co-developed with the concept of distinct observational phases. Early analytical modeling of forming stars (e.g. Larson, 1969; Penston, 1969; Ulrich, 1976; Shu, 1977; Cassen & Moosman, 1981; Terebey et al., 1984) suggested a general progression wherein material infalling from a rotating, collapsing core would feed a disk surrounding a central protostar. This mathematical model was in turn extended to the realm of observation (e.g. Adams & Shu, 1985, 1986), indicating that as a young stellar object evolved, the contribution of the reservoir supplying the protostar with mass to the resulting SED decreased relative to that of the protostar (and disk) as material continued to be accreted. This coincided with the creation of distinct categories for observed YSO candidates (Lada, 1987), cementing the canonical qualitative protostellar evolutionary sequence (Adams et al., 1987). In the creation of Class 0, Andre et al. (1993) also provided an initial quantitative separation within the earliest (embedded) phase of this view of star formation, adding more detail to the classical picture.

However, as star formation research continued to develop, and in particular as the capacity to perform radiative transfer over large parameter spaces increased, evidence began to arise that the influence of observational effects (e.g. the angle at which a YSO is viewed) posed significant challenges to a simple mapping between qualitative evolutionary stages and Classes (e.g. Whitney et al., 2003a,b, 2004). In order to promote clarity of discussion, Robitaille et al. (2006) proposed the use of formal “Stages” which would quantify the formerly qualitative picture of YSO evolution developed alongside the Class system; these would correspond to physical properties of a YSO such as its disk mass or infall rate rather than observational ones such as its bolometric temperature or spectral index. The Stage definitions of this work used a YSO’s infall rate \dot{M}_{env} , instantaneous protostellar mass M_{\star} , and instantaneous disk mass M_{disk} to draw boundaries between Stages I, II, and III. No attempt was made by this work to distinguish a Stage 0, though

the existence of such a stage is implied; however, the physical criterion proposed by Andre et al. (1993) to correspond to Class 0 YSOs appears to have been subsequently folded into the framework of Stages as a quantitative definition. Crapsi et al. (2008) provided an alternative distinction between Stages I and II based on the total mass remaining in an envelope M_{env} ; this boundary was set by translating the \dot{M}_{env} boundary of Robitaille et al. (2006) to the envelopes created in their radiative transfer modeling. Using their models, they also predicted that YSOs would exhibit monotonic evolution in the ratio of $M_{\text{disk}}/M_{\text{env}}$ with time; van Kempen et al. (2009) proposed a set of Stage definitions that made use of this prediction while also generally aligning with the colloquial Stages and Andre et al. (1993) Stage 0/I divide. More recently, Richardson et al. (2024) and Richardson et al. (2025) attempted to extend the textual definitions of Crapsi et al. (2008) to include a Stage 0. They evaluated the observational consequences of dividing lines between Stages 0 and I based on both the temperature and mass of a YSO's central protostar within the context of their YSO models (extensions of the Robitaille (2017) set) and arrived at separating those Stages by protostellar mass in a manner akin to Andre et al. (1993).

The commonly-used (or proposed) definitions for Stage are as follows:

Stage 0:

- An envelope-dominated YSO in which a protostar is deeply embedded within its natal material. Outflows and disks may have formed. (Colloquial)
- $M_{\star} < M_{\text{env}}$ (Andre et al., 1993)
- $M_{\text{disk}}/M_{\text{env}} \ll 1$, $M_{\star} \sim M_{\text{env}} + M_{\text{disk}}$, deeply embedded (van Kempen et al., 2009)
- $M_{\text{env}} > 0.1M_{\odot}$, $M_{\star} < M_{\star, \text{final}}/2$ (Richardson et al., 2025)

Stage I:

- A YSO where the envelope is significant, but less so than in Stage 0. Outflows and disks have formed. (Colloquial)
- $\dot{M}_{\text{env}}/M_{\star} > 10^{-6} \text{ yr}^{-1}$ (Stage 0/I) (Robitaille et al., 2006)
- $M_{\text{env}} > 0.1M_{\odot}$ (Crapsi et al., 2008)
- $0.1 < M_{\text{disk}}/M_{\text{env}} < 2$, $M_{\star} > M_{\text{env}} + M_{\text{disk}}$, embedded (van Kempen et al., 2009)

- $M_{\text{env}} > 0.1M_{\odot}$, $M_{\star} > M_{\star, \text{final}}/2$ ([Richardson et al., 2025](#))

Stage II:

- A YSO where the dominant mass component is the protostar/disk system, and any remaining envelope is minimal (or no envelope exists). (Colloquial)
- $\dot{M}_{\text{env}}/M_{\star} < 10^{-6} \text{ yr}^{-1}$, $M_{\text{disk}}/M_{\star} > 10^{-6}$ ([Robitaille et al., 2006](#))
- $M_{\text{env}} < 0.1M_{\odot}$ ([Crapsi et al., 2008](#); [Richardson et al., 2024](#))
- $M_{\text{env}} = 0$, $M_{\text{disk}}/M_{\star} \ll 1$ ([van Kempen et al., 2009](#))

Stage III:

- A protostar with minimal or absent circumstellar material. (Colloquial)
- $\dot{M}_{\text{env}}/M_{\star} < 10^{-6} \text{ yr}^{-1}$, $M_{\text{disk}}/M_{\star} < 10^{-6}$ ([Robitaille et al., 2006](#))
- PMS stars with “tenuous” disks ([van Kempen et al., 2009](#))
- PMS stars with no non-ambient circumstellar material ([Richardson et al., 2024](#)).

Few other quantitative Stage definitions have been proposed in the intervening years. As Stages are conceived as purely theoretical categories whose coincidence with observational quantities is not guaranteed (and prominent existing definitions rely on protostellar properties which can be difficult to measure, particularly for embedded protostars), working in terms of Stages can be a largely academic endeavor. However, some attempts have been made both to assess the observational significance of the Stage system and to find alternate ways of tracing YSO evolution; see Chapter 4.4 (and in particular §4.4.3).

Synthesis. While various quantitative definitions have been proposed for Stages, few attempts have been made to assess how well they agree. Though colloquial definitions for the qualitative states meant to correspond to Stages 0-III exist, most works that attempt to quantify these do not extend to every state: [Andre et al. \(1993\)](#) only defines a Stage 0, [Robitaille et al. \(2006\)](#) combines Stages 0/I, and [Crapsi et al. \(2008\)](#) only distinguishes Stages I and II. Moreover, some schemes are difficult to extricate from the theories used to construct them. For example, the Robitaille definitions incorporate envelope infall rate and disk mass based on expectations for the evolution

of these properties set by the canonical qualitative picture of star formation. However, between the general lack of understanding of how disk mass is expected to evolve with time—for example, [Tobin et al. \(2020a\)](#) and [Sheehan et al. \(2022\)](#) find opposite trends for this evolution (although both trends are by admission somewhat weak)—and the difficulty of measurement and wide theory space for envelope infall, the Robitaille scheme cannot easily “converse” with models and schemes that make different assumptions. Direct comparison between full “stagification” schemes is consequently difficult, and the reward for doing so is somewhat unclear given the nebulous connection of the schemes to observables.

[Richardson et al. \(2025\)](#) compared various definitions for Stages 0 and I within the context of predictions made through their YSO modeling framework, finding that while the traditional M_\star/M_{env} Stage 0 definition with the half-stellar-mass-assembly definition posed in that work behaved similarly, a Stage 0/I divide at $M_\star = M_{\star, \text{final}}/2$ did not exhibit a dependence on the efficiency of mass accretion, making it more theoretically robust. This is mainly due to the assumptions underlying [Andre et al. \(1993\)](#), which proposed the former criterion; the dividing line at $M_\star = M_{\text{env}}$ emerged from the core-collapse model circa 1993, which was generally prior to any indication that the efficiency of star formation differed significantly from 100% (e.g. [André et al., 2010](#); [Holman et al., 2013](#)); it also did not consider the effects of external infall. Consequently, if accretion is not 100% efficient, $M_\star = M_{\text{env}}$ and $M_\star = M_{\star, \text{final}}/2$ occur at different times. (A full discussion on accretion efficiency is outside the scope of this review, but in this context, the efficiency of mass accretion is a measure of the relationship between the initial mass of a core and the final mass of a star. A theoretical scenario wherein an isolated prestellar core collapses to form a protostar but ejects some of the accreted mass through outflows (e.g. [Matzner & McKee, 2000](#); [Machida & Matsumoto, 2012](#)) has sub-100% efficiency, while a scenario wherein a minimal core is continuously replenished by external infall (e.g. [Fischer et al., 2017](#)) has super-100% efficiency.)

4.4 Congruence

With the history and various definitions of Class and Stage laid out, I turn to the task of critically evaluating the relationship between the two systems of categorization to physical reality.

The core question at the heart of the Stage and Class systems is whether or not the somewhat arbitrary bounds drawn between various categories actually correspond to anything physical, and beyond that, whether any physical correspondence is observable. It is perhaps more helpful to ask, having long since established a set of expected phases of YSO evolution, *which* observables are *useful* as identifiers for each phase. Throughout this section, my objective will be to survey the effectiveness of various proposed tracers of evolution. To some degree, this is an examination of how they relate to Stages; however, as some tracers exist outside of that paradigm, I also examine the concept of “evolution” on a broader scale.

4.4.1 Class

The foremost observable used to trace the evolutionary status of a YSO is, of course, its Class. Early attempts to tie the evolution of a YSO’s Class to its physical state by modeling (e.g. [Adams et al., 1987](#); [Myers et al., 1998](#); [Young & Evans, 2005](#)) generally indicated a smooth progression through the various Classes with time, both in α and T_{bol} . From a more observational angle, [Enoch et al. \(2009\)](#) found a general (though not uniformly strong) correspondence between the SEDs of YSOs sorted into groups with increasing T_{bol} and the SEDs of the models of [Whitney et al. \(2003a\)](#), which are constructed to trace out a rough evolutionary sequence. (It is worth noting that these modeling efforts were done prior to the development of most quantitative Stages save the 0/I boundary of [Andre et al. \(1993\)](#), so uses of the word “Stage” in these works mostly invoke the qualitative definitions.)

However, some problems pervaded this view of star formation. The majority of these results were generated through the assumption of theories akin to the simple isothermal core-collapse model of [Shu \(1977\)](#), or parameter values consistent with ones therefrom. While this model provided a basis for more detailed and physically motivated study of forming stars, it had also been plagued by the so-called “luminosity problem”—wherein the protostellar luminosities measured from real YSOs were on average considerably lower than those expected from isothermal-sphere accretion ([Kenyon et al., 1990](#))—since roughly the origin of the Class system. This discrepancy only worsened as observing capabilities increased and large, detailed surveys of

YSOs (e.g. [Evans et al., 2009b](#)) were conducted. Simultaneously, as computational radiative transfer became a more commonly used tool, astronomers began to use it to create models with more detailed structure (i.e. disks, outflow cavities, asymmetric envelopes) and portraying more combinations of parameters than early analytical modeling, though generally remaining within the same overall core-collapse paradigm (e.g. [Whitney et al., 2003a,b](#); [Robitaille et al., 2006](#); [Crapsi et al., 2008](#)). Results from these models indicated that the observed Classes of these models, both by α and T_{bol} , was capable of diverging from the underlying evolutionary state in a nontrivial fraction of cases, primarily due to viewing angle.

In an effort to resolve the luminosity problem, [Dunham et al. \(2010\)](#) performed a comprehensive study of the effect that various complexities introduced into models of YSO structure and evolution had on the evolution of T_{bol} and $L_{\text{smm}}/L_{\text{bol}}$ as determined by radiative transfer modeling. Their results reinforced the general findings of contemporary studies centering around radiative transfer modeling; while a connection between Class and evolutionary status existed in the simple case, more detailed geometry obscured that connection for both Class indicators. In addition, they also modeled the impact on luminosities of an accretion history that was variable and episodic as opposed to the roughly constant accretion of SIS collapse, which was proposed as a possible solution to the luminosity problem in its original statement ([Kenyon et al., 1990](#)). This brought the spread of simulated luminosities into closer agreement with observations; however, it simultaneously destroyed any semblance of smooth or monotonic progression in T_{bol} and $L_{\text{smm}}/L_{\text{bol}}$, rendering Class a poor tracer of real evolution in such a scenario. The results from this study therefore implied a strong dependence of the Class system on the assumed model of accretion (and therefore the broader picture of star formation). However, despite the growing evidence for episodic accretion ([Fischer et al., 2023](#)) and other theoretical solutions to the luminosity problem (including tapered accretion, accelerating accretion, and mixed-mode accretion, e.g. [Offner & McKee, 2011](#); [Dunham & Vorobyov, 2012](#); [Fischer et al., 2017](#); [Sheehan et al., 2022](#)) in the intervening years, little effort has been made to reevaluate the physical

significance of the Class system across the growing theory space¹, although many alternate tracers of evolution have been proposed within that time (§4.4.3 provides more detail).

Some recent work has directly probed the connection between Classes and Stages, both in observation and theory. Richardson et al. (2025) attempted to quantify the degree to which Classes—based on $L_{\text{smm}}/L_{\text{bol}}$ and α —and Stages—defined according to an extended Crapsi et al. (2008) framework (§4.3)—would be confused in observations following multiple accretion histories, comparing the Classes and Stages of radiative transfer YSO models from a formation-agnostic set (Robitaille, 2017; Richardson et al., 2024) associated with modeled protostellar evolutionary tracks. Results from their modeling indicated that the relationship between Class and Stage was not one-to-one, as in the cases of previous works incorporating radiative transfer models. Furthermore, they showed that the existing relationship exhibited some dependence on the assumed accretion model and was capable of varying with stellar mass, efficiency of mass accretion, and the sensitivity of an instrument (although they did not attempt to quantify the magnitude of this variation). In addition, they repeated the comparison between Class by T_{bol} and by $L_{\text{smm}}/L_{\text{bol}}$ done by Dunham et al. (2014) on subsets of radiative transfer models identified both as being consistent with their accretion history models and as having lower-luminosity ($< 100 L_{\odot}$) sources, assigning Stages to the included models. They did not find an apparent correlation between Stage 0 and either Class 0, a minimal relationship between Stage I and Class I, and a relatively strong relationship between Stage II and Class II by T_{bol} , although some edge-on or particularly low-luminosity Stage II models were still considered Class 0/I by both metrics. (As in Dunham et al. (2014), α -defined Classes were not included in this comparison.)

In observation, Gezer et al. (2025) compared the Classes and Stages of YSOs from the catalog of Roquette et al. (2024). They determined Classes through the augmented α -based scheme of Großschedl et al. (2019)—with modifications by Hernandez et al. (2024)—and Stages by

1 In a recent review of accretion variability in YSOs, Fischer et al. (2023) recommended retiring the framing of this phenomenon as a “problem” in favor of a “luminosity spread”, given the many current theoretical explanations which peacefully coexist with observations.

fitting the SEDs of objects in the catalog to the models of Richardson et al. (2024)². In their results, Stages II and III exhibited very good correspondence with Classes II and III, with particularly strong agreement for the “no thin disk” Class III objects (i.e. those with $\alpha < -2.5$). YSOs in preceding Classes, on the other hand, generally do not have concordant Stages; many of the Class 0 and I models are weighted towards Stage II. (However, Class 0/I objects do not comprise a significant fraction of their sample, which is generally weighted towards objects detected with Gaia, 2MASS, and WISE W1/W2. The resulting catalog is consequently less likely to trace more extincted objects than dedicated IR surveys (e.g. Evans et al., 2009b; Stutz et al., 2013; Furlan et al., 2016; Pokhrel et al., 2023) by construction.)

In summary: Given the present level of uncertainty in the qualitative picture of star formation, it seems appropriate to say that the relationship between the Class system as originally conceived and YSO evolution is at best a correlation. Moreover, the tightness of that correlation appears to depend at least partially on which Class is being considered. In attempts to evaluate the correspondence of Classes and Stages, Classes II and III routinely exhibit partial to good (if not perfect) correspondence with their companion Stages, particularly if classifying according to spectral index. However, multiple studies have shown through multiple methodologies (including alternate tracers of evolution not yet discussed; see the following sections) that Class 0 and I exhibit varying levels of correspondence to their associated Stages when factoring in aspects of a YSO like its geometry and assumed accretion history across commonly used definitions; at present, the full extent of this variation has not been quantified.

In this light, Class is possibly best framed as a decent tracer of extinction from dust, but one that cannot reliably distinguish between *sources* of that extinction, hence why evolved sources may appear to have an “earlier” Class if viewed through a highly inclined disk, why the presence of outflow cavities in a source may cause its Class to vary, why Class may be impacted by reddening from interstellar extinction (e.g. McClure et al., 2010), and so on. Early-stage, more embedded

2 Richardson et al. (2025) recommended that the definitions for Stages 0 and I in Richardson et al. (2024) be deprecated if possible; however, this catalog does not include many objects in Stage 0 or I, so the impact on the results is minimal.

sources present more avenues for confusion from extinction due to their more complex geometries and the fact that they are expected to be undergoing accretion at a rate higher than less embedded sources with smaller reservoirs to draw on, hence the higher potential for variation. Later-stage sources which have cleared most of their surroundings, on the other hand, have fewer opportunities to be misclassified because some of these avenues are closed off by the comparative lack of dust, although phenomena like inclined disks and environmental extinction remain possible.

4.4.2 Colors

In addition to Class, the infrared colors exhibited by a YSO are sometimes used to probe their evolutionary status, as well as to distinguish them from more evolved stars (e.g. [Allen et al., 2004](#); [Megeath et al., 2004](#); [Gutermuth et al., 2008, 2009](#); [Kryukova et al., 2012](#); [Megeath et al., 2012](#)). To some extent, this is akin to the Class system; sorting an object into a particular Class necessitates multi-wavelength photometric information on that object, and the categories themselves are based on how much divergence an object exhibits from a regular stellar SED. However, Class is generally limited to examining the slope of an SED between the fixed endpoints of 2–25 μm . Colors, on the other hand, can be calculated across many different wavelength ranges, and the large number of filters and photometric data currently available expands the amount of information that can be gleaned from an SED. As a consequence, I examine their utility as a probe for YSO evolution separately from Class.

A few works have attempted to directly connect a YSO’s color to its evolutionary state, both in theory and observationally. [Robitaille et al. \(2006, R06\)](#) and [Richardson et al. \(2024, R24\)](#) map their radiative-transfer YSO models into various Spitzer and JWST color-color spaces by Stage³. These works find regions of color space across instruments that are mainly occupied by models with particular Stages. In NIR color space—JHK for R06, NIRCam for R24—R06 models with $J - H$ and $H - K > 2$ generally tend to be Stage I, while R24 find a similar trend for

³ It should be noted that the Stages 0 and I of [Richardson et al. \(2024\)](#) are separated based on protostellar temperature instead of mass, resulting in smaller demographic variety in the population of YSOs considered “Stage 0” in that work than would be expected by other definitions. Adopting an alternate definition for Stage 0 would likely affect the bounds of the regions of color space occupied by Stage 0 models, though the specific nature and extent of this change is unclear. However, this does not affect Stages II or III.)

[F115W]–[F150W] and [F150W]–[F200W], although both works note that the identified region is along the direction of extinction, meaning that confusion with Stage II or III is possible. In the MIR–IRAC [3.6]–[4.5]/[5.8]–[8.0] for R06, MIRI [F560W]–[F770W]/[F770W]–[F1500W] for R24—both works again find a region mainly occupied by models in Stage I, and also that some Stage I and II models are redder in the colors involving longer-wavelength emission than is possible through extinction. While models of both Stages I and II can exist in this long-redward space, the occupants are weighted towards Stage II, indicating that colors involving MIR wavelengths are effective at tracing disk emission. Both works also construct color spaces incorporating further-MIR emission–IRAC [3.6]–[5.8]/[8.0]–MIPS [24.0] for R06, [F200W]–[F444W]/[F770W]–[F2550W] for R24—and find that doing so reliably separates models of various Stages into distinct regions, generally moving blueward in both colors (although not uniformly).

These works also compare the positions of Stages in their color spaces to the positions of Classes; [Robitaille et al. \(2006\)](#) includes an indicator of where the Class II models of [Allen et al. \(2004\)](#) fall in IRAC color space, while [Richardson et al. \(2024\)](#) assigns each of their models a Class based on its spectral index. In each case, while there is overlap between the regions occupied by corresponding Classes and Stages, they largely do not find complete agreement between the two. Successive Classes generally exhibit a monotonically blueward progression, while Stages may redden or remain red in colors involving longer wavelengths ($\sim 15 - 24 \mu\text{m}$) until Stage III due to emission from disks.

Observations making use of color to distinguish the Class of a YSO is fairly common practice. However, comparisons between observations and regions of color space corresponding to particular Stages are less frequent. [Evans et al. \(2009b\)](#) explicitly place their YSOs in the IRAC + MIPS 24 μm color space of R06, comparing their positions (and Classes, as determined by spectral index) with the positions occupied by R06’s Stages. In general, the observed YSOs align well with the expected Stage boundaries, including good agreement between Stage and Class within this color space, particularly after dereddening. (However, this comparison is somewhat

incomplete since R06 do not separate Stages 0 and I and the observed Class 0/I YSOs are not distinguished by these colors.)

Overall, color appears to be a tracer of evolutionary status at least on par with Class, if not an improvement due to a better ability to leverage the observed correspondence of particular physical features to particular wavelength ranges (e.g. MIR emission as a tracer of disks).

4.4.3 Other

With the recognition that Class is an uneven indicator of protostellar evolution and given the wide range of available data outside the IR, some efforts have been made to tie the general evolution of a YSO through avenues distinct from Class (and its derivatives). I provide a general overview of quantities used or proposed as alternate tracers of evolution in this section.

Many works infer the general evolutionary state of a YSO by comparing broad “summary” properties accessible through a YSO’s SED—typically total protostellar luminosity L_{tot} and M_{env} —to predictions from simple evolutionary models (e.g. [Duarte-Cabral et al., 2013](#); [Fischer et al., 2017](#); [Sheehan et al., 2022](#)). Typically, efforts of this type are only used to infer the likelihood of the occurrence of particular accretion histories and do not connect these evolutionary models to the evolution of specific properties or SEDs. Measurements of these summary properties remain subject to observational effects, particularly L_{tot} , which often comes from the variable and inclination-dependent L_{bol} ([Tobin & Sheehan, 2024](#)).

In addition to probing the connection between Class and Stage, [Crapsi et al. \(2008\)](#) used their radiative transfer models to predict in-band fluxes, finding a strong correlation between envelope mass and millimeter dust continuum emission when corrected for disk mass, which they did by subtracting the modeled emission over a smaller (< 300 AU) scale. By the same token, their models indicated a correlation between the ratio of disk mass to total mass and the ratio of predicted small-scale to total flux. Based on these results, they suggested such a ratio (small-scale vs. large-scale millimeter flux) as a good diagnostic of evolutionary status that could be probed effectively by combining single-dish and interferometric observations. [Jørgensen et al. \(2009\)](#) applied a similar technique to a sample of Class 0 and I sources, using the flux ratio between

millimeter interferometric data with a baseline of $50 k\lambda$ and $850 \mu\text{m}$ single-dish data with a beam size of $15''$ as their probe. They found a general upward trend in their inferred $M_{\text{disk}}/M_{\text{env}}$ with T_{bol} , though they performed their own radiative transfer modeling and did not directly repeat the approach of Crapsi et al. (2008).

Recent analogues to these approaches using more modern tools and instruments have been independently proposed. Sheehan et al. (2022) suggested a diagnostic for YSO evolution based on the ratio of envelope mass to total system mass, which they measured through their radiative transfer modeling with some assumptions about the birth masses of stars. Further refinement of this approach is possible through measurements of system dynamics to more accurately determine the true masses of protostars (e.g. Tobin et al., 2020b). Federman et al. (2023) proposed the ratio of fluxes measured from a source using the ALMA 12 m configuration and the Atacama Compact Array (ACA) at $870 \mu\text{m}$ as a probe of evolutionary status, with $R \equiv 12 \text{ m}/\text{ACA}$ indicating the transition from envelope domination of submillimeter flux ($R < 0.5$) to disk domination ($R > 0.5$). As the capacity to probe the detailed structure of YSOs increases, these may serve as the core of a more formal or quantitative framework.

The broader idea inherent in Crapsi et al. (2008) and Jørgensen et al. (2009) of tracing YSO morphology as a diagnostic for evolution has also been explored. Andre & Montmerle (1994) observed a general distinction between the physical sizes of a sample of YSOs in ρ Oph with various Classes, finding that Class 0/I objects were generally resolved within their $12''$ beam while Class II/III objects were not. van Kempen et al. (2009) proposed a more comprehensive set of observational indicators for Stage I and II sources based on the physical extent and position of gas within identified YSOs, utilizing dust continuum emission and the HCO+ 4-3 and C¹⁸O 3-2 emission lines (common tracers of high- and low-density gas, respectively). Stage I sources were generally hypothesized by these works to be more extended and centrally concentrated than Stage II sources, conceived as less extended and less intense. These alternate definitions were intended to provide easily accessible observables that would reliably distinguish between more and less embedded protostars without the pitfalls of inclination dependence and confusion possible with

traditional Class metrics. This general approach to Stage identification has since been applied by some other works with varying levels of morphological consideration and specific emission lines ([Heiderman & Evans, 2015](#); [Carney et al., 2016](#)), but is subject to availability of detailed spectral and spatial information for gas tracers and dust.

Most recently, [Richardson et al. \(2025\)](#) modeled the evolution of YSO SEDs as a function of time and accretion history by linking radiative transfer YSO models with protostellar evolutionary tracks. Examining the expected progression of YSOs at $100\text{ }\mu\text{m}$ and 3 mm across multiple accretion histories, they predicted two distinct behavioral phases which are generally characterized by increasing and decreasing flux. Further, they found that their Stage definitions occupied distinct regions of this flux space, with the Stage 0/I dividing line generally separating the two observed phases; as a result, they suggested a probe of Stage based on a YSO's position in this flux space.

4.5 Closing Remarks

The ability to determine the evolutionary state of a YSO is paramount to the study of star formation. I have reviewed the various definitions for separate Stages, which guide thinking about when the boundaries between qualitatively different states occur. I have also provided a census of the techniques and quantities either used or proposed for inference of a YSO's status with a particular focus on Class, the most well-developed and widely used observable.

Class has a long history of use as a probe of YSO evolution. A good deal of early modeling indicated a correspondence between both the infrared spectral index and/or the bolometric temperature of a YSO and its general state, leading to the creation both of conceptual evolutionary stages and divisions in those observables. However, with the complexity achievable in more recent models and the wider theory space for accretion onto protostars, the connection between Class and evolution faces substantive challenges. Class appears to be an uneven tracer of evolution, performing adequately on less extincted sources but often failing to correctly identify or distinguish YSOs in earlier phases. Given the current state of the field, the uncertainties in early-stage star formation (viewing angle, accretion history, age, etc.) are a sizeable confounding factor to using Class as a direct probe. Instead, Class may be better thought of as a tracer of dust

extinction. This inarguably happens more in earlier evolutionary stages, but may emerge from multiple sources (edge-on disks, foreground extinction) and is not a good estimator of the base expected brightness of a protostar, hence uncertainty from accretion history.

The IR colors of a YSO are also sometimes used as an indicator of evolution. The theory behind color as a diagnostic tool is akin to that behind Class, and many surveys and companion works use color as a basis to assign a Class, thereby taking on the baggage of the Class system. However, some works have made an effort to map out how successive evolutionary phases appear in various color spaces. Colors involving mid-infrared emission appear to be good tracers for disks, making it generally possible to distinguish more embedded and less embedded sources in color space, particularly with the use of wavelengths towards the far end of the range ($\sim 25 \mu\text{m}$).

Beyond Class and its derivatives, alternate tracers of evolution have been proposed, but do not appear to have seen widespread use due to recency or necessity for large amounts of data. Some of these tracers are morphological, probing the spatial scale and distribution of gas and dust, while others compare emission either across size scales or wavelengths. These show promise, but have largely not been applied at scale; more development is needed to shape these into useful probes of the state of a YSO.

Given current instruments, data, and modeling ability, the field of star formation appears well poised to evaluate the relationship between the various proposed tracers of evolution and reality. In particular, the hypothesized embedded phase of forming stars appears to remain a source of great uncertainty, and requires a careful approach—likely spanning multiple wavelength regimes and/or size scales—in order to be accurately characterized. A classification system that reliably separates distinct behavioral/qualitative phases of YSOs should be a goal, sought through a combination of multiple independent lines of observational evidence and modeling that factors in the complexities of star formation.

CHAPTER 5

A FRAMEWORK FOR MODELING THE EVOLUTION OF PROTOSTELLAR POPULATIONS

5.1 Motivation

Star formation is a highly complex process, and considerable uncertainties remain within the current theoretical picture. Much of this picture is built on studying individual young stellar objects (YSOs). The modeling infrastructure for YSOs is well-developed, spanning decades of work; consequently, it is possible to extract detailed information from observations and test theoretical predictions against data. However, while it is possible to obtain reasonably complete surveys of YSOs in nearby regions of the Milky Way (e.g. [Dunham et al., 2015](#); [Furlan et al., 2016](#); [Großschedl et al., 2019](#); [Pokhrel et al., 2023](#)), and even to identify candidates in local galaxies with current instrumentation ([Peltonen et al., 2024](#)), a significant amount of visible star formation occurs at distances over which resolution of individual stars is impossible.

Much of the view of star formation is instead limited to populations of forming stars, hereinafter called “protoclusters”. However, the current infrastructure of theoretical modeling is not as developed for protoclusters as it is for individual forming stars. While efforts to model the formation and evolution of protostellar populations have been made using analytic (e.g. [McKee & Offner, 2010](#); [Offner & McKee, 2011](#); [Myers, 2011, 2012, 2014](#)) and numerical (e.g. [Bate, 2009, 2012](#); [Grudić et al., 2021](#)) methods, the quantities that can be directly predicted through these approaches are generally limited to “summary” properties of protoclusters, such as the emergent mass distribution of formed stars—i.e. the stellar initial mass function (IMF)—the luminosity distribution of protocluster constituents, or the dynamics and spatial configurations of forming stars. These summary properties are broad, population-level quantities and are oftentimes theoretical concepts that must be inferred from observational analogues (e.g. the IMF). Consequently, while population models of these types are often used to provide evidence for the importance of particular physics in star formation or the plausibility of particular accretion models, they do not connect directly to observational data.

Forays into protocluster modeling aimed at producing more direct observables are fewer in number. A notable recent example is that of Molinari et al. (2019), which generated a large grid of SED models for protoclusters by combining broadband fluxes from a set of individual YSO radiative-transfer models (Robitaille et al., 2006, 2007) selected by proximity to the masses and ages of cluster constituents sampled from a mass reservoir according to an assumed star formation history (SFH), i.e. the distribution of formation start times across a population. However, the objective of this work is mainly to provide templates for SED fitting of protoclusters; as a result, it limits itself to a fairly narrow range of permissible scenarios, including only a single model for both IMF and SFH. Moreover, the evolution of these protoclusters occurs in the fraction of total cluster mass contained in compact sources rather than the constituents of clusters, whose masses and ages are randomly sampled for each cluster realization, meaning that the models do not evolve self-consistently. Consequently, the theory space spanned by these models is relatively narrow, placing limits on their use as a probe of star formation theory.

In this chapter, I present a newly developed method for simulating protoclusters which is able to directly link theory with observations. This method connects theoretical models for mass accretion onto protostars, the IMF, and a population’s SFH with preexisting radiative transfer YSO models to create protoclusters with continuous and self-consistent evolutionary histories associated with SEDs. The resulting simulated protoclusters predict the evolution of both the physical properties and radiation of the members in a population, effectively acting as a protostellar analogue to simple stellar populations. Consequently, this method for modeling the evolution of protoclusters enables a comprehensive examination of the observational consequences of various aspects of star formation theory and extends the detailed interpretation and measurement of properties possible for individual YSOs to populations of forming stars. In Chapter 5.2, I outline this protocluster simulation framework and detail the theory space spanned by each of the components. Chapter 5.3 presents initial predictions from simulated clusters and illustrates how the underlying theoretical components affect the resulting evolution of summary properties and observables. I make concluding remarks in Chapter 5.4.

5.2 Cluster Construction

In this section, I outline my procedure for modeling protostellar populations and discuss the theory space spanned by the components of the framework.

5.2.1 Procedure

Each cluster begins with a set of final stellar masses sampled from a mass function, which is taken to be one of several forms for the stellar IMF. Masses are drawn from the IMF until a provided final cluster mass is reached; this threshold (M_{cl}) is a variable parameter in cluster construction. I use the `imf` python package¹ to construct and sample from mass functions. Section 5.2.2.1 provides further detail on the mechanics of sampling and the adopted mass functions.

Once the final masses of cluster members are determined, I use these masses to construct corresponding models of evolving YSOs. In order to make this process efficient, I precompute template models corresponding to a set of final stellar masses, $m_{\text{final}} \in (0.2, 0.4, 0.6, 0.8, 1, 2, 3, 4, 5, 6, 7, 8, 10, 12, 14, 16, 20, 24, 28, 32, 40, 48, 56, 64, 80, 100, 120 M_{\odot})$, and interpolate between these. I do not construct YSO models for stars with final masses outside of this range, on the grounds that less massive stars will contribute very little to the observed radiation (and are often below the completeness limit of observational surveys), while more massive stars are extremely rare. I employ the YSO modeling framework developed in Richardson et al. (2025, R25) to construct these templates (this is the subject of Chapter 3). The base function of this framework is to simulate the evolution of YSOs by linking radiative transfer YSO SED models from a formation-agnostic set (Richardson et al., 2024, R24) with protostellar evolutionary histories generated by a modified Klassen et al. (2012) code which produce a star of a given final mass. (Here, as in R25, I adopt the convention that a “YSO” refers to the combined system of luminosity source and circumstellar dust while a “protostar” is only the former.) This link is made by identifying radiative transfer models with similar source temperatures (T_{\star}), total protostellar luminosities² (L_{\star}), and envelope masses (M_{env}) as the ones predicted by a given protostellar

1 <https://github.com/keflavich/imf>

2 “Total” includes the intrinsic luminosity of the protostar as well as luminosity from accretion.

evolutionary model, and predicting the SED of the evolving YSO by averaging over the SEDs of a set of these nearest-neighbor radiative transfer models. The resulting models track the evolution of a YSO’s SED, beginning at the time that a protostar forms and spanning the time in which the protostar is actively accreting, in addition to that of traditionally observed summary properties such as bolometric temperature. Employing this framework to model cluster constituents therefore allows direct comparison between the radiation from a protostellar population with model-predicted observables across a wide theory space. The SEDs of these simulated YSOs are inclination-dependent; each cluster member is assigned a viewing inclination between 0° (face-on) and 90° (edge-on). I provide an overview of the SED models and implemented histories in Sections 5.2.2.2 and 5.2.2.3, respectively, while a fuller description of my approach to YSO model construction is contained in Chapter 3.2.

R25 links protostellar evolutionary models and radiative transfer models by mapping the mass of a protostar (tracked by protostellar evolution) to the mass contained in an envelope around the star (tracked by the R24 models). This mapping is performed by assuming an efficiency of mass accretion onto a protostar, ϵ_{SF} , such that $M_{\star, \text{final}} = \epsilon_{\text{SF}} \times M_{\text{core, initial}}$; as a result, the mass of the envelope evolves as $M_{\text{core}}(t) = M_{\text{core, initial}} - M_{\star}(t)/\epsilon_{\text{SF}}$. In this work, I consider ϵ_{SF} s of 1/3 and 1. 1/3 is a commonly adopted value for ϵ_{SF} , based on the observed relationship between the masses of cores and stars (e.g. Motte et al., 1998; Alves et al., 2007; Nutter & Ward-Thompson, 2007; André et al., 2010), while an efficiency of 1 is intended to capture scenarios with external infall, where the protostellar envelope is replenished by mass from outside the system (e.g. Fischer et al., 2017). A wide range of values has been used in modeling across the literature, including efficiencies that vary with mass (e.g. Duarte-Cabral et al., 2013; Zhang & Tan, 2018); for the purposes of this work, I limit to a small sample of values which are emblematic of distinct theoretical paradigms (though I leave open the possibility of considering more values in the future).

Once the evolution of each YSO in the protostellar population is modeled, I impose boundary conditions on each track corresponding to the time immediately prior to and following

accretion, which R25 does not model. Prior to accretion, I model each constituent as a Bonnor-Ebert sphere. Properties of the sphere (mass, size, density profile) are determined by assuming they form in a cloud with total mass $M_{\text{cl}}/\epsilon_{\text{SF}}$ and radius 1 pc, allowing P_s/k_B to be set for the sphere using the average gas pressure within the cloud. I assume these spheres emit as modified blackbodies at temperature of 10 K, calculating their optical depth using the profile of average surface density $\bar{\Sigma}(R)$ and the dust opacity used in the R24 model set (see §5.2.2.2). Immediately after accretion, each constituent is modeled as a blackbody at the source temperature predicted by the evolutionary model at the end of accretion.

Finally, in order to be able to model scenarios where formation of an observed population does not begin all at once, I assign each population member an age following an assumed history of star formation. Each YSO model is generated with an accompanying timeline, with $t = 0$ corresponding to the beginning of collapse of the second hydrostatic core. Time is then added to each YSO’s timeline according to the implemented history. Section 5.2.2.5 provides additional details on the available histories.

5.2.2 Components

In this section, I discuss each of the theoretical components included in my procedure for modeling protoclusters, in addition to the range of theories and values implemented into the modeling framework. Table 5-1 provides a general overview of these components; more details on each are presented in the following subsections.

5.2.2.1 Mass function

Multiple forms of the stellar IMF have been developed based on measurements performed on populations within the Milky Way. I implement the power-law IMF of Salpeter (1955), the broken power law of Kroupa (2001), and the log-normal + power law of Chabrier (2003), which are the most used functional forms across the literature. For each mass function, I adopt a possible stellar mass range of 0.03-120 M_\odot in order to capture a range representative of MW populations (though YSO models resulting in stars below 0.2 M_\odot are not created; see Chapter 5.2.1). In addition to the canonical shape for each IMF, I also consider power-law (Salpeter-like) IMFs with $\alpha \in (1.75, 2, 3)$

Table 5-1. Overview of the components of my protostellar population modeling framework.

Component	Implementations	Comments
Mass function	Salpeter (1955) ^a , Kroupa (2001), Chabrier (2003)	$m_l = 0.03, m_u = 120 M_\odot$
SED models	Richardson et al. (2024)	Extends Robitaille (2017)
Accretion history	IS, TC, CA, Exp. taper ^b	M10 histories also tapered
Scaling parameters	$T_{\text{dust}} = 10 \text{ K}, \Sigma_{\text{cl}} = 0.1 \text{ g cm}^{-2}$, $\bar{n}_H = 10^4 \text{ cm}^{-3}, \tau = 1.3 \times 10^5$ yr	Fiducial values for respective histories
Mass accretion efficiency (ϵ_{SF})	1/3, 1	–
Multiple systems	f_b from Offner et al. (2023) Table 1 multiplicity fractions	Modeled as two equal-mass stars; $m_{\text{tot, min}} = 0.4 M_\odot$
Star formation history	Constant (“constant”), Normally distributed start (“normalstart”), Normally distributed end (“normalend”)	$t_{\text{SF}}, t_\sigma \in (0.1, 1, 10) \text{ Myr}$

a Salpeter power-law slope $\alpha \in (1.75, 2, 2.35, 3)$.

b Exp. taper from Duarte-Cabral et al. (2013), all else from McKee & Offner (2010).

akin to the values measured in some starburst clusters (e.g. Lu et al., 2013; Schneider et al., 2018) and across galaxies with varying star formation rates and of various types (e.g. Gunawardhana et al., 2011; Conroy & van Dokkum, 2012) in order to capture scenarios in which the IMF varies.

Stars are sampled from a mass function until the mass threshold M_{tot} is reached; however, since a randomly sampled population will likely not meet this threshold exactly, the treatment of that mass limit can have significant impacts on a resulting population (e.g. Weidner & Kroupa, 2006; Haas & Anders, 2010; da Silva et al., 2012; Cerviño et al., 2013; Popescu & Hanson, 2014), particularly for the high-mass end. The implementation of sampling therefore has a consequential impact on the total radiation from a population, particularly in cases where the available mass is small ($\lesssim 10^4 M_\odot$). Krumholz et al. (2015) explores this effect in more detail and implements a number of sampling “stop criteria” determining which stars drawn from an IMF are included in a simulated population. `imf`, the software used to perform sampling, implements a subset of these criteria. In brief, the ones used in this work are:

- “nearest”: Include the final draw from an IMF only if it decreases the absolute difference from the target mass.

- “before”: Never include the final draw.
- “after”: Always include the final draw.
- “sorted”: Draw $M_{\text{rem}} / \langle M \rangle$ stars from an IMF (where M_{rem} is $M_{\text{tot}} - M_{\text{pop, current}}$, the total remaining mass not contained in sampled stars, and $\langle M \rangle$ is the IMF’s mass-weighted average) repeatedly until original cluster mass is exceeded, then include or exclude the most massive star based on the “nearest” criterion.

It also implements the “optimal sampling” method of [Kroupa et al. \(2013\)](#), which draws from an IMF in such a way as to perfectly reproduce its shape regardless of total available mass; I also include this method. Some draws are treated as multiple systems; Section [5.2.2.4](#) provides additional details.

5.2.2.2 SED models

All YSO models are based on the set of radiative transfer SED models from R24 (i.e. Chapter [2](#)), which is an updated version of [Robitaille \(2017\)](#). This section is a brief review of the aspects of the model set relevant to this paper; more detail is presented in the companion works.

The R24 model set is composed of several subsets, hereinafter “geometries”, defined by the inclusion of circumstellar dust density structures including envelopes, disks, bipolar cavities, and ambient media. Each of these structures has an associated set of parameters that determine its shape and density profile (e.g. disk scale height, cavity opening angle). All models in a geometry exhibit the same combination of these features; however, the values of the shape parameters for each model are randomly sampled. Details on the available model geometries and shape parameters are contained in Tables 1 and 2 of [Robitaille \(2017\)](#). YSO models in this work are constructed using all geometries with circumstellar envelopes, as in R25, since the primary intent is to portray actively accreting protostars.

Each model in R24 has an SED modeling dust continuum emission, created through the use of the Monte Carlo radiative transfer code Hyperion ([Robitaille, 2011](#)). The SEDs are given as flux densities (i.e. S_ν) in units of mJy. They are calculated over the wavelength range of 0.01-5000 μm within a series of circular apertures that have radii evenly log-spaced between 10^2 - 10^6 au. All

dust in R24 is a model from [Draine \(2003a,b, D03\)](#) with the [Weingartner & Draine \(2001\)](#) Milky Way grain size distribution A for $R_V = 5.5$ and carbon abundance C/H renormalized to 42.6 ppm.

R24 models in geometries that introduce a θ dependence into their dust density profiles (i.e. those with disks, cavities, or flattened envelopes) have SEDs with nine lines of sight randomly sampled from ten-degree bins from 0° - 90° . Models with no θ dependence have only one SED, since they are spherically symmetric and look the same along every sightline. Because the SEDs of the YSO models are averages of models from multiple geometries (see R25), many of which are θ -dependent, this inclination dependence is retained in the YSO models, averaging models separately within each inclination bin. Models with only one SED contribute that SED to each bin.

R24 also calculates the circumstellar mass for each source within spherical regions of the same radii as the SEDs, assuming a gas-to-dust ratio of 100 to derive a total material mass from the native dust density profiles. This mass is used to identify which R24 models are representative of YSOs following a particular evolutionary history; see Chapter [5.2.1](#) and R25 for more detail.

5.2.2.3 Accretion

The impact of accretion on protostellar populations is modeled through the evolutionary histories of their constituent YSOs. These histories are created through the use of a modified version of code from [Klassen et al. \(2012\)](#), which simulates the evolution of protostars following the prescription of [Offner et al. \(2009\)](#). This code connects the evolution of a protostar's accretion rate with that of its intrinsic properties (mass, radius, luminosity, etc.) from the initiation of collapse to arrival on the main sequence. I use this code to generate evolutionary tracks for protostars following several models for accretion, which are discussed in the following paragraphs. I illustrate the predicted evolution of accretion rate for a solar-mass star according to every implemented model in Figure [5-1](#).

The YSO models created for R25 followed three implemented accretion histories: isothermal-sphere (IS, [Shu, 1977](#)), turbulent-core (TC, [McKee & Tan, 2002, 2003](#)) and competitive (CA, [Bonnell et al., 1997, 2001](#)) accretion histories. Each of these were modeled according to prescriptions for accretion rates laid out in [McKee & Offner \(2010, M10\)](#), which all

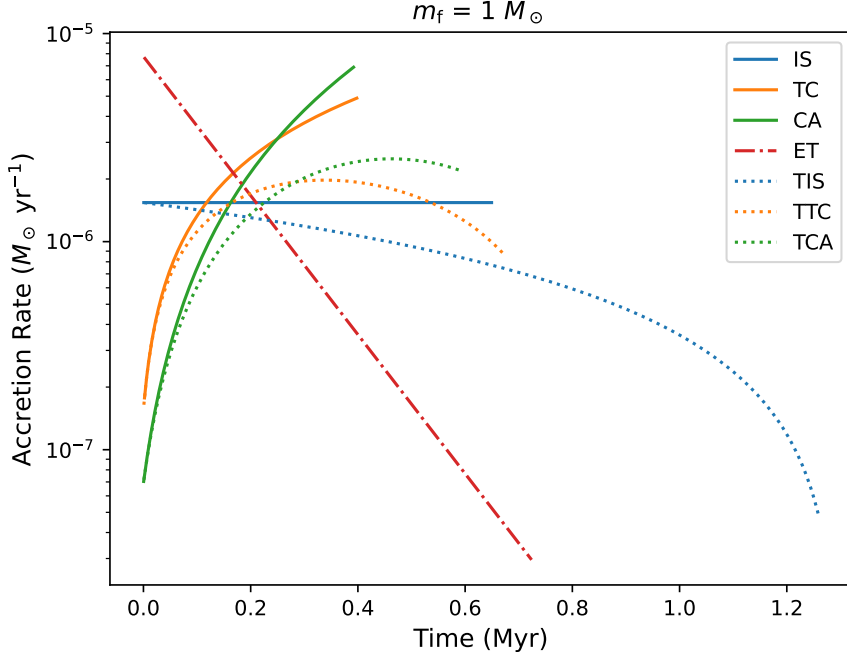


Figure 5-1. Accretion rates for a $1 M_{\odot}$ star as a function of time for each of the modeled histories. Isothermal-sphere (IS), turbulent-core (TC), and competitive (CA) accretion are the same as in R25; I also include tapered versions of each (models with a leading ‘T’) and an exponentially tapered accretion model (‘ET’).

had the general form:

$$\dot{m} = \dot{m}_1 \left(\frac{m}{m_f} \right)^j m_f^{j_f} \quad (5-1)$$

for final stellar mass m_f , real-valued exponents j and j_f which vary with accretion history, and final accretion rate for a star of unit mass \dot{m}_1 . This last is set through a scaling parameter, which is a physical quantity important within the wider theory surrounding the accretion rate. In M10, these parameters were gas temperature T , gas clump surface density Σ_{cl} , and average number density of hydrogen atoms across a cloud \bar{n}_{H} for IS, TC, and CA respectively. In R25, these parameters were held invariant at their respective fiducial values of 10 K, 0.1 g cm^{-2} , and 10^4 cm^{-3} ; I continue to do so here. Variation of each scaling parameter is expected to change the timescale of accretion and to influence flux predictions at wavelengths sensitive to accretion (e.g. FIR wavelengths: Fischer et al., 2024), but quantifying the magnitude of this effect is beyond this work.

In addition to including the accretion histories modeled for R25, I have implemented new histories within this framework. R25 primarily dealt with simple models representing distinct theoretical paradigms for accretion, with the goal of establishing a procedure for creating evolving YSO models able to accommodate the many physical scenarios developed to explain the formation of stars. However, none of the implemented models exhibited decreasing (i.e. tapered) accretion rates, which have significant supporting evidence (e.g. [Dunham & Vorobyov, 2012](#); [Duarte-Cabral et al., 2013](#); [Fischer et al., 2017](#); [Sheehan et al., 2022](#)).

I have implemented several prescriptions for tapered accretion into my framework for population modeling. M10 prescribes tapering through the application of a tapering factor $[1 - (t/t_f)^n]$ to the existing accretion rate. t_f is the time where a protostar reaches its final mass, given by:

$$t_f = \left(\frac{n+1}{n} \right) \frac{m_f^{1-j_f}}{(1-j)\dot{m}_1} \quad (5-2)$$

Tapered versions of IS, TC, and CA are created following this roadmap. As in M10, I limit consideration to the $n = 1$ case. My treatment of these histories is otherwise unchanged, i.e. the same array of scaling parameters is retained. Furthermore, I implement the exponentially tapered (ET) accretion rate of [Bontemps et al. \(1996\)](#) as treated by [Duarte-Cabral et al. \(2013\)](#):

$$\dot{m}_\star = \epsilon_{SF} \times \left(\frac{M_{\text{core}}}{\tau} \right) e^{-t/\tau}. \quad (5-3)$$

The accretion rate of this model is tuned such that 90% of a star's final mass is accreted in 3×10^5 yr, which places τ at $\sim 1.3 \times 10^5$ yr. The resulting total accretion timescale is roughly 0.7 Myr.

I note that each of the implemented histories prescribes steady-state accretion, while observations of YSOs indicate that accretion is variable over a wide range of time scales and is often episodic ([Fischer et al., 2023](#)). However, modeling variable accretion is beyond the scope of this work; doing so would likely require either translating observed variability into a parameterized form (extending the approach of [Duarte-Cabral et al., 2013](#)) or deriving “realistic”

accretion histories from MHD simulations (c.f. [Dunham & Vorobyov, 2012](#)), both of which are nontrivial tasks.

I also note that due to this treatment of accretion and mass accretion efficiency (see §[5.2.1](#)), many of the assumed histories create a scenario in which accretion onto a star within a star + core system remains constant or accelerates despite a decrease in the total system mass (due to outflows, radiation pressure, dynamic interactions, etc.). This is unphysical for cases where accretion is primarily driven by gravitational collapse (i.e. is IS-like) and a protostar's mass reservoir is not replenished by external infall, as decreasing mass leads to a decreasing free-fall time and hence a decreasing accretion rate. Some models of evolving YSOs created and employed in this work are consequently inconsistent with current understanding of star formation. This work implements a number of histories exhibiting decreasing accretion rates in addition to these scenarios. Moreover, accelerating accretion within a single core is explicitly modeled by some theories (e.g. TC), making it a necessary inclusion in order to capture the full theory space.

5.2.2.4 Multiple systems

In Section [5.2.2.1](#), masses sampled from the IMF are initially treated as individual stars. However, stars are capable of forming in multiple stellar systems, and observational evidence indicates that such occurrences grow increasingly common as the mass of a star increases ([Moe & Di Stefano, 2017](#); [Offner et al., 2023](#)). I factor the presence of multiple systems into the populations by treating some draws from the IMF as the total stellar mass of an equal-mass binary. In doing so, I model cases where both constituents of a binary system contribute to observed radiation, as opposed to cases where the primary star dominates, which can be approximated by single-star modeling. (I limit consideration to binaries for the sake of simplicity, since they make up the majority of multiple systems regardless of mass.) Each draw has a probability of $f_b(m_{\text{draw}})$ to be converted, where $f_b(m)$ is the fraction of formed stars with mass m in binaries. f_b comes from the multiplicity fractions of Table 1 in [Offner et al. \(2023\)](#). As computed, these fractions refer to all multiple systems, rather than solely equal-mass binaries. For the purposes of this work, I do not make this distinction, i.e. all multiple systems are equal-mass binaries. My treatment of

multiple systems is therefore an extreme case: more systems with members of comparable mass are created than would likely be expected in observation. However, quantifying the degree to which this is true is a nontrivial problem which is beyond this work.

To model these systems, I have constructed an additional set of binary “evolutionary track” templates which are versions of the single-protostar tracks with altered T and L values¹. I make the simplifying assumption that both members of the binary grow at the same rate, meaning that mass accreted from the envelope is evenly split between the members, which exhibit identical temperatures and radii as they evolve. The resulting binary source is taken to have the same temperature and twice the intrinsic luminosity of a protostar which grows to half the total final mass of the binary following the same accretion history. The luminosity originating from accretion onto the luminosity source is held to be the same as in the single-star case, since the amount of material being accreted does not change. Once this set of template evolutionary tracks is constructed, I construct template flux tracks for each as described in Chapter 5.2.1 and interpolate between these binary flux tracks for sources chosen to be binaries as in the single-star case. In keeping with the lower mass limit used for modeling single stars, the lowest-mass binary template corresponds to a total final mass of $0.4 M_{\odot}$. While multiple systems occur below this point (e.g. [Fontanive et al., 2018](#); [Winters et al., 2019](#)), I do not model them on similar grounds as low-mass stars, i.e. their contribution to observed radiation is expected to be minimal.

I compare YSOs with single-star and binary sources in Figure 5-2, recreating the $100 \mu\text{m}/3 \text{ mm}$ flux plots of R25. The impact of binary conversion on modeled YSOs manifests as lower flux, driven by a reduction in the luminosity of the source. This fall-off in luminosity for binary sources relative to single sources with the same total mass is in line with expected behavior, given the strong dependence of main-sequence stellar luminosity on mass ($L \propto M^{3.5}$). This effect is expected to be more pronounced at wavelengths sensitive to the properties of the central source; in Figure 5-2, it is primarily contained to the submillimeter regime, which is closely tied to

¹ I note that the radii, stages, and polytrope numbers from the original tracks are not changed, meaning that they are unrepresentative of the modeled binary source.

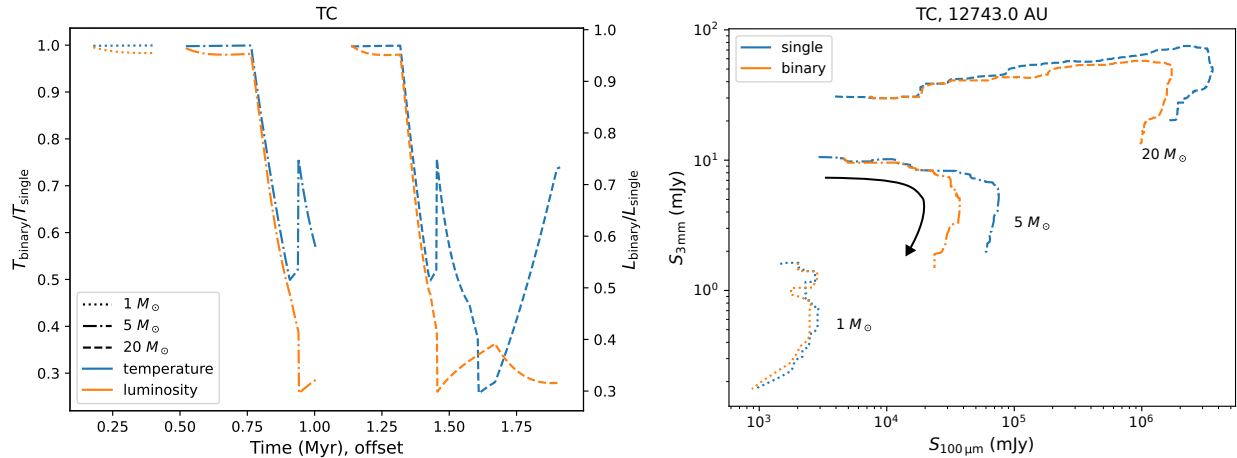


Figure 5-2. Left: Ratios of the temperatures and luminosities of binary to single-star sources for systems with final masses 1 (*left*), 5 (*middle*), and 20 (*right*) M_{\odot} , according to a turbulent-core accretion history. Single tracks are generated using a modified [Klassen et al. \(2012\)](#) code; these tracks are then modified to produce the binary tracks as outlined in Section 5.2.2.4. The scale of time is consistent for each set of tracks, but start times have been offset for display purposes. **Right:** Evolution of modeled YSOs with final system masses of 1(*dotted*), 5 (*dash-dotted*), and 20 (*dashed*) M_{\odot} in the 100- $\mu\text{m}/3\text{-mm}$ flux space, as in Figure 3 of R25. The direction of travel is indicated by an arrow. The left edge of each track corresponds to the time at which each YSO develops a protostellar source, i.e. the transition between protostellar Stages 0 and 1 from [Klassen et al. \(2012\)](#); this time is different for single and binary systems, with binaries typically starting later. (Note that these Stages are distinct from a YSO's Stages 0 and I, which deal with YSO system properties rather than solely protostellar ones.)

protostellar luminosity (as seen in [Fischer et al. \(2024\)](#), although here the intrinsic luminosity of the sources is effectively varied, instead of the luminosity from accretion).

However, the observed reduction in flux is muted for lower-mass YSOs. This apparent mass dependence emerges from the behavior of the central sources. Most luminosity and temperature evolution occurs after deuterium burning begins, and the more massive the star, the earlier this point occurs when compared to the timescale of accretion. Consequently, the central sources of low-mass stellar systems, which accrete most of their mass prior to deuterium ignition, do not have the opportunity to diverge within the time frame modeled by R25. It can also be muted by circumstellar dust; the flux reduction in high-mass stars begins near the “knee” features in Figure 5-2, which I hypothesize to be similar to the “envelope clean-up” phase ([Molinari et al., 2008](#);

[Elia et al., 2010](#)). (This also roughly corresponds to the beginning of a YSO’s Stage I as defined by R25, which incorporated the [Fischer et al. \(2017\)](#) Stage 0/I dividing line when half the mass of the central source is assembled.) On the whole, the impact of modeling multiple systems on the simulated populations is likely to be felt most strongly in the fluxes of massive and bright systems at later times in their evolution, with minimal impact to the lower-mass constituents.

Beyond the impact on predicted flux, creating binaries necessarily requires changing the final masses of stars in a simulated population from those drawn from the IMF; hence, the stellar IMF of the emerging population can be expected to diverge from the “system” IMF created through the draws. Since one of the objectives of this work is to be able to probe the IMF through comparison to simulated populations, an understanding of the relationship between the stellar and system IMF is required. To quantify this, I construct system IMFs with a total mass of $5000 M_{\odot}$ for each of the implemented forms (Table 5-1, §5.2.2.1), perform binary conversions, and fit a power law to the resulting stellar population within the mass range of the initial IMF’s power law tail. This tail covers the entire Salpeter IMF, anything above $0.5 M_{\odot}$ for Kroupa, and anything above $1 M_{\odot}$ for Chabrier. (Any members of the resulting population below the IMF lower mass limit of $0.03 M_{\odot}$ are excluded from the fit, on the grounds that they are no longer stars.) My implementation of binary conversion is stochastic in nature; to reduce noise, the system IMFs are optimally sampled, i.e. they perfectly reproduce the underlying distributions, and 1000 conversions are done for each system IMF. I perform fitting using the `powerlaw` python package² ([Alstott et al., 2014](#)), which implements the statistical fitting methods derived in [Clauset et al. \(2009\)](#) and [Klaus et al. \(2011\)](#).

I show the results of the fits in Figure 5-3. As expected, binary conversion alters the shape of the stellar IMF, shifting stellar masses towards its low-mass end. The high-mass slope of the stellar IMF is consistently steeper than that of the system IMF for all of the modeled functional forms, becoming more so as the starting mass for the tail increases. However, the average difference between system and stellar IMF is well within the error of all but the most precise

² <https://github.com/jeffalstott/powerlaw>

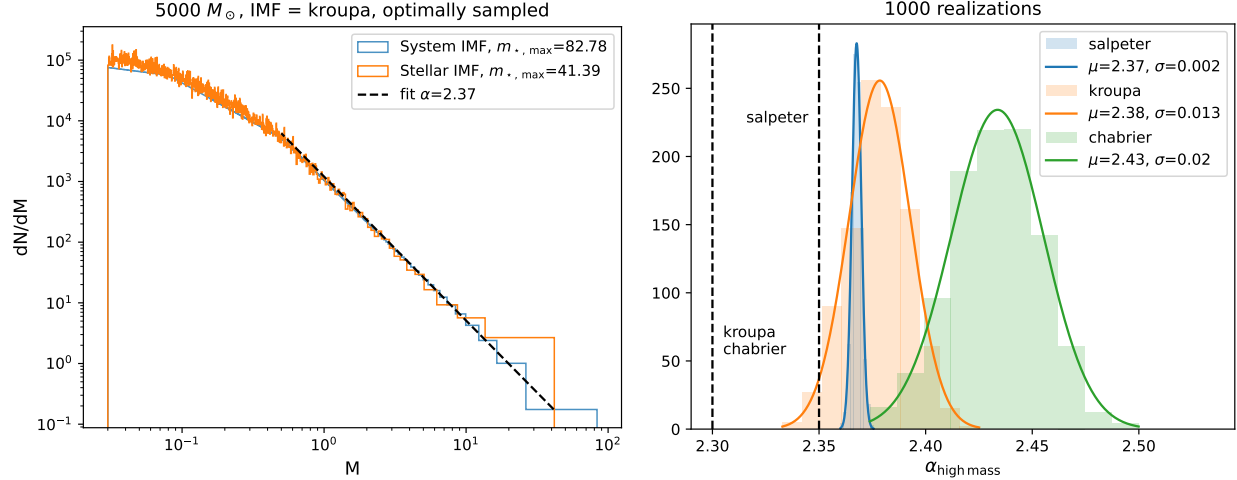


Figure 5-3. **Left:** A comparison between a system IMF and a stellar IMF after some draws have been converted to binaries following my procedure. I fit a power law to the high-mass tail of the stellar IMF, which starts at $0.5 M_{\odot}$. **Right:** The distributions of exponents for power laws fit to the high-mass tails of stellar IMFs emerging from performing 1000 binary conversions on each of the implemented system IMFs. I fit Gaussian distributions to each. I also plot the locations of the exponents for the system IMFs (*black, dashed*) for reference.

measurements (e.g. [Weisz et al., 2015](#)), implying that the impact of multiple systems on the shape of the underlying mass function is fairly minimal in practice.

5.2.2.5 Star formation history

In order to track the ages of population members, I sample a start time for each from a distribution representing a particular history of star formation. I implement three star formation history models into the simulated populations. The first of these is a history of constant stellar birth, similar to the models of [Myers \(2011, 2012, 2014\)](#). I treat this similarly to [Molinari et al. \(2019\)](#) by randomly drawing start times from a uniform distribution between 0 and t_{SF} , where t_{SF} is the time elapsed since the beginning of star formation. The remaining two histories are ones where the majority of stars either start or finish accreting at roughly the same time; these can capture scenarios where star formation is triggered by a single event or when a population exhausts its mass reservoir. These models draw their start or end times from a Gaussian distribution with a $1-\sigma$ width of t_{σ} . Both t_{SF} and t_{σ} are allowed to vary within (0.1, 1, 10 Myr) in order to capture a wide array of measured formation timescales, from the near-instantaneous

formation of [Kudryavtseva et al. \(2012\)](#) to the few-Myr timescale of [Palla & Stahler \(2000\)](#) to observed ~ 10 Myr age spreads ([Smith et al., 2010](#); [De Marchi et al., 2011](#)).

Beyond the implemented histories, I also provide the option to create a custom history for a simulated population by manually inputting a set of start times.

5.2.2.6 Unmodeled processes

The protocluster models created for this work implement a number of additions designed to bring the simulated populations in line with current understanding of star formation theory, in addition to allowing for cross-theory testing. However, I do not currently include prescriptions for an intra-cluster medium or the spatial position of stars within a population, which are considered in other works. For example, [Molinari et al. \(2019\)](#) assign each YSO in their simulated populations a 3D position within a star-forming clump, determined through a random draw from a power-law density profile. The addition of dust is expected to introduce extinction to the emission of YSOs within a cluster. However, such extinction is likely to be on average degenerate with additional interstellar extinction (and can therefore be compensated for in such a manner); the magnitude of this extinction will also likely be secondary to that from dust within a YSO for deeply embedded members.

Furthermore, as a consequence of a lack of spatial positioning, I do not model mass segregation within the populations. The degree of mass segregation within star clusters has fairly large ramifications for how they are expected to form and evolve ([Portegies Zwart et al., 2010](#)), and evidence (including recent observations and modeling, e.g. [Plunkett et al., 2018](#); [Pavlík et al., 2019](#)) indicates that segregation may be seeded early in the process of collapse. However, most work done so far has focused on the dynamics and spatial distributions of forming stars. Quantifying the impact of mass segregation on the expected emission from a star-forming cluster is a separate question which is out of scope for this work, although I leave open the possibility of a return to this question with these tools.

5.3 Model Populations

I have created an infrastructure for synthesizing populations of forming stars capable of simulating their evolution according to several modeled prescriptions for mass accretion and histories of star formation. In this section, I turn to characterizing the ways in which these aspects of the simulated protoclusters alter the expected evolution of various observation and theoretical quantities.

To provide a basis for comparison, I generate a set of sample protoclusters following each of the implemented accretion histories (see §5.2.2.3). Figure 5-4 illustrates the kind of information that can be extracted from the simulations; this spans the physical properties of the constituents (e.g. mass, luminosity) and the expected flux across the wavelength range of the model SEDs (see §5.2.2.2). Within the figure, I show predicted fluxes at 4 μm , 21 μm , and 1 mm; these wavelengths occur within parts of the near/mid-infrared and radio regimes accessible with current-generation instruments and are commonly used as probes of the dust around forming stars. Throughout the remainder of this section, I use the 1-mm fluxes as the primary vehicle for comparison, as the modeling procedure of R25 exhibits better performance at long wavelengths (see §3.2 of that work for further discussion). All flux values are calculated at a distance of 1 kpc. Each protocluster has M_{cl} (i.e. final stellar mass) = $1000M_{\odot}$; members are optimally sampled from a Kroupa IMF. The emerging system IMF is therefore the same for each cluster, although binary conversion is performed for each independently (see §5.2.2.4), meaning that the luminosities of members with the same system mass may differ. I assume an ϵ_{SF} of 1/3.

5.3.1 Accretion History

In order to assess the impact of accretion history on the simulations, I compare the quantities shown in Figure 5-4 across accretion histories. By default, all members in a protocluster begin accreting at the same time; this is held true here to avoid confusion between accretion history and SFH, but varies in Section 5.3.2.

In Figure 5-5, I compare the cumulative distribution functions (CDFs) of protostellar masses and luminosities created by the implemented accretion histories. As in my YSO construction

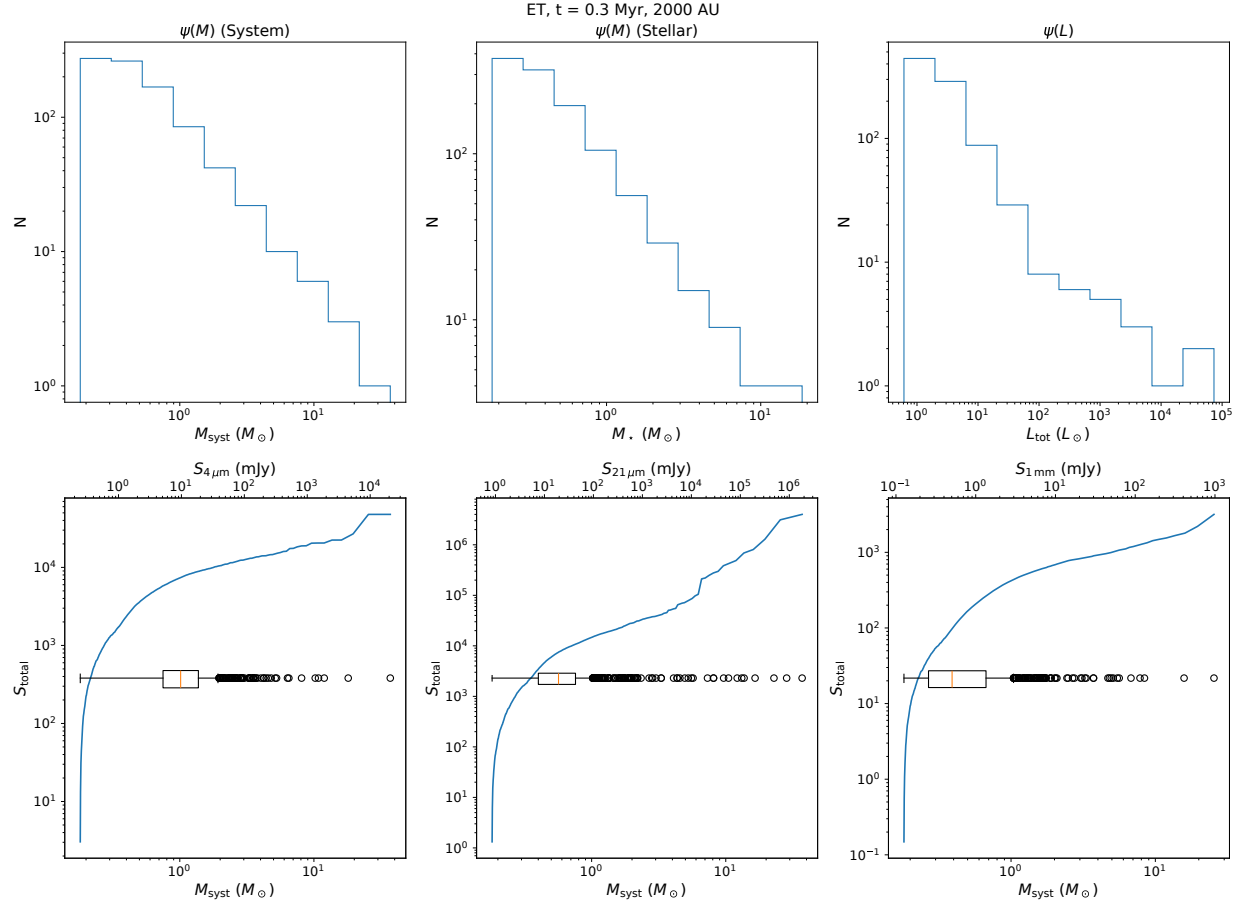


Figure 5-4. Output from a simulated protocluster. **Top row:** The distributions of protostellar masses (left, middle) and luminosities (textit{right}). **Bottom row:** Box plots showing the fluxes predicted for protocluster members at $4 \mu\text{m}$, $21 \mu\text{m}$, and 1mm . The cumulative flux at each wavelength as a function of protostellar mass is shown in blue. All values are sampled from a protocluster generated according to an exponentially tapered accretion history at $t = 0.25 \text{ Myr}$. Flux values are calculated within an aperture with a physical radius of 2000 au . All other cluster properties are as described in Chapter 5.3.

procedure (see §5.2.1 and R25), both mass and luminosity are total system values, i.e. mass includes both members of binary systems and luminosity includes both intrinsic and accretion-driven components. I sample each cluster at both 0.1 and 0.5 Myr; this is roughly in line with the timescale on which accretion meaningfully varies for the histories which prescribe variable accretion.

It is apparent that the assumed accretion history has pronounced impacts on the expected evolution of the mass distribution of protostars, particularly early in the process of mass assembly. The rapid early growth of protostars following an ET history results in a mass CDF with both a higher mean value (reaching its halfway point by $\sim 0.3 M_{\odot}$, the highest of the modeled histories) and a rightward-shifted value range relative to the constant-rate or accelerating histories at 0.1 Myr (i.e. shortly after beginning accretion). This is particularly true at the high-mass end; the highest-mass system in an ET scenario has already attained a mass of $\sim 20 M_{\odot}$, as opposed to the $\sim 2 M_{\odot}$ maximum for CA-like accretion, which is the next most massive. The shape of the ET mass CDF is similar at 0.1 and 0.5 Myr, with the main difference being a slight rightward shift as most of the remaining mass is accreted. TC and CA, by contrast, model accelerating accretion; as a result, protostars following these histories do the majority of their mass assembly towards the end of their accretion time. Consequently, their CDFs are comparatively skewed towards lower masses across the board, particularly at 0.1 Myr, when their CDFs also exhibit a steeper rise at lower masses than ET accretion. In addition, TC exhibits a narrower range of masses than CA at both times. Due to the varying rates of acceleration and levels of mass dependence in their implementations, lower-mass stars accrete faster and higher-mass stars accrete slower following TC histories compared to CA. At 0.1 Myr, this results in a narrower CDF on both ends for the TC cluster than the CA cluster, while at 0.5 Myr, the high-mass end of the TC CDF is lower than CA and ET, as the highest-mass TC systems have not yet finished accreting. (The timescale for CA following my implementation is ~ 0.4 Myr with the adopted scaling parameters; see Table 5-1.) By contrast to every variable-rate history, constant-rate (IS) accretion exhibits minimal spread in mass, as expected given that every protostar is modeled as accreting at the same rate regardless of

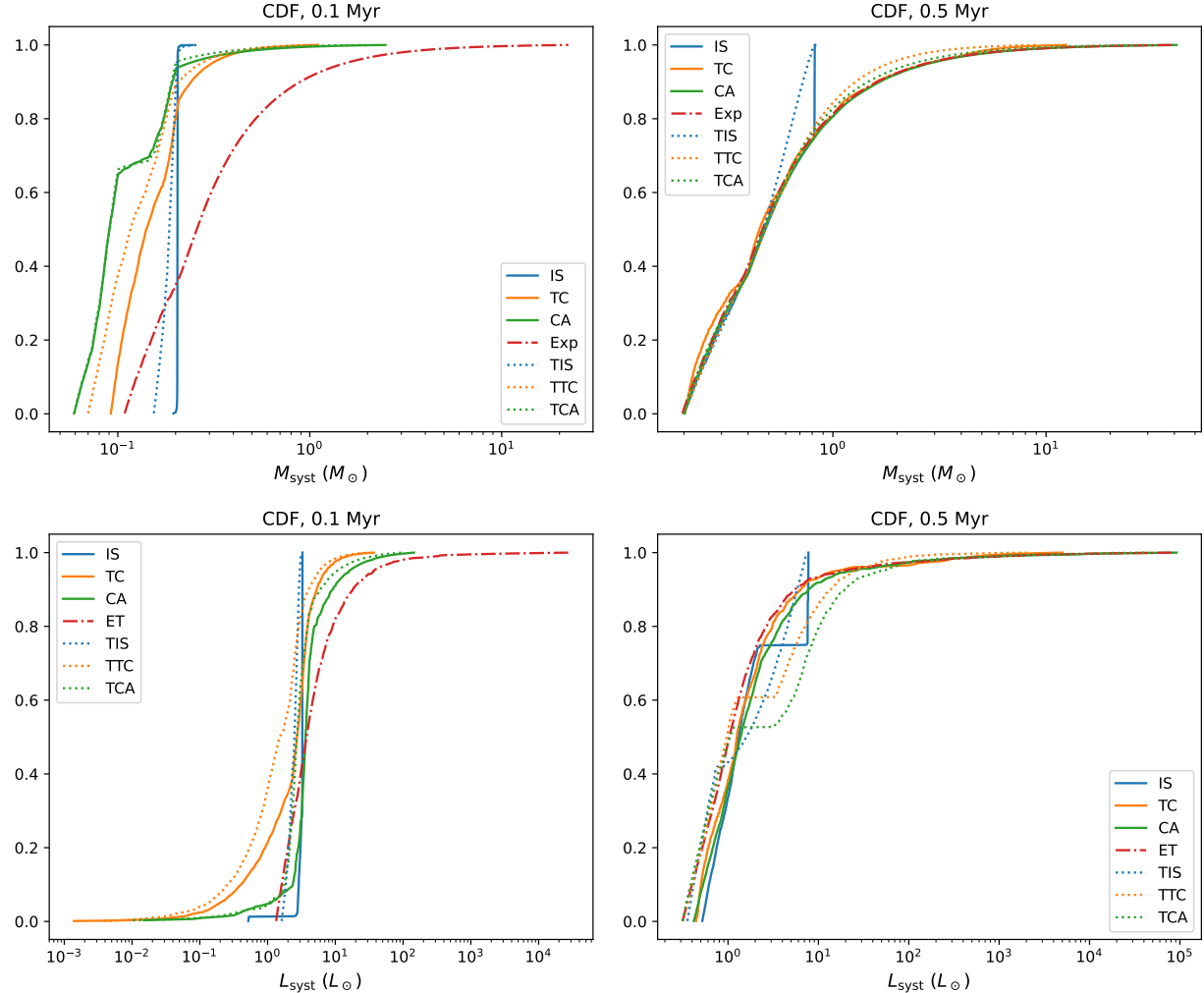


Figure 5-5. Cumulative distribution functions for the instantaneous protostellar masses (*top*) and luminosities (*bottom*) of YSOs in simulated protoclusters. Values are sampled at both 0.1 (*left*) and 0.5 (*right*) Myr. Cluster properties are described in §5.3.

mass. The CDF exhibits a sharp cutoff, marking the maximum possible mass attainable by an IS protostar by a given time according to the accretion model. The tapered versions of IS, TC, and CA generally behave very similarly to their un-tapered counterparts.

The general trends present in the evolution of protostellar masses also occur when examining their luminosities. ET protostars exhibit quick increases in luminosity driven by rapid accretion, making the population significantly more luminous at early times than clusters following other histories. Meanwhile, the accelerating-rate histories begin at very low luminosities given their initial low accretion rates, but grow to match the ET distribution as time progresses. The constant accretion rate of IS protostars sets a luminosity floor of $\sim 3 L_\odot$ while accreting, resulting in a very concentrated CDF that gradually spreads as time passes. The main difference in behavior between mass and luminosity results from the fact that as accretion shuts off, the total system luminosity decreases, resulting in “jumps” in the CDF for low-mass systems where accretion dominates the total luminosity. Some of these jumps are visible at 0.5 Myr for the tapered TC and CA CDFs and in the IS CDF at both sample times.

I repeat this comparison for more directly observational metrics in Figure 5-6, extracting the distributions of predicted 1-millimeter flux densities at the same times. Cluster members are included in a distributions if they exhibit a flux greater than $\sim 10^{-2}$ mJy, roughly corresponding to the maximum sensitivity attainable with ALMA.

Once again, the various classes of accretion history models exhibit divergent behavior as a function of time. The shape and value range of the distributions is fairly similar at 0.1 Myr regardless of accretion history, although there are slight differences. IS clusters exhibit lower maximum fluxes than TC, CA, and ET by up to an order of magnitude, while CA clusters have fewer members with fluxes lower than ~ 10 mJy. As accretion progresses, the lower-mass members of constant- and accelerating-rate clusters begin to deplete their envelopes, resulting in both a rightward shift in the distribution and a reduction in the number of models populating the distribution. This depopulation happens at different rates for different histories; CA precedes TC, which precedes IS, consistent with the timescales of accretion set out by the protostellar

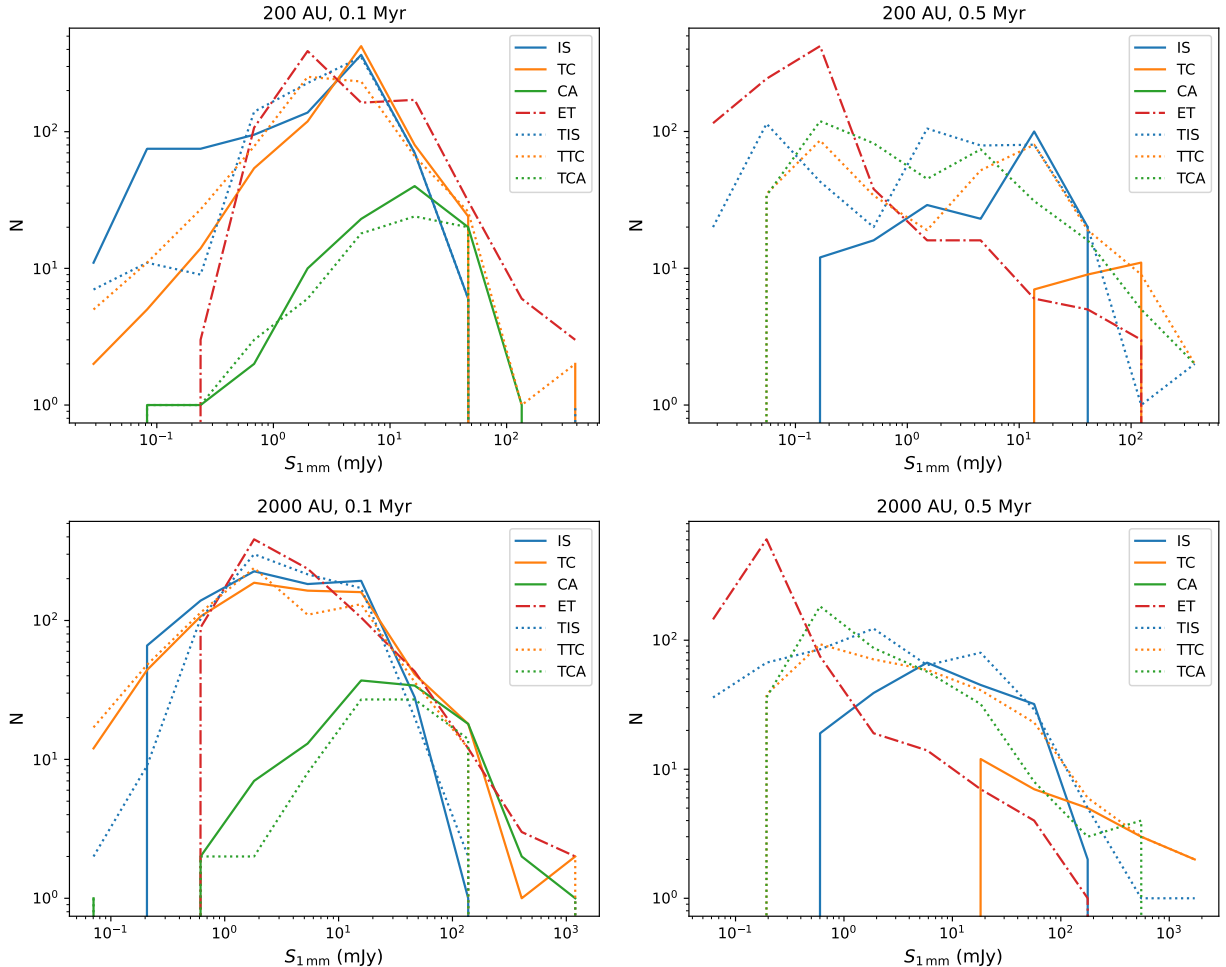


Figure 5-6. Histograms of 1-millimeter flux for the modeled protoclusters of Figure 5-5. Values are calculated in apertures of 200 (*top*) and 2000 (*bottom*) au and sampled at 0.1 (*left*) and 0.5 (*right*) Myr.

evolutionary models. Their tapered counterparts lag behind, but follow the same general path of evolution. Meanwhile, the distribution of ET YSOs shifts to the left as time progresses, since they are modeled as depleting their envelopes on the same (~ 0.7 Myr) timescale regardless of mass.

The predicted behavior of the modeled protoclusters is generally consistent with expectations from individual modeled YSOs. The long-wavelength flux of a YSO is not expected to vary much while its central protostar is deeply embedded, i.e. while the YSO is in Stage 0, but begins to decrease once it has begun to disperse its envelope, i.e. once it enters Stage I. (This behavior is displayed in the right panel of Figure 5-2. See R25 for further discussion on Stages.) The lack of variation in the embedded phase is primarily driven by protostellar evolution; since the central protostar is increasing in temperature and consequently transferring an increasing amount of energy into its surroundings, additional emission from heated dust roughly balances the loss of emission from dust being accreted, and can even outweigh it for the highest-mass YSOs. Extending this to the protoclusters: The high-mass IS YSOs populating the high-flux end of the distribution accrete very slowly on average, but begin accreting faster than TC or CA (see Figure 5-1). Consequently, they have depleted more of their envelope than TC or CA YSOs by 0.1 Myr, but their central sources have not grown enough to offset the loss in flux as in the ET scenario, hence why the high-flux ends of the IS distributions are less well-populated than following the other accretion models. By the same token, CA protostars grow the slowest at early times, meaning that low-mass CA YSOs form protostars later than other histories. Consequently, the low-flux ends of the CA distributions are depopulated at early times, since the protostars that power dust emission at that end are slower to appear.

The observed trends are consistent across aperture sizes; however, in smaller apertures, the calculated flux distributions appear to be slightly more weighted to the right, particularly at 0.5 Myr. This rightward shift is likely due to the higher proportion of heated dust in smaller apertures, which plays an outsize role in total emission.

5.3.2 Star Formation History

With the impact of accretion history on the protoclusters characterized, I do the same with the SFH. To isolate the impact of SFH on my predictions, I limit examination to the protocluster following an ET accretion history; since the implementation is tuned such that all stars accrete their mass on the same timeline, the impact of the formation history is easier to separate from that of variability in accretion. I compare two formation history models: constant star formation with $t_{\text{SF}} \in (1, 10)$ Myr and “normal start” star formation (where formation start times follow a normal distribution) with $t_{\sigma} \in (0.1, 1)$ Myr. I show the output in Figures 5-7 and 5-8, sampling at the same timesteps as in Section 5.3.1.

As expected, including a history of star formation delays the evolution of the distributions of protostellar properties. In general, the CDF of protostellar masses maintains a similar shape with time, with the main difference between scenarios manifesting in the mean mass, range of mass values, and the timescale of evolution. Constant star formation over 1 Myr exhibits a higher maximum mass than any other non-simultaneous SFH early on, but by the second sample time, the distribution of masses for “normal start” formation with a 0.1 Myr width is the closest to the simultaneous case. Since the average start time for $t_{\sigma} = 0.1$ Myr is ~ 0.3 Myr, most of the “normal start” population has begun accreting by 0.5 Myr, resulting in a more evolved population on average than the constant case. The same dynamic can be seen taking shape with 10-Myr constant formation and $t_{\sigma} = 1$ Myr formation. Formation history also primarily manifests in the range of values for luminosity, although since ET accretion decelerates with time, populations with a non-simultaneous formation history have CDFs shifted to higher values due to the dominance of accretion luminosity over the intrinsic luminosity of most stars. (The CDF does not include members of the population without a defined luminosity, i.e. those without protostellar sources; protoclusters with non-simultaneous SFHs exhibit more of these at early times.)

Examining the 1-millimeter fluxes for different SFH models, the general effect of introducing a formation history appears to be a broadening of the resulting distribution. In the simultaneous case (§5.3.1, Figure 5-6), the distribution of ET YSOs shifts towards fainter fluxes

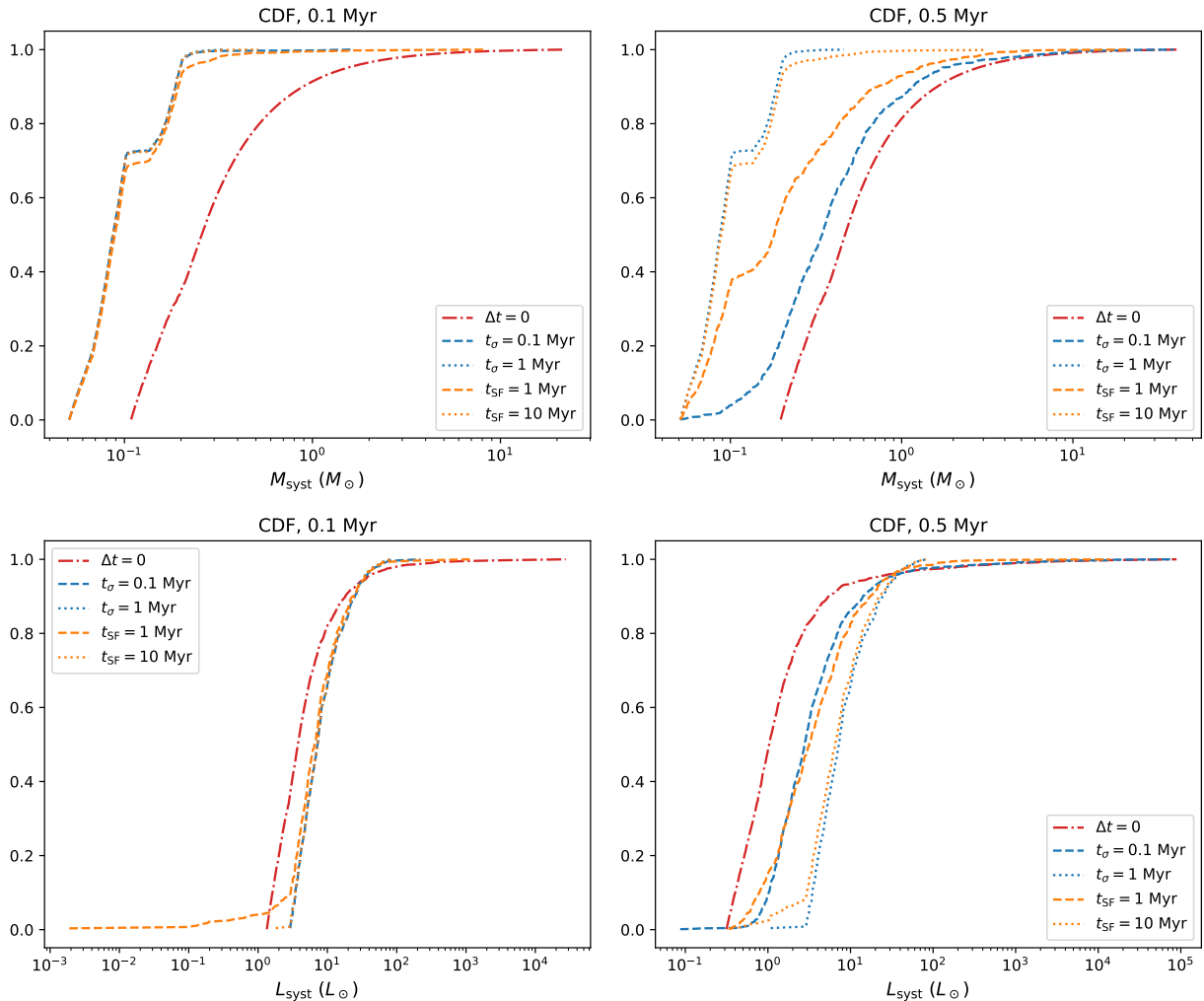


Figure 5-7. The same as Figure 5-5, but varying SFH in place of the assumed accretion model.

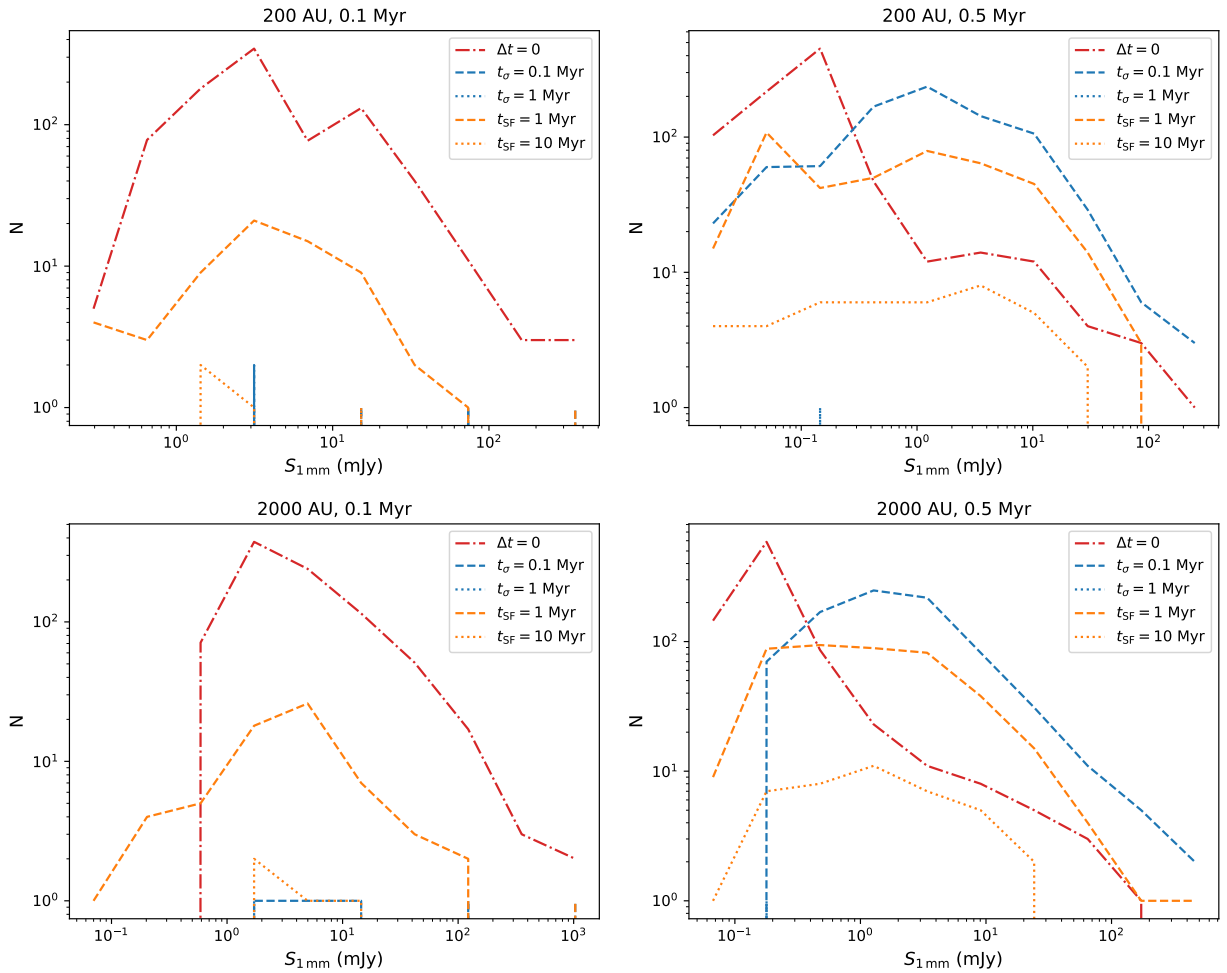


Figure 5-8. The same as Figure 5-6, but varying SFH in place of the assumed accretion model.

with time as the envelopes are accreted and dispersed. As the start times of accretion vary, the shape of the simultaneous distribution is smeared out, generally exhibiting a rightward skew (i.e. against the direction of evolution). “Normal start” formation still exhibits a visible peak, since most stars begin accreting at roughly the same time, but the peak occurs at higher flux and is less sharp than the simultaneous case. Meanwhile, the distribution of fluxes in both constant-formation scenarios is flattened significantly. At the times sampled, the protocluster with the $t_\sigma = 1$ Myr does not exhibit any defined fluxes, since the majority of stars will begin to form between 2-4 Myr.

Comparing fluxes across apertures, the distributions appear once again to exhibit a slight rightward shift in the 200 AU aperture relative to those in the 2000 AU aperture. Here, as in Section 5.3.1, this is likely driven by the higher average dust temperatures in smaller apertures.

5.4 Closing Remarks

Good models of forming stellar populations are necessary to gain a complete understanding of the star formation process. I have created a new approach to protocluster modeling that combines population-level statistics, protostellar evolutionary histories, and radiative transfer models, enabling the creation of protoclusters which evolve self-consistently and can be used to predict direct observables in addition to the theoretical quantities accessible by other models. As a result, my models allow for direct comparison of predictions to observations across a wide range of values and a wide theory space, greatly increasing the potential significance of future observations.

I have used this modeling framework to predict the evolution of protoclusters following various prescribed models for protostellar accretion and history of star formation, following both the properties and long-wavelength fluxes of cluster constituents. Initial results indicate that both accretion history and SFH are expected to have discernible impacts on the distribution of fluxes. Accretion models that prescribe constant or accelerating rates tend to create distributions shifting to higher flux over time as low-mass members finish accreting more quickly, and accretion models that prescribe decreasing rates tend to create distributions shifting to lower flux over time as both the luminosity and dust content of protocluster members decrease. Introducing a history of

formation appears to generally smooth and broaden the distribution of fluxes across a protocluster, with this broadening occurring more for less centrally concentrated formation histories (i.e. uniformly distributed start times as opposed to normally distributed).

The observed differences in model behavior point to the possibility of inferring the operative mechanism of accretion and SFH of observed populations through comparison to measured fluxes, in addition to other components included in the models such as the stellar initial mass function or multiplicity fractions of forming stars. The ability to directly infer these theoretical quantities through comparison to direct observables would represent a large step forward in the study of star formation. More work will be required to fully characterize the observational impact of adopting various theoretical scenarios, necessitating a multi-wavelength comparison of model behavior across a wider theory space. Further, using these protocluster models as measurement tools will require development of an infrastructure to match models to observations.

CHAPTER 6

SUMMARY AND CONCLUSIONS

Stars are a crucial component of the visible Universe, shaping the evolution of molecules and dust grains, galaxies, and everything in between. The lives of stars are strongly dictated by their initial properties, making a fully-developed picture of stellar birth necessary for a full understanding of planet formation, galaxy evolution, and other processes impacted by the behavior of stars. Despite this, considerable unknowns remain in our current knowledge of the earliest phases of a star's life; these include central questions such as how their mass is assembled, whether low- and high-mass stars follow disparate formation pathways, or the absolute timescale over which stars form.

Greater understanding of the process of star formation is typically gained by comparing observations of forming stars to predictions from theoretical models. However, the range of theories proposed to explain star formation is wide, encompassing many different physical processes and characteristic values. Current models that attempt to leverage theory to interpret observations therefore often encounter difficulties constraining the theory space of star formation. Sets of radiative transfer models of YSOs, usually developed as measurement tools, are often bound to a specific theory or narrow range of parameter values and morphologies, limiting their use as probes of theory. Meanwhile, attempts to self-consistently model the evolution of forming stars—individually or in groups—often do not extend their predictive capacity to direct observables, making it difficult to connect theory with observation.

Throughout this work, I have sought to develop a collection of models and modeling tools that addresses these deficiencies. I have expanded the information associated with a large, diverse, and formation-agnostic set of radiative transfer YSO models, increasing their utility as a measurement tool for YSO properties. I have used this augmented set of models as a base for a newly developed approach to modeling the evolution of individual YSOs. This approach associates radiative transfer models with models of protostellar evolution, directly relating observational predictions to the theory of stellar mass assembly. This modeling technique is generally able to return the expected fluxes of models within my set at the wavelengths commonly

used to observe star formation, particularly at the long wavelengths which track the luminosity and mass of YSOs. I incorporate this YSO modeling approach into a framework for modeling the evolution of populations of forming stars, creating a widely applicable modeling tool capable of probing the theory space of mass accretion onto protostars, the stellar initial mass function, and a protocluster’s history of star formation.

I have also used these models to examine several current practices within the study of star formation, in addition to making initial predictions for how variations in star formation theory will manifest in observation. The major findings of my work are summarized below:

- Based on results from radiative transfer modeling, the practice of inferring the mass of cores by comparing their radiation to that of optically thin dust generally returns good mass estimates (to within $\sim 50\%$) if an appropriate dust temperature is used. However, modeling also indicates that the value of the “appropriate” dust temperature varies with the flux observed and the resolution of the observing instrument. The common assumption of 20 K dust is therefore not generally applicable, and may lead to significant mis-estimation of mass.
- Different models for protostellar accretion should be expected to manifest in observables. Comparing the far-IR and radio fluxes exhibited by modeled YSOs, forming stars corresponding to the same final mass exhibit distinct behavior as a function of time following prescriptions for accretion rate motivated by disparate theories.
- The construction of radiative transfer models is capable of having a pronounced impact on predicted results, with the varying dust models and disk treatments of Richardson et al. (2024) and Zhang & Tan (2018) resulting in an average disparity between predicted long-wavelength fluxes of $\sim 30\%$ for models with the same properties. While an extreme case, this illustrates an additional source of uncertainty in model predictions.
- Class, the traditional method for determining the evolutionary status of a YSO, appears to exhibit a tenuous and variable connection to physical properties. This is particularly true during the hypothesized embedded phase of star formation, where the physical state of a YSO may be obscured by a number of theoretical and observational phenomena, including YSO morphology, accretion, viewing angle, and foreground extinction. I provide a tool to infer Class from Stage based on models consistent with several theoretical prescriptions for protostellar evolution and propose the development of an evolutionary indicator based off of a YSO’s far-IR and radio fluxes.
- Different prescriptions for protostellar accretion and history of star formation exhibit distinct behavior on a population level, both in terms of the summary properties commonly used to evaluate star formation theory and the flux distributions of population members.

This work opens a path to performing a comprehensive and impactful examination of the theory of star formation through direct comparison with data. Future work will focus on development of the tools necessary to compare observed flux distributions with the output of simulated populations and application of the models across wavelength regimes. In addition, I intend to continue improving the capabilities of these models both through expanding the accessible theory space and improving the precision of flux predictions in the IR in order to make full use of current- and next-generation data.

APPENDIX A MODEL BOLOMETRIC LUMINOSITIES

I compare the luminosity of the central source in each YSO model, calculated directly from the model parameters, to the isotropic luminosity projected from the flux density calculated by Hyperion. In effect, this permits a check on energy conservation within the models. Luminosity is recovered with the equation:

$$L = 4\pi d^2 \int S_\nu d\nu \quad (\text{A-1})$$

where d is the distance to the source, here 1 kpc. Results for a 10,000 AU aperture are collected in Figure A-1; plots are colored by viewing angle for models that depend on it in Figure A-2 and density scale for models with envelopes in Figure A-3 to highlight the dependence of observed features on these properties. For the geometry with no density structures, the source luminosity is successfully recovered. Geometries with dust deviate from the source due to contributions from dust and observational effects.

Many geometries experience a spread in recovered luminosity regardless of source brightness. This spread occurs in all geometries that have a θ dependence—rotational flattening, cavities, etc.—and is particularly true for disk-only models, where the largest spreads can be seen (*ex. Figure A-1, top right*). This is a consequence of viewing angle; light traveling from the source is scattered out of the denser edge-on lines of sight and into the less dense face-on angles, resulting in a respective deficit/excess in flux. This inclination dependence is highlighted in Figure A-2.

Many model geometries also exhibit over-luminous “wedges” from $\approx 10^{-4} - 10^{-1} L_\odot$; this can be seen clearly in Figure A-1 (*bottom row, middle panel*). Figure A-3 shows that models with higher dust density scales generally have higher recovered luminosities, indicating that the heightened luminosities result from emission by heated dust surrounding the central source—the more dust surrounding the source, the greater the discrepancy can be.

Finally, the introduction of an ambient medium results in the appearance of under-luminous “dip” features driven by extinction. Such a dip can be seen at $\approx 1 L_\odot$, visualized clearly in Figure A-1 (*top row, middle panel*). These features are persistent across geometries and increasingly

pronounced with aperture size as more dust, whether from an envelope or the ambient medium, is included in the aperture. High-luminosity models experience a second dip beginning at $\approx 10^4 L_\odot$ as models with more heated dust (due to higher input luminosity and density scale) also experience extinction from the ambient medium, which is showcased in Figure A-3. This higher-luminosity dip is a feature that is present by virtue of having widespread dust, but is reduced or absent in some panels of Figure A-1 due to post-processing for S/N; see Section 4.2.4 of R17 for details.

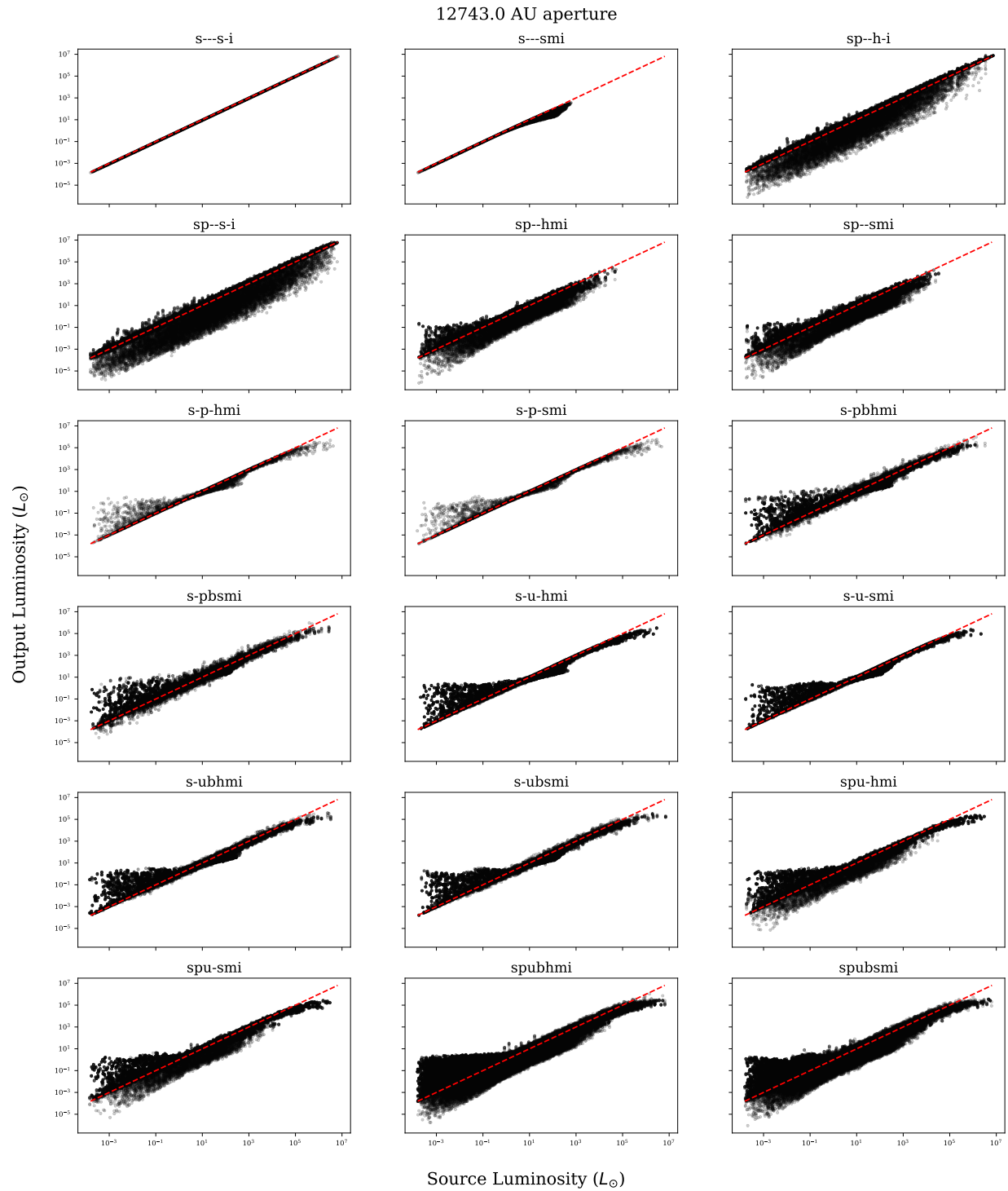


Figure A-1. Luminosities recovered from every model SED using Eq. (A-1) plotted against the luminosities of the sources at the center of each model. A 1-1 line is plotted in red. All SEDs are observed in an aperture of radius $\approx 10,000$ AU at a distance of 1 kpc. For SEDs with multiple viewing angles, recovery is done for each independently.

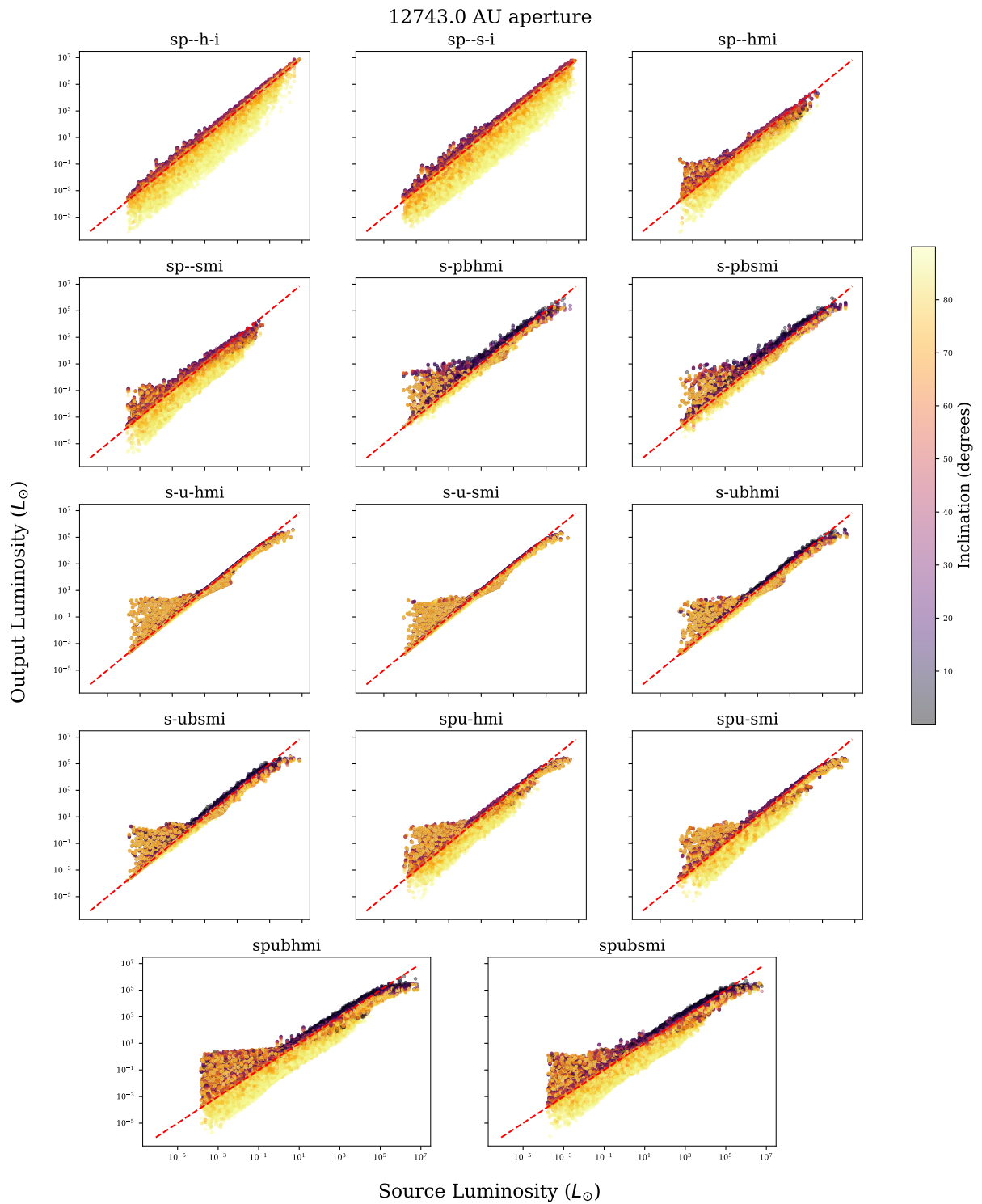


Figure A-2. The same as Figure A-1, but limited to models with θ dependence and colored by the viewing angle (see §2.2.3 for more details.)

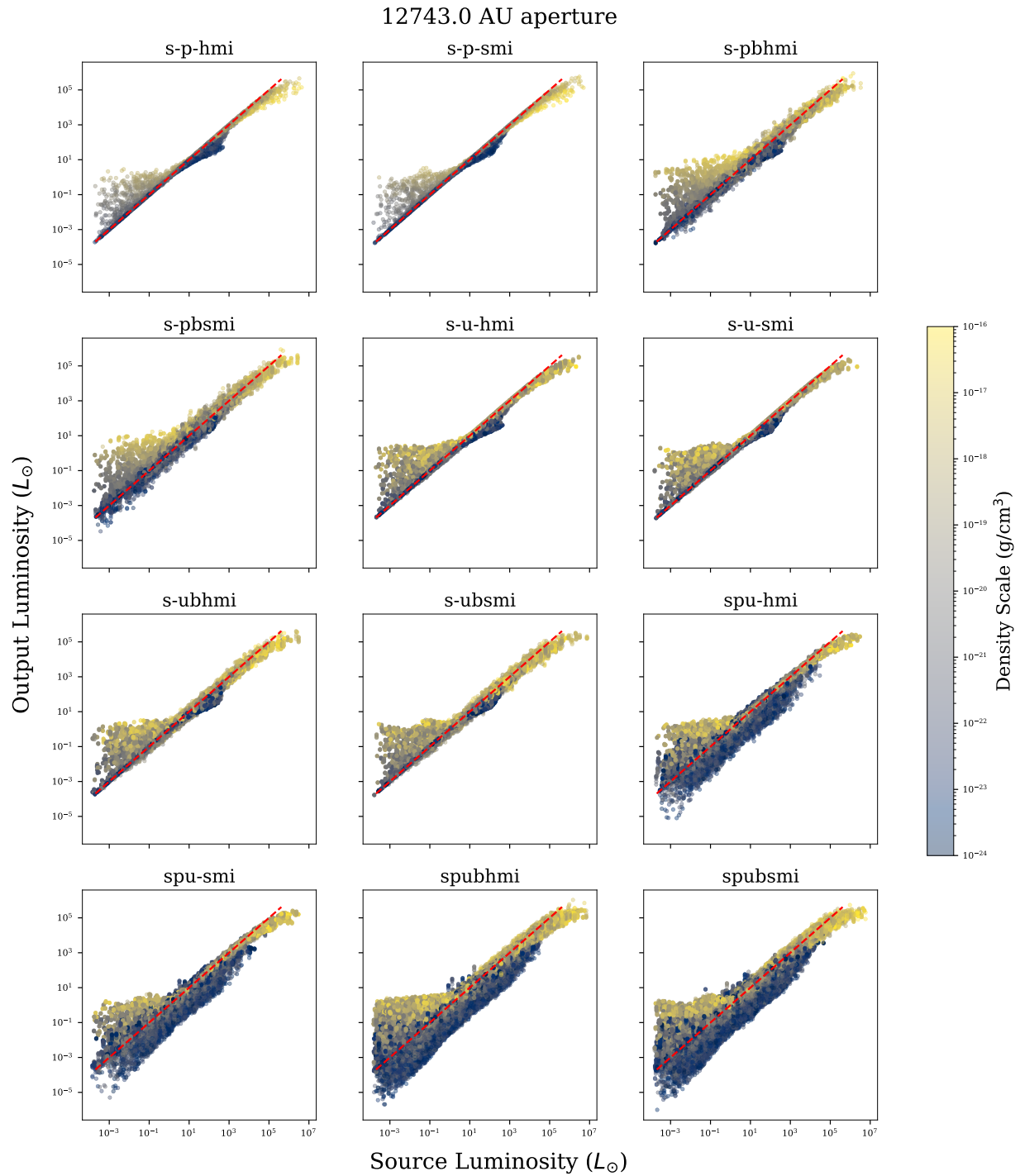


Figure A-3. The same as Figure A-1, but limited to models with envelopes and colored by the density scale of the envelope (see §2.2.1.1 for more details).

APPENDIX B ADDITIONAL COLOR-COLOR DIAGRAMS

In Sections 2.4.2.1 and 2.4.2.2, I separated the radiative transfer YSO models of Richardson et al. (2024) by Class and Stage and visualized them in JWST color space. In this appendix, I return to Figures 2-10 and 2-11 but instead plot the number of models of each Class and Stage as a percentage of the total in Figures B-1 and B-2. These plots generally reinforce observations made using the non-percentage versions. Class I objects are very red, and successive Classes become less so. Successive Stages, however, trace out a more complicated (and distinct) path in color space, with disk-only models tending to be preferentially reddened in colors involving mid-IR wavelengths compared to models that are either envelope-dominated or do not have disks.

In Figure 2-11, noteworthy fractions of the models in Stages II and III exhibit red colors. This redness can be attributed to additional emission from the ambient medium driven by exposed sources with high luminosity. To isolate this effect, I consider the s---smi geometry, which is composed solely of models with a source and an ambient medium. In Figure B-3, I illustrate the dependence of position in NIRCam and MIRI color space on source temperature. There is a clear correlation between redness and temperature, and this medium-only geometry reproduces the shape of the Stage III models in Figure 2-11. To determine the cause of this redness, I compare the SEDs of s---smi models with cold sources to models with hot sources. In general, I find that the medium around hot sources dominates the NIR/MIR range of the SED, while colder sources tend to be brighter than their surrounding medium over the same range. Examples are plotted in Figure B-4. Dust emission from the medium around hot sources therefore results in more IR flux, which in turn causes these models to appear redder.

Between Chapter 2.4.2 and this appendix, I have mapped out the positions of the models in JWST color-color space, as well as how those positions change as a function of spectral class and evolutionary stage. To demonstrate that these results are consistent with previous work, I reproduce plots from Robitaille et al. (2006, R06) using my updated model set. In addition to evolutionary Stage, R06 breaks its grid down in color space by properties intrinsic to each model: the envelope accretion rate, inner radius of a model's envelope/disk (in terms of dust sublimation

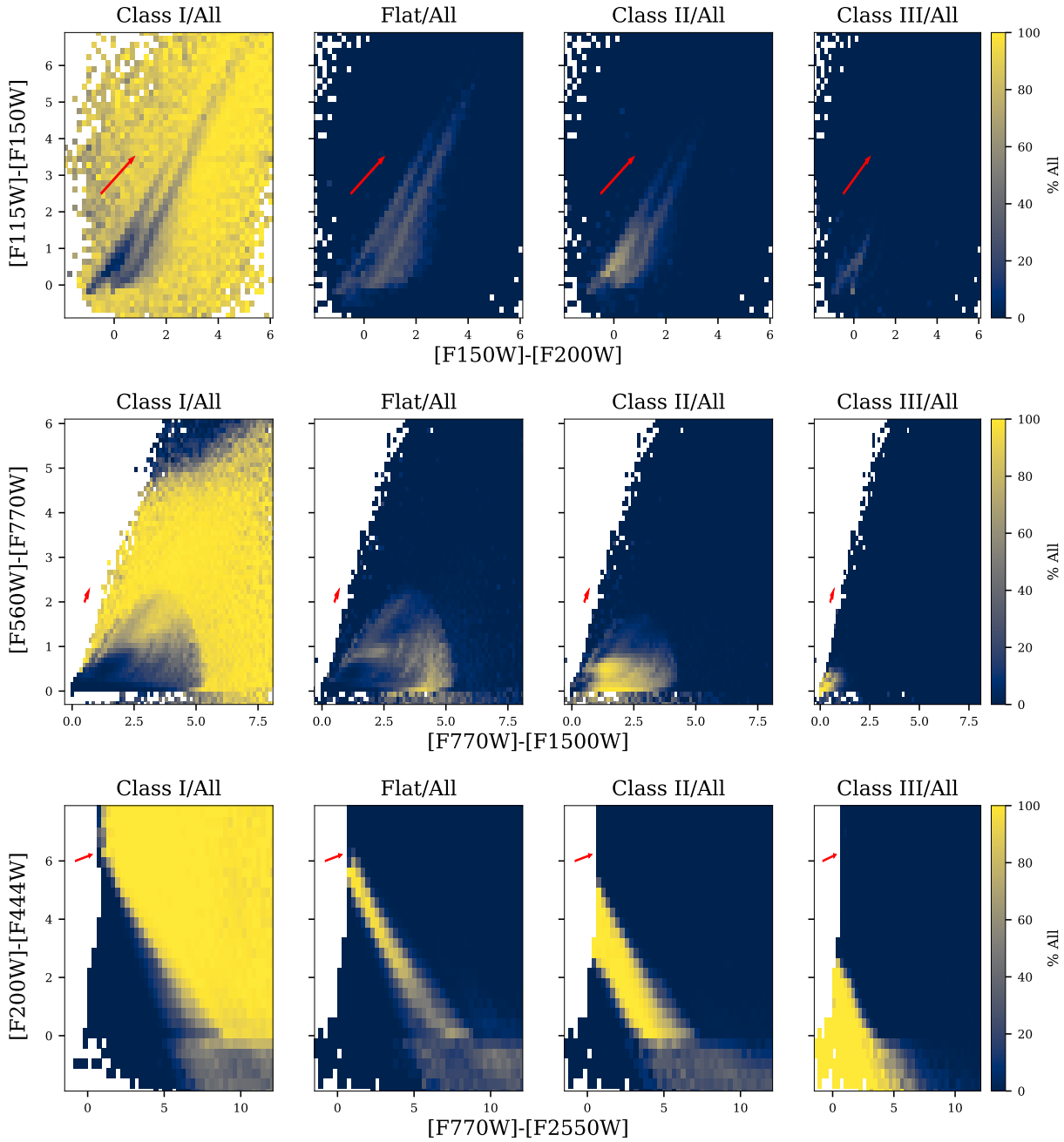


Figure B-1. 2D histograms of the models in the same color-color spaces as in Figure 2-10, but colored by the number of models that occupy each bin as a percentage of the total. (The more yellow a bin is, the larger the share of all models in that bin with that Class.) See §2.4.2.1 for details on classification.

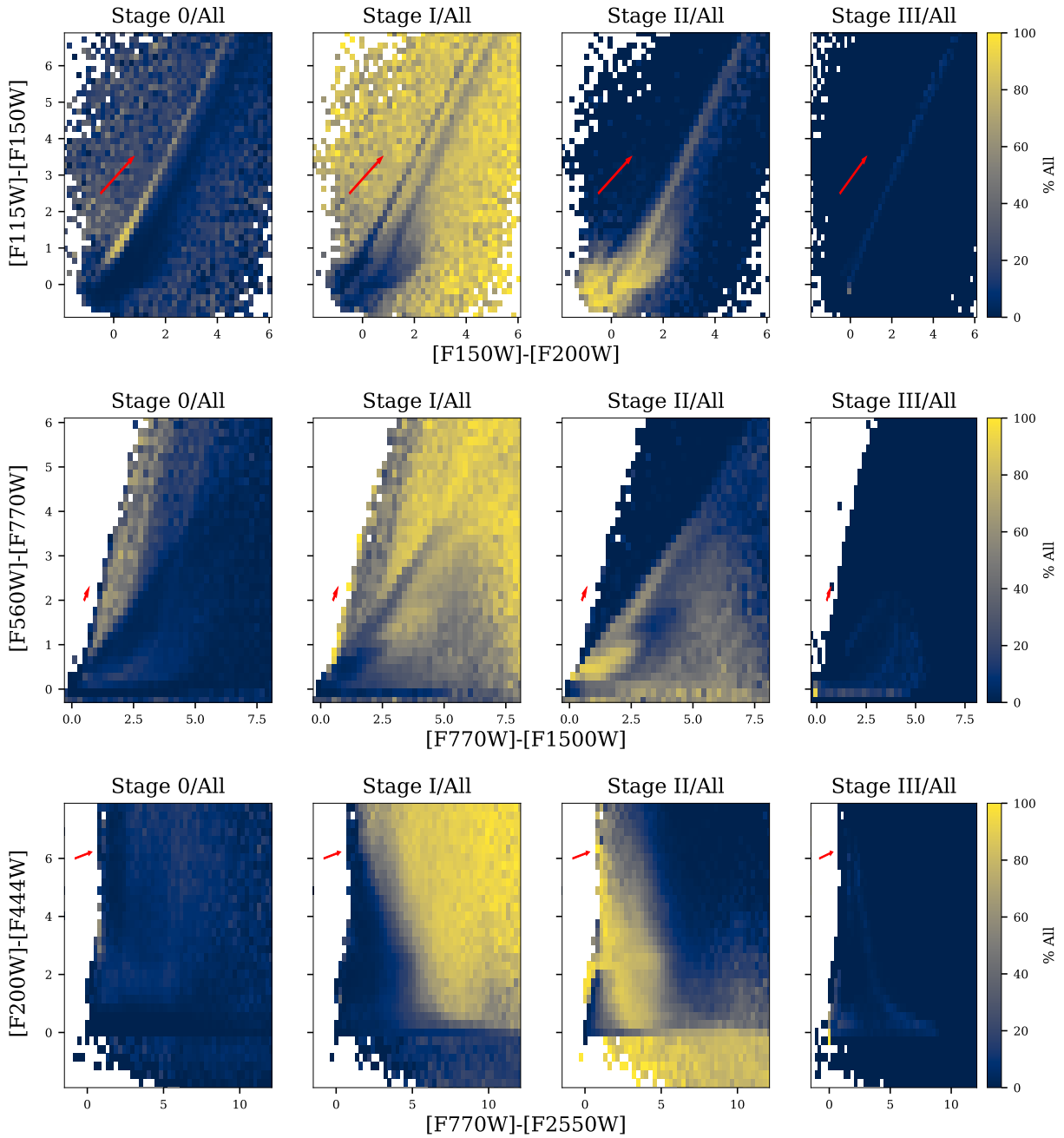


Figure B-2. The same as Figure B-1, but separated by Stage instead. See §2.4.2.2 for details on Stage assignment.

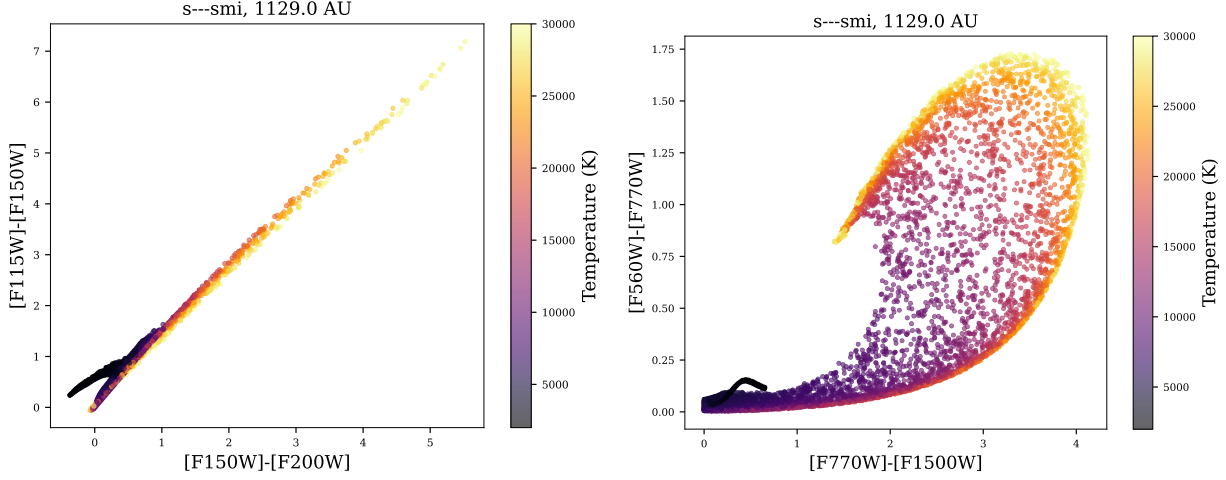


Figure B-3. NIRCam and MIRI color-color diagrams for the `s---smi` geometry (akin to Stage III from Figure 2-11) colored by the temperature of the source in each model. Models with hotter sources are redder than those with colder sources in both color spaces.

radius), and the temperature of the central source. My set of models can also be separated by source temperature and inner radius in the same way as in R06, as these parameters are common to both sets of models. I recreate these plots in Figure B-5.

I find general agreement between my results and those of R06. Models with higher temperatures are redder on average, in accordance with R06’s generalization of the findings of Whitney et al. (2004) to near- and mid-IR wavelengths. As the inner radius of the models increases, there is a clear evolution from being preferentially reddened in [I1]-[I2] to [I3]-[I4], to the point where most models in the largest radius bin have a color close to zero in [I1]-[I2]. A similar phenomenon occurs in R06; it is explained there as a result of a shift in flux from shorter to longer wavelengths as the dust temperature around the source decreases. As this shift occurs, the shorter-wavelength fluxes increasingly become solely due to stellar photospheres, which means that the models exhibit photospheric colors (which tend close to zero). In general, my results exhibit more spread in color-color space than their counterparts in R06, likely due to the increased size and randomly sampled nature of the models. However, it is clear that despite this spread, the behavior of my model set comports with that of the R06 grid.

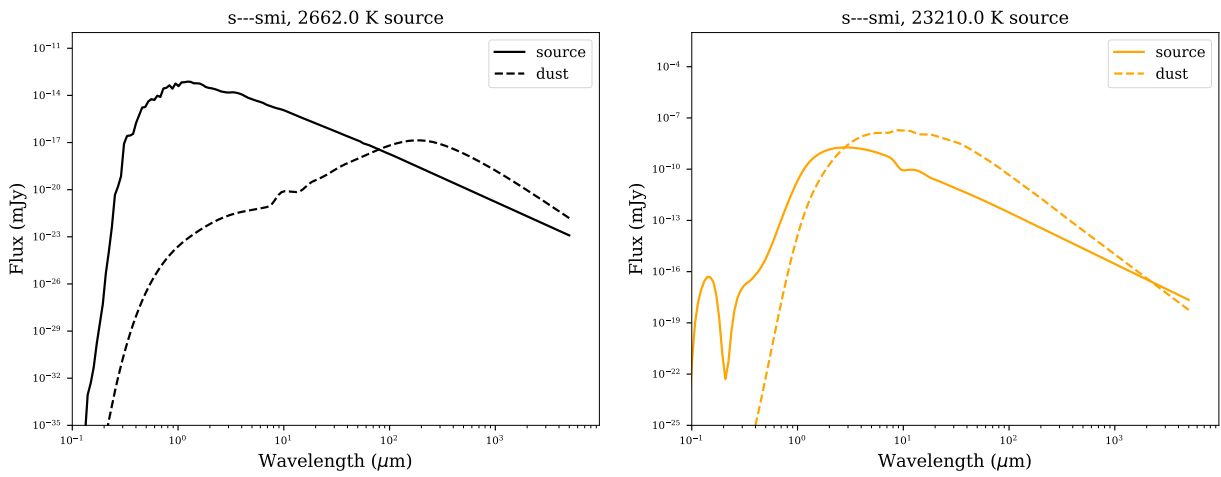


Figure B-4. SEDs from the **s---****smi** geometry for a model with a cold source (*left*) and a hot source (*right*), broken down by component. The dust around the hot source is clearly dominant in the near- and mid-IR, unlike that around the cold source. The viewing aperture for both SEDs is chosen to be as close to the aperture used in Figure B-3 as possible.

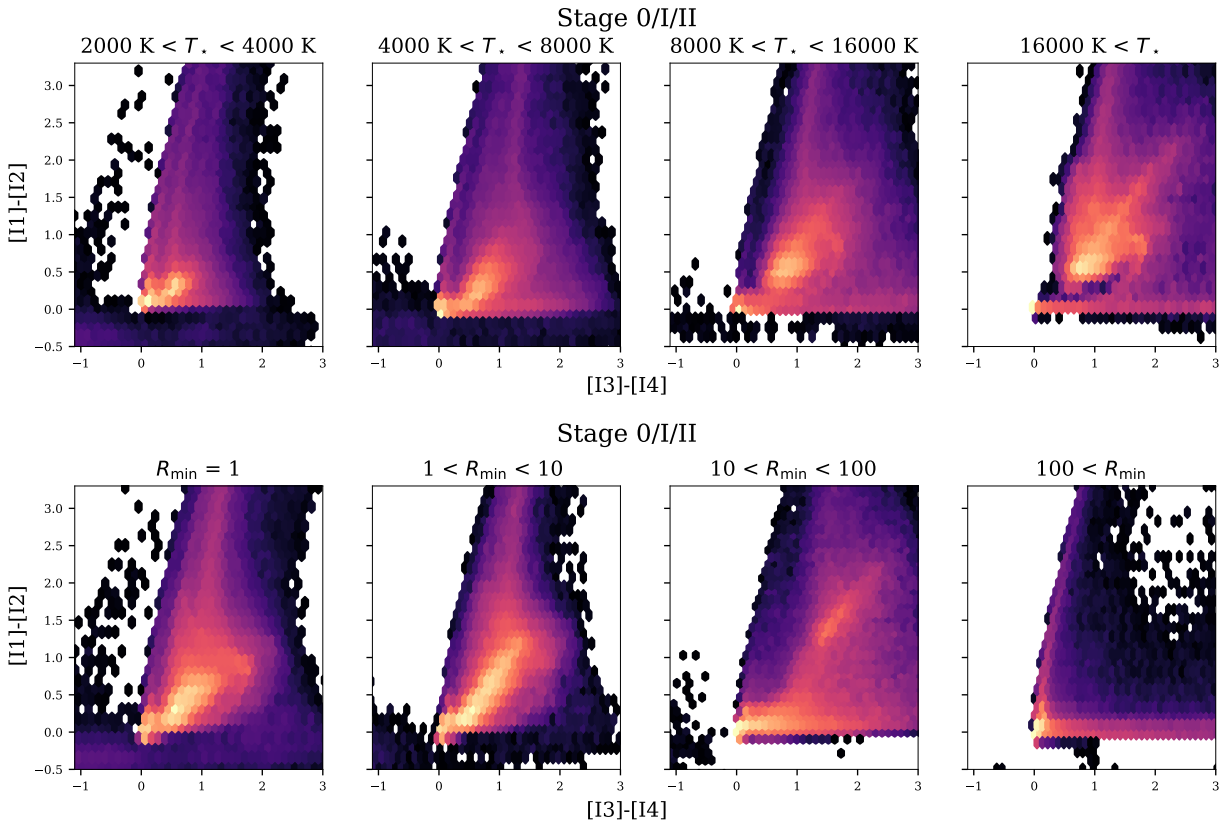


Figure B-5. Plots of R24 models in IRAC color-color space, separated by stellar temperature (*top*) and inner radius of circumstellar envelope/disk, in terms of dust sublimation radius (*bottom*). These are analogous to Figures 26-28 in R06, which separates its models in a similar way. All models that fall into Stages 0, I, and II (see §2.4.2.2) are included in both plots.

APPENDIX C THE IMPACT OF ACCRETION LUMINOSITY

In Section 3.2.2, I outlined my procedure for making models of evolving YSOs. In order to match RTMs to PEMs, I construct a multidimensional parameter space based on shared quantities, one of which is the luminosity of the YSO’s central source. However, the PEMs track both the intrinsic luminosity of the source (i.e. purely thermal radiation from the protostar itself stemming from contraction/deuterium burning/etc.) and the total luminosity, which includes accretion. The presence of both of these components in the PEMs raises the question of how the inclusion or exclusion of accretion luminosity impacts the results, and as a consequence, which scenario is more appropriate for modeling purposes.

As modeled by K12, accretion luminosity is often the dominant component of total luminosity. This is particularly true for protostars with final stellar masses less than $\sim 3 - 4 M_{\odot}$, but is also the case at early times for more massive protostars. Figure C-1 serves as an illustration; following an IS accretion history, the intrinsic luminosity of a $1 M_{\odot}$ protostar will be subdominant for its entire accretion time, and the same will be true for roughly half the accretion time of a $5 M_{\odot}$ protostar.

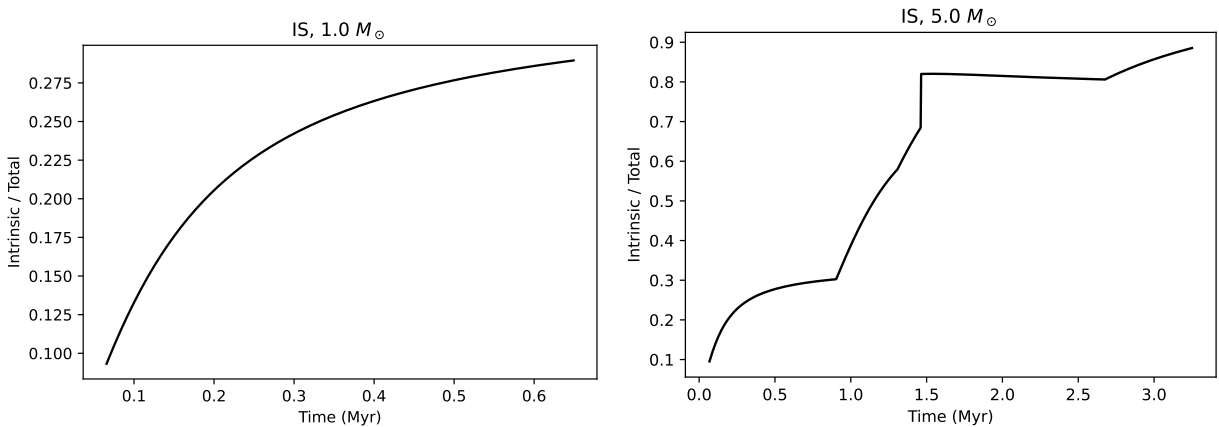


Figure C-1. Intrinsic luminosity as a fraction of total luminosity for two PEMs following an isothermal sphere accretion history. Plotted for protostars with final masses of one (left) and five (right) M_{\odot} .

The disparity between the intrinsic and total luminosity of the PEMs means that the choice of luminosity affects the RTMs that are chosen to correspond to a PEM. In turn, this affects the

fluxes predicted using those RTMs (as in 3.3.1), at least for wavelengths that are dependent on the luminosity of the central source. As a way to quantify the effects of this choice, I compare flux predictions made using intrinsic and total luminosity in Figure C-2.

The choice of luminosity has a large impact on the predicted 100- μm fluxes. For low-mass stars, there is roughly an order-of-magnitude difference in the flux values over their entire accretion time between the “intrinsic” and “total” tracks, regardless of accretion history. This disparity is less present in higher-mass stars that are eventually able to outshine luminosity from accretion, but still exists early in their accretion time when the instantaneous mass of the protostar is low. The increase in flux due to accretion luminosity is qualitatively consistent with behavior observed in the modeling of Fischer et al. (2024), reaffirming the utility of far-infrared radiation as a tracer of protostellar accretion. The effects of accretion luminosity on the 3-mm flux, on the other hand, are fairly muted regardless of mass. On the whole, however, it is clear that since accretion makes up a nontrivial component of the total luminosity of many protostars across time and is capable of greatly affecting flux predictions, the total luminosity should be preferred.

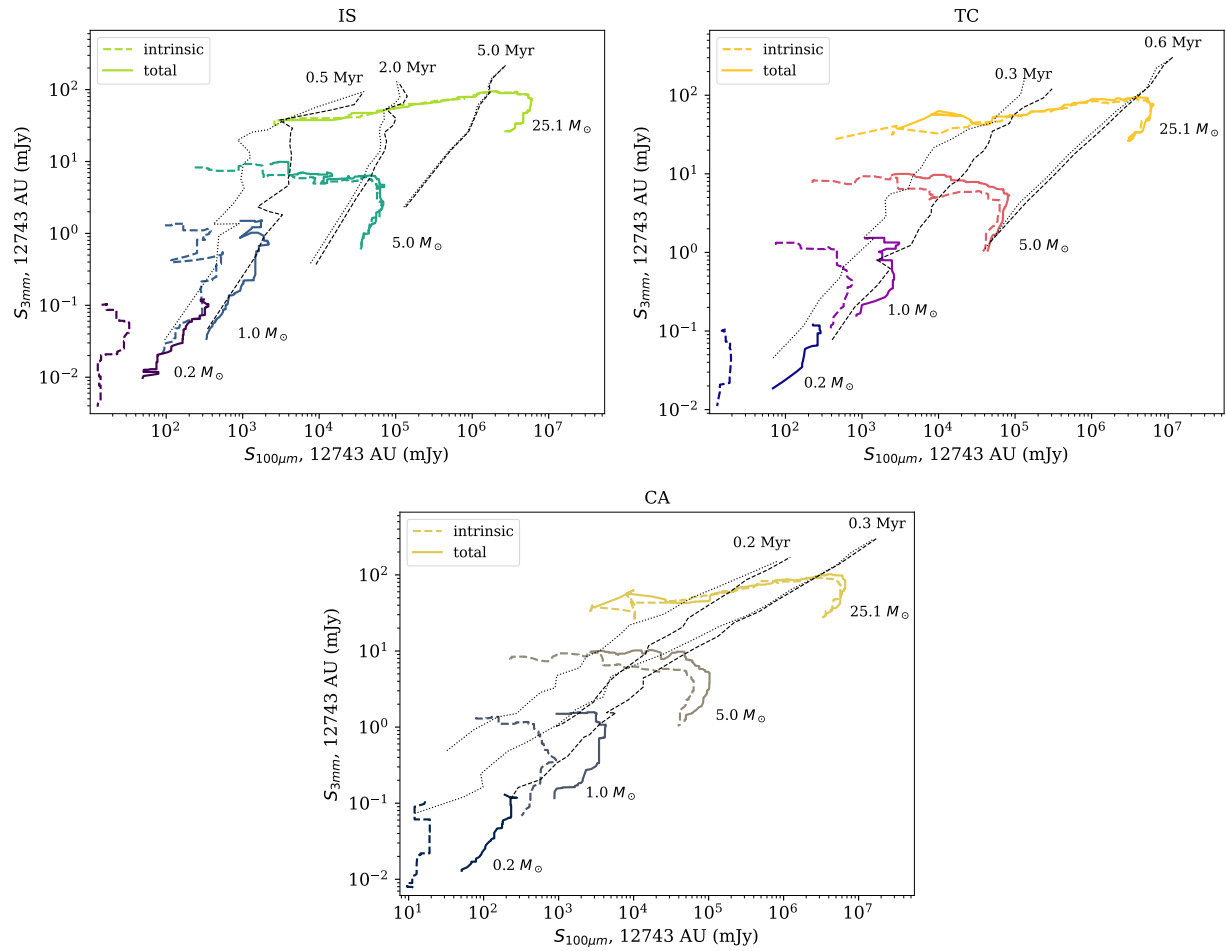


Figure C-2. 100- μm vs. 3-mm flux tracks for a set of modeled YSOs as in Figure 3-3, but plotted using RTMs matching the intrinsic (dashed) and total (solid) luminosities of the base PEMs. Isochrones showing the position of intrinsic (dotted) and total (dashed) luminosities in this flux space are also plotted.

APPENDIX D MORE ON YSO COMPOSITION

In Chapter 3.3.2 I provided a diagnostic for the accuracy of my flux predictions: attempting to reproduce the fluxes of models within my set by averaging over their ten nearest neighbors, as I do when modeling YSO SEDs (§3.2.2). This approach leads to good accuracy and reasonable precision. However, since the number of neighbors and the definition of “nearest” determine the size and composition of the sample of RTMs picked to represent a YSO, I evaluate the performance of my framework as these are varied here.

My definition of distance is Equation 3-2, which is based on the cumulative distribution functions of the tracked properties (the “quantile distance”). (See §3.2.3 for details.) In the course of this research, I have developed alternate definitions; here I provide an overview.

One of the main motivations behind my definition is the large disparity between the possible values between dimensions. T_\star is limited between $\sim 10^3\text{-}10^4$ K while L_\star and M_{core} can vary by multiple orders of magnitude, meaning that a standard Cartesian distance is likely to place unequal weight on dimensions for reasons independent from physics, which is not desired. One way of compensating for the level of difference is to transform every value to log-space and take the Cartesian distance there instead, which I call the “log distance”:

$$D^2 = \log^2 \left(\frac{T_{\text{model}}}{T_{\text{track}}} \right) + \log^2 \left(\frac{L_{\text{model}}}{L_{\text{track}}} \right) + \log^2 \left(\frac{M_{\text{model}}}{M_{\text{track}}} \right) \quad (\text{D-1})$$

From here, I perform a normalization of sorts: dividing each value by the maximum possible range in each dimension in log space (e.g. $\log(T_\star) \rightarrow \log(T_\star) / \log(T_{\max}/T_{\min})$) so that when distance is calculated, the offset in each dimension is weighed by its magnitude relative to the total span of values. This is the “normalized log distance”:

$$D^2 = \frac{\log^2(T_{\text{model}}/T_{\text{track}})}{\log^2(T_{\max}/T_{\min})} + \frac{\log^2(L_{\text{model}}/L_{\text{track}})}{\log^2(L_{\max}/L_{\min})} + \frac{\log^2(M_{\text{model}}/M_{\text{track}})}{\log^2(M_{\max}/M_{\min})} \quad (\text{D-2})$$

Since the parameter space is built with long-wavelength emission in mind, I also create a definition for distance that weights the dimensions by their effect on the long-wavelength flux in order to prioritize the quantities that matter most. As in the main body of this work, I use 1 millimeter as the representative for long wavelengths. I make the ansatz that the 1-mm flux behaves as follows:

$$S_{1\text{mm}}(T_\star, L_\star, M_{\text{core}}) = A \times T_\star^\alpha + B \times L_\star^\beta + C \times M_{\text{core}}^\gamma \quad (\text{D-3})$$

or in other words, the flux has a power law dependence on each quantity. To calculate the unknowns, I divide each dimension into twenty evenly log-spaced bins and fit the flux as a function of each term within bins of the other two parameters (for example, fitting $S_{1\text{mm}} = A \times T_\star^\alpha$ within bins of L_\star and M_{core}). Doing so effectively holds the non-fit parameters as constant at possible while still maintaining good sample size (I do not consider bins with less than fifty models to avoid outliers). Once this fit is performed within each combination of bins, I find the mean of the results.

The resulting values for the exponents are $\alpha = 0.02$, $\beta = 0.28$, and $\gamma = 0.91$. There is some physical basis for these values. In the limit of optically thin dust at long wavelengths, the flux for a YSO with an envelope is expected to vary roughly as:

$$S_{\lambda, \text{long}} \propto M_{\text{core}} T_{\text{core}} = M_{\text{core}} L_{\text{core}}^{1/4} \quad (\text{D-4})$$

Core temperature is highly insensitive to the source temperature, meaning that the observed flux should not depend on source temperature significantly, which I find to be the case. Conversely, core mass should vary roughly linearly with the 1-millimeter flux, which I also find to be the case. The luminosity exponent implied by Equation D-4 is 0.25, which is close to what I find assuming that core luminosity is proportional to L_\star .

With the determination of weights, I can now define the “weighted distance”:

$$D^2 = \log^2 \left(\frac{T_{\text{model}}}{T_{\text{track}}} \right)^\alpha + \log^2 \left(\frac{L_{\text{model}}}{L_{\text{track}}} \right)^\beta + \log^2 \left(\frac{M_{\text{model}}}{M_{\text{track}}} \right)^\gamma \quad (\text{D-5})$$

where the exponents derived through the power-law fitting are applied to the respective dimension of the log distance. As in the log case, I further divide each dimension by the maximum span to normalize distances. This results in the “normalized weighted” distance:

$$\begin{aligned} D^2 = & \left(\frac{\log^2(T_{\text{model}}/T_{\text{track}})}{\log^2(T_{\max}/T_{\min})} \right)^{1/\alpha} + \left(\frac{\log^2(L_{\text{model}}/L_{\text{track}})}{\log^2(L_{\max}/L_{\min})} \right)^{1/\beta} \\ & + \left(\frac{\log^2(M_{\text{model}}/M_{\text{track}})}{\log^2(M_{\max}/M_{\min})} \right)^{1/\gamma} \end{aligned} \quad (\text{D-6})$$

Since normalization ensures that each distance value will now be at most 1, I invert the exponents to ensure that a smaller exponent in a dimension reduces the relative contribution from that dimension instead of magnifying it.

In Figure D-1, I compare the quality of 1-millimeter R24 model fluxes recovered using these definitions to that of ones obtained using the default method, as well as allowing the number of selected nearest-neighbor models to vary. This figure characterizes the performance of different distance definitions through percentile values from the distribution of the ratios of recovered to original model fluxes, and from log-normal distributions fit to the distribution of σ_{MADS} (scaled to standard deviation and the recovered flux value); see Figure 3-5 and Chapter 3.3.2 for context.

Among the definitions, the quantile distance is consistently a good performer in both accuracy and precision. It consistently produces distributions of flux ratios with a 50th percentile close to 1 and one of the consistently lowest spreads between P_{16} and P_{84} , regardless of the number of neighbors; that uncertainty improves slightly when adding more neighbors, but that improvement is marginal beyond 10 models. The scaled σ_{MADS} (derived from the SEDs of selected RTMs) for the quantile distance generally hover around 0.5, i.e. 50% of the recovered value. σ_{MAD} receives a very slight boost in performance from more neighbors before the

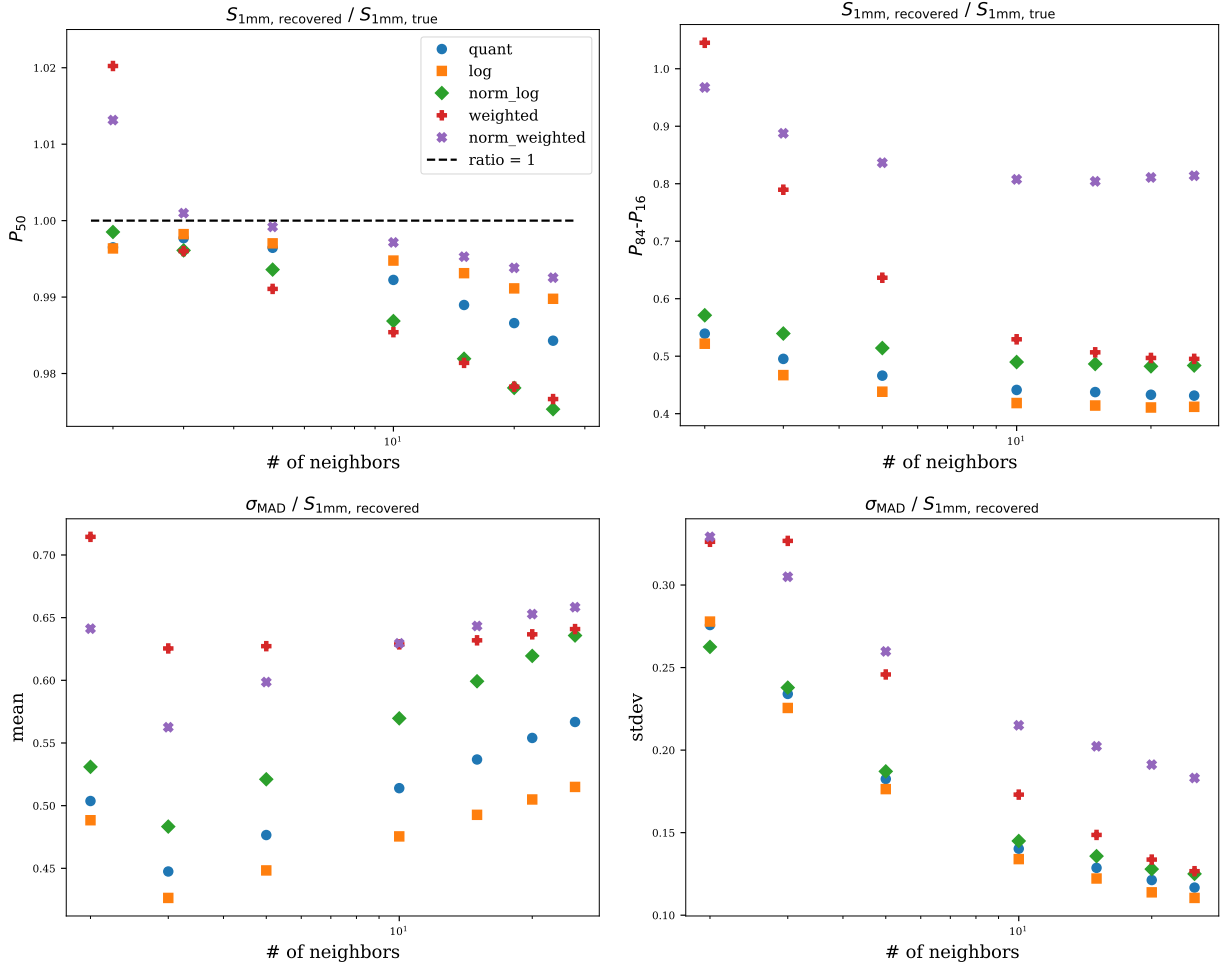


Figure D-1. Comparing the quality of 1-mm flux reproductions, as derived from plots like Figure 3-5, for all definitions of distance and with varying numbers of selected models. The top row shows the 50th percentile of the distribution of flux ratios (*left*) and the difference between the 84th and 16th percentiles (*right*). The bottom row shows the arithmetic means (*left*) and standard deviations (*right*) of log-normal distributions fit to the distribution of σ_{MAD} s of the RTM SEDs that are averaged over to produce recovered SEDs (scaled by the recovered value).

increased number begins to cause more deviation from the median. This upward trend with more neighbors provides another incentive to stop at about 10. Combined with the flux ratios, 10 neighbors represents the last point where adding a model to the pool used to recover the flux will increase the precision of flux recovery while maintaining an average recovered flux value within 1% of the true value and limiting the rise in the uncertainty of each individual predicted SED.

Interestingly, results from the log distance are slightly more precise than those from the quantile distance, both having a slightly lower spread in flux ratio and a slightly lower σ_{MAD} . However, the improvement is small, and this definition of distance is not as universally applicable as the quantile distance to different scenarios (e.g. five parameters that are a mix of log- and linearly-sampled). Meanwhile, the normalized log distance and both flux-weighted definitions have uncertainties that are uniformly higher than the best performers.

APPENDIX E ADDITIONAL PLOTS

Here, I display versions of Figure 3-2 for stars of different masses to illustrate the variance in behavior of the protostellar evolutionary models implemented in Chapter 3.

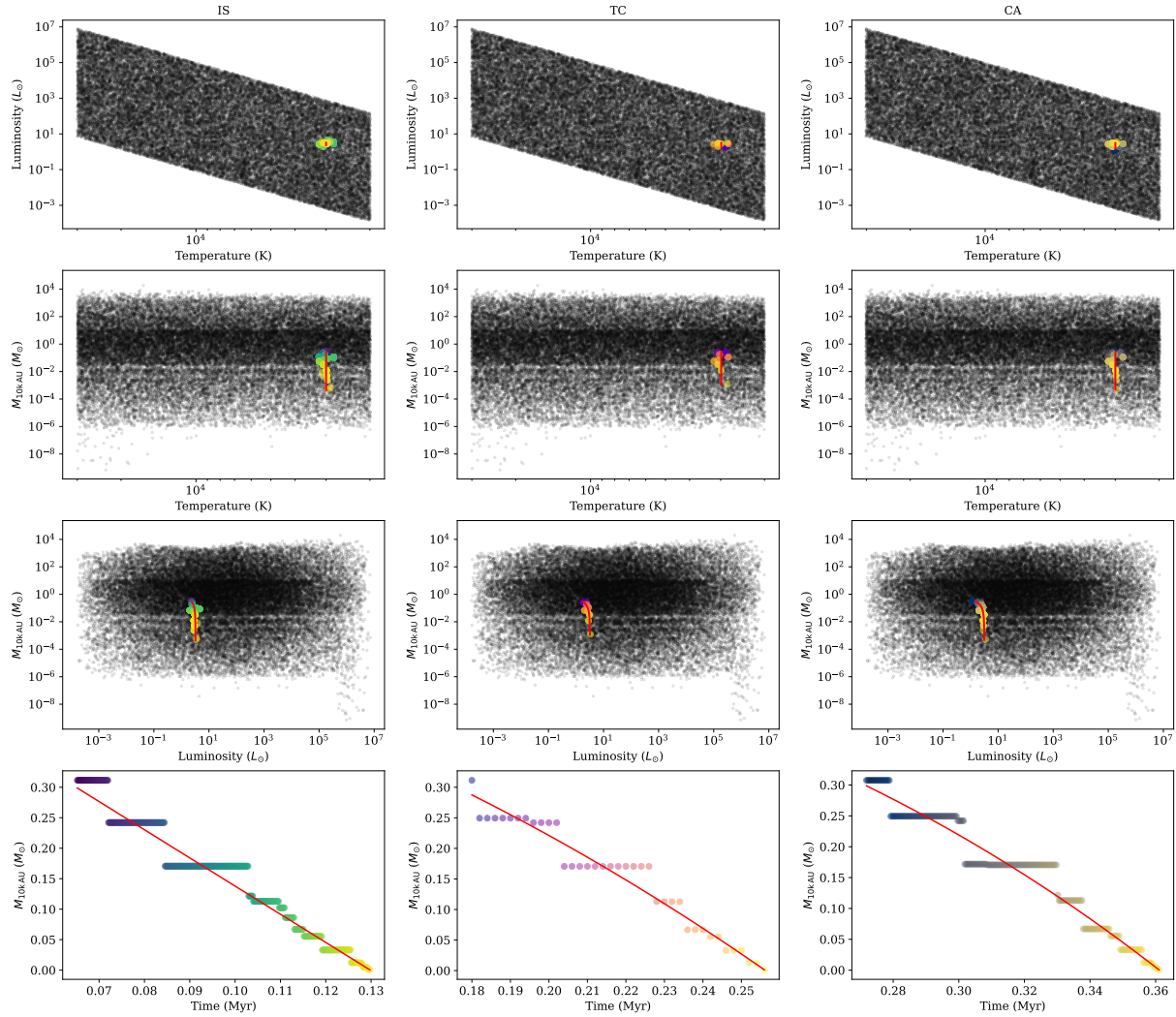


Figure E-1. The same as Figure 3-2 for $0.2M_{\odot}$ stars.

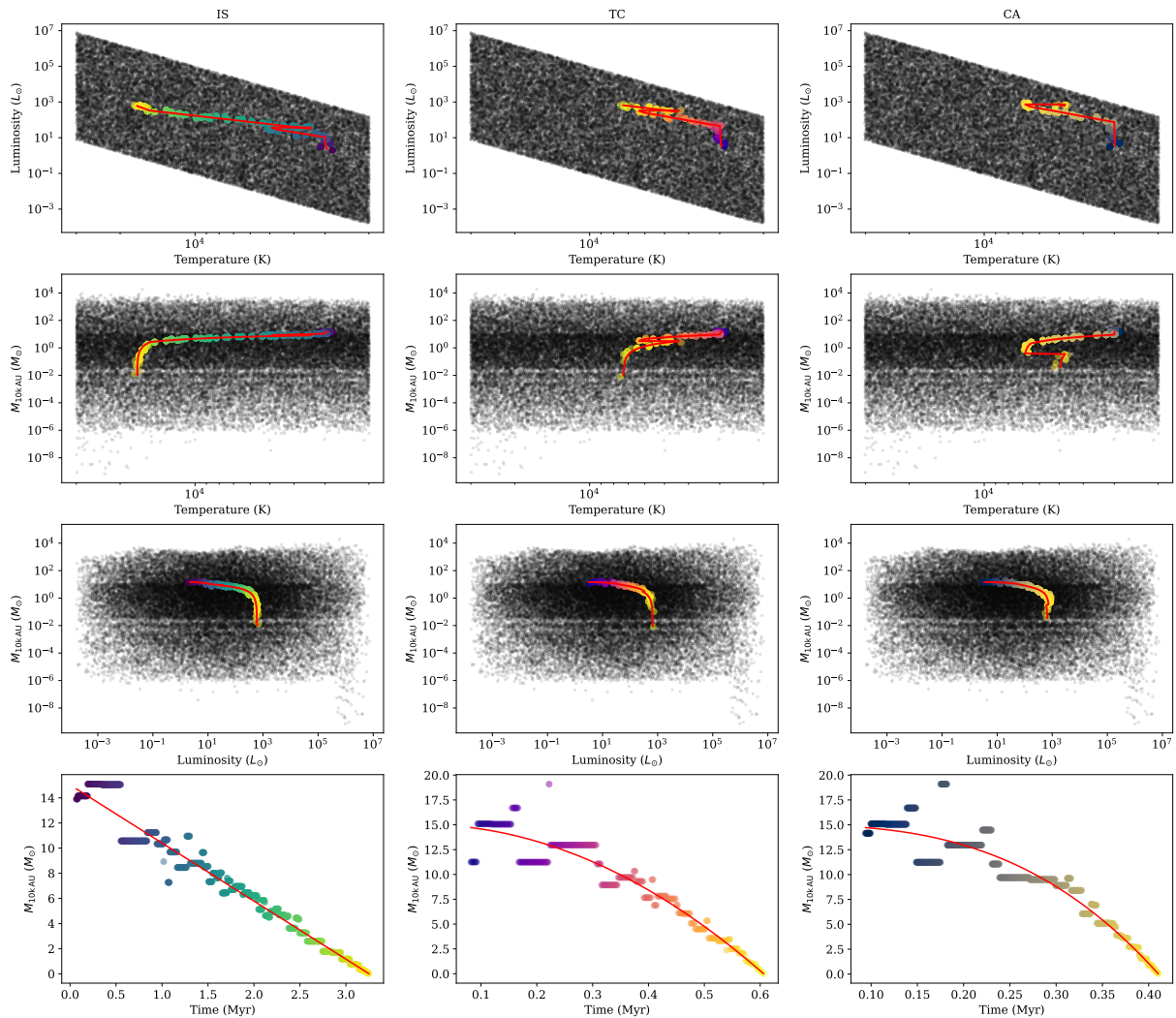


Figure E-2. The same as Figure 3-2 for $5M_{\odot}$ stars.

APPENDIX F ZHANG & TAN (2018) CLASS-CLASS PLOTS

In Section 3.4.2.3, I used the ability to associate the radiative transfer models of Richardson et al. (2024, R24) with evolutionary histories to probe the connection between various definitions of Class 0, an empirically determined observational category for YSOs meant to identify the most deeply embedded protostars, and Stage 0, the deeply embedded physical state. However, multiple other sets of YSO models exist beyond R24, most of which are more explicitly built to capture particular areas of parameter space or portray specific evolutionary scenarios than the randomly sampled models of R24. As a result, it is possible that trends that differ from those observed with the models of R24 will appear in grids constructed under different assumptions.

In order to investigate the possibility of more targeted modeling yielding different conclusions on the effectiveness of Class as a measure of Stage, I repeat the analysis of Section 3.4.2.3 on the YSO models of Zhang & Tan (2018, ZT18), a grid based on the turbulent-core theory of protostellar growth (see Chapter 3.4.1 for further work with these models). The ZT18 models are explicitly created with specific evolutionary histories in mind which generally follow a scaled-up paradigm of traditional core-collapse star formation (though with the addition of support from turbulence), making it a straightforward task to assign them Stages. I calculate the bolometric temperature and ratio of submillimeter to bolometric luminosity for each model directly from their SEDs; the boundaries for Class 0 remain the same. Meanwhile, I assign the models a Stage using two different definition schemes in order to visualize their effects; that developed by Richardson et al. (2025, R25) and the traditional Stage 0/I divide of Andre et al. (1993, A93). (The difference between these dividing lines is explored further in Figure 3-13 and Section 3.4.2.3.) As neither scheme identifies any models of Stage II or later within ZT18, both may be used across the entire grid. I show the results in Figure F-1.

Examining the distribution of ZT18 models within this space, most models that are Class 0 by luminosity ratio are also Class 0 by T_{bol} . However, many models that are Class 0 by T_{bol} would be considered Class I by luminosity ratio. This is a reversal of the relative distribution of models

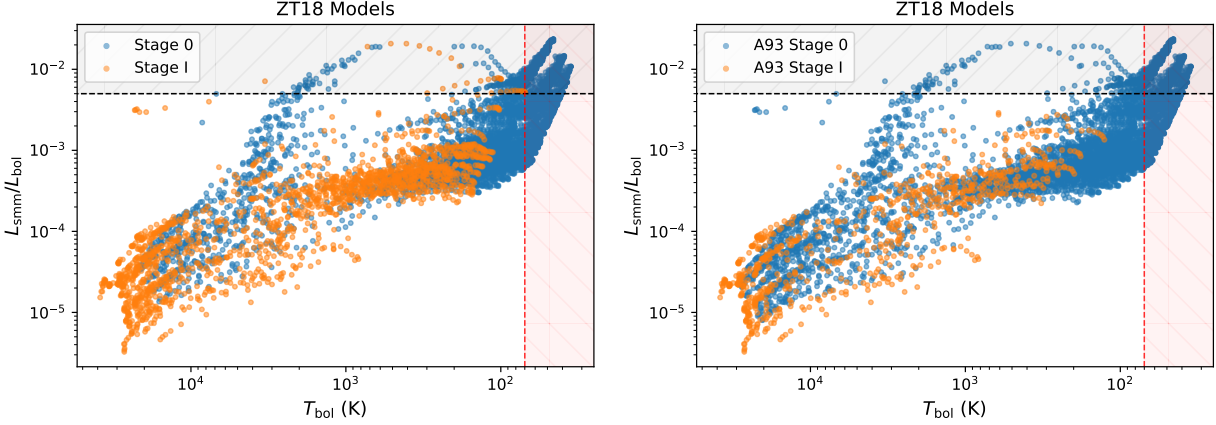


Figure F-1. The same as Figure 3-12, but done for the models of the ZT18 grid. Models are assigned stages following both the R25 definition (§3.4.2) (*left*) and the Andre et al. (1993) definition for Stage 0 (*right*). The black shaded area contains models deemed Class 0 through their luminosity ratios, while the red region indicates Class 0 by bolometric temperature. See Section 3.4.2.3 and Chapter 4 for a fuller discussion on the import of Classes and Stages.

in R24 as well as the relative proportions of observed YSOs in Dunham et al. (2014), though the physical ramifications of this difference is unclear.

Turning to the positions of Stages, the range of values exhibited by Stage 0 models is generally shifted to lower T_{bol} and higher $L_{\text{smm}}/L_{\text{bol}}$ than Stage I models, with the lowest temperature for Stage I across both definitions falling at roughly 70 K, the Class 0/I divide. As such, nearly all Stage I models would not be assigned Class 0 by either scheme, and would therefore not be mistaken for Stage 0 YSOs based on Class. However, it is evident that beyond that, that the two Stages are generally distributed in roughly the same way, and furthermore that said distribution departs significantly from that expected by the traditional Class system. Many of these models would be considered Class II or even III by T_{bol} , and exhibit a wide range of values in $L_{\text{smm}}/L_{\text{bol}}$, illustrating that the Class of these models is an imperfect gauge of their evolutionary state. This is generally in line with the trends observed in Section 3.4.2.3.

Comparing the two Stage definition schemes, more of ZT18's models are considered Stage 0 following the A93 definition, which sets its dividing line at the point where M_{\star} meets M_{env} . This is a natural consequence emerging from the theory behind ZT18, which (unlike the

traditional core-collapse scenario underpinning A93) assumes that not all of the mass initially present within a YSO’s envelope will eventually reach the star. Consequently, the point at which the mass of the central star exceeds that of the envelope comes after the central star has accreted half of its mass—the R25 dividing line—thereby pushing models which were Stage I by the latter definition into Stage 0. As a result, Stage 0 covers a wider range of T_{bol} and $L_{\text{smm}}/L_{\text{bol}}$ and the range of Stage I is shifted to higher T_{bol} and lower $L_{\text{smm}}/L_{\text{bol}}$. (It is perhaps worth noting that this shift in Stage I means that a clear majority of Stage I models by the A93 definition have $T_{\text{bol}} > 650$ K, placing them in a class “later” than I.)

ZT18 includes a number of properties for its YSO models; in Figure F-2, I examine the relationship between a model’s position in $T_{\text{bol}} - L_{\text{smm}}/L_{\text{bol}}$ space and its initial core mass M_{core} , parent clump surface density Σ_{cl} , ratio of instantaneous envelope mass to intial core mass $M_{\text{env}}/M_{\text{core}}$, and inclination. M_{core} does not exhibit a significant correlation with position, although there appears to be a slight downward trend in the luminosity ratio of a core with its initial mass at low T_{bol} . Σ_{cl} seems to occasionally separate the models into distinct strips of luminosity ratios, particularly for $T_{\text{bol}} \gtrsim 5000$ K, but this behavior is inconsistent. There is a general trend towards higher T_{bol} and lower $L_{\text{smm}}/L_{\text{bol}}$ as an envelope is accreted, in line with the general expectations for Class progression; however, this trend is not monotonic. Likewise, there is a clear split in the models visible through inclination, with more edge-on sources typically having lower bolometric temperatures and higher luminosity ratios than more face-on sources. This provides an illustration of the dependence of observational diagnostics like T_{bol} on observational effects such as viewing angle.

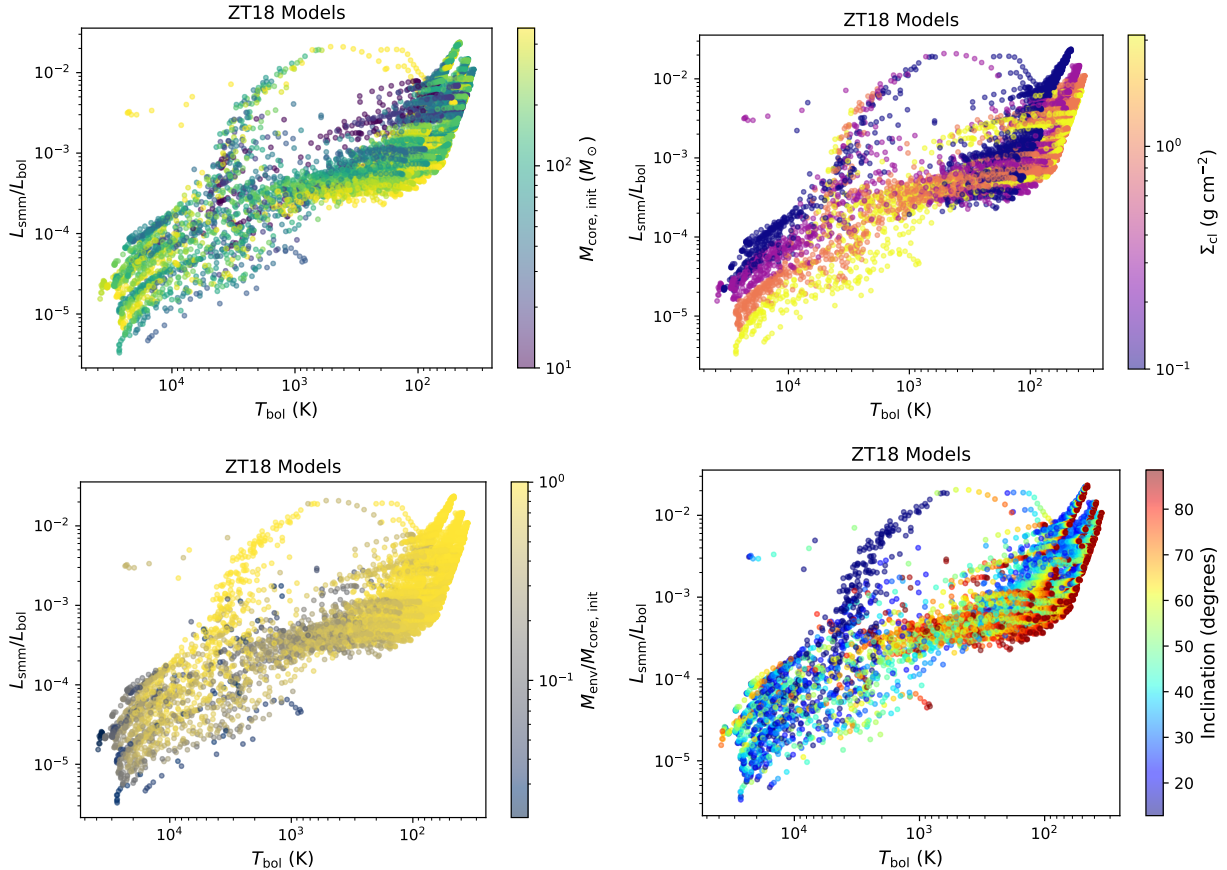


Figure F-2. Figure F-1 with models colored by various properties, including the initial core mass associated with each model (*top left*), clump surface density (*top right*), instantaneous envelope mass as a fraction of initial core mass (*bottom left*) and viewing angle (*bottom right*).

LIST OF REFERENCES

- Adams, F. C. 1990, ApJ , 363, 578, doi: [10.1086/169367](https://doi.org/10.1086/169367)
- Adams, F. C., Lada, C. J., & Shu, F. H. 1987, ApJ , 312, 788, doi: [10.1086/164924](https://doi.org/10.1086/164924)
- Adams, F. C., & Shu, F. H. 1985, ApJ , 296, 655, doi: [10.1086/163483](https://doi.org/10.1086/163483)
- . 1986, ApJ , 308, 836, doi: [10.1086/164555](https://doi.org/10.1086/164555)
- Allen, L., Megeath, S. T., Gutermuth, R., et al. 2007, in Protostars and Planets V, ed. B. Reipurth, D. Jewitt, & K. Keil, 361, doi: [10.48550/arXiv.astro-ph/0603096](https://arxiv.org/abs/0603096)
- Allen, L. E., Calvet, N., D'Alessio, P., et al. 2004, ApJS , 154, 363, doi: [10.1086/422715](https://doi.org/10.1086/422715)
- Alstott, J., Bullmore, E., & Plenz, D. 2014, PLoS ONE, 9, e85777, doi: [10.1371/journal.pone.0085777](https://doi.org/10.1371/journal.pone.0085777)
- Alves, J., Lombardi, M., & Lada, C. J. 2007, A&A , 462, L17, doi: [10.1051/0004-6361:20066389](https://doi.org/10.1051/0004-6361:20066389)
- Andre, P., & Montmerle, T. 1994, ApJ , 420, 837, doi: [10.1086/173608](https://doi.org/10.1086/173608)
- Andre, P., Ward-Thompson, D., & Barsony, M. 1993, ApJ , 406, 122, doi: [10.1086/172425](https://doi.org/10.1086/172425)
- André, P., Men'shchikov, A., Bontemps, S., et al. 2010, A&A , 518, L102, doi: [10.1051/0004-6361/201014666](https://doi.org/10.1051/0004-6361/201014666)
- Astropy Collaboration, Robitaille, T. P., Tollerud, E. J., et al. 2013, A&A , 558, A33, doi: [10.1051/0004-6361/201322068](https://doi.org/10.1051/0004-6361/201322068)
- Astropy Collaboration, Price-Whelan, A. M., Sipőcz, B. M., et al. 2018, AJ , 156, 123, doi: [10.3847/1538-3881/aabc4f](https://doi.org/10.3847/1538-3881/aabc4f)
- Astropy Collaboration, Price-Whelan, A. M., Lim, P. L., et al. 2022, ApJ , 935, 167, doi: [10.3847/1538-4357/ac7c74](https://doi.org/10.3847/1538-4357/ac7c74)
- Bally, J., & Zinnecker, H. 2005, AJ , 129, 2281, doi: [10.1086/429098](https://doi.org/10.1086/429098)
- Bastian, N., Covey, K. R., & Meyer, M. R. 2010, ARA&A , 48, 339, doi: [10.1146/annurev-astro-082708-101642](https://doi.org/10.1146/annurev-astro-082708-101642)
- Bate, M. R. 2009, MNRAS , 397, 232, doi: [10.1111/j.1365-2966.2009.14970.x](https://doi.org/10.1111/j.1365-2966.2009.14970.x)
- . 2012, MNRAS , 419, 3115, doi: [10.1111/j.1365-2966.2011.19955.x](https://doi.org/10.1111/j.1365-2966.2011.19955.x)
- Bernasconi, P. A., & Maeder, A. 1996, A&A , 307, 829
- Bohren, C. F., & Huffman, D. R. 1983, Absorption and scattering of light by small particles (Wiley)
- Bonnell, I. A., Bate, M. R., Clarke, C. J., & Pringle, J. E. 1997, MNRAS , 285, 201, doi: [10.1093/mnras/285.1.201](https://doi.org/10.1093/mnras/285.1.201)

- . 2001, MNRAS , 323, 785, doi: [10.1046/j.1365-8711.2001.04270.x](https://doi.org/10.1046/j.1365-8711.2001.04270.x)
- Bonnell, I. A., Larson, R. B., & Zinnecker, H. 2007, in Protostars and Planets V, ed. B. Reipurth, D. Jewitt, & K. Keil, 149, doi: [10.48550/arXiv.astro-ph/0603447](https://arxiv.org/abs/astro-ph/0603447)
- Bontemps, S., Andre, P., Terebey, S., & Cabrit, S. 1996, A&A , 311, 858
- Brott, I., & Hauschildt, P. H. 2005, in ESA Special Publication, Vol. 576, The Three-Dimensional Universe with Gaia, ed. C. Turon, K. S. O'Flaherty, & M. A. C. Perryman, 565, doi: [10.48550/arXiv.astro-ph/0503395](https://arxiv.org/abs/astro-ph/0503395)
- Calvet, N., Hartmann, L., Kenyon, S. J., & Whitney, B. A. 1994, ApJ , 434, 330, doi: [10.1086/174731](https://doi.org/10.1086/174731)
- Carney, M. T., Yıldız, U. A., Mottram, J. C., et al. 2016, A&A , 586, A44, doi: [10.1051/0004-6361/201526308](https://doi.org/10.1051/0004-6361/201526308)
- Cassen, P., & Moosman, A. 1981, Icarus , 48, 353, doi: [10.1016/0019-1035\(81\)90051-8](https://doi.org/10.1016/0019-1035(81)90051-8)
- Castelli, F., & Kurucz, R. L. 2003, in IAU Symposium, Vol. 210, Modelling of Stellar Atmospheres, ed. N. Piskunov, W. W. Weiss, & D. F. Gray, A20, doi: [10.48550/arXiv.astro-ph/0405087](https://arxiv.org/abs/astro-ph/0405087)
- Cerviño, M., Román-Zúñiga, C., Luridiana, V., et al. 2013, A&A , 553, A31, doi: [10.1051/0004-6361/201219504](https://doi.org/10.1051/0004-6361/201219504)
- Chabrier, G. 2003, ApJL , 586, L133, doi: [10.1086/374879](https://doi.org/10.1086/374879)
- Chen, H., Myers, P. C., Ladd, E. F., & Wood, D. O. S. 1995, ApJ , 445, 377, doi: [10.1086/175703](https://doi.org/10.1086/175703)
- Choi, J., Dotter, A., Conroy, C., et al. 2016, ApJ , 823, 102, doi: [10.3847/0004-637X/823/2/102](https://doi.org/10.3847/0004-637X/823/2/102)
- Clauzet, A., Shalizi, C. R., & Newman, M. E. J. 2009, SIAM Review, 51, 661, doi: [10.1137/070710111](https://doi.org/10.1137/070710111)
- Conroy, C., & van Dokkum, P. G. 2012, ApJ , 760, 71, doi: [10.1088/0004-637X/760/1/71](https://doi.org/10.1088/0004-637X/760/1/71)
- Cotera, A. S., Whitney, B. A., Young, E., et al. 2001, ApJ , 556, 958, doi: [10.1086/321627](https://doi.org/10.1086/321627)
- Crapsi, A., van Dishoeck, E. F., Hogerheijde, M. R., Pontoppidan, K. M., & Dullemond, C. P. 2008, A&A , 486, 245, doi: [10.1051/0004-6361:20078589](https://doi.org/10.1051/0004-6361:20078589)
- da Silva, R. L., Fumagalli, M., & Krumholz, M. 2012, ApJ , 745, 145, doi: [10.1088/0004-637X/745/2/145](https://doi.org/10.1088/0004-637X/745/2/145)
- Dask Development Team. 2016, Dask: Library for dynamic task scheduling.
<http://dask.pydata.org>

- De Marchi, G., Paresce, F., Panagia, N., et al. 2011, *ApJ*, 739, 27,
doi: [10.1088/0004-637X/739/1/27](https://doi.org/10.1088/0004-637X/739/1/27)
- Dotter, A. 2016, *ApJS*, 222, 8, doi: [10.3847/0067-0049/222/1/8](https://doi.org/10.3847/0067-0049/222/1/8)
- Draine, B. T. 2003a, *ApJ*, 598, 1017, doi: [10.1086/379118](https://doi.org/10.1086/379118)
- . 2003b, *ApJ*, 598, 1026, doi: [10.1086/379123](https://doi.org/10.1086/379123)
- Draine, B. T., Dale, D. A., Bendo, G., et al. 2007, *ApJ*, 663, 866, doi: [10.1086/518306](https://doi.org/10.1086/518306)
- Duarte-Cabral, A., Bontemps, S., Motte, F., et al. 2013, *A&A*, 558, A125,
doi: [10.1051/0004-6361/201321393](https://doi.org/10.1051/0004-6361/201321393)
- Dunham, M. M., Evans, II, N. J., Terebey, S., Dullemond, C. P., & Young, C. H. 2010, *ApJ*, 710, 470, doi: [10.1088/0004-637X/710/1/470](https://doi.org/10.1088/0004-637X/710/1/470)
- Dunham, M. M., & Vorobyov, E. I. 2012, *ApJ*, 747, 52, doi: [10.1088/0004-637X/747/1/52](https://doi.org/10.1088/0004-637X/747/1/52)
- Dunham, M. M., Arce, H. G., Allen, L. E., et al. 2013, *AJ*, 145, 94,
doi: [10.1088/0004-6256/145/4/94](https://doi.org/10.1088/0004-6256/145/4/94)
- Dunham, M. M., Stutz, A. M., Allen, L. E., et al. 2014, in *Protostars and Planets VI*, ed. H. Beuther, R. S. Klessen, C. P. Dullemond, & T. Henning, 195–218,
doi: [10.2458/azu_uapress_9780816531240-ch009](https://doi.org/10.2458/azu_uapress_9780816531240-ch009)
- Dunham, M. M., Allen, L. E., Evans, II, N. J., et al. 2015, *ApJS*, 220, 11,
doi: [10.1088/0067-0049/220/1/11](https://doi.org/10.1088/0067-0049/220/1/11)
- Elia, D., Schisano, E., Molinari, S., et al. 2010, *A&A*, 518, L97,
doi: [10.1051/0004-6361/201014651](https://doi.org/10.1051/0004-6361/201014651)
- Elia, D., Molinari, S., Fukui, Y., et al. 2013, *ApJ*, 772, 45, doi: [10.1088/0004-637X/772/1/45](https://doi.org/10.1088/0004-637X/772/1/45)
- Enoch, M. L., Evans, II, N. J., Sargent, A. I., & Glenn, J. 2009, *ApJ*, 692, 973,
doi: [10.1088/0004-637X/692/2/973](https://doi.org/10.1088/0004-637X/692/2/973)
- Evans, N., Calvet, N., Cieza, L., et al. 2009a, arXiv e-prints, arXiv:0901.1691,
doi: [10.48550/arXiv.0901.1691](https://doi.org/10.48550/arXiv.0901.1691)
- Evans, II, N. J., Dunham, M. M., Jørgensen, J. K., et al. 2009b, *ApJS*, 181, 321,
doi: [10.1088/0067-0049/181/2/321](https://doi.org/10.1088/0067-0049/181/2/321)
- Federman, S., Megeath, S. T., Tobin, J. J., et al. 2023, *ApJ*, 944, 49,
doi: [10.3847/1538-4357/ac9f4b](https://doi.org/10.3847/1538-4357/ac9f4b)
- Federrath, C., & Klessen, R. S. 2012, *ApJ*, 761, 156, doi: [10.1088/0004-637X/761/2/156](https://doi.org/10.1088/0004-637X/761/2/156)
- Fischer, W. J., Hillenbrand, L. A., Herczeg, G. J., et al. 2023, in *Astronomical Society of the Pacific Conference Series*, Vol. 534, *Protostars and Planets VII*, ed. S. Inutsuka, Y. Aikawa, T. Muto, K. Tomida, & M. Tamura, 355, doi: [10.48550/arXiv.2203.11257](https://doi.org/10.48550/arXiv.2203.11257)

Fischer, W. J., Megeath, S. T., Stutz, A. M., et al. 2013, Astronomische Nachrichten, 334, 53,
doi: [10.1002/asna.201211761](https://doi.org/10.1002/asna.201211761)

Fischer, W. J., Megeath, S. T., Furlan, E., et al. 2017, ApJ , 840, 69,
doi: [10.3847/1538-4357/aa6d69](https://doi.org/10.3847/1538-4357/aa6d69)

Fischer, W. J., Battersby, C., Johnstone, D., et al. 2024, AJ , 167, 82,
doi: [10.3847/1538-3881/ad188b](https://doi.org/10.3847/1538-3881/ad188b)

Fitzpatrick, E. L. 1999, PASP , 111, 63, doi: [10.1086/316293](https://doi.org/10.1086/316293)

Fontanive, C., Biller, B., Bonavita, M., & Allers, K. 2018, MNRAS , 479, 2702,
doi: [10.1093/mnras/sty1682](https://doi.org/10.1093/mnras/sty1682)

Furlan, E., Fischer, W. J., Ali, B., et al. 2016, ApJS , 224, 5, doi: [10.3847/0067-0049/224/1/5](https://doi.org/10.3847/0067-0049/224/1/5)

Gezer, I., Marton, G., Roquette, J., et al. 2025, arXiv e-prints, arXiv:2502.18629.
<https://arxiv.org/abs/2502.18629>

Ginsburg, A., Csengeri, T., Galván-Madrid, R., et al. 2022, A&A , 662, A9,
doi: [10.1051/0004-6361/202141681](https://doi.org/10.1051/0004-6361/202141681)

Greene, T. P., Wilking, B. A., Andre, P., Young, E. T., & Lada, C. J. 1994, ApJ , 434, 614,
doi: [10.1086/174763](https://doi.org/10.1086/174763)

Großschedl, J. E., Alves, J., Teixeira, P. S., et al. 2019, A&A , 622, A149,
doi: [10.1051/0004-6361/201832577](https://doi.org/10.1051/0004-6361/201832577)

Grudić, M. Y., Guszejnov, D., Hopkins, P. F., Offner, S. S. R., & Faucher-Giguère, C.-A. 2021,
MNRAS , 506, 2199, doi: [10.1093/mnras/stab1347](https://doi.org/10.1093/mnras/stab1347)

Gunawardhana, M. L. P., Hopkins, A. M., Sharp, R. G., et al. 2011, MNRAS , 415, 1647,
doi: [10.1111/j.1365-2966.2011.18800.x](https://doi.org/10.1111/j.1365-2966.2011.18800.x)

Gutermuth, R. A., Megeath, S. T., Myers, P. C., et al. 2009, ApJS , 184, 18,
doi: [10.1088/0067-0049/184/1/18](https://doi.org/10.1088/0067-0049/184/1/18)

Gutermuth, R. A., Bourke, T. L., Allen, L. E., et al. 2008, ApJL , 673, L151,
doi: [10.1086/528710](https://doi.org/10.1086/528710)

Haas, M. R., & Anders, P. 2010, A&A , 512, A79, doi: [10.1051/0004-6361/200912967](https://doi.org/10.1051/0004-6361/200912967)

Harris, C. R., Millman, K. J., van der Walt, S. J., et al. 2020, Nature, 585, 357,
doi: [10.1038/s41586-020-2649-2](https://doi.org/10.1038/s41586-020-2649-2)

Haworth, T. J., Clarke, C. J., Rahman, W., Winter, A. J., & Facchini, S. 2018, MNRAS , 481, 452,
doi: [10.1093/mnras/sty2323](https://doi.org/10.1093/mnras/sty2323)

Heiderman, A., & Evans, II, N. J. 2015, ApJ , 806, 231, doi: [10.1088/0004-637X/806/2/231](https://doi.org/10.1088/0004-637X/806/2/231)

- Hennebelle, P., & Grudić, M. Y. 2024, ARA&A , 62, 63,
doi: [10.1146/annurev-astro-052622-031748](https://doi.org/10.1146/annurev-astro-052622-031748)
- Hernandez, D., Roquette, J., Gezer, I., et al. 2024, In prep
- Holman, K., Walch, S. K., Goodwin, S. P., & Whitworth, A. P. 2013, MNRAS , 432, 3534,
doi: [10.1093/mnras/stt705](https://doi.org/10.1093/mnras/stt705)
- Hopkins, A. M. 2018, PASA , 35, e039, doi: [10.1017/pasa.2018.29](https://doi.org/10.1017/pasa.2018.29)
- Hosokawa, T., & Omukai, K. 2009, ApJ , 691, 823, doi: [10.1088/0004-637X/691/1/823](https://doi.org/10.1088/0004-637X/691/1/823)
- Hosokawa, T., Yorke, H. W., & Omukai, K. 2010, ApJ , 721, 478,
doi: [10.1088/0004-637X/721/1/478](https://doi.org/10.1088/0004-637X/721/1/478)
- Hunter, J. D. 2007, Computing in Science & Engineering, 9, 90, doi: [10.1109/MCSE.2007.55](https://doi.org/10.1109/MCSE.2007.55)
- Indebetouw, R., Mathis, J. S., Babler, B. L., et al. 2005, ApJ , 619, 931, doi: [10.1086/426679](https://doi.org/10.1086/426679)
- Jørgensen, J. K., van Dishoeck, E. F., Visser, R., et al. 2009, A&A , 507, 861,
doi: [10.1051/0004-6361/200912325](https://doi.org/10.1051/0004-6361/200912325)
- Kauffmann, J., Bertoldi, F., Bourke, T. L., Evans, II, N. J., & Lee, C. W. 2008, A&A , 487, 993,
doi: [10.1051/0004-6361:200809481](https://doi.org/10.1051/0004-6361:200809481)
- Kennicutt, R. C., & Evans, N. J. 2012, ARA&A , 50, 531,
doi: [10.1146/annurev-astro-081811-125610](https://doi.org/10.1146/annurev-astro-081811-125610)
- Kenyon, S. J., Hartmann, L. W., Strom, K. M., & Strom, S. E. 1990, AJ , 99, 869,
doi: [10.1086/115380](https://doi.org/10.1086/115380)
- Kim, S.-H., Martin, P. G., & Hendry, P. D. 1994, ApJ , 422, 164, doi: [10.1086/173714](https://doi.org/10.1086/173714)
- Kirkpatrick, J. D. 2005, ARA&A , 43, 195, doi: [10.1146/annurev.astro.42.053102.134017](https://doi.org/10.1146/annurev.astro.42.053102.134017)
- Klassen, M., Pudritz, R. E., & Peters, T. 2012, MNRAS , 421, 2861,
doi: [10.1111/j.1365-2966.2012.20523.x](https://doi.org/10.1111/j.1365-2966.2012.20523.x)
- Klaus, A., Yu, S., & Plenz, D. 2011, PLoS ONE, 6, e19779,
doi: [10.1371/journal.pone.0019779](https://doi.org/10.1371/journal.pone.0019779)
- König, C., Urquhart, J. S., Csengeri, T., et al. 2017, A&A , 599, A139,
doi: [10.1051/0004-6361/201526841](https://doi.org/10.1051/0004-6361/201526841)
- Könyves, V., André, P., Men'shchikov, A., et al. 2015, A&A , 584, A91,
doi: [10.1051/0004-6361/201525861](https://doi.org/10.1051/0004-6361/201525861)
- Kroupa, P. 2001, MNRAS , 322, 231, doi: [10.1046/j.1365-8711.2001.04022.x](https://doi.org/10.1046/j.1365-8711.2001.04022.x)
- Kroupa, P., Weidner, C., Pflamm-Altenburg, J., et al. 2013, in Planets, Stars and Stellar Systems. Volume 5: Galactic Structure and Stellar Populations, ed. T. D. Oswalt & G. Gilmore, Vol. 5 (Springer, Dordrecht), 115, doi: [10.1007/978-94-007-5612-0_4](https://doi.org/10.1007/978-94-007-5612-0_4)

- Krumholz, M. R. 2014, PhR , 539, 49, doi: [10.1016/j.physrep.2014.02.001](https://doi.org/10.1016/j.physrep.2014.02.001)
- Krumholz, M. R., Fumagalli, M., da Silva, R. L., Rendahl, T., & Parra, J. 2015, MNRAS , 452, 1447, doi: [10.1093/mnras/stv1374](https://doi.org/10.1093/mnras/stv1374)
- Kryukova, E., Megeath, S. T., Gutermuth, R. A., et al. 2012, AJ , 144, 31, doi: [10.1088/0004-6256/144/2/31](https://doi.org/10.1088/0004-6256/144/2/31)
- Kudryavtseva, N., Brandner, W., Gennaro, M., et al. 2012, ApJL , 750, L44, doi: [10.1088/2041-8205/750/2/L44](https://doi.org/10.1088/2041-8205/750/2/L44)
- Lada, C. J. 1987, in IAU Symposium, Vol. 115, Star Forming Regions, ed. M. Peimbert & J. Jugaku, 1
- Lada, C. J. 1991, in NATO Advanced Study Institute (ASI) Series C, Vol. 342, The Physics of Star Formation and Early Stellar Evolution, ed. C. J. Lada & N. D. Kylafis, 329, doi: [10.1007/978-94-011-3642-6_9](https://doi.org/10.1007/978-94-011-3642-6_9)
- Lada, C. J., & Wilking, B. A. 1984, ApJ , 287, 610, doi: [10.1086/162719](https://doi.org/10.1086/162719)
- Lada, C. J., Muench, A. A., Luhman, K. L., et al. 2006, AJ , 131, 1574, doi: [10.1086/499808](https://doi.org/10.1086/499808)
- Ladd, E. F., Adams, F. C., Casey, S., et al. 1991, ApJ , 366, 203, doi: [10.1086/169553](https://doi.org/10.1086/169553)
- Ladd, E. F., Lada, E. A., & Myers, P. C. 1993, ApJ , 410, 168, doi: [10.1086/172735](https://doi.org/10.1086/172735)
- Larson, R. B. 1969, MNRAS , 145, 271, doi: [10.1093/mnras/145.3.271](https://doi.org/10.1093/mnras/145.3.271)
- Launhardt, R., Stutz, A. M., Schmiedeke, A., et al. 2013, A&A , 551, A98, doi: [10.1051/0004-6361/201220477](https://doi.org/10.1051/0004-6361/201220477)
- Lee, Y.-N., Offner, S. S. R., Hennebelle, P., et al. 2020, SSRv , 216, 70, doi: [10.1007/s11214-020-00699-2](https://doi.org/10.1007/s11214-020-00699-2)
- Louvet, F., Hennebelle, P., Men'shchikov, A., et al. 2021, A&A , 653, A157, doi: [10.1051/0004-6361/202040053](https://doi.org/10.1051/0004-6361/202040053)
- Lu, J. R., Do, T., Ghez, A. M., et al. 2013, ApJ , 764, 155, doi: [10.1088/0004-637X/764/2/155](https://doi.org/10.1088/0004-637X/764/2/155)
- Luhman, K. L. 2012, ARA&A , 50, 65, doi: [10.1146/annurev-astro-081811-125528](https://doi.org/10.1146/annurev-astro-081811-125528)
- Machida, M. N., & Matsumoto, T. 2012, MNRAS , 421, 588, doi: [10.1111/j.1365-2966.2011.20336.x](https://doi.org/10.1111/j.1365-2966.2011.20336.x)
- Matzner, C. D., & McKee, C. F. 2000, ApJ , 545, 364, doi: [10.1086/317785](https://doi.org/10.1086/317785)
- McClure, M. K., Furlan, E., Manoj, P., et al. 2010, ApJS , 188, 75, doi: [10.1088/0067-0049/188/1/75](https://doi.org/10.1088/0067-0049/188/1/75)
- McKee, C. F., & Offner, S. S. R. 2010, ApJ , 716, 167, doi: [10.1088/0004-637X/716/1/167](https://doi.org/10.1088/0004-637X/716/1/167)

- McKee, C. F., & Tan, J. C. 2002, *Nature* , 416, 59, doi: [10.1038/416059a](https://doi.org/10.1038/416059a)
- . 2003, *ApJ* , 585, 850, doi: [10.1086/346149](https://doi.org/10.1086/346149)
- Megeath, S. T., Allen, L. E., Gutermuth, R. A., et al. 2004, *ApJS* , 154, 367, doi: [10.1086/422823](https://doi.org/10.1086/422823)
- Megeath, S. T., Gutermuth, R., Muzerolle, J., et al. 2012, *AJ* , 144, 192, doi: [10.1088/0004-6256/144/6/192](https://doi.org/10.1088/0004-6256/144/6/192)
- Moe, M., & Di Stefano, R. 2017, *ApJS* , 230, 15, doi: [10.3847/1538-4365/aa6fb6](https://doi.org/10.3847/1538-4365/aa6fb6)
- Molinari, S., Pezzuto, S., Cesaroni, R., et al. 2008, *A&A* , 481, 345, doi: [10.1051/0004-6361:20078661](https://doi.org/10.1051/0004-6361:20078661)
- Molinari, S., Baldeschi, A., Robitaille, T. P., et al. 2019, *MNRAS* , 486, 4508, doi: [10.1093/mnras/stz900](https://doi.org/10.1093/mnras/stz900)
- Motte, F., Andre, P., & Neri, R. 1998, *A&A* , 336, 150
- Motte, F., Bontemps, S., Csengeri, T., et al. 2022, *A&A* , 662, A8, doi: [10.1051/0004-6361/202141677](https://doi.org/10.1051/0004-6361/202141677)
- Myers, P. C. 2011, *ApJ* , 743, 98, doi: [10.1088/0004-637X/743/1/98](https://doi.org/10.1088/0004-637X/743/1/98)
- . 2012, *ApJ* , 752, 9, doi: [10.1088/0004-637X/752/1/9](https://doi.org/10.1088/0004-637X/752/1/9)
- . 2014, *ApJ* , 781, 33, doi: [10.1088/0004-637X/781/1/33](https://doi.org/10.1088/0004-637X/781/1/33)
- Myers, P. C., Adams, F. C., Chen, H., & Schaff, E. 1998, *ApJ* , 492, 703, doi: [10.1086/305048](https://doi.org/10.1086/305048)
- Myers, P. C., & Ladd, E. F. 1993, *ApJL* , 413, L47, doi: [10.1086/186956](https://doi.org/10.1086/186956)
- Nakano, T., Hasegawa, T., Morino, J.-I., & Yamashita, T. 2000, *ApJ* , 534, 976, doi: [10.1086/308765](https://doi.org/10.1086/308765)
- Nakano, T., Hasegawa, T., & Norman, C. 1995, *ApJ* , 450, 183, doi: [10.1086/176130](https://doi.org/10.1086/176130)
- Nandakumar, G., Schultheis, M., Feldmeier-Krause, A., et al. 2018, *A&A* , 609, A109, doi: [10.1051/0004-6361/201731918](https://doi.org/10.1051/0004-6361/201731918)
- Nutter, D., & Ward-Thompson, D. 2007, *MNRAS* , 374, 1413, doi: [10.1111/j.1365-2966.2006.11246.x](https://doi.org/10.1111/j.1365-2966.2006.11246.x)
- Offner, S. S. R., Clark, P. C., Hennebelle, P., et al. 2014, in *Protostars and Planets VI*, ed. H. Beuther, R. S. Klessen, C. P. Dullemond, & T. Henning, 53–75, doi: [10.2458/azu_uapress_9780816531240-ch003](https://doi.org/10.2458/azu_uapress_9780816531240-ch003)
- Offner, S. S. R., Klein, R. I., McKee, C. F., & Krumholz, M. R. 2009, *ApJ* , 703, 131, doi: [10.1088/0004-637X/703/1/131](https://doi.org/10.1088/0004-637X/703/1/131)

- Offner, S. S. R., & McKee, C. F. 2011, ApJ , 736, 53, doi: [10.1088/0004-637X/736/1/53](https://doi.org/10.1088/0004-637X/736/1/53)
- Offner, S. S. R., Moe, M., Kratter, K. M., et al. 2023, in Astronomical Society of the Pacific Conference Series, Vol. 534, Protostars and Planets VII, ed. S. Inutsuka, Y. Aikawa, T. Muto, K. Tomida, & M. Tamura, 275, doi: [10.48550/arXiv.2203.10066](https://doi.org/10.48550/arXiv.2203.10066)
- Ossenkopf, V., & Henning, T. 1994, A&A , 291, 943
- Padoan, P., Pan, L., Juvela, M., Haugbølle, T., & Nordlund, Å. 2020, ApJ , 900, 82, doi: [10.3847/1538-4357/abaa47](https://doi.org/10.3847/1538-4357/abaa47)
- Palla, F., & Stahler, S. W. 2000, ApJ , 540, 255, doi: [10.1086/309312](https://doi.org/10.1086/309312)
- Pavlík, V., Kroupa, P., & Šubr, L. 2019, A&A , 626, A79, doi: [10.1051/0004-6361/201834265](https://doi.org/10.1051/0004-6361/201834265)
- Paxton, B., Bildsten, L., Dotter, A., et al. 2011, ApJS , 192, 3, doi: [10.1088/0067-0049/192/1/3](https://doi.org/10.1088/0067-0049/192/1/3)
- Paxton, B., Cantiello, M., Arras, P., et al. 2013, ApJS , 208, 4, doi: [10.1088/0067-0049/208/1/4](https://doi.org/10.1088/0067-0049/208/1/4)
- Paxton, B., Marchant, P., Schwab, J., et al. 2015, ApJS , 220, 15, doi: [10.1088/0067-0049/220/1/15](https://doi.org/10.1088/0067-0049/220/1/15)
- Pedregosa, F., Varoquaux, G., Gramfort, A., et al. 2011, Journal of Machine Learning Research, 12, 2825
- Pelkonen, V. M., Padoan, P., Haugbølle, T., & Nordlund, Å. 2021, MNRAS , 504, 1219, doi: [10.1093/mnras/stab844](https://doi.org/10.1093/mnras/stab844)
- Peltonen, J., Rosolowsky, E., Williams, T. G., et al. 2024, MNRAS , 527, 10668, doi: [10.1093/mnras/stad3879](https://doi.org/10.1093/mnras/stad3879)
- Penston, M. V. 1969, MNRAS , 144, 425, doi: [10.1093/mnras/144.4.425](https://doi.org/10.1093/mnras/144.4.425)
- Plunkett, A. L., Fernández-López, M., Arce, H. G., et al. 2018, A&A , 615, A9, doi: [10.1051/0004-6361/201732372](https://doi.org/10.1051/0004-6361/201732372)
- Pokhrel, R., Megeath, S. T., Gutermuth, R. A., et al. 2023, ApJS , 266, 32, doi: [10.3847/1538-4365/acbfac](https://doi.org/10.3847/1538-4365/acbfac)
- Popescu, B., & Hanson, M. M. 2014, ApJ , 780, 27, doi: [10.1088/0004-637X/780/1/27](https://doi.org/10.1088/0004-637X/780/1/27)
- Portegies Zwart, S. F., McMillan, S. L. W., & Gieles, M. 2010, ARA&A , 48, 431, doi: [10.1146/annurev-astro-081309-130834](https://doi.org/10.1146/annurev-astro-081309-130834)
- Pouteau, Y., Motte, F., Nony, T., et al. 2022, A&A , 664, A26, doi: [10.1051/0004-6361/202142951](https://doi.org/10.1051/0004-6361/202142951)
- Richardson, T., Ginsburg, A., Indebetouw, R., & Robitaille, T. P. 2024, ApJ , 961, 188, doi: [10.3847/1538-4357/ad072d](https://doi.org/10.3847/1538-4357/ad072d)

- Richardson, T., Ginsburg, A., Rosolowsky, E., Peltonen, J., & Indebetouw, R. 2025, submitted
- Robitaille, T. P. 2011, *A&A* , 536, A79, doi: [10.1051/0004-6361/201117150](https://doi.org/10.1051/0004-6361/201117150)
- . 2017, *A&A* , 600, A11, doi: [10.1051/0004-6361/201425486](https://doi.org/10.1051/0004-6361/201425486)
- Robitaille, T. P., Whitney, B. A., Indebetouw, R., & Wood, K. 2007, *ApJS* , 169, 328, doi: [10.1086/512039](https://doi.org/10.1086/512039)
- Robitaille, T. P., Whitney, B. A., Indebetouw, R., Wood, K., & Denzmore, P. 2006, *ApJS* , 167, 256, doi: [10.1086/508424](https://doi.org/10.1086/508424)
- Rodrigo, C., & Solano, E. 2020, in XIV.0 Scientific Meeting (virtual) of the Spanish Astronomical Society, 182
- Rodrigo, C., Solano, E., & Bayo, A. 2012, SVO Filter Profile Service Version 1.0, IVOA Working Draft 15 October 2012, doi: [10.5479/ADS/bib/2012ivoa.rept.1015R](https://doi.org/10.5479/ADS/bib/2012ivoa.rept.1015R)
- Roquette, J., Hernandez, D., Gezer, I., et al. 2024, In prep
- Salpeter, E. E. 1955, *ApJ* , 121, 161, doi: [10.1086/145971](https://doi.org/10.1086/145971)
- Schneider, F. R. N., Sana, H., Evans, C. J., et al. 2018, *Science*, 359, 69, doi: [10.1126/science.aan0106](https://doi.org/10.1126/science.aan0106)
- Sheehan, P. D., Tobin, J. J., Looney, L. W., & Megeath, S. T. 2022, *ApJ* , 929, 76, doi: [10.3847/1538-4357/ac574d](https://doi.org/10.3847/1538-4357/ac574d)
- Shu, F. H. 1977, *ApJ* , 214, 488, doi: [10.1086/155274](https://doi.org/10.1086/155274)
- Smith, N., Povich, M. S., Whitney, B. A., et al. 2010, *MNRAS* , 406, 952, doi: [10.1111/j.1365-2966.2010.16792.x](https://doi.org/10.1111/j.1365-2966.2010.16792.x)
- Smith, R. J. 2020, *ARA&A* , 58, 577, doi: [10.1146/annurev-astro-032620-020217](https://doi.org/10.1146/annurev-astro-032620-020217)
- Stutz, A. M., Tobin, J. J., Stanke, T., et al. 2013, *ApJ* , 767, 36, doi: [10.1088/0004-637X/767/1/36](https://doi.org/10.1088/0004-637X/767/1/36)
- Tan, J. C., & McKee, C. F. 2004, *ApJ* , 603, 383, doi: [10.1086/381490](https://doi.org/10.1086/381490)
- Terebey, S., Shu, F. H., & Cassen, P. 1984, *ApJ* , 286, 529, doi: [10.1086/162628](https://doi.org/10.1086/162628)
- Tobin, J. J., & Sheehan, P. D. 2024, *ARA&A* , 62, 203, doi: [10.1146/annurev-astro-052920-103752](https://doi.org/10.1146/annurev-astro-052920-103752)
- Tobin, J. J., Sheehan, P. D., Megeath, S. T., et al. 2020a, *ApJ* , 890, 130, doi: [10.3847/1538-4357/ab6f64](https://doi.org/10.3847/1538-4357/ab6f64)
- Tobin, J. J., Sheehan, P. D., Reynolds, N., et al. 2020b, *ApJ* , 905, 162, doi: [10.3847/1538-4357/abc5bf](https://doi.org/10.3847/1538-4357/abc5bf)

- Ulrich, R. K. 1976, ApJ , 210, 377, doi: [10.1086/154840](https://doi.org/10.1086/154840)
- van Kempen, T. A., van Dishoeck, E. F., Salter, D. M., et al. 2009, A&A , 498, 167, doi: [10.1051/0004-6361/200810445](https://doi.org/10.1051/0004-6361/200810445)
- Virtanen, P., Gommers, R., Oliphant, T. E., et al. 2020, Nature Methods, 17, 261, doi: [10.1038/s41592-019-0686-2](https://doi.org/10.1038/s41592-019-0686-2)
- Weidner, C., & Kroupa, P. 2006, MNRAS , 365, 1333, doi: [10.1111/j.1365-2966.2005.09824.x](https://doi.org/10.1111/j.1365-2966.2005.09824.x)
- Weingartner, J. C., & Draine, B. T. 2001, ApJ , 563, 842, doi: [10.1086/324035](https://doi.org/10.1086/324035)
- Weisz, D. R., Johnson, L. C., Foreman-Mackey, D., et al. 2015, ApJ , 806, 198, doi: [10.1088/0004-637X/806/2/198](https://doi.org/10.1088/0004-637X/806/2/198)
- White, R. J., Greene, T. P., Doppmann, G. W., Covey, K. R., & Hillenbrand, L. A. 2007, in Protostars and Planets V, ed. B. Reipurth, D. Jewitt, & K. Keil, 117, doi: [10.48550/arXiv.astro-ph/0604081](https://arxiv.org/abs/0604081)
- Whitney, B. A., Indebetouw, R., Bjorkman, J. E., & Wood, K. 2004, ApJ , 617, 1177, doi: [10.1086/425608](https://doi.org/10.1086/425608)
- Whitney, B. A., Robitaille, T. P., Bjorkman, J. E., et al. 2013, ApJS , 207, 30, doi: [10.1088/0067-0049/207/2/30](https://doi.org/10.1088/0067-0049/207/2/30)
- Whitney, B. A., Wood, K., Bjorkman, J. E., & Cohen, M. 2003a, ApJ , 598, 1079, doi: [10.1086/379068](https://doi.org/10.1086/379068)
- Whitney, B. A., Wood, K., Bjorkman, J. E., & Wolff, M. J. 2003b, ApJ , 591, 1049, doi: [10.1086/375415](https://doi.org/10.1086/375415)
- Winters, J. G., Henry, T. J., Jao, W.-C., et al. 2019, AJ , 157, 216, doi: [10.3847/1538-3881/ab05dc](https://doi.org/10.3847/1538-3881/ab05dc)
- Wood, K., Wolff, M. J., Bjorkman, J. E., & Whitney, B. 2002, ApJ , 564, 887, doi: [10.1086/324285](https://doi.org/10.1086/324285)
- Young, C. H., & Evans, II, N. J. 2005, ApJ , 627, 293, doi: [10.1086/430436](https://doi.org/10.1086/430436)
- Zhang, Y., & Tan, J. C. 2011, ApJ , 733, 55, doi: [10.1088/0004-637X/733/1/55](https://doi.org/10.1088/0004-637X/733/1/55)
- . 2018, ApJ , 853, 18, doi: [10.3847/1538-4357/aaa24a](https://doi.org/10.3847/1538-4357/aaa24a)
- Zhang, Y., Tan, J. C., & McKee, C. F. 2013, ApJ , 766, 86, doi: [10.1088/0004-637X/766/2/86](https://doi.org/10.1088/0004-637X/766/2/86)

BIOGRAPHICAL SKETCH

Theo Richardson is an active astronomer, originally from Herndon, VA. He has written, developed, and contributed to many published results and open-source software packages at the leading edge of star formation research. He graduated from the University of Florida in 2025, obtaining an M.S. and Ph.D. in astronomy during his time there. Prior to graduate school, he received a B.A. in astronomy from Cornell University in 2019. In his spare time, he also enjoys making music, expanding his cooking repertoire, and playing spirited (if not technically proficient) games of golf and pickleball.